Synthesis and characterization of particles fabricated by layer-by-layer assembly

Dissertation

zur Erlangung des Doktorgrades
der Naturwissenschaften
(Dr. rer. nat.)

dem
Fachbereich Physik
der Philipps-Universität Marburg

vorgelegt von

Xiang Yu

aus
Sichuan, China

Marburg, 2014

Vom Fachbereich Physik der Philipps-Universität (Hochschulkennziffer 1180)
als Dissertation angenommen am:

Erstgutachter: Prof. Dr. Wolfgang J. Parak
Zweitgutachter: Prof. Dr. Martin Koch
Prüfer: Prof. Dr. Peter Lenz
Prüfer: Prof. Dr. Marc Schneider
Tag der mündlichen Prüfung:

Die vorliegende Arbeit wurde am Fachbereich Physik
der Philipps-Universität Marburg unter der Anleitung von

Herrn Prof. Dr. Wolfgang J. Parak

in der Zeit von September 2010 bis September 2014 angefertigt.

Zusammenfassung

Das Thema der vorliegenden Dissertation ist die Synthese und Charakterisierung von Mikrokapseln und Nanopartikeln, welche durch das Layer-by-Layer-Verfahren hergestellt wurden. Dieses Verfahren basiert auf der Adsorption von Schichten positiv und negativ geladener Polymere, ähnlich der Schichtstruktur einer Zwiebel. Die Synthesen von Polyelektrolytmehrfachschichten wurden durch elektrostatische Anziehung auf Kalziumkarbonat-Mikropartikeln und Gold-Nanopartikeln durchgeführt. Aufgrund des Größenunterschieds der Partikel wurden zwei verschiedene Strategien für die Beschichtung gewählt.

Das erste Ziel war die Beschichtung von sphärischen Kalziumkarbonatpartikeln mit einem Durchmesser von 1-6 µm mit unterschiedlich geladenen Polyelektrolyten. Dabei wurden Polyelektrolyte mit verschiedenen Eigenschaften benutzt, um die Kapseln herzustellen. Das System biologisch abbaubarer Kapseln bestand aus Dextransulfat und Poly-Arginin (DEXS/PARG), während die nichtabbaubaren Kapseln aus Poly(Natrium-4-Styrolsulfat) und Poly-Allylamin-Hydrochlorid (PAH/PSS) bestand. Weiterhin wurden Kapseln mit einer Silicahülle hergestellt, die aufgrund ihrer Ladungsneutralität und Bioabbaubarkeit ausgewählt und mit den anderen Kapselsorten verglichen wurde. Für das Beladen der Partikel wurden zwei verschiedene Ansätze verfolgt: i) die Co-Precipitation-Methode und ii) das Post-Loading. Die Effizienz der Kapselbeladung wurde untersucht.

Desweiteren wurden multifunktionelle Kapseln produziert, indem magnetische Nanopartikel oder Gold-Nanopartikel in die Hülle der Kapseln eingebettet wurden. Die Funktionalisierung wurde dabei wieder durch elektrostatische Anziehung zwischen Nanopartikeln und Polyelektrolyten bedingt. Verschiedene Anwendungen dieses Systems für Transportaufgaben und Detektion wurden untersucht. i) Polyelektrolytkapseln mit und ohne magnetische Nanopartikel in der Hülle wurden per Post-Loading mit dem pH-Indikator Seminaphtarodafluor (SNARF) beladen. Der Aufbau dieser Kapseln war $(PSS/PAH)_2$(Magnetnanopartikel)$(PSS/PAH)_2$. Die Ergebnisse zeigen, dass das eingekapselte ionensensitive Fluorophor ein Ionensensor mit kurzer Reaktionszeit (500 ms im Fall von SNARF) ist, der desweiteren im Magnetfeld bewegt werden kann. ii) Kubische, magnetische Nanopartikel wurden in die Hülle der Kapseln eingebettet, wobei Poly(acrylamid-co-diallyldimethylammoniumchlorid) P(Am-DDA) anstelle von PAH verwendet wurde, da die große Ladung von P(Am-DDA) zur besseren Anlagerung der Nanopartikel führte. Die Struktur der Hülle war (PSS/PAH)- (PSS/P(Am-DDA)-Magnetnanopartikel(PAH)$(PSS/PAH)_2$. Da magnetische Nanopartikel durch Anregung mit einem alternierenden Magnetfeld Hitze erzeugen, können die Kapseln auf diese Weise geöffnet werden. iii) Bioabbaubare und mit Licht anregbare Kapseln mit einer Hülle aus Polyelektrolyten und Silica wurden

hergestellt, wobei optothermische Goldnanopartikel in die Hülle eingearbeitet wurden. Die Struktur der Kapseln war (1) mPEG-SH@SiO_2@PARG, (2) (PSS/PAH)@AuNP@mPEG-SH-@SiO_2@PARG, (3) $(DEXS/PARG)_5$, (4) $(DEXS/PARG)_3$AuNP$(DEXS/PARG)_2$, (5) $(PSS/PAH)_5$, and (6) $(PSS/PAH)_3$AuNP$(PSS/PAH)_2$. Zusätzlich wurde die Zytotoxizität dieser Kapseln untersucht. Weitere Charakterisierungsmethoden wie TEM und Zeta-Potential wurden ebenso angewandt.

Die Gold-Nanopartikel wurden mittels des Layer-by-Layer-Verfahrens mit verschiedenen Polyelektrolythüllen beschichtet. Jede Schicht trug 0,5 bis 2 nm Dicke zur Hülle bei, abhängig von den äußeren Bedingungen der Synthese. Indem verschiedene Anzahlen von Polyelektrolytschichten adsorbiert wurden, wurden Hüllen verschiedener Dicke hergestellt. Abhängig von der äußeren Schicht wurden sowohl positive als auch negative Nanopartikel hergestellt. Damit konnte die elektrostatische Bindung von unterschiedlich geladenen Nanopartikeln untersucht werden. Unter Verwendung von stark verdünnten Lösungen von positiven und negativen Partikeln wurden hauptsächlich Dimere aus positiven und negativen Partikeln gebildet.

Ergänzend zu diesen zwei Hauptaspekten der Arbeit können die verschiedenen Charakterisierungsmethoden, die bei beiden Sorten Partikeln (Kalziumkarbonat- und Goldpartikel) zur Anwendung kamen, weitere Informationen über derartige Layer-by-Layer-Synthesen liefern.

Abstract

The subject of this doctoral dissertation is the synthesis and characterization of microcapsules and nanoparticles fabricated by Layer-by-Layer (LbL) assembly. The technique is based on the electrostatically-driven alternated adsorption of cationic and anionic charged polymers in a layer-by-layer fashion, similar to the layer structure of an onion. During these syntheses polyelectrolyte multilayer shells were formed via electrostatic interactions on calcium carbonate ($CaCO_3$) microparticles and gold (Au) nanoparticles (NPs). Due to differences in the size range between microcapsules and nanoparticles, two different strategies were used for the self-assembly of polyelectrolytes.

This work first aimed to investigate the LbL assembly of polyelectrolytes oppositely charged on calcium carbonate spherical particles, which size diameter ranges from 1 to 6 μm. Polyelectrolytes with different nature property have been employed to produce polyelectrolyte multilayer (PEM) capsules: i) sulfate/poly-arginine (DEXS/PARG) for biodegradable shell formation and ii) poly(sodium-4-styrenesulfonate)/poly(allylamine hydrochloride) (PSS/PAH) for non-biodegradable shell formation. In addition, one kind of silica (SiO_2) capsules have been fabricated and their properties such as degradability and release of molecules have been compared with polyelectrolyte capsules. In order to encapsulate different molecular cargo inside the capsules (with silica or polyelectrolyte shells), two main procedures have been employed: i) co-precipitation (or pre-loading) and ii) post-loading. The encapsulation efficiency of both procedures has been investigated.

Moreover, multifunctional capsules have been produced by embedding magnetic NPs or plasmonic NPs into the hull of the capsule. The functionalization was performed using again electrostatic interactions as the major driving force in the assembly between nanoparticles and polyelectrolytes. Thus, some applications of these carrier systems for delivery and sensing were investigated. Firstly, polyelectrolyte capsules post-loaded with the pH indicator seminaphtharhodafluor (SNARF) in their cavity with and without polymer coated iron oxide NPs in their hull were synthesized. The composition of the walls of these magnetic PEM capsules was $(PSS/PAH)_2$ magnetic NPs $(PSS/PAH)_2$. The results indicated that encapsulated ion-sensitive fluorophores can be used to detect fast changes of pH and the capsules can be manipulated (*i.e.*, change the location) in microfluidic devices using magnetic fields. Finally, non-biodegradable capsules loaded with cubic magnetic NPs were produced to study their opening upon the application of an alternating magnetic field. The polymer poly(acrylamide-co-diallyl-dimethyl-ammonium chloride) (P(Am-DDA)) which is strongly positively charged was added within the polyelectrolyte shell to enhance the attachment and increase

the concentration of magnetic NPs. The final architecture of the LbL shell was (PSS/PAH)(PSS/P(Am-DDA) magnetic NPs (PAH)$(PSS/PAH)_2$. Magnetic NPs can be heated by the application of an alternating magnetic field. This fact was used to disrupt and open PEM capsules containing magnetic nanoparticles in the shell. The capsules released then their molecular cargo loaded in their interior.

Regarding the synthesis and application of the aforementioned silica capsules they were fabricated to be degradable and light-responsive. Their efficiency as carriers for delivery of molecules into cells was studied and compared with different kinds of PEM capsules. The architecture of the capsules that were compared was: (1)mPEG-SH@SiO_2@PARG, (2)(PSS/PAH)@AuNPs@mPEG-SH-@SiO_2@PARG, (3)$(DEXS/PARG)_5$, (4)$(DEXS/PARG)_3$AuNPs$(DEXS/PARG)_2$, (5)$(PSS/PAH)_5$, and (6)$(PSS/PAH)_3$AuNPs$(PSS/PAH)_2$. Furthermore, the cytotoxicity of these six kinds of capsules have been investigated. Full characterization of the six kinds of capsules was performed with techniques such as TEM or dynamic light scattering.

In the nanoscale, the LbL approach was applied for the coating of Au NPs. Each layer could contribute between 0.5 and 2 nm in thickness depending on the conditions during the self-assembly. By using different numbers of PE layers, shells with different thicknesses have been generated. Depending on the polarity of the last polyelectrolyte layer, either positively or negatively charged Au NPs were obtained. This gave the opportunity to study the electrostatically-driven linkage between nanoparticles with opposite charges. When negatively and positively charged NPs were mixed together under diluted concentrations, predominantly NP dimers were formed.

Complementary to the main aforementioned studies, all the characterization results recorded during the layer by layer process on the two kinds of nanoparticles (i.e., micro $CaCO_3$ and Au NPs) can offer more information about the conditions to carry out such self-assembly process.

Table of Contents

Zusammenfassung III
Abstract V
Table of Contents VII
1. Introduction 1
1.1 General introduction about Layer by Layer. 1
1.2 Calcium carbonate microparticles 2
1.3 Gold nanoparticles 3
2. General principle of Layer-by-Layer assembly on particles 6
3. Layer by Layer assembly on calcium carbonate micro particle for multifunctional capsules 7
3.1 Methods 7
3.1.1 Synthesis of calcium carbonate cores 7
3.1.2 Co-precipitation of high molecular weight cargos 8
3.1.3 Post-loading of hydrophilic small molecular weight cargos 9
3.1.4 Post-loading of hydrophobic small molecular weight cargos 10
3.1.5 Fabrication of different capsule shells 11
3.1.6 Multifunctionalization of capsules *via* attached nanoparticles inside the hull 13
3.1.7 Cytotoxicity assay of capsules 14
3.2 Result and Discussion 16
3.2.1 Synthesis of calcium carbonate cores 16
3.2.2 Encapsulation efficiency of different cargos in capsules 17
3.2.3 Characterization of capsules 20
3.2.4 Study of time response of pH sensor capsules 22
3.2.5 Opening of capsules with an alternating magnetic fields 25
3.2.6 Opening of capsules with light 29
3.2.7 Cytotoxicity assay of capsules 31
4. Distance control in-between plasmonic nanoparticles 33
4.1 Methods 33
4.1.1 Polyelectrolytes coating of gold nanoparticles via Layer-by-Layer 33
4.1.2 Au dimer formation 34
4.2 Results 35
4.2.1 Control over the shell thickness of gold nanoparticles 35
4.2.2 Dimer formation 38
5. Conclusions and outlook 44
6. Publications 46
6.1 Polyelectrolyte capsules 46
6.2 Nanoparticles on bioapplication 47
7. Materials 49
Chemicals 49
Techniques 49

8. Abbreviations 51
9. List of the capsule 52
10. References 54
Acknowledgement 64
Appendix 65

1. Introduction

1.1 General introduction about Layer by Layer.

The so called Layer-by-Layer (LbL) adsorption technique rose as a wide spread technique around 1990 [1] [2]. It consists in the self-assembly of building blocks (e.g., polymers) to form multilayers. The driving forces can be electrostactic, formation of hydrogen bonds, etc. LbL has already been widely used to fabricate multicomposite films and particles. The LbL technique has many advantages, such as low cost, fast coating speed, environmental protection and stability for long term storing, etc. In order to make functional LbL materials that can be sensitive to different stimulus, more and more organic and inorganic compounds are being used as potential building blocks for LbL. The building blocks of LbL multilayers can be polyelectrolytes [3], DNA [4], proteins [5], polysaccharides [6], and even colloid nanoparticles (NPs) such as quantum dots (QDs) [7], magnetic NPs[8], [9], [10], plasmonic NPs [11], etc.

The first trial of LbL attempt was carried out on a thin glass [1]. In order to enrich the electric statistic potential to the positive charge, the glass template have to be modified with anion polyelectrolytes materials preliminary and make the first opposite charge electrolytes layer attached tightly, (Figure 1).

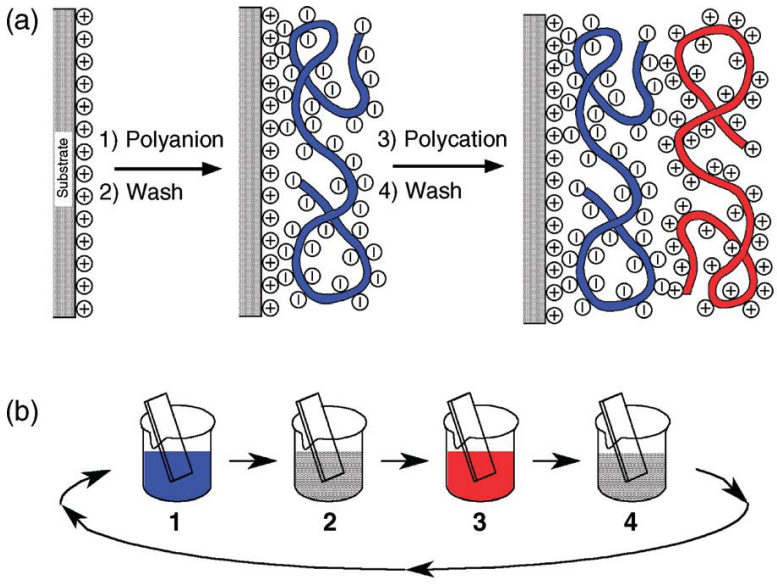

Figure 1. (a) Illustration of the LbL adsorption of a bilayer made of a polyelectrolyte negatively charged and a polyelectrolyte positively charged on a glass slide. The polyelectrolytes self-assemble due to electrostatic interactions (b) Schematic representation of the LbL process. Step 2 and step 4 represent rinsing steps. These four steps are the base of the coating circles. This image was adopted from [1].

LbL assembly is not only limited to thin film formation on glass surfaces. Other kinds of materials can be coated with this technique such as silicon wafers [12] and metal plates [9]. Moreover, the coating can be performed on particles. This was first reported by T. Mallouk in 1995 [13]. Afterwards, Möhwald, Sukhorukov and coworkers, improved and extended the technique to many colloidal particles [14], [15] [16-19] [16, 20] [21].

1.2 Calcium carbonate microparticles

As the last chapter illustrated, particles (colloidal or bigger) can be promising templates for LbL surface modification. Hereby, an ideal particle template for LbL should have the following properties: i) particles should be charged or able to adsorb polyelectrolytes on their surface, ii) particles should be stable against agglomeration during the LbL process that often required high ionic strength and iii) particles should be easily washed and recovered from solution. If the LbL is used to produce capsules then, the particle template should be easily removed by calcinations or dissolution. Until now, many materials have been employed to produce LbL capsules such as latex particles [22], [23], [24]. Latex particles have homogeneous morphology and they are easily coated with charged polyelectrolytes. The main disadvantage is that these particles required tetrahydrofuran (THF) to be dissolved, which is not convenient if the capsules are used for biological applications. Another popular templates are silica (SiO_2) microparticles, but they also required hydrogen fluoride (HF) to be dissolved which is toxic.

An alternative template is calcium carbonate ($CaCO_3$), instead of other templates mentioned above. $CaCO_3$ is a common mineral in nature that can be found in most of rocks. It is also the main component of the shell or skeleton of several biological organisms. In the last decade, this material gained significant attention due to its biocompatibility and low-cost production [16], [25]. Other carbonates such as cadmium carbonate ($CdCO_3$) have been used for material scientists in preliminary investigations [17] but the biocompatibility of these materials is limited by the toxicity of the osmotic cadmium ions (Cd^{2+}). These ions stayed attached to the LbL shell once the capsule is formed after dissolution of the core. Besides, $CaCO_3$, is not toxic and can be dissolved by ethylenediaminetetraacetic acid (EDTA). Moreover, $CaCO_3$ can be loaded by coprecipitation with molecules of biological interest that are also not sensitive to the dissolution conditions. Thus, $CaCO_3$ has many advantages compared with other templates for biological applications.

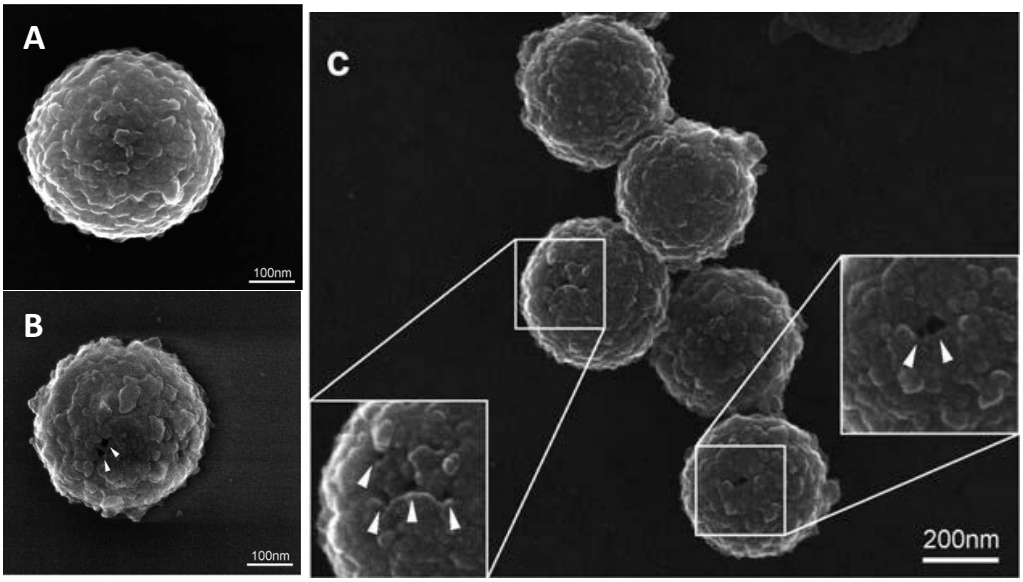

Figure 2. Scanning electron microscopy (SEM) images of (A) freeze-dried multilayer-coated particles and (B and C) freeze-dried capsules recorded at different magnifications. The white arrows indicate holes in the LbL shell. The insets in (C) are magnified 2 times. Image adopted from [26].

During the LbL process, the surface of the coated particles is not perfectly homogeneous but porous as it can be seen in Figure 2. During the dissolution of the template to produce empty shells the osmotic pressure produce as well bigger pores that could be observed by Krzyzanek et al [26]. This phenomenon explains the loss of cargo molecules after core dissolution if they were previously loaded in the $CaCO_3$.

1.3 Gold nanoparticles

Over the past two decades, Au NPs have attracted tremendous attention due to their unique electronic and optical properties arising from their quantum-size effects. The physicochemical properties of Au NPs lead to numerous application, such as biodiagnostics [27, 28], nanomedicine [29], drug delivery [30-32] and plasmonics [33, 34].

Regarding the localized surface plasmon resonance (LSPR), which unique governed by some nobel metal NPs, for example, AuNPs are able to lead collective oscillation of the nonostruction's conduction band electron resonance, to against the restoring force of positive nuclei. The LSPR spectrum can be employed as a monitor tool because it is tightly related on the NPs's size, structure, shape, density, and surface dielectric constant, etc (*Figure 3*) [35].

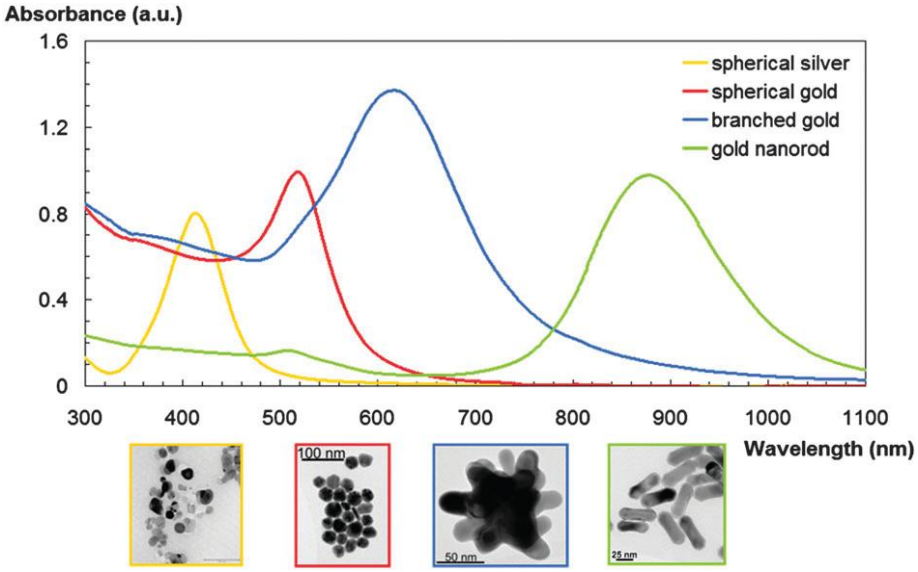

Figure 3. The plasmon resonance of metal NPs is dependent on the size, shape and material. Silver nanoparticles exhibit a plasmon resonance around 400 nm whereas spherical Au NPs have their resonance around 520 nm. Special shaped Au NPs exhibit plasmon resonance at longer wavelength [35].

It was investigated that when metal NPs got closer than their particle diameter, a red-shift of the LSPR induced by the aggregation could be observed [36]. Moreover, the exchange of ligands on the metal NPs often induces a change of the refractive index of the particles that can be detected with UV-vis spectroscopy. Thus, based on this approach, the sensitively measurement are able to monitor the coating behavior of NPs, but this technique requires the extremely low cost and fast instrument such as UV-Vis spectrophotomer.

Since some pioneers coated microparticles with polyelectrolytes successfully [37, 38], this technique to modify particle surfaces was extended to the nano scale regime [39]. However, the stability of particles decreases mainly due to their high surface energy. Therefore, the main challenge was to avoid particle agglomeration during the LbL assembly of polyelectrolytes on nanoparticles. Similarly to the microparticle coating some of the parameters that can affect the stability during the LbL coating of nanoparticles are: i) concentration of nanoparticles, ii) ionic strength, iii) pH, iv) assembly time, v) temperature and vi) length of polyelectrolyte [40]. Schneider et al. investigated the ideal parameters of the LbL procedure [41] (Figure 4) and introduced more applications of the LbL shells such as distance control between nanoparticles [42].

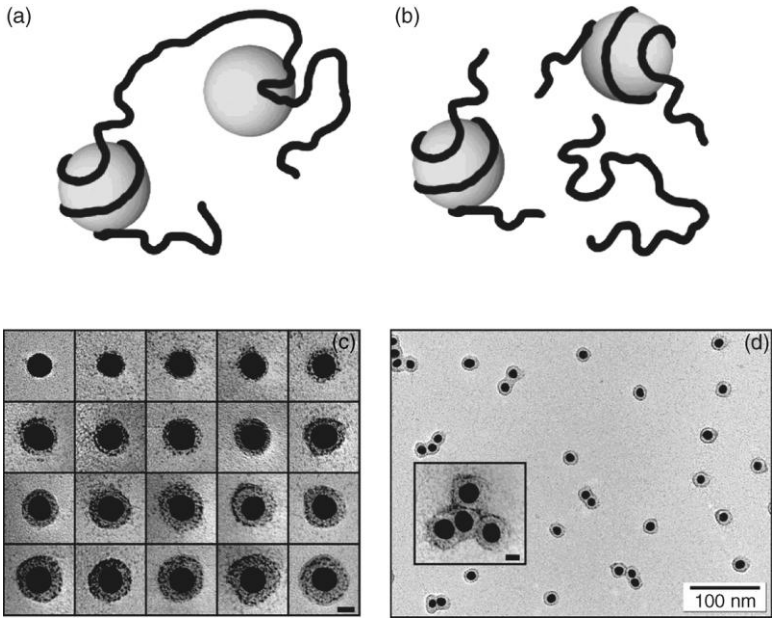

Figure 4. Schematic representation of 13 nm diameter gold NPs being aggregated by bridging flocculation (A) and being successfully wrapped by polyelectrolyte chains (B); lower left part (C) shows the TEM images of several layer polyelectrolytes (the color of the polymer stained by the (osmium tetroxide) coated from 1 to 20 layer; (D)shows particles dominant highly disperse individually after coating finished.

Near-field interactions between plasmonic objects are distance dependent. This is not only related with plasmonic coupling of adjacent metal NPs, but also for enhancement or quenching effects of fluorophores close to plasmonic surfaces [43]. In order to investigate these properties of the fluorophores linked with the NP surface to controlled distance. As new approach, the surface of plasmonic NPs covered with a thin insulating shell or the dye is attached to the surface of the shell successful, which has been demonstrated such as silica shells [44]. Distance control NPs tightly related with the plasmons coupling, which lead quit flexible design about the plasmonic, in particular with lithograph and related technologies [45-47], highlight focused on ion beam [48], or atomic force microscopy [49]. Then, the approach made upon plasmonic colloid NPs assembly by the polymer [50] or wrapped DNA [51]. As the specific monofunctional single NPs are able to binding toward another related specific modified single NPs, the dimer gained successfully as well [52]. These coupling plasmonic NPs mention above were not able to control the inter distance precisely, but, they still performance remarkable effect such as photothemal heating. Thus, combine the approach upon the NPs LbL assemble with polyelectrolytes and the purpose for precise inter distance control of gold dimer, the issue of inter NPs distance control within plasmonic coupling based on the fundamental research rise as a desirable challenge.

In conclusion, the LbL technique can be described as a versatile tool for shell formation due to their highly flexible composition. In this dissertation, two different size scales were investigated: microparticles and nanoparticles.

Multifunctional particles/capsules were fabricated and their biological applications were studied. Full characterization of the LbL particles was performed.

2. General principle of Layer-by-Layer assembly on particles

In LbL deposition procedures, a wide range of materials can be chosen as fabricating multilayer film upon different size scale templates. By using mainly electrostatic attraction as the driving force, different shell compositions are allowed to be built. Thus, many parameters must be chosen depending on the application of the LbL shell. Between these parameters the most relevant are: i) particle template nature, size and shape, ii) nature of shell (degradable, pH sensitive, etc) iii) number of polyelectrolyte layers, iv) final surface charge. During the LbL assembly the stability of the shell and its thickness is affected by: i) the concentration of polyelectrolytes, ii) the molecular weight of the polyelectrolytes, iii) the pH of the solution during the assembly and iv) ionic strength. Nevertheless, there are general principles about the LbL assembly that can be mentioned:

1) The polyelectrolyte assembly deposition upon the template could be claimed achieve in a highly disperse way, but, the beginning assemble circles below third or fourth monolayers should be paid more attention in both nano and micro scale depositions process. It is easy to understand that enough time ensure the assembling process reach to the plateau level. However, the extremely long term such as overnight might bring the agglomeration or even induce aggregation, cause the surface multilayer still not gain enough charge to against the attractive power from Van der Waals' (VDW) force [53] and electrostatic attraction, especially while there are rarely layer polyelectrolytes obtained. Thus, beside the other parameters, control the deposition time in a reasonable period can avoid the aggregation when carry on the LbL process toward the unstable status templates.

2) Polyelectrolytes with similar molecular weight should be chosen for the LbL assembly. As the surface of the spherical template must be obtain the smoothness property, otherwise, in further assemble process, the non-uniform molecular weight polyelectrolytes lead to crosslink and wrap each other toward one dimension instead of three dimension homogenous spherical orientation.

3) As the naked template will aggregate when there is no coating protection, in order to obtain stable core-shell particles the first washing step before the LbL is done only once. After polyelectrolyte coating there are three washing steps between the deposition of a layer of polyelectrolyte and the next one. The washing steps are necessary to ensure an efficient attachment of the polyelectrolytes.

4) There were several characterizations employed for monitoring the LbL

deposition process. Transmission electron microscopy (TEM) is the most direct proof to monitor the polyelectroytes coating, which benefit is easy being understood the disperse property of colloid, but they are still not able to provide more detail of the surface property upon the polyelectrolyte multilayer structure in nanoscale thickness. In addition, due to the polymer nature property, the multilayer structure easy get shrinking or swelling because the energy adsorb induced by strong density electron powder from TEM beam. The UV-spectra do not only observed the disperse stability of colloid NPs, it can be used for detection number of the polyelectrolytes at 226nm in spectra as well [3]. The limit here is quite obviously, because the UV-spectra absorbance related with the concentration of the template, thus, the concentration of the template need to be controlled at same parameter during carry out the whole measurement process. Dynamic light scattering (DLS) usually employed to investigate the size distribution of NPs, it is able to record the non-significant size change especially for NPs. The Zeta potential measurement here provide the direct proof that multilayer build up process is driven by electrostatic attraction (further layer gain) [20]. Therefore, combine both results in DLS and zeta-potential reveal the electrostatic repulsion effect (maintain the same charge template in disperse status individually) due to the LbL.

Hence, even through the general LbL assembly technique enable re-product template in several repeat, it is still recommend to performance in a constant way.

3. Layer by Layer assembly on calcium carbonate micro particle for multifunctional capsules

3.1 Methods

3.1.1 Synthesis of calcium carbonate cores

$CaCO_3$ cores employed as the model template in this work, and the polyelectrolyte are able to attach on the surface of $CaCO_3$ template, even though the core zeta potential close to electric neutrality. Afterwards, $CaCO_3$ template can be removed by EDTA solution and leave the different interesting cargos in capsule, while the hull of the capsule still obtained in stable status as the hollow structure.

The size of the capsule is a compromise issue, which depends on the size of templates. A lot of evidence proved that there is no typical vary about the size of capsules after the core removing [20, 6, 54, 55]. In other words, the size of the cores/ template directly controls the size of the capsules.

Here by, larger bulk capsule not only can stand for loading huge amount of cargos, the disperse property can also be improved upon the colloid stability due to the

Van der Waals' (WDW) power, and the static electric adsorb power will be ignored in the same time [2, 56-58]. However, in living cell uptake assay, bigger capsule perhaps lead the low uptake effective, because the capsule size (6-8 μm) beyond the cells uptake capability (cell size is about 50 μm). In this case, different size of the cores will be synthsized for different applications via controlling the ratio of precursor in order to get the core arrange from 1-2 μm and 2-8 μm diameter.

Whenever the size of $CaCO_3$ templates ranged from 1-2 μm, particles were synthesized by the following protocol. Firstly, in a 250 mL glass beaker, 24.6 mL of 0.33 M $CaCl_2$ solution were mixed with 30.8 mL of 5 mg/mL dextran. With a magnetic stirring of 1200 rpm/min, 4.6 mL of 0.33 M Na_2CO_3 solution was added immediately and stirred only for 30 s, afterwards, the mixture was left without stirring for 2 min in order to grow the core. In this case, the molar ratio Ca^{2+}/CO_3^{2-} was 5.3 which was reported to improve the size distribution of the spherical particles[59],

Then, with the centrifuge (0.2 g for 30 s), the formed spherical $CaCO_3$ was precipitated in the bottom, after discarding the supernatant, the white pellet was washed twice with Milli-Q water, and final once with acetone in order to remove water left from the last rinse step. The total volume of 60 mL of $CaCO_3$ particles was divided in two tubes and the corresponding 1.25 g of particles in each tube were wrapped *via* the LbL approach with different polyelectrolytes.

On the other hand, the bigger $CaCO_3$ cores from 2-8 μm were produced by varying the ratio of the precursors. Simply, aqueous solution of $CaCl_2$ (5 mL, 0.33 M) was mixed with Na_2CO_3 (5 mL, 0.33 M) under magnetic stirring at room temperature [60], following the same protocol as above paragraph described, the bigger core could be gained by vary the ratio as 1:1.

3.1.2 Co-precipitation of high molecular weight cargos

In the co-precipitation procedure, the $CaCO_3$ template was firstly synthesized which contained the expected load cargos; after LbL assembling process, the microsphere core was then emulsified by employing the EDTA and removed from the capsule, while the loaded cargos were still encapsulated in the polyelctrolytes capsules and couldn’t be destroyed by EDTA. As the Figure 5 described, the encapsulation of proteins, fluorescein 5-isothiocyanate bovine serum albumin (FITC-BSA, 66 k Da), was carried out with the co-precipitation procedure as described above, the macromolecules were co-precipitated with $CaCO_3$ during the particle formation; after emulsion with EDTA, the core was removed and the proteins will finally be encapsulated in the capsule.

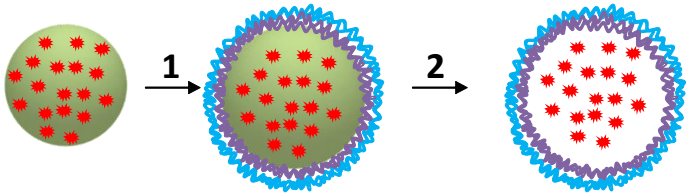

Figure 5. Scheme of the co-precipitation procedure: the 1st step is the process of LbL assembly, the 2nd step represents the process of core removal.

The $CaCO_3$ cores were prepared as described elsewhere [60-62]. Specifically, under magnetically stirring, 615 µL of 0.33 M $CaCl_2$ solution, 770 µL of 50 mg/mL FITC were mixed with 615 µL of 0.33M Na_2CO_3 for 30 s, the solution was then transferred into a tube and further incubated for 2 min. Afterwards, the $CaCO_3$ particles were washed with 1 mL Milli-Q water in three times. Harvest cores by centrifugation at low speed at 110×g at 1min. For further consecutive LbL process or multifunctional application, it should be assembled immediately, otherwise, the naked cores without charges will induce agglomeration. In order to store the naked cores in a long time and avoid agglomeration, the acetone can be used to rinse the core in twice times while the water removed, hence keep the cores highly disperse.

3.1.3 Post-loading of hydrophilic small molecular weight cargos

The method so called as post-loading always applied with small molecular cargo. Regarding the co-precipitate protocol (see the protocol in chapter 3.1.2), the small molecular always easily flee away from the cavity of capsule during the process of $CaCO_3$ templates removal, because of the porous structure of polyelectrolyte hull on the surface of capsules [26]. Not only due to the small hole mentioned above, after removed the cores by EDTA, there are a huge amount of small molecular weight lower than 20-30 kDa were leaked through the porous capsules wall [11].

In the post-loading process, the dextran (2000 kDa) were employed which can be loaded in the co-precipitate process as chapter 2.3 mentioned, this mass molecular weight of dextran has the net structure which can grasp small hydrophilic cargos, such as FITC@Dextran15kDa and Cascade blue@Dextran15kDa. After removing the $CaCO_3$ templates, high concentration of small hydrophilic cargos were added to the capsule solution to produce great concentration range between the outer (high) and inner space (low) of capsules, then the molecular lower than 20-30kDa are allowed to permeate into the cavity of the capsule driving by the concentration range. Meanwhile, in order to promote the permeation speed, the capsules can heated to 65 ºC for 1 h with shrinking until the capsules saturated loaded with the small hydrophilic cargos, followed cooling down the capsules slowly under room temperature. Finally, the capsules were rinsed with water just to remove the extra loading cargos solution but not able to take out the inner capsules loaded cargos, which have been stabilized by the dextran matrix. The sketch at *Figure 6* shows the entire strategy of post-loading method.

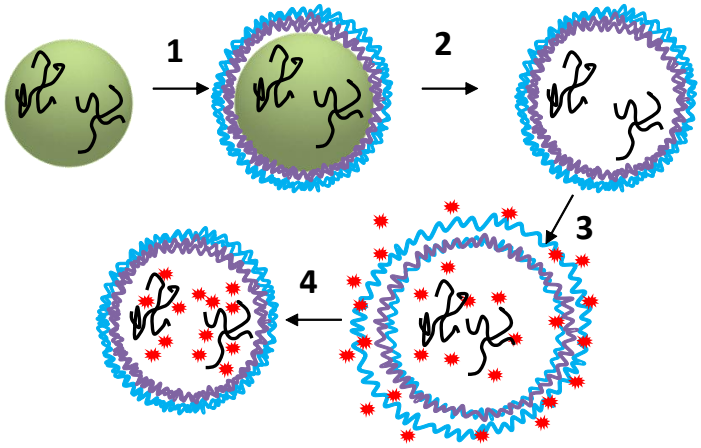

Figure 6. Sketch showing the post-loading strategy for the loading of small hydrophilic molecules. The 1st step illustrates the LbL assembly after the cores made in an co-precipitation method with Dextran; the 2nd step represents the core removal (e.g., $CaCO_3$ by EDTA); The 3rd step describes the process post-loading through the swelling of the polyelectrolyte shell; the 4th step is the cooling process to close the capsules and stop the penetration process. .Afterwards, the sample was washed twice to remove the excess of cargos in solution.

3.1.4 Post-loading of hydrophobic small molecular weight cargos

Most of cancer medicines have the challenges to dissolve in water for future clinical applications, for example, paclitaxel (PTX), doxorubicin hydrochloride (DOX) which can affect the cell uptake efficiency and lead the cells to die.

Here, we employ the DOX (0.58kDa) as the model cargo, investigated the encapsulation effect and related characterization. The encapsulation of DOX was achieved by co-precipitation of polystyrene- block- poly(acrylic acid) (PS-b-PAA) micelles and further post-loading as reported by Tong et al [54]. For this purpose, 10 mg of PS-b-PAA block copolymer was dissolved in 1 mL of dimethylformamide (DMF) and dropwise mixed with 10 mL of Na_2CO_3 (0.33 M) solution under vigorous magnet stirring. After mixing for 30 min, 10 mL of $CaCl_2$ solution was added rapidly and the resulting suspension of $CaCO_3$ particles enriched with PS-b-PAA micelles was mixed for another 30 s. Afterwards, the particles left for 5 min of ripening, and then washed 3 times with ethanol in order to remove unbound exceed PS-b-PAA. Finally, the particles were washed 3 times again with Milli-Q water. The coating procedures of different assemble materials or functional particles for other purpose are similar as last chapter described.

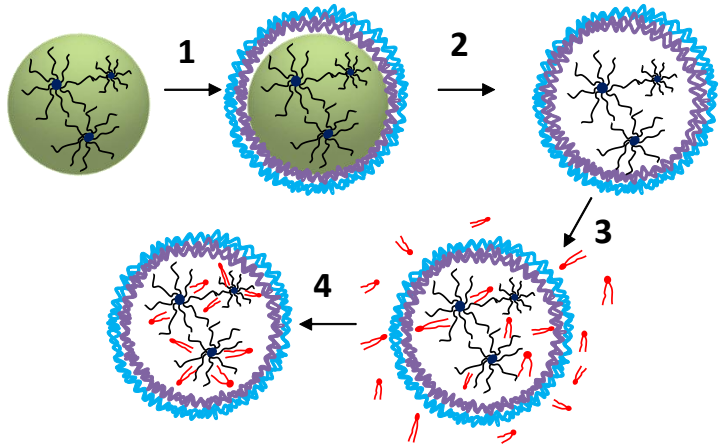

Figure 7 Sketch showing the post-loading strategy for small hydrophobic molecules. The 1st step indicates the LbL assembly after embedded with PS-b-PAA during the co-precipitation process, which is used as the matrix to entrap hydrophobic cargos; the 2nd step shows the core removal process; the 3rd step indicates the capsule incubation with hydrophobic cargos dissolved in an appropriated solvent; the 4th step illustrates the final capsule after 2 washing steps to remove the excess of cargo molecules in solution.

The removal of $CaCO_3$ template was performed with EDTA solution (0,2 M; pH 5,5) for 30 min. Resulting capsules were washed 3 times with Milli-Q water and supernatant solution was removed. Then, the capsules were dispersed in 200 µL of an aqueous solution, which contained the hydrophilic cargo molecules, or in an organic solution with the hydrophobic cargo material for 3 h.

Finally, the capsules were washed 3 times with water to remove unbound cargo substrate and reverse micelle phases towards hydrophilic exterior if they are suspended in organic solvent.

3.1.5 Fabrication of different capsule shells

1) Non-biodegradable polyelectrolyte materials

The poly(sodium 4-styrenesulfonate) (PSS) and poly(allylamine hydrochloride) (PAH) are two kind of polyelectrolyte materials, their stable chemical property and strongly electrostatic charge have been used widely for LbL assembly.

CaCO3 template has slightly positive charge ($\zeta \approx +3$mV), so the following first coating layer of negative polyelectrolyte was PSS (Mw ≈ 70 kDa), then, followed by the positive polyelectrolyte PAH (Mw ≈ 56 kDa), both of polyelectrolyte were chosen with similar molecular weight to avoid agglomeration, might due to the surface coverage with different length molecular lead wrapping crosslink. Each polyelectrolyte was dissolved in 0.5M NaCl solution to get the concentration of 2 mg/mL, and pH value of 6.5 following pervious work. [63, 11]. Then the LbL

assembly was repeated with the same circle until fulfilling the last layer. Finally, the $CaCO_3$ template was completely assembled with the polyelectrolyte shell.

The PSS/PAH structure do not lead to the degradation property, thus, this kind of capsule can be used under the crude solution such as cell culture medium for remote controlling or used as the control group to contrast with degradable capsule in cells uptake assay. In addition, for further multifunctional works, these capsules are able to attach vary kinds of NPs because of the electrostatics between the NPs polymer and capsules electrolytes hull.

2) Biodegradable polyelectrolytes materials

Positively charged $CaCO_3$ particle can also be used as template to prepare biodegradable capsule. The preparation of this core was carried out as described previously, for the synthesis capsules formation of the polyelectrolyte shell. Enzymatically degradable LbL capsules were made with dextran sulfate (DEXS, 40 kDa in negatively charged) and poly-Larginine hydrochloride (PARG, 70 kDa in positively charged) capsules construction. Except the concentration of PARG prepared at 1mg/mL, other parameters for the assemble solution are the same as PSS and PAH solution, which was shown in the last part, as well as removing the $CaCO_3$ from the last chapter.

3) Biodegradable and inorganic materials (Silica)

After $CaCO_3$ cores prepared as described above, they can be used as templates for the formation of the silica capsule which can be employed to encapsulate different molecules[61, 64]. This kind of silica capsules were achieved by wrapping the $CaCO_3$ cores with methoxy-polyethyleneglycol with thiol terminus (mPEG-SH) in ethanol solution, for stabilization the silica adsorbing toward the $CaCO_3$ cores.

Here, we assume that the number of $CaCO_3$ particles was 10^8 in 1 mL, the $CaCO_3$ radius was about 2.5 μm, this corresponded to 40 mPEG-SH molecules added per nm^2 of $CaCO_3$ surface, which was based on the calculation which employed on Au rod stabilized by mPEG-SH molecules [65]. In this case, 3 mg of mPEG-SH in 1 mL Milli-Q water was added to the $CaCO_3$ cores solution and leave the mixture shaking more than 30 min. Afterwards, the $CaCO_3$ particles were washed twice with 1 mL Milli-Q water and once with ethanol (EtOH) in order to remove the exceed mPEG-SH. Then, these templates were transferred phase with 4.5 mL of ethanol to a 40 mL glass vial, following added Milli-Q water 4 mL, ethanol 13.6 mL, and an ammonium hydroxide (NH_4OH) solution at 230 μL. Under fast magnet stirring at 750 rpm, 90 μL of tetraethyl orthosilicate (TEOS) was added, with the stirring at a steady speed of 400 rpm for 3 h. Afterwards, a silica shell had formed around the $CaCO_3$ particles. The particles were then washed twice with ethanol and once with Milli-Q water, followed with adding 1 mL of 0.2 M EDTA at pH 5.5 to dissolve the

$CaCO_3$ cores as it has been reported before[8, 66]. The resulting silica capsules were rinsed three times by water, finally, adding 1 mL of 1 mg/mL (in 0.5 M of NaCl) PARG solution to the capsules to make their final layer in positive charge for further application and long term storing.

3.1.6 Multifunctionalization of capsules *via* attached nanoparticles inside the hull

1) Magnetic NPs attached in the hull of capsules

Control release of the encapsulation cargos can be achieved by using an external stimulus to trigger opening of the capsules. For example, light addressable capsules have been prepared by incorporating metal nanoparticles into the capsule wall.

During the functionalization process, the strong charge NPs are very easily be assembled into the typical capsules due to the charge attraction; while, the weak charges are much difficult to be functionalized to the hull of the typical capsules. In this case, two bilayers of polyelectrolytes will be applied separately for two kinds of NPs.

These strong negative charge maghemite nanoparticles (MNPs, γ-Fe_2O_3) with a core diameter of 31.3 ± 6.3 nm have been synthesized previously following the procedure reported by Hyeon et al [67]. The consecutively coated with amphiphilic polymer (poly(isobutylene-alt-maleic anhydride) as hydrophilic backbone, dodecylamine as hydrophobic ligands) to render the nanoparticles hydrophilic and negatively charged (ζ = -38.9 ± 4 mV) [68] [69] [70].

MNPs (0.2 μM, 0.1 mL) and the two more bilayers electrolytes coated template were mixed in 1 mL of Milli-Q water under vortex shaking overnight. After the sample rinsed twice with water, two more polyelectrolyte bilayers were assembled toward the core-shell structure. Upon core dissolution with EDTA disodium salt, the final PEM capsule architected as $(PSS/PAH)_2$ γ-Fe_2O_3 $(PSS/PAH)_2$. In order to make the magnetic PEM capsules sensitive to pH, seminaphtharhodafluor conjugated dextran (SNARF-dextran, Mw ≈ 10 kDa) was loaded into the empty capsules cavity through the so-called post-loading procedure as mentioned at chapter 3.1.3. Similarly, a second kind of PEM capsules were synthesized without MNPs ($(PSS/PAH)_4$), but loaded the ion sensitive fluorophore SNARF-dextran, in order to study the influence of the MNPs within the polymeric shell in the transport of ions.

For the weak charge NP adsorbing, after desirable layers of polyelectrolyte assembled toward the $CaCO_3$ templates, instead of PAH in the 4th layer, a strong positively charged polymer, poly(acrylamide-co-diallyl-dimethylammonium

chloride) (P(Am-DDA)), was assembly to the LbL shell. This polymer can improve the attachment of magnetic NPs. Specifically, the magnetic NPs were attached to the capsule shell on the positive layer of P(Am-DDA) *via* their negative charge (zeta potential of the magnetic NPs ζ = -24.2 ± 8 mV) , as it was previously reported[8]. The typical final architecture of the LbL shell here such as (PSS/PAH)(PSS/P(Am-DDA) NPs (PAH)$(PSS/PAH)_2$.

2) AuNPs attached as the trigger component in the microcapsule

Au NPs with certain size, shape, and degree of agglomeration are able to absorb IR-light and transform it into heat [71-73]. Cytosolic release triggered *via* light irradiation was achieved in this way by illuminating the gold NPs in the non-degradable shell. Aggregation of Au NPs were assembly *via* electrostatic interactions on top of the bilayer' surface as reported previously [60, 74], the NPs aggregation made by adding the 0.5M NaCl solution in a sonic bath. After the Au NPs attach process finished, rinse step was followed by water in twice to remove exceed uncoated AuNPs. To protect the AuNPs, the final structure of the capsule should be covered more polyelectrolyte layers at least in 4 monolayers. In the synthesis procedure for the non-degradable capsules, the thiol groups bound strongly to the surface of the Au NPs, providing the particles stability in the ethanol/water mixture for rinse during the coating process.

3.1.7 Cytotoxicity assay of capsules

In the cytotoxicity assays, capsules play the role of 'foreign matters'. Previous research have pointed out that the capsule components are not able to induce acute toxicity in living cells[75]. However, capsules are not essential nutrients for cells, which means that they might be harmful or unprofitable for cells. In detail, capsules might contain toxicity effect toward living cells in the three main potential sources shown in below. Firstly, toxicity come from the polyelectrolyte materials either biodegradable or non-biodegradable; secondly, toxicity come from different type functional magnetic or gold nanoparticles attached in the hull of capsule which were a certain extent harmful for cells; in addition, the loaded cargo in the cavity of capsule might contain cytotoxicity effect with living cells which depends on the type of cargo.

Here by, the influence of material type of polyelectrolyte and the type of nanoparticles have been investigated carried out by cytotoxicity assay followed in this part.

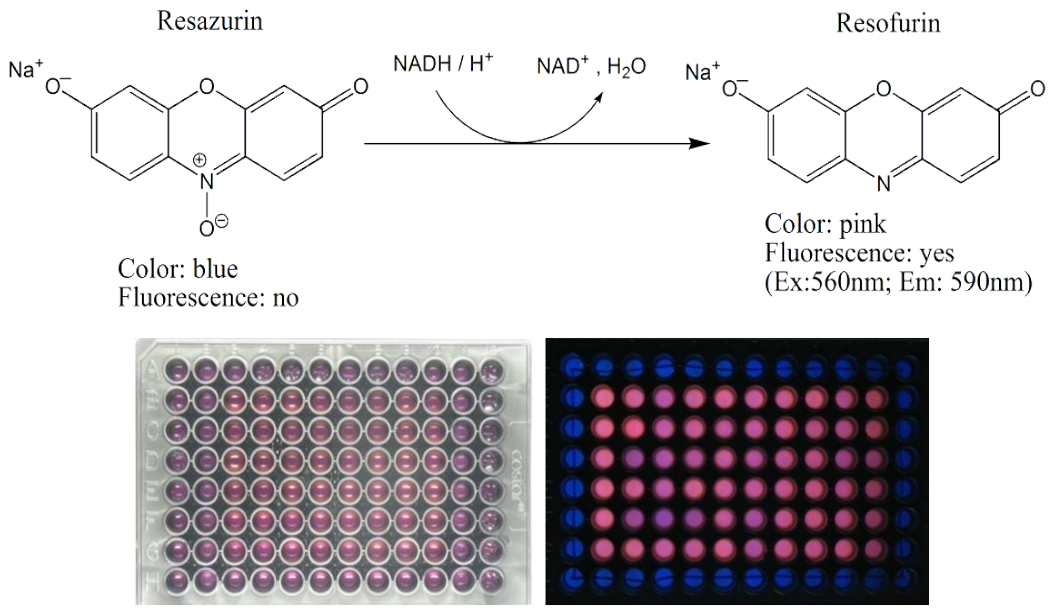

Figure 8. shown in the up describe reduct equation of resazurin to fluorescent resofurin in living cells , shown in down illustrate the 96wells plate seed 20,000 MDA-MB-231 cells per well fill with 10% resazurin media after 4 hours under light (down left)and under UV light(down right).

The strategy here to investigate the cytotoxicity effect based on living cells viability, several kinds of alternative kit could be employed as cell viability monitoring candidates.

We prefer resazurin (7-Hydroxy-3H-phenoxazin-3-one 10-oxide) in this work, resazurin is a minimally toxic non-fluorescent compound, which in living cells is converted into irreversibly fluorescent resorufin, see *Figure 8*, it is employed as an oxidation reduction indicator in cell viability assays e.g. for bacteria and mammalian cells[76].

When huge number of cells were incubated with solution containing resazurin for an extended time, for instance, more than 8 h, a secondary reduction reaction may occur and the fluorescent resorufin can be further reduced to colorless, non-fluorescent hydro-resorufin. This secondary reduction phenomenon perhaps dependent on the cell type employed in the assay[76]. To avoid this, incubation time with resazurin were fixed at 3 h for each cell line, respectively.
In this work, two different cell lines, which density set at 15000 MDA-MB-231 cells and 10000 HeLa cells in one well, were used for this experiment. Firstly, the cells were seeded per well in a 96-well plate (360 μL medium/well, 0.32 cm^2/well surface area), then, incubated for 48 h. Subsequently different concentrations of 1-SiO_2, 1-Au-SiO_2, 2-(DEXS/PARG), 2-Au(DEXS/PARG), 3-(PSS/PAH) and 3-Au(PSS/PAH) capsules were added to the cells and incubated for 48 h. The experiments repeated three times for each capsule concentration. The cells which were not incubated with capsules was used as control experiments. Before adding

10% of resazurin, the cells were washed with phosphate buffered saline (PBS); after incubation with resazurin (37 °C and 5% CO_2) for 3 h, the samples were analyzed with a fluorometer (excitation 560 nm, emission between 572 and 650 nm). The background emission was subtracted from each value of fluorescence emission, and the fluorescence emission intensity at 584 nm was used for evaluation, which is assumed to correlate with the viability of the cells. This protocol was described before [77]

3.2 Result and Discussion

3.2.1 Synthesis of calcium carbonate cores

Microcapsules layer by layer assembly was conducted on $CaCO_3$ microparticles, thus, the size of the template decide the microcapsules diameter. In addition, different property cargos were loaded based on two different strategies here as co-precipitation and post-loading.

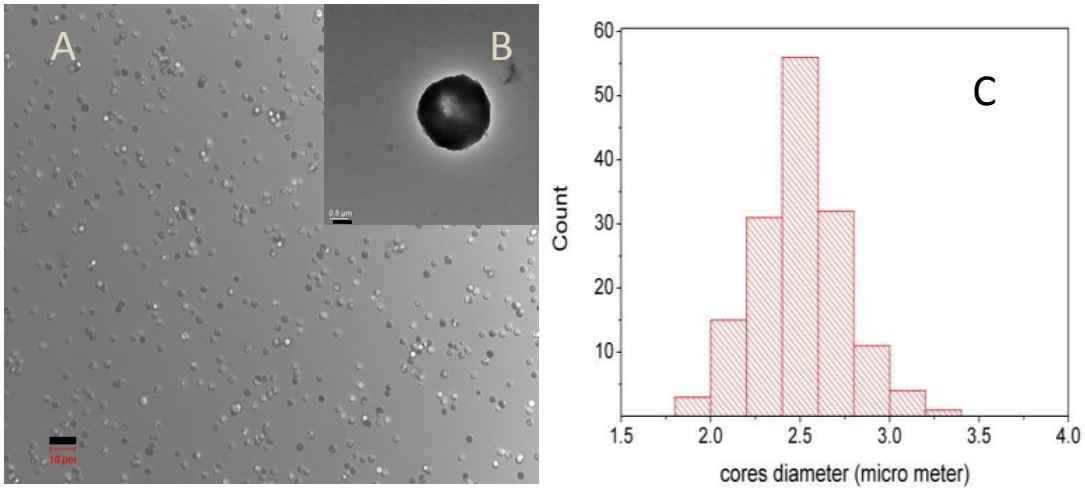

Figure 9. Bare CaCO3 cores filled with Dextran2000k Da. (A) Optical microscopy image (scale bar corresponds to 10 µm) and in the inset TEM image of the bare particles (scale bar corresponds to 0.5 µm).(B). Distribution diagram of the CaCO3 core size(C).

As the $CaCO_3$ core's forming according to the theory of crystal growth, the formation of a new solid phase from a solution is initiated through nucleation. The activation energy for nucleation, ΔG_N , is given as [59]:

$$\Delta G_N = \frac{16\pi(\Delta G_I)^3}{3(kT\ln S)^2} \qquad (1)$$

and

$$\mathrm{In}\, S = \mathrm{In}\left[a\left(\mathrm{Ca}^{2+}\right)a\left(\mathrm{CO}_3^{2-}\right)\right]/K_{sp} \qquad (2)$$

Where ΔG_I represents the energy required to form the new interface, k is Boltzmann constant, T is the temperature, S is the supersaturation of the medium, a is the ionic activity, and K_{sp} is the solubility product of the solid phase. Correspondingly, the nucleation rate J_N is given as:

$$J_N = A\exp\left(-\frac{\Delta G_N}{kT}\right) \qquad (3)$$

Where A is a constant. The phase selection of $CaCO_3$ changed from calcite to vaterite in the presence of charged solution like PSS which they employed [59]. They employed the PSS as the model charged molecular and gained small particles diameter around 500-1000 nm, it can be conclude from the following two main reasons: one main reason is the decrease in interfacial energy (ΔG_I)to form vaterite (cores) instead of other polymorphs. In Eqs. (1) and (2), showed the synthesis take in high precursor concentration, an increase in supersaturation (S) observed due to the increased ionic activity product from the complexing effect between the negatively charged PSS or other slight charge loaded cargos, for example, protein (negative) or FITC-Dextran(slightly negative). In this case, verify the ratio of the precursor and load different charge moleculars lead the different size of the carbonate cores.

3.2.2 Encapsulation efficiency of different cargos in capsules

1) Pre loading big hydrophilic molecular

Firstly, the ability for encapsulating high molecular weight molecules (FITC-BSA, ~ 66 kDa) in the cavity of the capsules was studied in this experiment. This model-protein was incorporated into the capsules cavity by co-precipitation. It means that $CaCO_3$ cores were formed in the presence of a water solution of FITC-BSA. The polyelectrolyte shell assembly around the cores was carried out as described in chapter 3.1.5 with following the cores dissolution. These $CaCO_3$ microparticles in same batch loaded with FITC-BSA was used to produce the six different types of capsules, listed as: 1-SiO_2; 1-Au-SiO_2; 2-(DEXS/PARG); 2-Au-(DEXS/PARG); 3-(PSS/PAH); 3-Au(PSS/PAH).

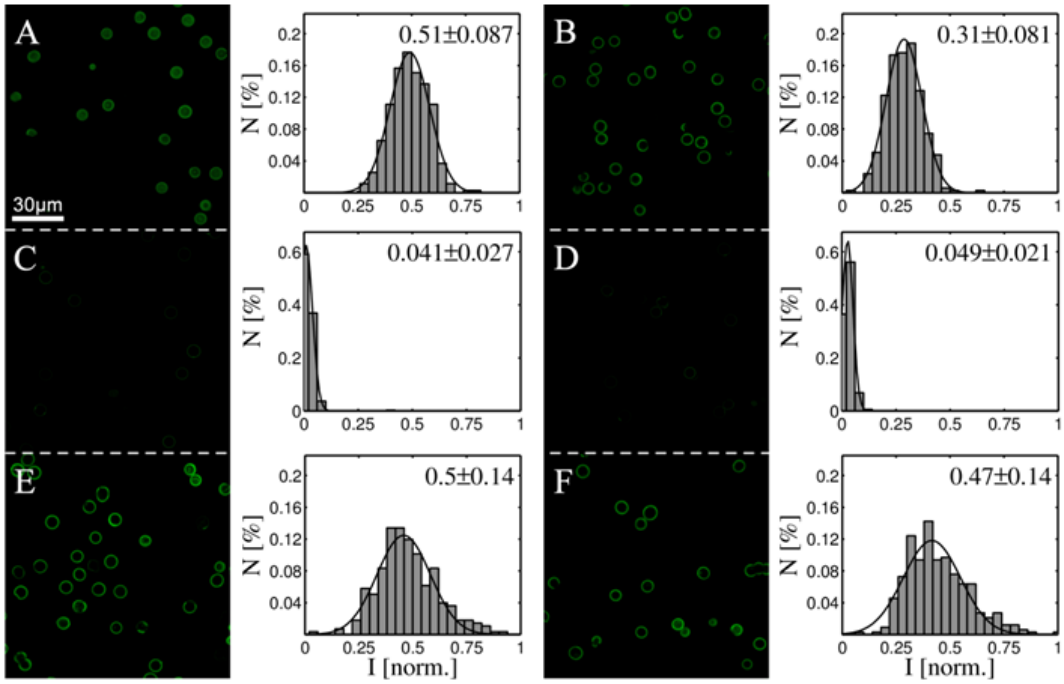

Figure 10. Confocal images of the green channel and the corresponding intensity distribution of FITC-BSA (66 kDa) loaded capsules obtained from the analysis of confocal micrographs: (A) 1-SiO_2, (B) 1-Au-SiO_2, (C) 2-(DEXS/PARG), (D) 2-Au(DEXS/PARG), (E) 3-(PSS/PAH) and (F) 3-Au(PSS/PAH). I - the normalized integrated fluorescent intensity of individual capsules and N - the frequency at which such intensity values occurred. Note that in all cases the encapsulated FITC-BSA is not homogeneously distributed in the capsule cavity, but rather sticks to the inner capsules shells.

In order to investigate the loading effective of the co-precipitate method, after core dissolution, the average amount of fluorescence labeled protein inside the capsules was evaluated by analyzing confocal micrographs which with a software written for this purpose in Matlab (Mathworks). Under control the same acquisition parameters, quantitative evaluation was recorded by measuring the integrated fluorescent intensity of individual capsules in images. The intensity ratio of the FITC-BSA loaded capsules 1-SiO_2: 1-Au-SiO_2: 2-(DEXS/PARG): 2-Au-(DEXS/PARG): 3-(PSS/PAH): 3-Au(PSS/PAH) was 1: 0.61 : 0.08: 0.10: 0.98: 0.92 as *Figure 10* illustrated. This result represent that except the silica capsules, the loading of the capsules with embedded Au NPs has a very similar result with the one without Au NPs.

There was an investigation focus on the NPs influence about permeability of the capsules's hulls during the core formation process, this result indicated the NPs might be as a drawback toward the loading cargos stabilization [78].

For our case, only the silica shells capsules shows the Au NPs occurred influence. The NPs attached in the multilayer hull of capsules changed the polyelectrolytes construction from plywood like structure in affinity to the NPs/frame structure, this

change make more cargo in small molecular weight are able to spread in outer low range concentration space, finally lead the phenomenon as loss the cargo cause this process is irreversible.

Compared with the DEXS/PARG capsules (8% successfully loading when calibrated the SiO_2 capsule's loading efficiency as 100%), the surface porous structure may quite different duo to their different composition. Here, as the high loading efficacy of molecules get the advantage than DEXS/PARG capsules, which also be used as the degradable vehicles.

2) Post loading small hydrophobic molecular

It is value to point out that heat shrinking is a highly efficient method to help encapsulate a wide variety small molecular weight cargo into the capsules. However, it is necessary to consider the biomaterials are quite sensitive about the temperature. In addition, different encapsulated material have totally property lead to vary postloading efficient here, and operation of heating shrink also induce variation performance of the loading result. Thus, here we just discuss with the postloading result without heat shrinking protocol.

The DOXS introduced in the method as an anti-cancer medicine but not able to dissolved in water, for encapsulated efficiency, it was evaluated by employing absorption of fluorescence spectrophotometry. The amount of free DOXS in the supernatant without encapsulated was measured after each step of the encapsulation procedure. The concentration of DOXS was calculated based on the extinction coefficient of DOXS at 480 nm ($\varepsilon_{480} = 11500\ M^{-1}\cdot s^{-1}$) and the known concentration of capsules as measured with a hemocytometer [79]. In addition, the integrated fluorescent intensity of individual capsules was determined from confocal micrographs, see *Figure 11*. Both of the results were compared as below.

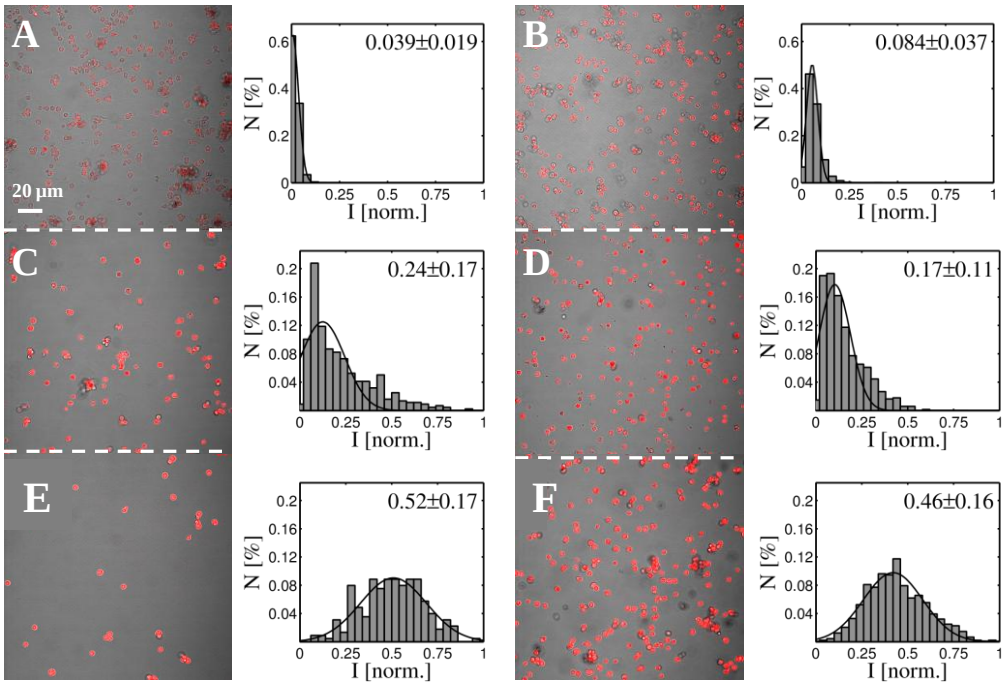

Figure 11. Confocal microscopy images of the overlay of the red fluorescence and transmission channel of DOXS loaded capsules and the corresponding intensity distribution obtained from the analysis of confocal micrographs: (A) 1-SiO2, (B) 1-Au-SiO2, (C) 2-(DEXS/PARG), (D) 2-Au(DEXS/PARG), (E) 3-(PSS/PAH) and (F) 3-Au(PSS/PAH). I - the normalized integrated fluorescent intensity of individual capsules; and N - the frequency at which such intensity values occurred. Note that in all cases the encapsulated DOXS is distributed rather homogeneously in the capsule cavity.

3.2.3 Characterization of capsules

The assembling process can be monitored by zetasizer. The zeta potential of the NPs in water was shown in *Figure 12*, it demonstrates clearly that the adsorption process of each polyelectrolyte layer leads to an overcompensation of the previous surface in opposite charge, it is match the assuming as the monitor tools for the LbL assembling. By this method, it is easy to fix the first layer as negative charge PSS to the slightly positive charge of the naked $CaCO_3$.

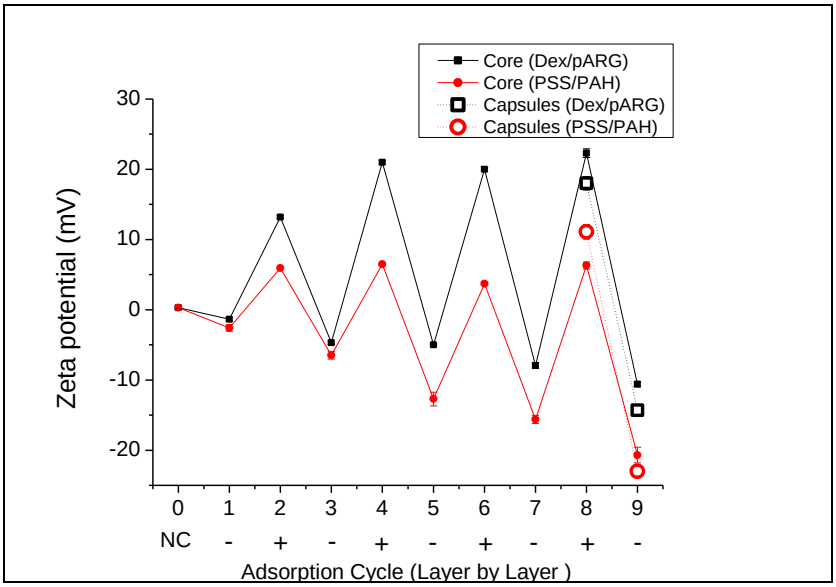

Figure 12. .Zeta potential changes during LBL coating of CaCO3 particles with final Zeta potential of four different polyelectrolyte capsules.

The transmission electron microscopy (TEM) images of microcapsule are shown in *Figure* and *Figure 14*. From the TEM images we can see, under the low magnification, there is no typically difference with different materials on the surface; while under higher magnification, it is can be recognized that the surface of $(DEXS;PARG)_4$ capsules are much smooth than the $(PSS/PAH)_4$ capsules.

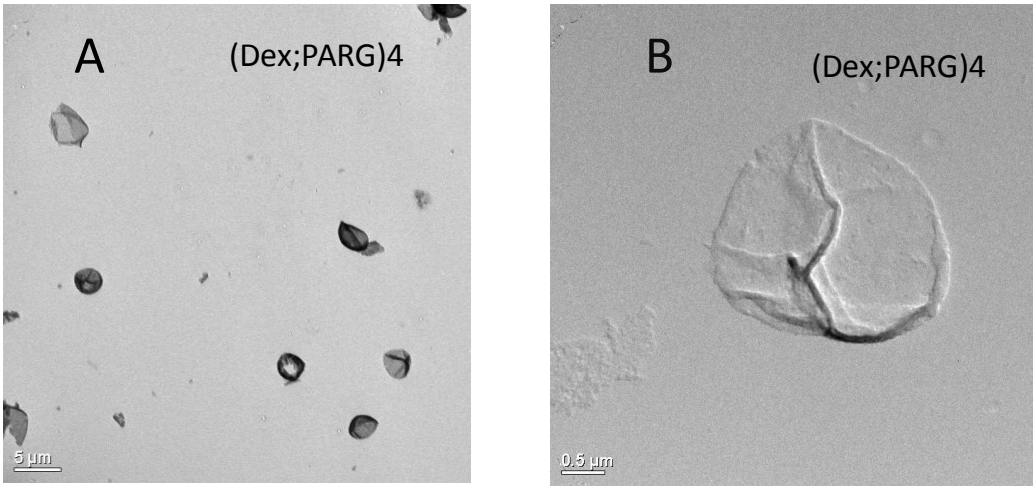

Figure 13. (DEXS;PARG)4 capsules magnification 1k (A) and 8k (B)

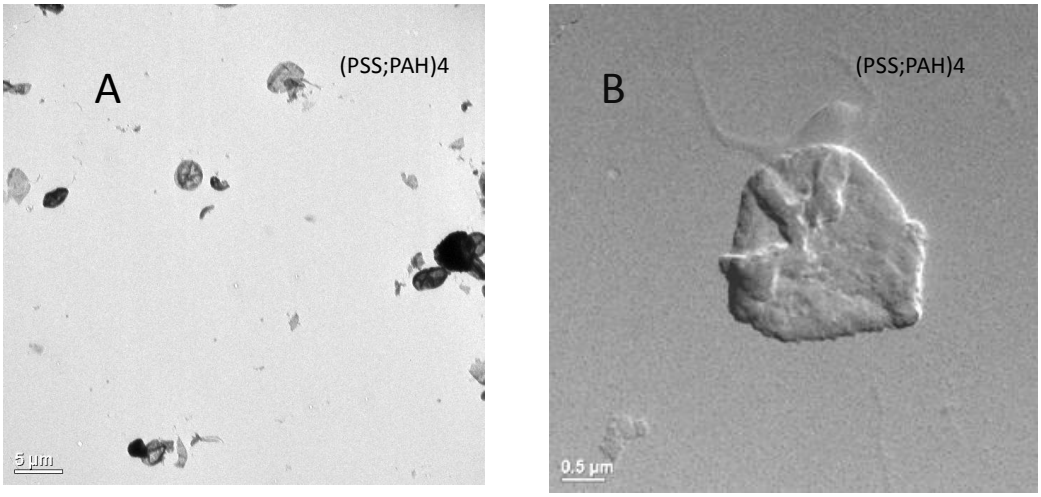

Figure14 . (PSS/PAH)4 capsules magnification 1k (A) and 8k (B)

3.2.4 Study of time response of pH sensor capsules

The PSS/PAH structure capsules are not biodegradable, this kind of capsule was allowed to used as a monitor for pH sensing under crude solution, such as cell culture medium for remote controlling under magnet field. Due to the Magnetic γ-Fe_2O_3 NPs attached in the hull of polyelectrolyte multilayer capsules, the capsules are allowed to control the movement under magnet field which typical architecture is (PSS/PAH)2 γ-Fe_2O_3 (PSS/PAH)2.

Due to the SNARF-Dextran 10 kDa as the loaded cargo in the capsule, give the capsule pH sensitive property. In detail, SNARF is a pH-sensitive fluorophore, which emits at two wavelengths depends on the pH of the solution, in acidic media SNARF emits light more in the yellow at 583 nm and in alkaline ones more in the red at 627 nm [80]

.

These capsules were exposed to a time-dependent pH concentration profile, while measuring the fluorescence response (I_y) in real-time as a pH sensor.

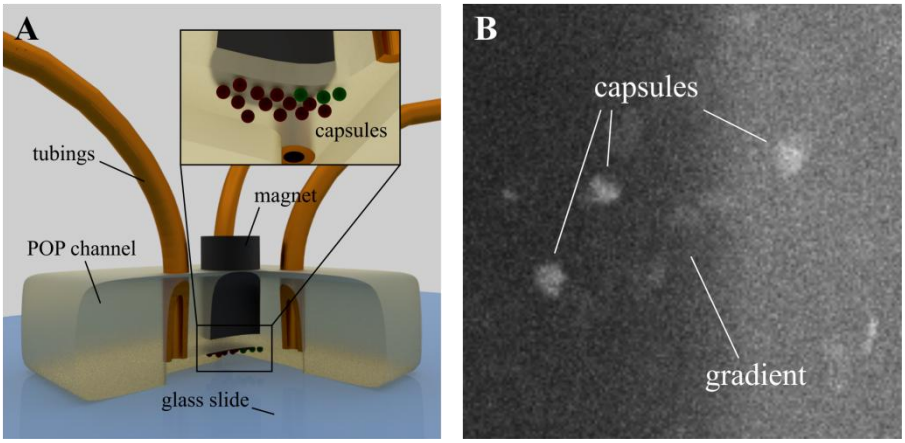

Figure 15. Microfluidic channel coupled to a fluorescence microscope where the PEM capsules are

magnetically trapped at the top of the channel. Two solutions (1, 2) with different concentrations of protons (c_1, c_2) and pressure (p_1, p_2) are mixed producing a gradient that can be moved perpendicular to the direction of the gradient plane by (p_1, p_2) modification. B) Fluorescence image of $(PSS/PAH)_2$ γ-Fe_2O_3 $(PSS/PAH)_2$ capsules trapped in the microfluidic channel in the vicinity of a static gradient (TRIS buffer adjusted to pH 9 on the left and MES buffer adjusted to pH6 labeled with TRITC on the right), image adopted from [9]

In order to dynamic control pH gradient vary, an microfluidic channel setup employed which connect two inlets and a single outlet, as *Figure* 15 illustrated. Before running the test, load the channel first with magnetic pH sensitive capsules which post-loaded SNARF-dextran.

A microfluidic channel with two inlets and a single outlet was used to generate a dynamic pH gradient (*Figure* 15), and the channel was molded by polyolefin polymer (POP). In order to load the channel with magnetic pH-sensitive PEM capsules, a suspension of the capsules (~ $7 \cdot 10^4$ mL^{-1}) was flushed through the channel, and capsules (with embedded magnetic NPs) were trapped at the top of the channel *via* a magnetic field.

To shift the pH from 6 to 9 and *vice versa*, two commercial buffers were used which is 10 mM of 2-(*N*-morpholino)ethanesulfonic acid (MES) with pH 6 and 1 mM of tris(hydroxymethyl)aminomethane (TRIS). In this assay, employed the emCCD camera and an inverted fluorescence microscope (Filters: ex 470/20BP, BS 510, em 575/50BP) to record the fluorescence shift.

During the magnetic trapping, the capsules always kept their spherical shape and no deform observed, see *Figure16* (D,F). The interframe time for the recording was set to 26.6 ms, and for each measurement, two pulses of pH 6 and pH 9 (duration: 10 s each) were applied and the intensity traces of individual capsules were extracted from the recorded image sequence as it is shown in *Figure* 17.

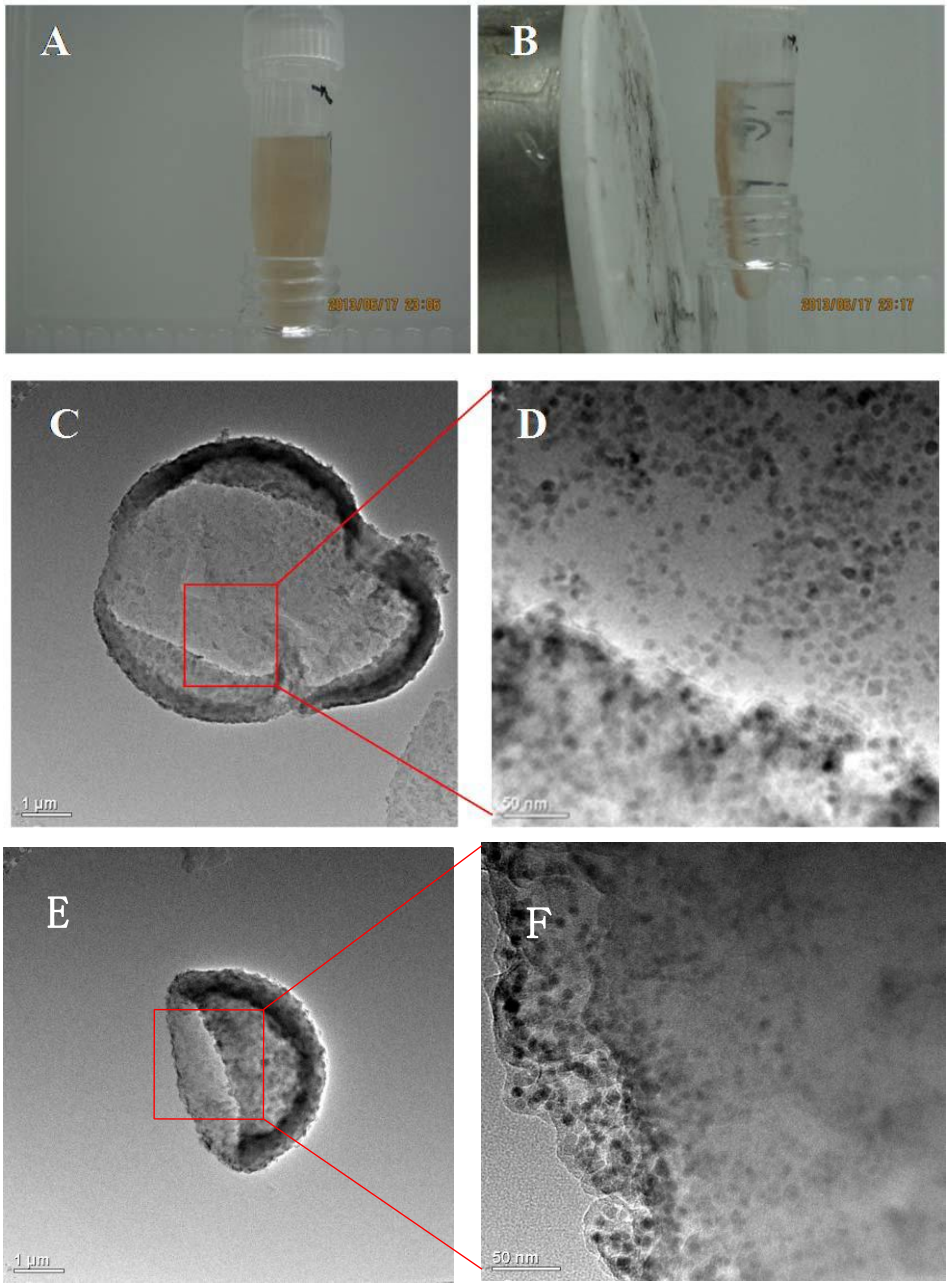

Figure16. Image of magnetic PEM capsules in aqueos solution in the absence (A) and presence of a magnetic field (B). Close to the magnet the capsules accumulated on the wall of the tube due to the presence of the magnetic field which had been applied for (B) 10 minutes. TEM images (C, D, E, F) of one of the capsules exposed to the magnetic field of the magnet for 10 minutes. (D， F) Detailed zoom in of the TEM image depicted in (C, D) showing the distribution of magnetic NPs within the capsule. Scale bars correspond to 1µm and 50 nm, respectively. Image adopted from [9].

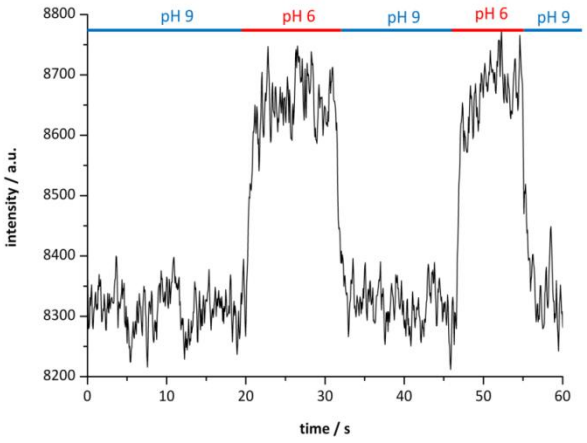

Figure 17. Changes of fluorescent emission intensity of individual capsules loaded with SNARF in a microfluidic chamber upon pH change from 9 to 6. Excitation wavelength was at 470 nm and emission wavelength was at 575 nm, adopt quote from [9] .

3.2.5 Opening of capsules with an alternating magnetic fields

There were vary strategies can be used to trigger capsule such as used heat magnetic NPs by radiofrequecies [81] [82], Plasmon NPs heating [74], magnetic mediated hyperthermia technique also been investigate due to the promising heating effect [83], which was done by alternating magnetic fields (AMF). However, this technology still not further applied toward trigger open the magnetic attached multifunctional capsules.

The capsules in 4.6 ± 0.4 µm diameter with a zeta potential of ζ = 12.05 ± 0.5 mV were successfully synthesized by the LbL approach ((PSS/PAH)(PSS/P(Am-DDA) NPs (PAH)$(PSS/PAH)_2$). Because of the presence of iron oxide nanocubes (size diameter is about 18 ± 2 nm), the capsules could be attracted by a magnet under magnet field which magnet resonance performance well lead to collected by magnet (0.2 T) in 5 min.

Despite the magnetic NPs employed here obtained weak charge like *Figure 20* shown, the NPs also could be attached in the PEM capsule but rely on the assistant of (P(Am-DDA)), which is the strong positively charged polymer and instead of one layer of PAH, as mentioned in chapter 3.1.6. *Figure 18* is the TEM image of iron oxide nanocubes in hydrophobic solvent, and *Figure 19* is the TEM image of NPs in hydrophilic phase after polymer coating with amphiphillic polymer. Through an alternating magnetic field, the magnetic nanoparticles were able to heat their surroundings material which not able to suffer high temperature, thus destroying the microcapsule walls, and leading to a final release of the embedded cargo to the surrounding solution.

The cargo release was monitored in solution by measuring the increase in absorbance and fluorescence further to the exposure to AMF. More information about the zeta-potential and size distribution of hydrophilic NPs was shown in *Figure 20*. The capsules loading with Cascade Blue-labelled dextran could be confirmed by optical microscopy (Figure 21).

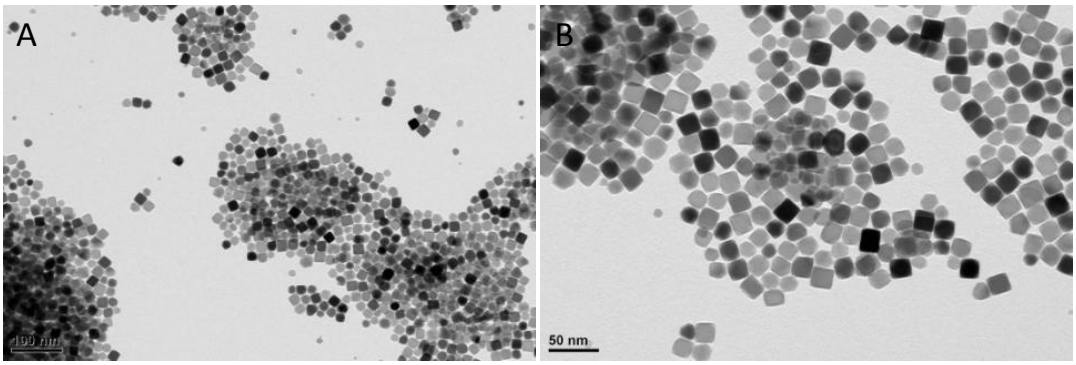

Figure 18. TEM images (A, B) of the magnetic nanoparticles in chloroform. The scale bars correspond to 100 nm (A) and 50 nm (B).

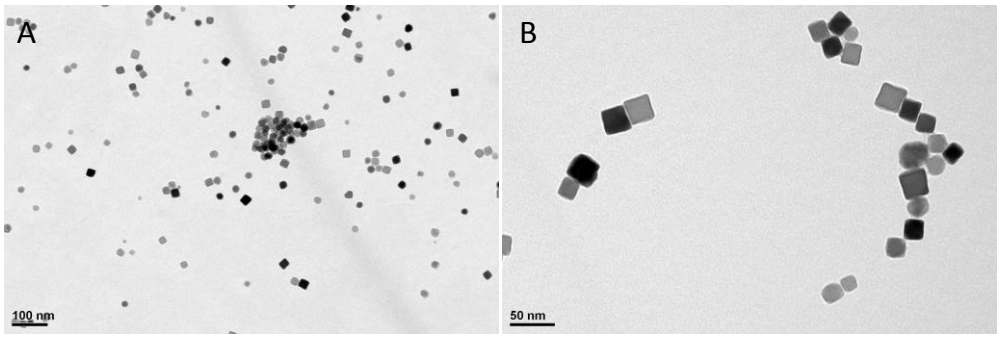

Figure 19. TEM images (A, B) of the water-soluble magnetic nanoparticles (i.e. after phase-transfer to water) used to produce the polyelectrolyte capsules sensitive to AMF. The scale bars correspond to 100 nm (A) and 50 nm (B).

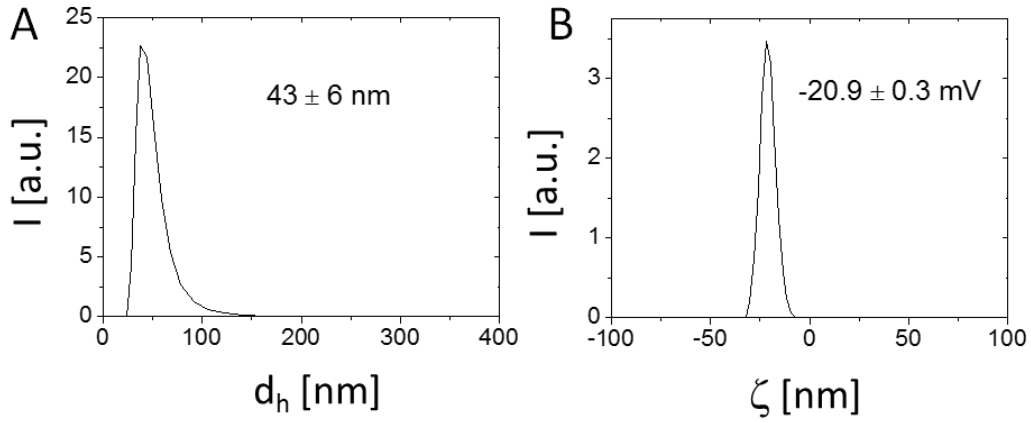

Figure 20. Distributions of the hydrodynamic diameter d_h (A) and ζ-potential (B) of the iron

oxide NPs, as determined in Milli-Q water. The shown values are the result of three independent measurements.

The TEM images from *Figure 22* were show the capsules still keep their spherical shape, even though there is high concentration of magnetic NPs functionalized on the surface and thus able to create the great heating effect.

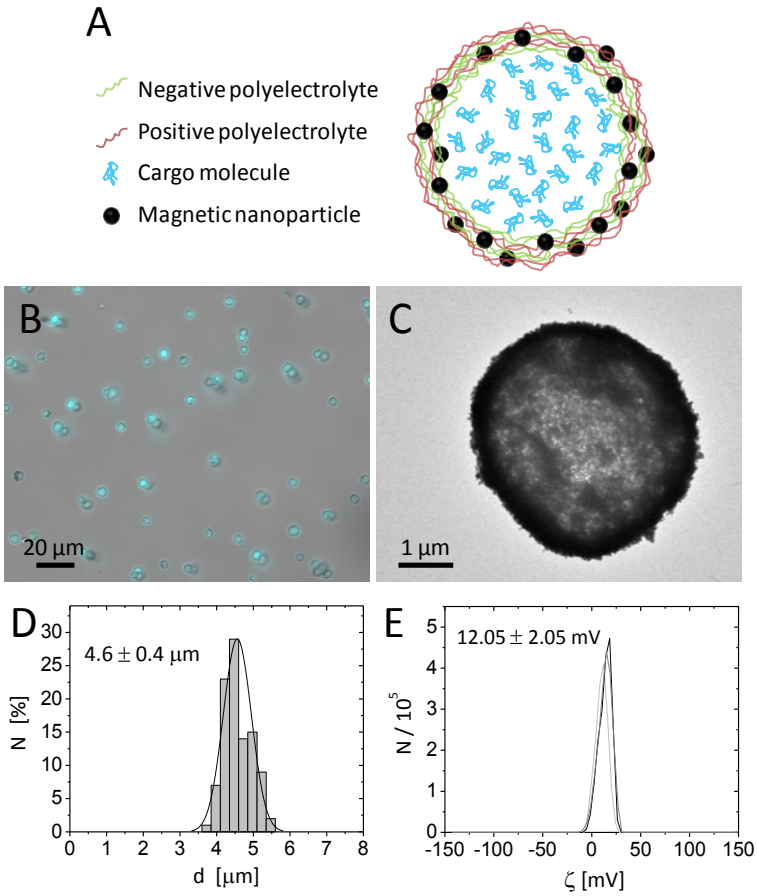

Figure 21. A) Sketch of one polyelectrolyte capsule comprising Cascade Blue-labelled dextran as fluorescent cargo in the cavity and magnetic NPs in the wall. B) Optical microscopy image of capsules dispersed in water, showing the bright field and blue fluorescence channel (excitation 365/50 nm, beam splitter 395 nm and emission 445/50 nm) corresponding to the emission of Cascade Blue-labelled dextran. The scale bar corresponds to 20 µm. C) TEM image of dried capsules. The scale bar corresponds to 1 µm. D) Histogram of the size distribution fitted with a Gaussian curve. E) ζ-potential measurements of the polyelectrolyte capsules in water. The values are the results of three independent measurements.

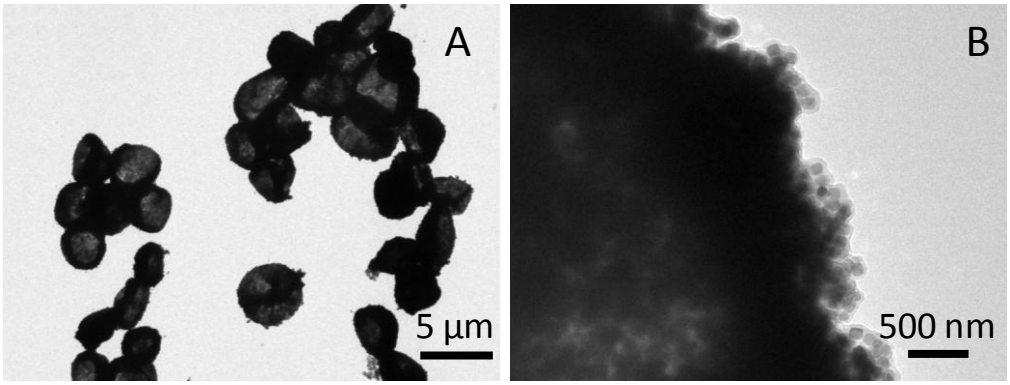

Figure 22. TEM images (A, B) at different magnifications of polyelectrolyte capsules decorated with magnetic NPs. The scale bars correspond to 5 µm (A) and 500 nm (B).

The TEM images in *Figure 23* were compared the difference between before and after the capsules opening. The capsules kept their spherical shape before opening (in image A); after opened by alternating magnetic fields, it is very easy to notice the detached NPs flee away from the near broken capsule (in image B).

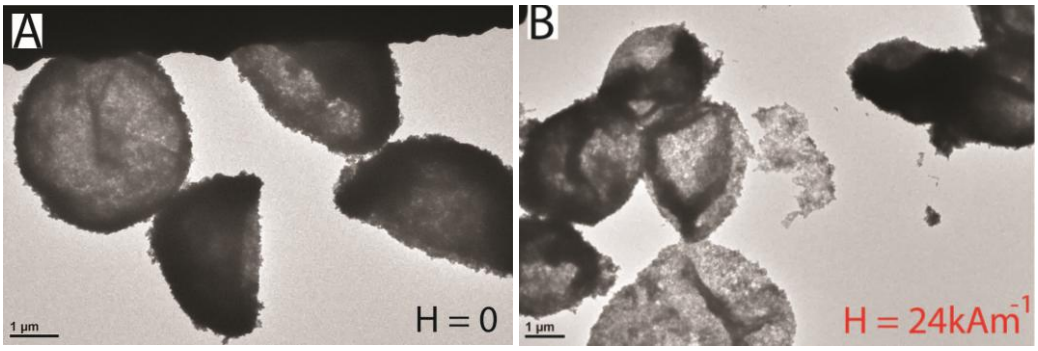

Figure 23. TEM images of iron oxide NPs decorated polyelectrolyte microcapsules after (A) and before (B) being exposed to alternating magnetic fields (AMF, 300 kHz, 24 kAm^{-1}) for 90 minutes.

In the AMF treated capsules, some damage in form of partially broken walls could be observed, together with the presence of some free magnetic NPs which had been released from the capsule walls. Both effects could not be found in the control capsules.

In order to probe CascadeBlue-labelled dextran release efficiency from the capsules upon AMF exposure, there were one assay achieved by record the absorption and fluorescence spectra of the collected supernatant, see *Figure* 24. Here by, besides the release of CascadeBlue-labelled dextran as observed by the fluorescence spectra, the heat generated under AMF might also partially damage the polymeric shell transfer into polymer fragments as the evidence, which absorb in the UV special region and fluorescence spectra indicate the cargos was successfully released.

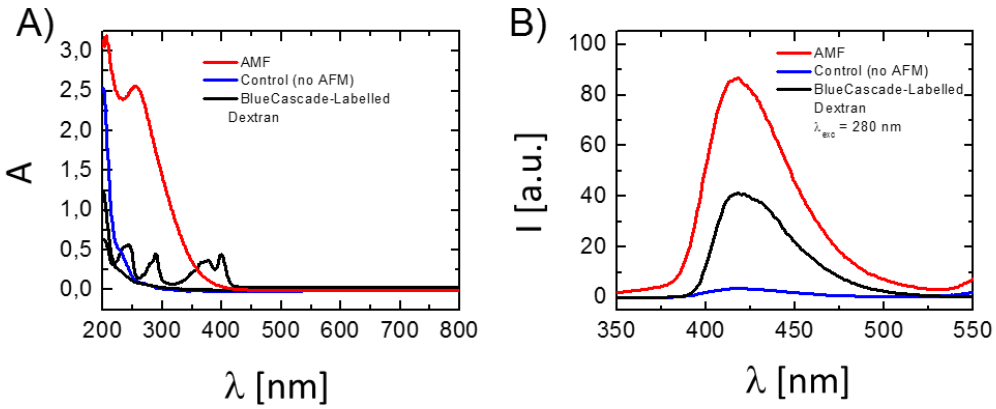

Figure 24. A) UV-vis absorption spectra, and B) fluorescence emission spectra (at λ_{exc} = 280 nm excitation) of i) free Cascade Blue-labelled dextran (black line), ii) the supernatant of a capsule solution which had been treated for 90 minutes under an AMF (300 kHz and 24 kAm^{-1}) (red line), and iii) the supernatant of a control sample of capsules which had been kept at room temperature for 90 minutes and thus had not been exposed to an no AMF (blue line).

Thus, as the high heating performance of iron oxide nanocubes, damage active in the polymer shell were prompted thorough an AMF, which allowed for control release of the encapsulated molecular cargo.

3.2.6 Opening of capsules with light

It has been shown that polyelectrolyte/gold nanoparticle capsules rupture upon exposure to short near-infrared laser pulses due to gold nanoparticle mediated heating of the capsule shell [74] [84]. The laser light energy was shown to have negligible effect on the living cells [74]. This approach was also shown to be feasible for the release of fluorescein-labeled dextran, a convenient model of high molecular weight biomaterials such as DNA [84], or mRNA[11] . For this light-assisted approach to be feasible, the targeted area must be optically accessible.

In this part, the possibility to release cargo molecules from silica capsules was evaluated containing Au NPs within their walls (i.e. 1-Au-SiO_2) and compared it with the light-mediated release from polyelectrolyte capsules. The capsules were post-loaded with SNARF-dextran (Mw:10 kDa). It is worth to mention that several light-addressable materials based on silica have been already reported.[85]

SNARF is a ratiometric pH indicator widely used for biological applications as their low cytotoxicity [86]. As mentioned in chapter 3.2.4, SNARF has a yellowish emission (at 583 nm) while at alkaline pH, intensity shifts towards the red emission peak after the pH decreased under 6.0 (at 627 nm). Thus, SNARF is a very sensitive tool to sense pH in different intracellular compartments. Here, we studied the possibility to release SNARF from 1-Au-SiO_2 capsules in a remote way via light illumination and control with a power density around 3.5 μW/μm^2 in short

time.

Figure 25 shows upon laser irradiation, only capsules which had been irradiated changed their fluorescence emission, whereas non-irradiated capsules kept their fluorescence emission. This demonstrates that only the lysosome where the capsule was located had been permeabilized upon local heat-generation. Where resulted in a change in the environment of the SNARF from acidic to alkaline pH.. These experiments demonstrate that photothermal release of encapsulated molecules from 1-Au-SiO_2 capsules to the cytosol is as efficient as the remote controlled release from polyelectrolyte capsules (2-Au(DEXS/PARG) and 3-Au(PSS/PAH)) that has been reported in previous work[74, 87]. Although the opening mechanism was not studied in detail, pre-existing structural defects in the silica capsule may play a role in the opening upon local heat production.

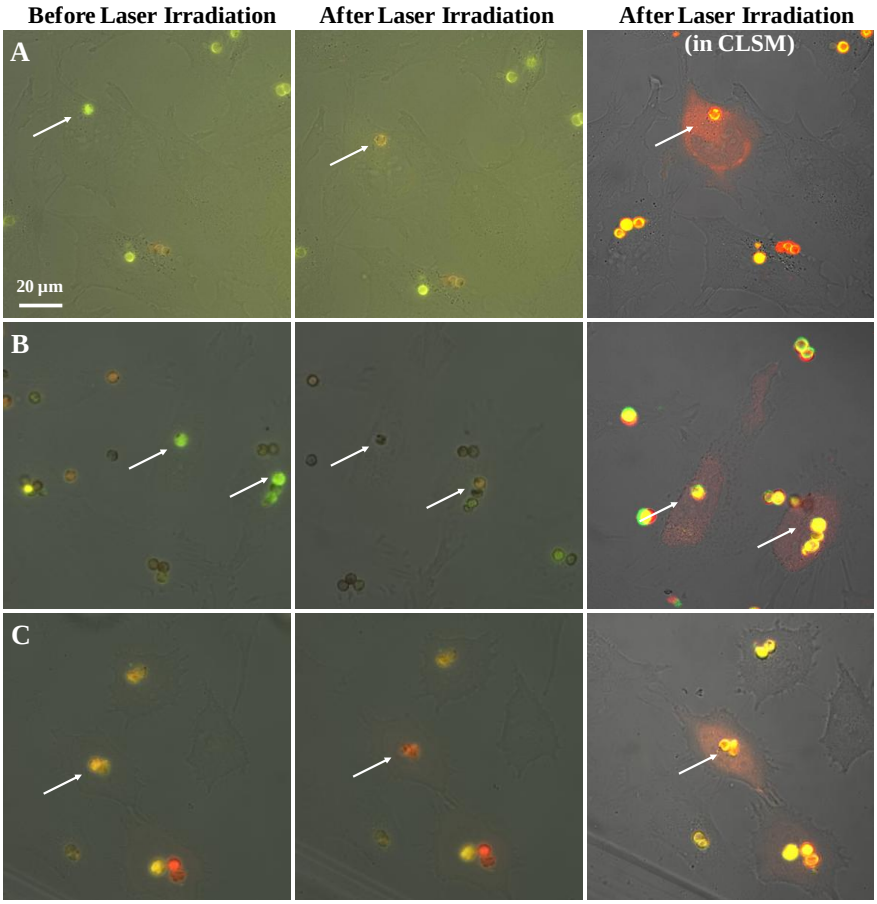

Figure 25. Images demonstrating the opening and the cytosolic release of dextran-SNARF (10 kDa) encapsulated in the inner cavity of capsules functionalized with Au NPs. In the images, the irradiated capsules changed the fluorescence emission (from yellowish to orange-red) due to the pH change upon the rupture of the acidic compartment (lysosome) in which they are located after cellular internalization. Confocal laser scanning microcopy (CLSM) was used to observe the homogeneous cytosolic release of SNARF-dextran. A laser power density of 3.5 µW/µm² had been

applied for a few seconds for the opening of the capsules. The scale bar corresponds to 20 μm.

In Table 1, the data conclude here clearly show that the transition from an acidic (lysosome) to a slightly alkaline neutral environment (cytosol) upon light-mediated release, the result of Au(PSS/PAH) capsules also match the assuming as well as Au-SiO_2 capusles.

Capsules construction	**Before IR radiation**	**After IR radiation**
1-Au-SiO_2	6.0 ± 1.1	8.0 ± 0.5
2-Au(DEXS/PARG)	< 6.5	7.8 ± 0.2
3-Au(PSS/PAH)	6.6 ± 0.5	7.9 ± 0.4

Table 1. Estimated pH values of capsules before and after opening of the silica capsules containing Au NPs with the calibration curve obtained with potassium rich buffers and nigericin.

3.2.7 Cytotoxicity assay of capsules

In previous chapter at 3.1.7, the cytotoxicity method showed that conversion of resazurin to resorufin by metabolically active cells results in the generation of a fluorescent product. The fluorescence produced is proportional to the number of viable cells. Thus, firstly, it is essential to fix the concentration of the each type cells in 96 wells plate, as the cells proliferation property are different and might induce magnify or underestimate actual fluorescence intensity of each cell. That is, as *Figure 26* showed, when MDA-MB-231 cell line number control under 20,000 cell per well performance 6-hour incubation period shows a linear correlation (r^2 = 0.98) between fluorescence and cell number. For the higher incubation cell number, there is a gain higher value of intensity of fluorescence but induces a loss of linearity above 12,500 cells/well. Finally, the number of the MDA-MB-231 cells fixed at 15000 cells and 10000 HeLa cells were seeded per well in a 96-well plate.

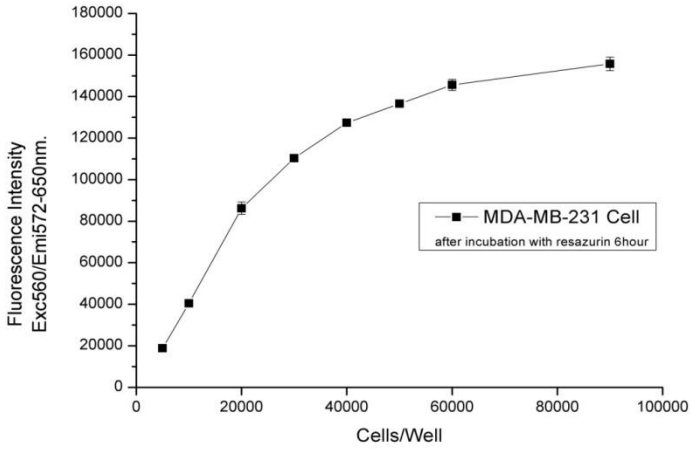

Figure 26. Serial dilutions of MDA-MB-231 cells were prepared at 100µl/well in a 96-well plate and cultured for 24 hours at 37°C. rezarurin (10µl/well) was added and cells were incubated for 6 hour before recording fluorescence (560(10)Ex/572-650Em)

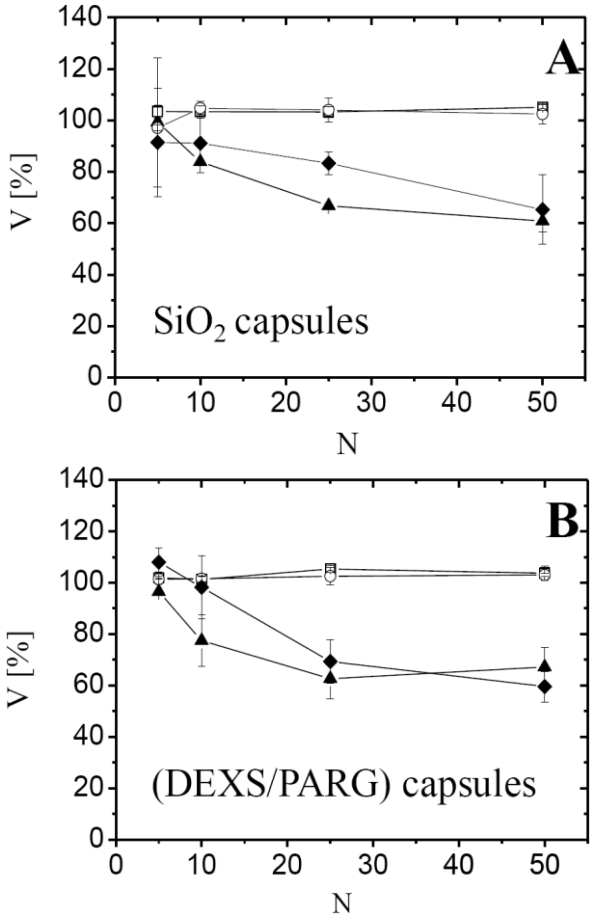

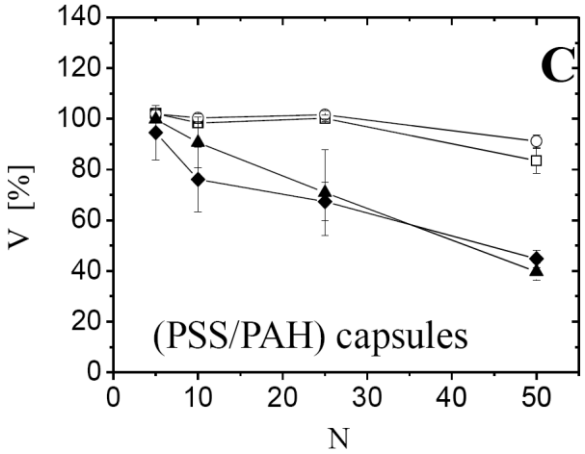

Figure 27. Viability of empty capsules as determined with a Resazurin assay for the six different types of capsules in HeLa cells (empty symbols: □, ○) and MDA-MB-231 cells (black symbols: ♦, ▲). Cells were incubated for 24 h with (A) 1-SiO_2 (□,♦), and 1-Au-SiO_2 (○, ▲), (B) 2-(DEXS/PARG) (□,♦) and 2-Au(DEXS/PARG) (○, ▲), and (C) 3-(PSS/PAH) (□,♦) and 3-Au(PSS/PAH) (○, ▲) capsules. V represents the percentage of viable cells and N the number of capsules that have been added per cell.

Figure 27 shows that 1-SiO_2 and 1-Au-SiO_2 capsules have similar toxicity compared with LbL capsules. Reduction of viability in HeLa cells is negligible for the used concentrations. In MDA-MB-231 cells a reduction in viability for concentrations above 25 capsules/cell was found. *Figure 27* B, C shows similar results obtained for 2-(DEXS/PARG), 2-Au(DEXS/PARG), 3-(PSS/PAH), and 3-Au(PSS/PAH) capsules. These results indicate that SiO_2 based capsules show similar toxicity as capsules based on degradable or synthetic polyelectrolytes.

4. Distance control in-between plasmonic nanoparticles

4.1 Methods

4.1.1 Polyelectrolytes coating of gold nanoparticles via Layer-by-Layer

Layer-by-Layer technique is not only can be applied on typically dissolved colloid particles, polyelectrolytes coated the metal nanoparticles (eg: AuNPs, AgNPs) also can be obtained.

For rinsing the exceed citrate which offered for stabilization of AuNPs, 2 mL of commercial citrate-stabilized Au NPs (concentration at $5.16 \cdot 10^{-5}$ µM, diamerter= 49.2 ± 4.9 nm) was precipitated by centrifugation (620×g, 60min), the supernatant was discarded. The red pellet was redispersed in 500 µL Milli-Q water to get the concentration of $2.064 \cdot 10^{-4}$µM due to obtain high concentration to avoid agglomeration.

Under magnetic stirring, this AuNPs solution was then dropwise added to 500µL of positively charged polyelectrolyte solution (PAH; pH ~ 4.8, 15 kDa) with the concentration of 2.0 mg/mL. With the protection from light, the mixture was kept stirring for at least 1 h to ensure the surface assembled entirely polyelectrolytes.

Afterwards, the AuNPs were precipated by centrifuge (930×g, 90 min) and dissolved in 500 µL Milli-Q water, the cleaning step was repeated twice to avoid the last layer exceed polyelectrolyte solution contaminated the next layer coating. Following the same procedure, the negatively charged polyelectrolyte (PSS, 15 kDa) was added to the positively charged Au NPs as the second layer. With the alternating positively and negatively charged polyelectrolyte, 1 to 10 monolayers coated Au NPs were carried out via LbL assembly as Figure *1* illustrated. In order to avoid aggregation, the solution was finally kept in the fridge (4 ºC) with free PSS or PAH, which depends on the last layer. This AuNPs solution can be further used after cleaning the free PE by centrifuge.

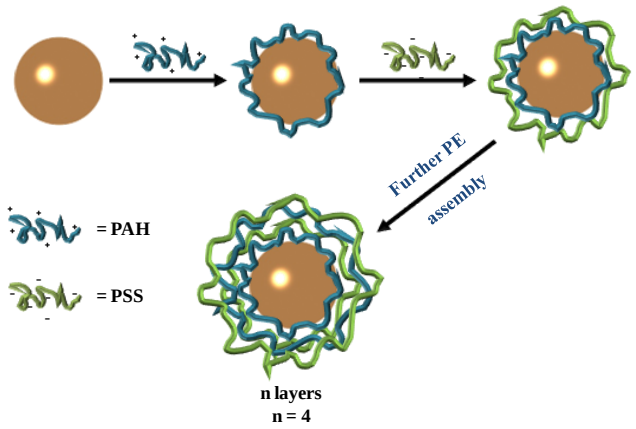

Figure 28. *Schematic representation of an Au NP with nadded PE layers by LbL deposition. In the present case n = 4 layers are shown.*

4.1.2 Au dimer formation

Due to the electrostatic affinity between the polyelectrolytes assembled negative and positive charged single AuNPs, two different charge solutions of Au NPs ($2.064 \cdot 10^{-10}$ M; d_c = 49.2 ± 4.9 nm, s = 1.1) with n and n+1 PE layers adsorbed. To clean the AuNPs, the first precipitated with centrifugation set at 930×g for 90 min in order to remove free PE molecules, which were present under storage conditions. Then, the Au NPs redispersed in Milli-Q water and diluted 20 times respect to the initial concentration. As *Figure 29* sketched up, two solutions of Au NPs in 100 µL coated with n and n+1 PE layers were mixed and after 10 min of gently shaking, a 10 µL drop of the mixture was deposited on a TEM grid, which was left to evaporated more than 2days in room temperature. TEM images were captured at different magnifications.

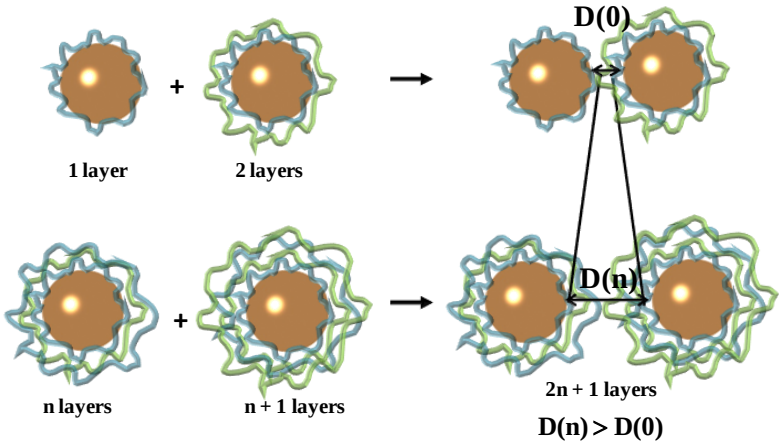

Figure 29. Schematic representation of the variation of inter-NP distance (D(0), D(1), ...D(n)), defined as surface-to-surface distance, for dimers produced by electrostatic interactions between two NPs with an increasing number of charged polymer layers on the surface (where n is the number of PE layers).

4.2 Results

4.2.1 Control over the shell thickness of gold nanoparticles

Nanoparticles can be coated with multiple thin polyelectrolyte (PE) shells using the layer-by-layer self-assembly technique [38, 39]. The technique is based on electrostatically-driven consecutive adsorption of oppositely-charged polymers in layer-by-layer geometry.

So called as Derjaguin−Landau−Verwey−Overbeek (DLVO) theory here is valuable to mentioned, see *Figure* 30, which reveal how orientated lead highly disperse NPs condition during the layer by layer process [88] [89].

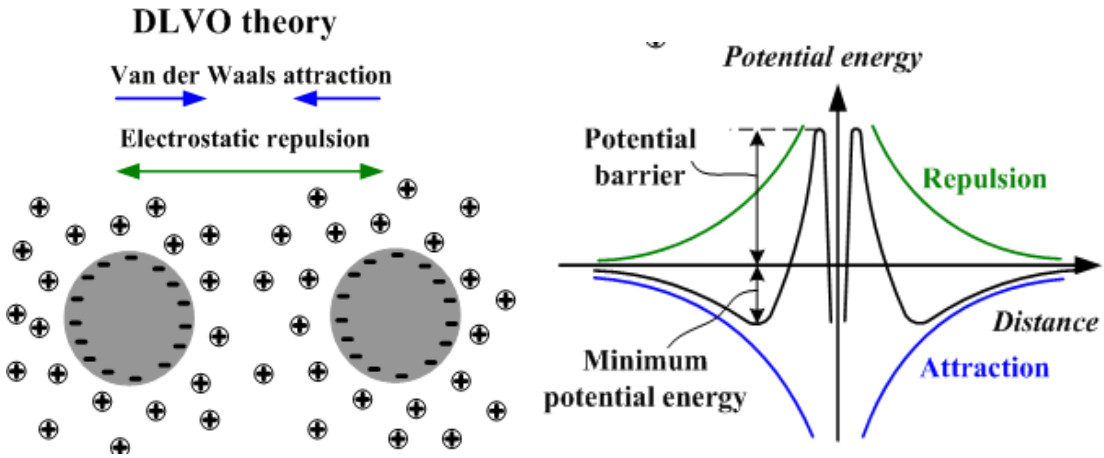

Figure 30. Schematic of the DLVO theory, left side illustrate the Van der Waals attraction increasing while the electrostatic repulsion tension increasing, this phenomenon related with the

colloid NPs distance. Right side image indicate the disperse property of colloids NPs influence by four main power.

One formula conclude from this theory below: Electric repulsive potential energy:

$$V_R = 2\pi\varepsilon\varepsilon_0 r\zeta^2 e^{-kx}$$

where: **ε** is dielectric constant of the solvent; ε is vacuum permittivity; ζ is zeta potential, and k represent a function of the ionic concentration (k-1 is the characteristic length of the electric double layer.

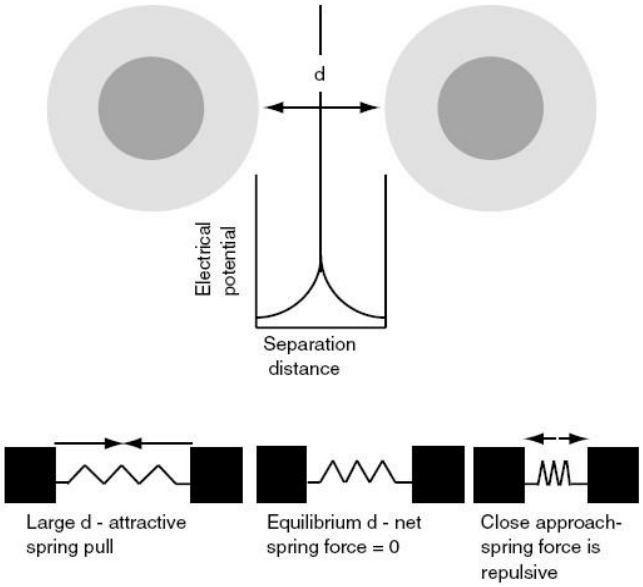

Figure. 31. The interactions between two colloidal particles with electrical double layers can be visualized as two connected by a spring. At large distances of separation the spring is stretched and applies a net force pulling the blocks together (attractive van der Waals interaction). At close approach, the spring is compressed producting a net repulsive force pushing the blocks apart (electrostatic repulsion). At some intermediate distance, the forces will be in equilibrium, image adopted from [90].

From DLVO theory, it has shown that the reasonable high concentration of the NPs, fullfil covering polyelectrolytes and super low ion strength are benefit to against agglomeration of colloid NPs during the assembling process; see *Figure31*.

The spectroscopic characterization UV-Vis absorption spectra were recorded by using an UV-Vis spectrophotometer. *Figure 32* shows a slight change of the plasmon band during the LbL process, which indicated that the addition of n layers of PEs on the Au NP surface produced a slight agglomeration of the sample; meanwhile, the slightly red-shift peak indicated the surface of the AuNPs assembling successfully.

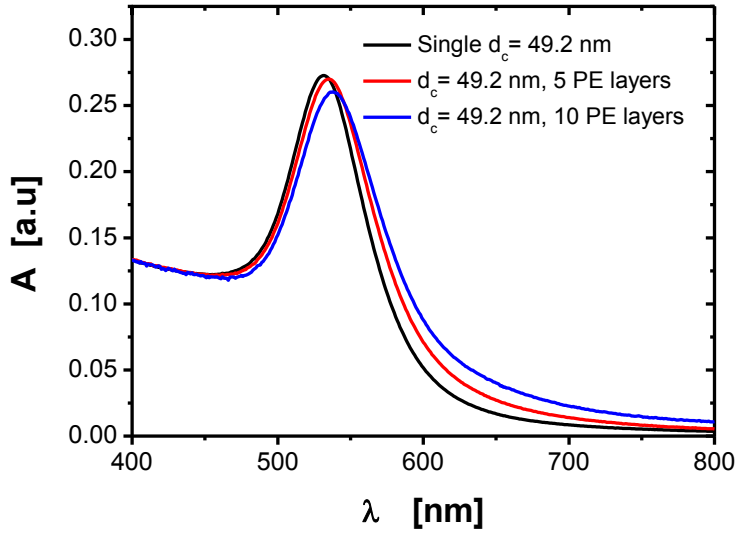

Figure 32. . UV-Vis absorption spectra A(λ) of citrate stabilized Au NPs (dc = 49.2 ± 4.9 nm, s = 1.1) before PE coating (black line), after (PAH, PSS)$_2$ PAH (n = 5; red line) and after (PAH, PSS)$_5$ (n = 10; blue line) coating.

As a direct monitoring tool, zeta-potential measurements using dynamic light scattering (DLS) were recorded. The zeta-potential following each PE adsorption step is plotted in *Figure 33*. The intensity-averaged hydrodynamic NP diameter d_h and the polydispersity index (PDI) values were calculated from cumulant-type analysis.

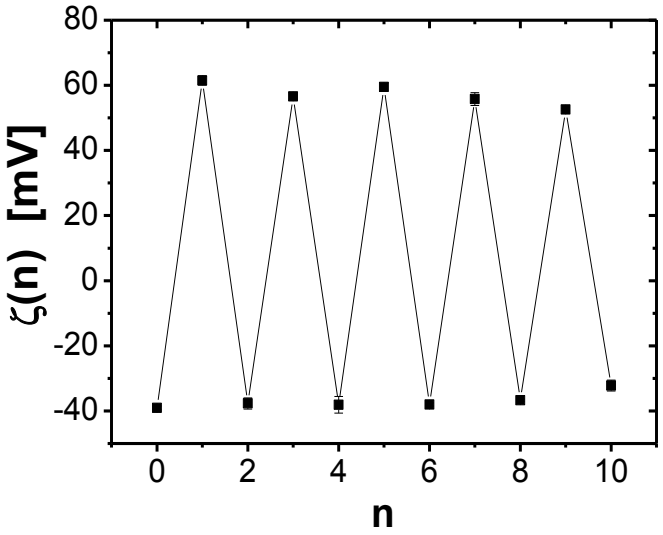

Figure 33. Zeta-potential ζ(n) of citrate-stabilized Au NPs (dc = 49.2 ± 4.9 nm, s = 1.1) to which n PE layers were adsorbed, as recoded in water. The plain NPs (n = 0) are negatively charged due to their citric acid coating. Addition of the first PE layer (PAH, n = 1) changes the charge of the NPs to a positive sign. Measurements were carried out in water solutions

Another direct tool for detecting the assembling process was employed, the rise of

the hydrodynamic diameter d_h upon addition of PE layers is plotted in *Figure 34* and illustrated in Table 2 The thickness of the PE coating (n layers) was calculated as ½·(d_h(n)-d_h(n=0)). The average thickness of each single layer was calculated by assuming that PSS and PAH contribute equally in the increase of the shell thickness as ½·(d_h(n)-d_h(n=0))/n. The mean thickness of a single PE layer d_{PE} = <½·(d_h(n) - d_h(n=0))/n>was 1.6 ± 0.4 nm based on the values of Table 2.

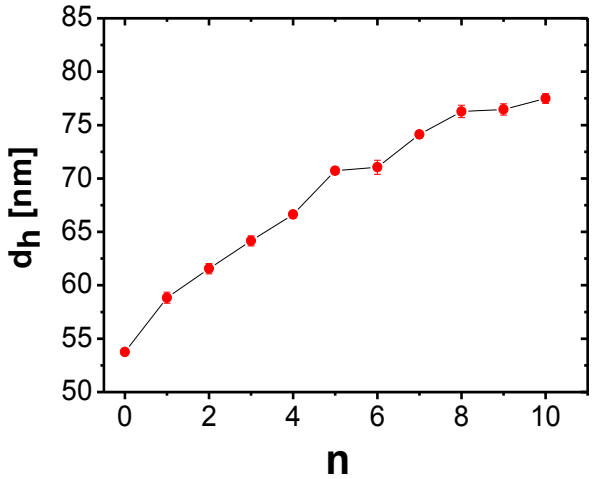

Figure 34. Hydrodynamic diameter dh of citrate-stabilized Au NPs (dc = 49.2 ± 4.9 nm, s = 1.1) upon layer-by-layer adsorption of n PEs layers. Data points correspond to mean values ± the standard deviation. Measurements were carried out in water solutions.

n	**0**	**1**	**2**	**3**	**4**	**5**	**6**	**7**	**8**	**9**	**10**
$_h$(n) [nm]	53.8 ±0.3	58.8 ±0.5	61.6 ±0.5	64.1 ±0.5	66.6 ±0.3	70.7 ±0.3	71.0 ±0.7	74.1 ±0.3	76.3 ±0.6	76.5 ±0.5	77.5 ±0.5
½·(d_h(n)-d_h(n=0))[nm]	0	2.5	3.9	5.2	6.4	8.5	10.2	11.2	11.2	11.3	11.9
d_{PE} [nm]	0	2.5	1.9	1.7	1.6	1.7	1.4	1.4	1.4	1.3	1.2

Table 2. The hydrodynamic diameters dh in dependence of the number n of the PE layers as displaced in Figure xx. The increase of the shell thickness in Au NPs due to PE adsorption is given as ½·(dh(n)-dh(n=0), and the corresponding single layer thickness as dPE = ½·(dh(n) - dh(n=0))/n.

4.2.2 Dimer formation

By using different numbers of PE layers, shells with different thicknesses can be generated. Depending on the polarity the last polyelectrolyte layer has opposite charge, either positively or negatively charged NPs can be obtained. This gives the opportunity for an electrostatically-driven linkage. When negatively and positively charged NPs are mixed together under diluted concentrations, predominantly NP

dimers will form besides some remaining NP monomers and some groupings which involve more than two NPs. Thus, the distance between the NP surfaces will be the sum of the thicknesses of the two PE shells around the NPs.

The UV-spectra again employed to investigate the dimer creating process. In Figure *1* showes there are indentify deceasing to the peak, which indicate the highly disperse property of single AuNPs, contrast with the AuNPs solution before mixing, the dimer spectra shows the typically agglomeration adsorb wavelength around 600nm to 700nm area.

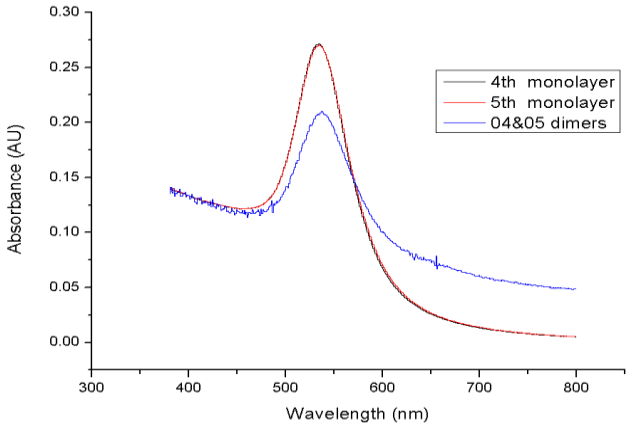

Figure 35. Illustrated the change of UV-visual spectra while dimer production process. The red line indicate the 4th and 5th monolayer coated as negative charge and positive charge polyelctrolytes, respectively; the blue line represent the dimer's spectra made from the mixture of 4th and 5th monolayer coated Au NPs.

When the reaction progresses in solution, bigger groupings of NPs will be formed. However, if the NPs are brought to a surface after appropriate reaction time like 10 min here, building-up of larger agglomerates can be avoided. In *Figure 36*, such NP assemblies are shown. Around 30% of the NPs form dimers (via calculation of radial distribution functions, as will be described later), and the rest mainly remains as individual NPs, in addition to some bigger assemblies.

Such moderate yield of dimers would exclude ensemble measurements (e.g. cuvette absorption spectroscopy) because the mixture of dimers with monomers usually results in a spectral broadening of the ensemble absorption peak compared to that of pure monomers, but the effect of plasmonic coupling may well be studied in a more quantitative way by monitoring the plasmon resonance shift through dark field analysis of individual dimers.

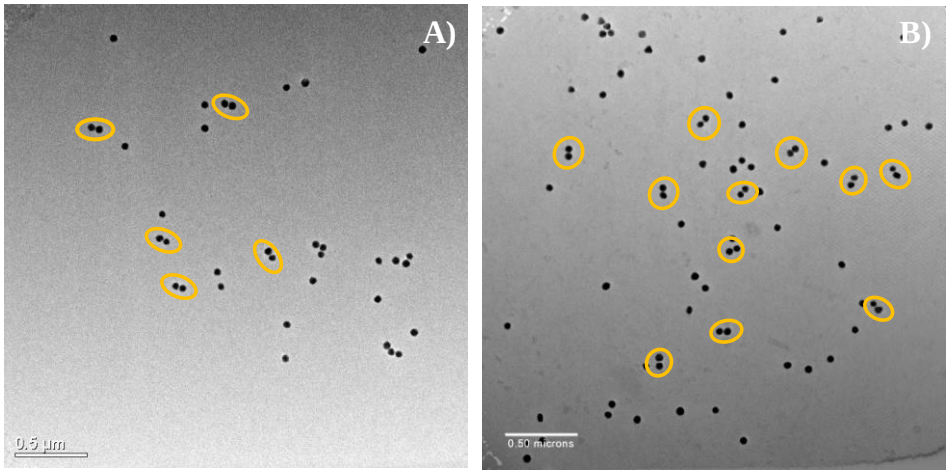

Figure 36. TEM images showing an area of 10 µm2 of a grid on which a mixture of Au NPs (dc = 49.2 ± 4.9 nm) coated with n and n+1 PE layers had been deposited. A) Around 30% of dimers are found in a mixture of Au (PAH) and Au (PAH, PSS) NPs (n = 1). B) Around 30% of dimers are found in a mixture of Au (PAH, PSS)$_4$ PAH and Au (PAH, PSS)$_5$ (n = 9). The scale bars correspond to 500 nm.

Nonspherical NP shape complicated the analysis not been include counting, see *Figure* 37. Inter-NP distances D (surface-to-surface) were measured with the software Image-J (version 3.0) for at least 50 different dimers, result see *Figure 38*.

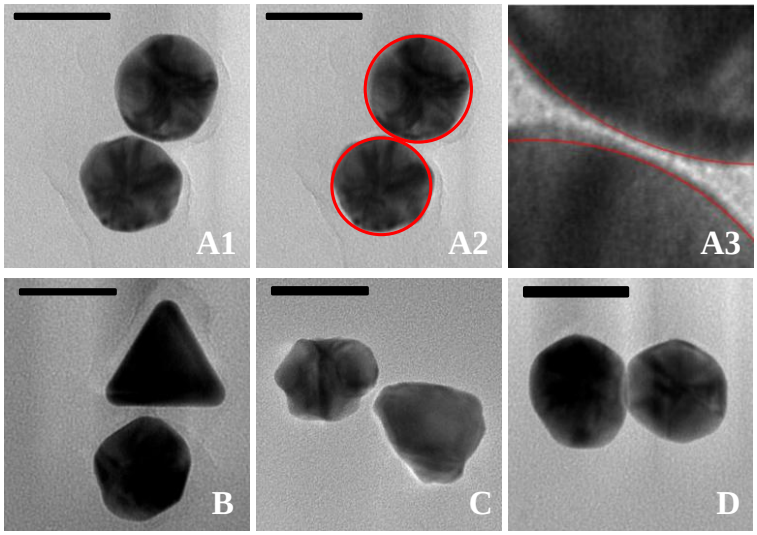

Figure 37. TEM images of dimers formed by quasi-spherical Au NPs with polyhedral shape (A1-A3), triangular and polyhedral shapes (B), very rough surface (C) and overlap of the Au cores. Image A2 points out the difference between a perfectly spherical shape (red circle) and the polyhedral shape of most of the Au NPs. Image A3 shows a zoom of image A2, where the red lines correspond to the border of the Au cores fitted with a perfectly spherical shape. The scale bars correspond to 50 nm.

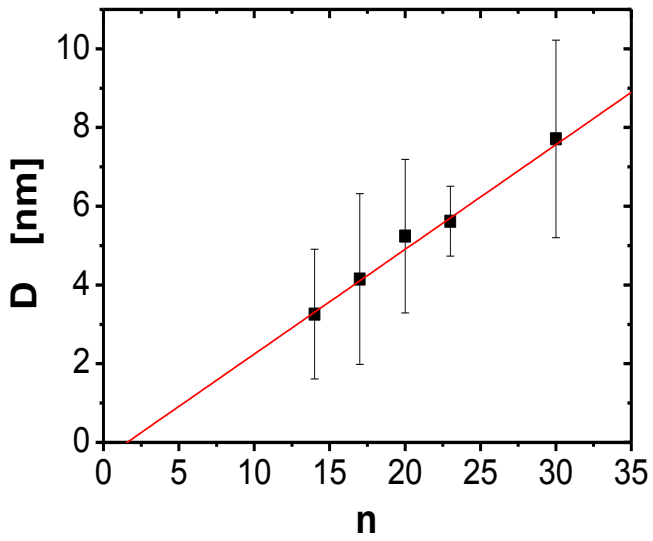

Figure 38. Inter-NP distance D (surface-to-surface) of Au NPs dimers formed by electrostatic interactions between oppositely charged NPs coated with n and n+1 PE layers (n = 14-30; data for smaller n are shown in the main manuscript). Data points correspond to mean values ± standard deviations. The red line is the linear mimic.

TEM images were captured at different magnifications. We considered groupings of two Au NPs with an inter-NP distance less than (2n+1)·1.6 nm as dimers, whereby $\Delta d_{½}$ = 1.6 nm is the average thickness per PE layer as obtained by DLS, Figure 39. We found that D increased following approximately a linear trend and the determined layer thickness dPE was consistently 0.13 ± 0.03 nm. However, for n > 9 the standard deviation of D increases dramatically, mainly due to the difficulty of producing PE coated Au NPs without non-specific agglomeration.

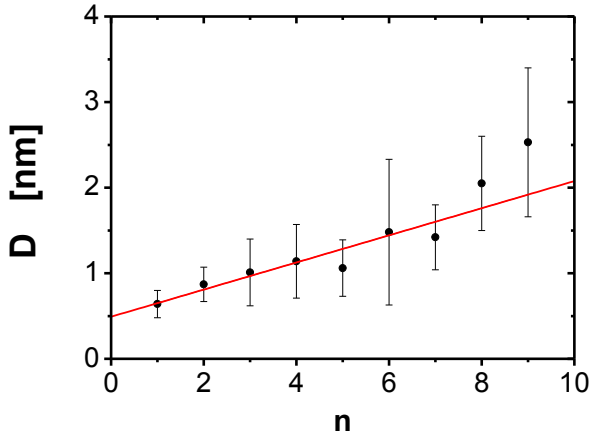

Figure 39. Inter-NP distance D of Au NP dimers (dc = 49.2 ± 4.9 nm, s = 1.1) formed by electrostatic interactions between oppositely-charged NPs coated with (n) and (n+1) PE layers with n = 1-9.

n	1	2	3	4	5	6	7	8	9
D [nm]	0.64 ±0.16	0.87 ±0.2	1.01 ±0.39	1.14 ±0.16	1.06 ±0.16	1.48 ±0.85	1.42 ±0.38	2.05 ±0.55	2.53 ±0.87
d_{PE}[nm]	0.21	0.17	0.14	0.12	0.10	0.11	0.09	0.12	0.13

Table 3. Surface-to-surface distance values D as obtained via TEM analysis for dimers (dc = 49.2 ± 4.9 nm, s = 1.1) made out of one NP with n and one NP with n+1 PE layers. The thickness of each PE layer dPE was estimated as dPE = D/(2n+1).

In order to offer more prove about the statistic and deprive the manually error from the agglomeration instead of dimer, the radial distribution function (RDF) analysis was recorded for the TEM images.

RDF functions were calculated from different TEM images by using MATLAB (software from MathWorks) [91]. Here, the RDF is defined as $g(r) = N(r)/(2\pi \cdot r \cdot \rho \cdot dr)$, where N(r) is the mean number of NPs which can be found in a ring of width dr at distance r from one NP, and ρ [m^{-2}] is the mean NP density. For each TEM image the NP positions were extracted and the RDF was generated with a binning distance dr of 1 pixel, equivalent to a spatial resolution of 0.5 nm. Artifacts due to image edges were reduced by dividing only through the fraction of the ring confined by the image dimensions instead of $2\pi r$. Finally, the distribution functions of all images were averaged.

The percentage of dimers calculated through RDF analysis was around 30%. Assuming that two NPs touched each other, then there would be peak in the g(r) distribution at $r = 2 \cdot (d_c/2) = d_c$. If there is a space between the NPs, the peak will be at higher r values. Thus, the first peak in the g(r) function refers to the center-to-center distance $r = D_{cc}$. The error ΔD_{cc} can be defined as the width at half-maximum of the peak $g(r = D_{cc})$. From the center-to-center distance D_{cc} the surface-to-surface distance D can be determined as $D = D_{cc} - d_c$.

Figure 40 shows RDFs g(r) for dimers made with n = 1 and n = 9. The position r of the peak in the RDFs corresponds to the mean center-to-center distance D_{cc} of the NPs in one dimer. The width of the peak g(r = Dcc) is defined as error ΔDcc. The same data as shown in *Figure 39*, thus, to determine D_{cc} as a peak in the g(r) distribution as $D_{cc} = 52 \pm 7$ nm (n = 1) and $D_{cc} = 54 \pm 13$ nm (n = 9).

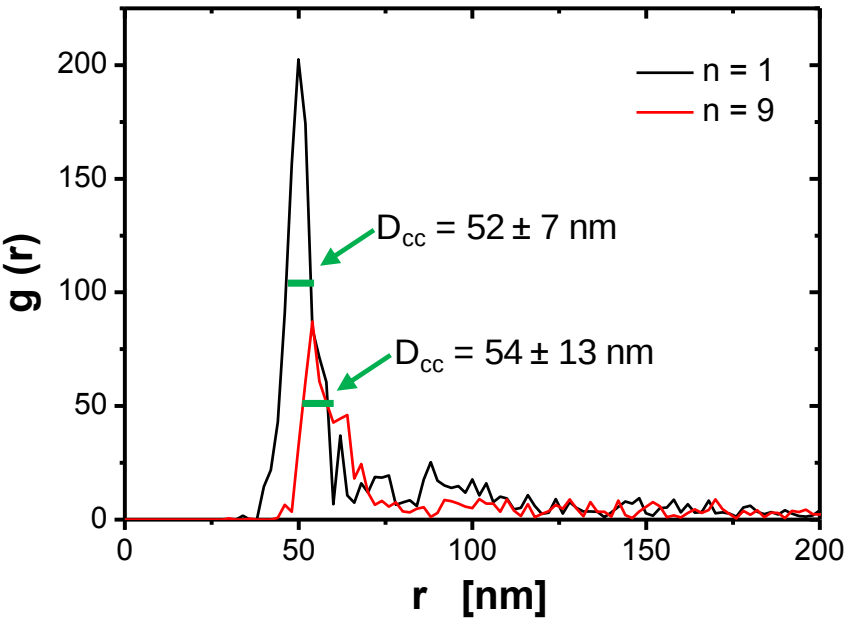

Figure 40. Radial distribution functions g(r) of the samples n= 1 and n= 9 (dc = 49.2 ± 4.9 nm). Data yield Dcc = 52 ± 7 nm (n = 1) and Dcc = 54 ± 13 nm (n = 9).

5. Conclusions and outlook

Polyelectrolyte multilayers are an emerging field with numerous application opportunities within interdisciplinary research areas. Since the LbL rose as a highly versatile tool in the last decade of the 20th century, more and more researchers have applied the technique to fabricate 2D (e.g., films) and 3D (e.g., particles/capsules) materials.

However, the synthesis of micro and nano sized colloidal particles produced by LbL assembly and their characterization could still be improved. For example in the case of LbL capsules, the sacrificial template is mainly chosen based on the application of the capsules. Calcium carbonate cores offer many advantages such as the possibility to entrap large molecules within their pores and mild conditions in the formation/dissolution but also many drawbacks. For example, not all the molecules co-precipitate efficiently inside the $CaCO_3$ cores and the size of such molecules should be above 20 kDa to not leak out of the capsule once the shell is formed. Another drawback is the control over the $CaCO_3$ particle size. In principle it is possible to produce particles from 0.5 to 10 µm but the smaller cores tend to dissolve during the LbL process. Regarding the shell, in some cases the aggregation of the capsules/particles made by LbL is likely to happen due to the charge of the polymers. The driving force during the LbL assembly is the electrostatic interaction. The particles/capsules are stable in solution due to electrostatic repulsions between particles with the same charge but particles/capsules are also sticky. In some conditions, the aggregation is hard to avoid.

The shell of LbL capsules is permeable in most cases to molecules as large as 10 kDa. This is an advantage to produce sensor capsules but a drawback for drug delivery since capsules leak out their encapsulated cargo. We have shown that it is possible to improve the loading of capsules by adding a degradable silica shell. We have compared two different kinds of LbL capsules with silica capsules in terms of loading efficiency and cargo release. Nevertheless, the loading effects still has a lot of capacity to be improved. In detail, an amount of cargo is always lost during the template dissolution. Post-loading of capsules and further decrease of capsule shell can be performed for molecules that are around 10 kDa. However, for much smaller molecules such as doxorubicin (cancer drug, ~0,6 kDa) it is not possible their entrapment within the porous shell unless micelles or liposomes are already inside the capsule. In conclusion, there is not an efficient and universal way to encapsulate molecules in the LbL capsules and every kind of molecule has its most efficient procedure. Understanding the parameters that affect the encapsulation is a key aspect for the improvement of the functional capsule formation.

Regarding gold nanoparticle coatings, it was possible to add by LbL up to 30 layers of polyelectrolytes on the gold surface. The change of zeta potential and the hydrodynamic ratio was measured. Gold dimers with increasing interparticle

distances were made by increasing the number of polyelectrolyte layers on their surface. Due to non-specific attractive interaction between the NPs, dimers could be easily confused with aggregates of particles. This method was compared with the production of dimers via biological interactions. The drawbacks of both techniques were pointed out.

In conclusion, the LbL has been applied to form different kinds of functional polyelectrolyte capsules and to form plasmonic particle dimers. Characterization of those materials has been performed using several techniques such as transmission electron microscopy and dynamic light scaterring. Some of the advantages and drawbacks of the LbL method have been pointed out. Finally, applications of LbL capsules and LbL Au coatings in control release, sensing and plasmonic coupling studies have been shown in this works.

6. Publications

This thesis shows part of my work about the self-assembly technology and the related publications produced between 2010 and 2014.The publications will be listed as below, meanwhile, my own contributions will be shown here.

6.1 Polyelectrolyte capsules

[A1] S. Carregal-Romero, P. Rinklin, S. Schulze, M. Schäfer, A. Ott, D. Hühn, X. Yu, B. Wolfrum, K. M. Weitzel, W. J. Parak, "Ion transport through polyelectrolyte multilayers", *Macromolecular Rapid Communications* **34**, 1820–1826 (2013).

The PEM capsules product by assemble LbL with polyelectrolyte materials in advance. Then, PEM shells encapsulated ion-sensitive fluorophores (SNARF), PEM shells act as semi-permeable fence between the SNARF and the surrounding media. Ion transport will be determined by the permeability of the capsule shell. Thus, the shell structure is able to influence the time response parameter for the ion-sensitive SNARF. We employed the magnetic NPs to control the capsule moving in flow pump setup, and we have recorded the time response of the encapsulated SNARF toward the pH changes. In addition, we also investigated this conductance of the PEM films for potassium ion.

Author's contribution in this paper：

- Synthesis of different LbL capsules loaded with a sensor dye or without cargos.
- Implemented the characterizations of capsules, in detail, .made the TEM images for all the capsule in the paper, also made the photograph of capsule by camera.

[A2] S.Carregal-Romero, P. Guardia, X. Yu, R. Hartmann, T. Pellegrino, W. J. Parak, "Magnetically triggered release of molecular cargo from iron oxide nanoparticle loaded microcapsules", *Nanoscale*, submitted.

Magnetic NPs playing the role as an alternative source for local heating, as the magnet field are much less absorbed by tissue than light, which lead to penetrated deeper of the tissue, and can be triggered by applying alternating magnetic field (AMF). One kind iron oxide nanocubes embedded microcapsules employed in this work as a platform for magnetically triggered molecular release. In detail, after post-loaded the cascade blue-labelled dextran represent as an model of encapsulation cargo, follow an AMF deal with the magnetic capsule, the shell was able to opened by the heat from the magnet cubes, leading the cargos release to the surrounding solution. The cargo release process was recorded by measuring the increase in absorbance and fluorescence under the exposure to AMF.

Author's contribution in this paper：

- Prepared the different capsules with/without magnetic NPs.
- Made the TEM images for the capsules and NPs attached in the hull of capsules,
  also showed the difference of TEM images in before/after the capsules opened by the heating.
- Made the histogram of the size distribution by DLS and recorded the zeta-potential of the polyelectrolytes capsules in water.

[A3] A. Ott, X. Yu, R. Hartmann, J. Rejman, A. Schütz, M. Ochs, W. J. Parak, S. Carregal-Romero, "Light-Addressable and Degradable Silica Capsules for Delivery of Molecular Cargo to the Cytosol of Cells", *Chemistry of Materials*, submitted.

In this work, there were two main release mechanisms of cargo molecules from degradable and light-responsive silica capsules. It was possible to load various molecules such as anti-cancer drugs (doxorubicin), proteins (bovine serum albumin) and nucleic acids (messenger RNA encoding green fluorescent protein).
In addition, to compared with several kind of PEM capsules, *in vitro* degradation and release assays have been investigated. Furthermore, the viability test showed that the cytotoxicity of silica capsule either with or without AuNPs have the similar influence as the degradable PEM capsules.

Author's contribution in this paper:

- Made some part of capsules, such as (DEXS/PARG), Au(DEXS/PARG), (PSS/PAH) and Au(PSS/PAH), measured the size histogram of these capsules.
- Made the TEM pictures for all of these capsules.
- Complementary of cytotoxicity assay for 6 groups of capsule with MDA-MB-231 cell line and Hela cell line.

6.2 Nanoparticles on bioapplication

[A4] X. Yu, D. Y. Lei, F. Amin, R. Hartmann, G. P. Acuna, A. Guerrero-Martínez, S. A. Maier, P. Tinnefeld, S. Carregal-Romero, W. J. Parak, "Distance control in-between plasmonic nanoparticles via biological and polymeric spacers", *Nano Today* **8**, 480 - 493 (2013).

The coupling of plasmons is exciting optical property, which can be generated between plasmonic NPs. This property is highly dependent on the inter-particle distance. This article was shown that controlling the distance of plasmonic particle can be obtained via biological spacers or polymer spacers.

Author's contribution in this paper:

- Firstly, I established the method for polyelectrolyte coating of AuNPs based

on LBL assembly. The zeta potential , UV-spectra, and size distribution data recorded after the cores of AuNPs coated with different layer of polyelectrolytes, respectively.

- Synthesis of AuNPs dimers via charges attract of different polyelectrolytes, measure the inner distance of the dimers.
- Made all the TEM images in this paper. Recorded the shape distribution of AuNPs.
- Wrote the part of LbL coating of AuNPs and dimer synthesis in the support information and help edit the main context partly.

[A5] R. Fenollosa, E. Garcia-Rico, S. Alvarez, R. Alvarez, X. Yu, I. Rodriguez, S. Carregal-Romero, C. Villanueva, P. Rivera-Gil, A. R. de Lera, W. J. Parak, F. Meseguer, Ramon A. Alvarez-Puebla, "Silicon nanoparticles as Trojan horses for potential cancer immunotherapy", *Journal of Nanobiotechnology*, submitted.

***Patent**:* R. Fenollosa, E. Garcia-Rico, S. Alvarez, R. Alvarez, X. Yu, I. Rodriguez, S. Carregal-Romero, C. Villanueva, P. Rivera-Gil, A. R. de Lera, W. J. Parak, F. Meseguer, Ramon A. Alvarez-Puebla, "Silicon nanoparticles as Trojan horses for potential cancer immunotherapy", European Union patent submitted.

An potential cancer treatment based on immunotherapy approach established in this work. We present here an immunotherapy approach for potential cancer treatment. The main idea is that a selective antibody conjugated with engineered silicon particles, lead to the surface of the target cancer cells enrich more engineered silicon particles than the control group, thus, induce massive target cells dead after long-term incubation. The *in vitro* uptake assay data indicate that the LD_{50} value of PSiNPs-HER-2 tumor cells is 15 fold lower than the LD_{50} value for control cells demonstrates specificity target effect. This is the new approach of potential chemotherapy agent against cancer in a target mechanism in particular.

Author's contribution in this paper：

- Culture MDA-MB-435 and SK-BR-3 cell lines, made the cytoxicity assay of silicon NPs.
- Made some TEM images for the silicon NPs.

7. Materials

Chemicals

The following chemicals were used for the preparation of the different nanoparticles, capsules and their modification. All the chemicals were used without further purification.

Material	Supplier	Order number
2-(N-morpholino) ethanesulfonic acid	Sigma-Aldrich	M3671
96-well plates for cell culture	Sigma-Aldrich	CLS3603
ammonium hydroxide solution	Sigma-Aldrich	320145
AuNPs (50nm colloidal gold)	British BioCell International	EM.GC50
calcium chloride	Sigma-Aldrich	223506
chloroform	Carl Roth	Y015.2
dextran sulfate sodium salt	Sigma-Aldrich	42867
dextran tetra methylrhodamine isothiocyanate	Sigma-Aldrich	T1287
doxorubicin hydrochloride	Sigma-Aldrich	D1515
ethanol	Carl Roth	9065.2
ethylenediamine-tetraacetic acid disodium salt	Sigma-Aldrich	E5134
Hela cells	ATCC	ATCC®CCL-2™
MDA-MB-231cells	ATCC	HTB-26™
methoxy-polyethyleneglycol with thiol terminus	Rapp Polymere GmbH	125000-40
poly(acrylamide-co-diallyl-dimethylammonium chloride)	Sigma-Aldrich	409181
poly(allylamine hydrochloride)	Sigma-Aldrich	283223
poly(sodium 4-styrenesulfonate)	Sigma-Aldrich	243051
poly-L-arginine hydrochloride	Sigma-Aldrich	P3892
Resazurin solution	Sigma-Aldrich	TOX8
SNARF-dextran (10k Da)	life technologies	D-3303
sodium carbonate	Sigma-Aldrich	S7795
sodium chloride	Carl Roth	HN00.2
tetraethyl orthosilicate	Sigma-Aldrich	86578
tris(hydroxymethyl)aminomethane	Carl Roth	4855
toluene	Carl Roth	9558.2

Techniques

The following techniques and equipments were used for the purification and characterization of the different capsules and AuNPs.

Centrifuge: Heraeus Variofuge 3.0RS MWCO

UV-Vis- and Fluorescence spectra: Agilent Technologies 8453 UV-Vis and Horiba FluoroLog

Dynamic light scattering (DLS): Malvern Zetasizer Nano ZS

Transmission electron microscopy (TEM): Jeol JEM-3010 TEM, copper grids from Plano (#160-3 for nanoparticles) and (#162-3 for microcapsules)

The software ImageTool (version 3.0) was used to derive the diameters of the template cores and silica capsules from the TEM images.

Fluorescence spectra of capsules were recorded with a fluorometer (Fluorolog-3 from Horiba JOBIN YVON).

Confocal fluorescent microscopy images of cells, which had been incubated with capsules, were acquired using a LSM 510 META microscope (Zeiss, Germany).

emCCD camera (C9100-13, Hamamatsu Photonics, Japan)

8. Abbreviations

Au	gold
AFM	alternating magnetic fields
BSA	bovine serum albumin
$CaCl_2$	calcium chloride
$CdCO_3$	cadmium carbonate
$CaCO_3$	calcium carbonate
DEXS	dextran sulfate sodium salt
DLS	dynamic light scattering
DLVO theory	Derjaguin−Landau−Verwey−Overbeek theory
DMEM	Dulbecco´s Modified Eagle Medium
DMF	dimethylformamide
DOX	doxorubicin hydrochloride
HF	hydrogen fluoride
EtOH	ethanol
EDTA	ethylene diamine tetraacetic acid disodium salt
FBS	fetal bovine serum
FITC	fluorescein 5-isothiocyanate
LbL	layer-by-layer
LSPR	localized surface plasmon resonance
mPEG-SH	methoxy-polyethyleneglycol with thiol terminus
MES	2-(*N*-morpholino)ethanesulfonic acid
MNPs	magnetic nanoparticles
Na_2CO_3	sodium carbonate
NPs	nanoparticles
NH_4OH	ammonium hydroxide solution
PAH	poly(allylamine hydrochloride)
PS-b-PAA	polystyrene- block- poly(acrylic acid)
P(Am-DDA)	poly(acrylamide-co-diallyl-dimethylammonium chloride)
PARG	poly-L-arginine hydrochloride
PEM	Polyelectrolytes micro
PSS	poly(sodium 4-styrenesulfonate)
PTX	paclitaxel
SEM	scanning electron microscopy
SNARF	seminaphtharhodafluor
TEM	transmission electron microscopy
THF	tetrahyfrofuran
TEOS	tetraethyl orthosilicate
TRIS	tris(hydroxymethyl)aminomethane
WDW power	Van der Waals' power

9. List of the capsule

Core Material	Core Diameter	Dissolvability	Positive Polyelectrolyte	Negative Polyelectrolyte	Cargo	Degradability	NPs in the shell	Publication of the Author in the dissertation	Typically Structure
Au NPs dimer	50 nm	No	PAH	PSS	No (Solid cores)	No	No	A4	Au@(PSS,PAH)$_n$+(PSS,PAH)$_{n+1}$ @Au
$CaCO_3$	2.6±0.3μm	Yes	PAH	PSS	Post SNARF-Dex10kDa	No, do not need	31±6 nm amphiphilic polymer (poly(isobutylene-alt-maleic anhydride)	A1	(PSS/PAH)$_2$ @-Fe2O3 (PSS/PAH)2g
$CaCO_3$	4.6±0.4μm	Yes	PAH	PSS	Post SNARF-Dex10kDa	No, opened by heating	iron oxide nanocubes 18±2 nm, z = -24.2 ± 8 mV	A2	(PSS/PAH)(PSS/P(Am-DDA) NPs (PAH)(PSS/PAH)$_2$
$CaCO_3$	same $CaCO_3$ core 5.3 ± 0.4 μm	Yes	No	No	PreFITC-BSA (~ 66 kDa,	Yes	No	A3	@mPEG-SH@SiO_2
$CaCO_3$	same $CaCO_3$ core 5.3 ± 0.4 μm	Yes	PAH	PSS	PreFITC-BSA (~ 66 kDa, PrePoly(styrene)-block-poly(acrylic acid) Postdoxorubicin (0.58 kDa) dextran-SNARF (10 kDa)	No, opened by Plasmon	Au	A3	@(PSS/PAH)Au@mPEG-SH@SiO$_2$
$CaCO_3$	same CaCO3 core 5.3 ± 0.4 μm	Yes	PARG	DEXS	PreFITC-BSA (~ 66 kDa, PrePoly(styrene)-block-poly(acrylic acid) Postdoxorubicin (0.58 kDa)	Yes	No	A3	(DEXS/PARG)$_5$
$CaCO_3$	same CaCO3 core 5.3 ± 0.4 μm	Yes	PARG	DEXS	PreFITC-BSA (~ 66 kDa, PrePoly(styrene)-block-poly(acrylic acid) Postdoxorubicin (0.58 kDa) dextran-SNARF (10 kDa)	No, opened by Plasmon	Au	A3	(DEXS/PARG)$_3$Au(DEXS/PARG)$_2$
$CaCO_3$	same CaCO3 core 5.3 ± 0.4 μm	Yes	PAH	PSS	PreFITC-BSA (~ 66 kDa, PrePoly(styrene)-block-poly(acrylic acid) Postdoxorubicin (0.58 kDa)	No, not able	No	A3	(PSS/PAH)$_5$
$CaCO_3$	same $CaCO_3$ core 5.3 ± 0.4 μm	Yes	PAH	PSS	PreFITC-BSA (~ 66 kDa, PrePoly(styrene)-block-poly(acrylic acid) Postdoxorubicin (0.58 kDa) dextran-SNARF (10 kDa)	No, opened by Plasmon	Au	A3	PSS/PAH)$_3$Au(DEXS/PAH)$_2$

$CaCO_3$	1.6 ± 0.3 µm	Yes	PAH	PSS	Dextran2000K	No	No	preparation	$(PSS/PAH)_4$
$CaCO_3$	1.6 ± 0.3 µm	Yes	PAH	PSS	Dextran2000K	No	No	preparation	$(PSS/PAH)_4PSS$
$CaCO_3$	1.6 ± 0.3 µm	Yes	PARG	DEXS	Dextran2000K	No	No	preparation	$(PARG/Dexs)_4$
$CaCO_3$	1.6 ± 0.3 µm	Yes	PARG	DEXS	Dextran2000K	No	No	preparation	$(PARG/Dexs)_4Parg$

10. References

[1]. Decher, G.; Hong, J.-D., Buildup of Ultrathin Multilayer Films by a Self-Assembly Process, 1 Consecutive Adsorption of Anionic and Cationic Bipolar Amphiphiles on Charged Surfaces. *Macormol. Symp., Macormol. Symp.* 1991, 46, 321 - 327.

[2]. Decher, G., Fuzzy nanoassemblies: Toward Layered Polymeric Multicomposites. *Science* 1997, 277, 1232-1237.

[3]. Decher, G.; Hong, J. D.; Schmitt, J., Buildup of Ultrathin Multilayer Films by a Self-Assembly Process.3. Consecutively Alternating Adsorption of Anionic and Cationic Polyelectrolytes on Charged Surfaces. *Thin Solid Films* 1992, 210, (1-2), 831-835.

[4]. Sukhorukov, G. B.; Lvov, Y. M.; Möhwald, H.; Decher, G., Assembly of polyelectrolyte multilayer films by consecutively alternating adsorption of polynucleotides and polycations. *Thin Solid Films* 1996, 284-285, 220-223.

[5]. Decher, G.; Lehr, B.; Lowack, K.; Lvov, Y.; Schmitt, J., New Nanocomposite Films For Biosensors - Layer-By-Layer Adsorbed Films Of Polyelectrolytes, Proteins Or Dna. *Biosensors & Bioelectronics* 1994, 9, (9-10), 677-684.

[6]. Rivera_Gil, P.; Koker, S. D.; De_Geest, B. G.; Parak, W. J., Intracellular processing of proteins mediated by biodegradable polyelectrolyte capsules. *Nano Letters* 2009, 9, (12), 4398-4402.

[7]. Yue, Z.; Khalid, W.; Zanella, M.; Abbasi, A. Z.; Pfreundt, A.; Rivera_Gil, P.; Schubert, K.; Lisdat, F.; Parak, W. J., Evaluation of Quantum Dots Applied as Switchable Layer in a Light-Controlled Electrochemical Sensor. *Analytical and Bioanalytical Chemistry* 2010, 396, (3), 1095-1103.

[8]. Abbasi, A. Z.; Gutierrez, L.; del Mercato, L. L.; Herranz, F.; Chubykalo-Fesenko, O.; Veintemillas-Verdaguer, S.; Parak, W. J.; Morales, M. P.; Gonzalez, J. M.; Hernando, A.; de la Presa, P., Magnetic Capsules for NMR Imaging: Effect of Magnetic Nanoparticles Spatial Distribution and Aggregation. *J. Phys. Chem. C* 2011, 115, (14), 6257-6264.

[9]. Carregal-Romero, S.; Rinklin, P.; Schulze, S.; Schäfer, M.; Ott, A.; Hühn, D.; Yu, X.; Wolfrum, B.; Weitzel, K.-M.; Parak, W. J., Ion transport through polyelectrolyte multilayers. *Macromolecular Rapid Communications* 2013, 34, 1820–1826.

[10]. Kotov, N. A.; Dekany, I.; Fendler, J. H., Layer-by-Layer Self-Assembly of Polyelectrolyte-Semiconductor Nanoparticle Composite Films. *The Journal of Physical Chemistry* 1995, 99, (35), 13065-13069.

[11]. Ochs, M.; Carregal-Romero, S.; Rejman, J.; Braeckmans, K.; De Smedt, S. C.; Parak, W. J., Light-addressable capsules as caged compound matrix for controlled in vitro release. *Angewandte Chemie International Edition* 2013, 52, (2), 695-699.

[12]. Wiegand, M.; Reiche, M.; Gösele, U.; Gutjahr, K.; Stolze, D.; Longwitz, R.; Hiller, E., Wafer bonding of silicon wafers covered with various surface layers. *Sensors and Actuators A* 2000, 86, (1-2), 91-95.

[13]. Keller, S. W.; Johnson, S. A.; Brigham, E. S.; Yonemoto, E. H.; Mallouk, T. E., Photoinduced charge separation in multilayer thin films grown by sequential adsorption of polyelectrolytes. *Journal of the American Chemical Society* 1995, 117, (51), 12879-12880.

[14]. Sukhorukov, G. B.; Donath, E.; Davis, S.; Lichtenfeld, H.; Caruso, F.; Popov, V. I.; Möhwald, H., Stepwise polyelectrolyte assembly on particle surfaces: a novel approach to colloid design. *Polymers for Advanced Technologies* 1998, 9, (10-11), 759-767.

[15]. Caruso, F.; Caruso, R. A.; Möhwald, H., Production of Hollow Microspheres from Nanostructured Composite Particles. *Chemistry of Materials* 1999, 11, (11), 3309-3314.

[16]. Antipov, A. A.; Shchukin, D.; Fedutik, Y.; Petrov, A. I.; Sukhorukov, G. B.; Möhwald, H., Carbonate microparticles for hollow polyelectrolyte capsules fabrication. *COLLOIDS AND SURFACES A-PHYSICOCHEMICAL AND ENGINEERING ASPECTS* 2003, 224, (1-3), 175-183.

[17]. Antipov, A. A.; Sukhorukov, G. B.; Leporatti, S.; Radtchenko, I. L.; Donath, E.; Möhwald, H., Polyelectrolyte multilayer capsule permeability control. *Colloids and Surfaces, A: Physicochemical and Engineering Aspects* 2002, 198, (Sp. Iss. SI), 535-541.

[18]. Ariga, K.; Hill, J. P.; Ji, Q., Layer-by-layer assembly as a versatile bottom-up nanofabrication technique for exploratory research and realistic application. *Phys Chem Chem Phys* 2007, 9, (19), 2319-40.

[19]. Leporatti, S.; Gao, C.; Voigt, A.; Donath, E.; Möhwald, H., Shrinking of ultrathin polyelectrolyte multilayer capsules upon annealing: A confocal laser scanning microscopy and scanning force microscopy study. *The*

European Physical Journal E - Soft Matter **2004, 5, (1), 13-20.**

[20]. Rivera Gil, P.; del Mercato, L. L.; del Pino, P.; Muñoz-Javier, A.; Parak, W. J., Nanoparticle-Modified Polyelectrolyte Capsules. *Nano Today* **2008, 3, (3-4), 12-21.**

[21]. De Cock, L. J.; Lenoir, J.; De Koker, S.; Vermeersch, V.; Skirtach, A. G.; Dubruel, P.; Adriaens, E.; Vervaet, C.; Remon, J. P.; De Geest, B. G., Mucosal irritation potential of polyelectrolyte multilayer capsules. *Biomaterials* **2011, 32, (7), 1967-1977.**

[22]. Sukhorukov, G. B.; Antipov, A. A.; Voigt, A.; Donath, E.; Mohwald, H., pH-controlled macromolecule encapsulation in and release from polyelectrolyte multilayer nanocapsules. *Macromolecular Rapid Communications* **2001, 22, (1), 44-46.**

[23]. Pastoriza-Santos, I.; Schöler, B.; Caruso, F., Core-Shell Colloids and Hollow Polyelectrolyte Capsules Based on Diazoresins. *Advanced Functional Materials* **2001, 11, (2), 122-128.**

[24]. Dejugnat, C.; Halozan, D.; Sukhorukov, G. B., Defined Picogram Dose Inclusion and Release of Macromolecules using Polyelectrolyte Microcapsules. *Macromolecular Rapid Communications* **2005, 26, 961-967.**

[25]. Fujiwara, M.; Shiokawa, K.; Morigaki, K.; Zhu, Y. C.; Nakahara, Y., Calcium carbonate microcapsules encapsulating biomacromolecules. *Chemical Engineering Journal* **2008, 137, (1), 14-22.**

[26]. Krzyzanek, V.; Sporenberg, N.; Keller, U.; Guddorf, J.; Reichelt, R.; Schoenhoff, M., Polyelectrolyte multilayer capsules: nanostructure and visualisation of nanopores in the wall. *Soft Matter* **2011, 7, (15), 7034-7041.**

[27]. Klar, T. A., Biosensing with plasmonic nanoparticles. In *Nanophotonics with Surface Plasmons*, **ed.; V.M., S.; S., K., 'Ed.'^'Eds.' Elsevier: The Netherlands, 2007; 'Vol.' p^pp 219-270.**

[28]. Yu, C.; Irudayaraj, J., Multiplex Biosensor Using Gold Nanorods. *Analytical Chemistry* **2007, 79, (2), 572-579.**

[29]. Boisselier, E.; Astruc, D., Gold Nanoparticles in Nanomedicine: Preparations, Imaging, Diagnostics, Therapies and Toxicity. *Chemical Society Reviews* **2009, 38, (6), 1759-1782.**

[30]. Ghosh, P.; Han, G.; De, M.; Kim, C. K.; Rotello, V. M., Gold

Nanoparticles in Delivery Applications. ***Advanced Drug Delivery Reviews*** **2008, 60, (11), 1307-1315.**

[31]. Han, G.; Ghosh, P.; Rotello, V. M., Functionalized gold nanoparticles for drug delivery. ***Nanomedicine (Lond)*** **2007, 2, (1), 113-23.**

[32]. Nativo, P.; Prior, I. A.; Brust, M., Uptake and intracellular fate of surface-modified gold nanoparticles. ***ACS Nano*** **2008, 2, (8), 1639-44.**

[33]. Moores, A.; Goettmann, F., The Plasmon Band in Noble Metal Nanoparticles: An Introduction to Theory and Applications. ***New Journal Of Chemistry*** **2006, 30, (8), 1121-1132.**

[34]. Wang, H.; Brandl, D. W.; Nordlander, P.; Halas, N. J., Plasmonic nanostructures: Artificial molecules. ***Accounts Of Chemical Research*** **2007, 40, (1), 53-62.**

[35]. Jans, H.; Huo, Q., Gold nanoparticle-enabled biological and chemical detection and analysis. ***Chemical Society Reviews*** **2012, 41, (7), 2849-2866.**

[36]. Ghosh, S. K.; Pal, T., Interparticle Coupling Effect on the Surface Plasmon Resonance of Gold Nanoparticles: From Theory to Applications. ***Chemical Reviews*** **2007, 107, 4797-4862.**

[37]. Caruso, F.; Caruso, R. A.; Möhwald, H., Nanoengineering of Inorganic and Hybrid Hollow Spheres by Colloidal Templating. ***Science*** **1998, 282, 1111-1114.**

[38]. Donath, E.; Sukhorukov, G. B.; Caruso, F.; Davis, S. A.; Möhwald, H., Novel Hollow Polymer Shells by Colloid-Templated Assembly of Polyelectrolytes. ***Angewandte Chemie International Edition*** **1998, 37, (16), 2202-2205.**

[39]. Gittins, D. I.; Caruso, F., Tailoring the Polyelectrolyte Coating of Metal Nanoparticles. ***Journal of Physical Chemistry B*** **2001, 105, (29), 6846-6852.**

[40]. Schneider, G.; Decher, G., From Functional Core/Shell Nanoparticles Prepared via Layer-by-Layer Deposition to Empty Nanospheres. ***Nano Letters*** **2004, 4, (10), 1833-1839.**

[41]. Schneider, G.; Decher, G., Functional core/shell nanoparticles via layer-by-layer assembly. investigation of the experimental parameters for controlling particle aggregation and for enhancing dispersion stability.

Langmuir **2008, 24, (5), 1778-89.**

[42]. Schneider, G.; Decher, G.; Nerambourg, N.; Praho, R.; Werts, M. H.; Blanchard-Desce, M., Distance-dependent fluorescence quenching on gold nanoparticles ensheathed with layer-by-layer assembled polyelectrolytes. *Nano Lett* **2006, 6, (3), 530-6.**

[43]. Coronado, E. A.; Encina, E. R.; Stefani, F. D., Optical properties of metallic nanoparticles: manipulating light, heat and forces at the nanoscale. *Nanoscale* **2011, 3, (10), 4042-59.**

[44]. Ma, X.; Fletcher, K.; Kipp, T.; Grzelczak, M. P.; Wang, Z.; Guerrero-Martinez, A.; Pastoriza-Santos, I.; Kornowski, A.; Liz-Marzan, L. M.; Mews, A., Photoluminescence of Individual Au/CdSe Nanocrystal Complexes with Variable Interparticle Distances. *Journal of Physical Chemistry Letters* **2011, 2, (19), 2466-2471.**

[45]. Beyer, S. R.; Ullrich, S.; Kudera, S.; Gardiner, A. T.; Cogdell, R. J.; Koehler, J., Hybrid Nanostructures for Enhanced Light-Harvesting: Plasmon Induced Increase in Fluorescence from Individual Photosynthetic Pigment-Protein Complexes. *Nano Letters* **2011, 11, (11), 4897-4901.**

[46]. Zhang, Y.; Wen, F.; Zhen, Y.-R.; Nordlander, P.; Halas, N. J., Coherent Fano resonances in a plasmonic nanocluster enhance optical four-wave mixing. *Proc. Natl. Acad. Sci. U. S. A.* **2013, (May 20 2013), 1-5, 5 pp.**

[47]. Zhao, J.; Frank, B.; Burger, S.; Giessen, H., Large-Area High-Quality Plasmonic Oligomers Fabricated by Angle-Controlled Colloidal Nanolithography. *ACS Nano* **2011, 5, (11), 9009-9016.**

[48]. Kinkhabwala, A.; Yu, Z.; Fan, S.; Avlasevich, Y.; Muellen, K.; Moerner, W. E., Large single-molecule fluorescence enhancements produced by a bowtie nanoantenna. *Nat. Photonics FIELD Full Journal Title:Nature Photonics* **2009, 3, (11), 654-657.**

[49]. Bek, A.; Jansen, R.; Ringler, M.; Mayilo, S.; Klar, T. A.; Feldmann, J., Fluorescence enhancement in hot spots of AFM-designed gold nanoparticle sandwiches. *Nano Letters* **2008, 8, (2), 485-490.**

[50]. Volodkin, D. V.; Madaboosi, N.; Blacklock, J.; Skirtach, A. G.; Mohwald, H., Surface-Supported Multilayers Decorated with Bio-active Material Aimed at Light-Triggered Drug Delivery. *Langmuir* **2009, 25, (24), 14037-14043.**

[51]. Nikoobakht, B.; Wang, Z. L.; El-Sayed, M. A., Self-Assembly of Gold Nanorods. *Journal of Physical Chemistry B* 2000, 104, (36), 8635-8640.

[52]. Montenegro, J.-M.; Grazu, V.; Sukhanova, A.; Agarwal, S.; Fuente, J. M. d. l.; Nabiev, I.; Greiner, A.; Parak, W. J., Controlled antibody/(bio-) conjugation of inorganic nanoparticles for targeted delivery. *Advanced Drug Delivery Reviews* 2013, 65, 677–688.

[53]. Verwey, E. J. W.; Overbeek, J. T. G., The Van Der Waals-London Attractive Forces. In *Theory of the Stability of Lyophobic Colloids*, ed.; 'Ed.'^'Eds.' Elsevier Publishing Company: Amsterdam, 1948; 'Vol.' p^pp 98-105.

[54]. Tong, W.; Zhu, Y.; Wang, Z.; Gao, C.; Mohwald, H., Micelles-encapsulated microcapsules for sequential loading of hydrophobic and water-soluble drugs. *Macromol Rapid Commun* 2010, 31, (11), 1015-9.

[55]. Tong, W. J.; Gao, C. Y.; Mohwald, H., Single polyelectrolyte microcapsules fabricated by glutaraldehyde-mediated covalent layer-by-layer assembly. *Macromolecular Rapid Communications* 2006, 27, (24), 2078-2083.

[56]. Ladam, G.; Schaad, P.; Voegel, J. C.; Schaaf, P.; Decher, G.; Cuisinier, F., In situ determination of the structural properties of initially deposited polyelectrolyte multilayers. *Langmuir* 2000, 16, (3), 1249-1255.

[57]. Richert, L.; Boulmedais, F.; Lavalle, P.; Mutterer, J.; Ferreux, E.; Decher, G.; Schaaf, P.; Voegel, J.-C.; Picart, C., Improvement of stability and cell adhesion properties of polyelectrolyte multilayer films by chemical cross-linking. *Biomacromolecules* 2004, 5, (2), 284-294.

[58]. Ruths, J.; Essler, F.; Decher, G.; Riegler, H., Polyelectrolytes I: Polyanion/Polycation Multilayers at the Air/Monolayer/Water Interface as Elements for Quantitative Polymer Adsorption Studies and Preparation of Hetero-superlattices on Solid Surfaces. *Langmuir* 2000, 16, (23), 8871-8878.

[59]. Wang, Y.; Moo, Y. X.; Chen, C.; Gunawan, P.; Xu, R., Fast precipitation of uniform CaCO3 nanospheres and their transformation to hollow hydroxyapatite nanospheres. *J. Colloid Interface Sci.* 2010, 352, (2), 393-400.

[60]. Carregal-Romero, S.; Ochs, M.; Rivera Gil, P.; Ganas, C.; Pavlov, A. M.; Sukhorukov, G. B.; Parak, W. J., NIR-light triggered delivery of macromolecules into the cytosol. *Journal of Controlled Release* 2012, 159, 120-127.

[61]. Petrov, A. P.; Volodkin, D. V.; Sukhorukov, G. B., Protein-Calcium Carbonate Coprecipitation: A Tool for Protein Encapsulation. *Biotechnol. Prog.* 2005, 21, (3), 918-925.

[62]. Volodkin, D. V.; Petrov, A. I.; Prevot, M.; Sukhorukov, G. B., Matrix polyelectrolyte microcapsules: New system for macromolecule encapsulation. *Langmuir* 2004, 20, (8), 3398-3406.

[63]. Carregal-Romero, S.; Ochs, M.; Parak, W. J., Nanoparticle-functionalized microcapsules for in vitro delivery and sensing. *Nanophotonics* 2012, 1, (2), 171-180.

[64]. She, Z.; Antipina, M. N.; Li, J.; Sukhorukov, G. B., Mechanism of protein release from polyelectrolyte multilayer microcapsules. *Biomacromolecules* 2010, 11, (5), 1241-7.

[65]. Fernandez-Lopez, C.; Mateo-Mateo, C.; Alvarez-Puebla, R. A.; Perez-Juste, J.; Pastoriza-Santos, I.; Liz-Marzan, L. M., Highly Controlled Silica Coating of PEG-Capped Metal Nanoparticles and Preparation of SERS-Encoded Particles. *Langmuir* 2009, 25, (24), 13894-13899.

[66]. Volodkin, D. V.; Larionova, N. I.; Sukhorukov, G. B., Protein encapsulation via porous $CaCO_3$ microparticles templating. *Biomacromolecules* 2004, 5, (5), 1962-1972.

[67]. Hyeon, T.; Lee, S. S.; Park, J.; Chung, Y.; Bin Na, H., Synthesis of Highly Crystalline and Monodisperse Maghemite Nanocrystallites without a Size-Selection Process. *J. Am. Chem. Soc.* 2001, 123, (51), 12798-12801.

[68]. Lin, C.-A. J.; Sperling, R. A.; Li, J. K.; Yang, T.-Y.; Li, P.-Y.; Zanella, M.; Chang, W. H.; Parak, W. J., Design of an Amphiphilic Polymer for Nanoparticle Coating and Functionalization. *Small* 2008, 4, (3), 334-341.

[69]. Fernández-Argüelles, M. T.; Yakovlev, A.; Sperling, R. A.; Luccardini, C.; Gaillard, S.; Medel, A. S.; Mallet, J.-M.; Brochon, J.-C.; Feltz, A.; Oheim, M.; Parak, W. J., Synthesis and Characterization of Polymer-Coated Quantum Dots with Integrated Acceptor Dyes as FRET-based Nanoprobes. *Nano Letters* 2007, 7, (9), 2613-2617.

[70]. Pellegrino, T.; Manna, L.; Kudera, S.; Liedl, T.; Koktysh, D.; Rogach, A. L.; Keller, S.; Rädler, J.; Natile, G.; Parak, W. J., Hydrophobic Nanocrystals Coated with an Amphiphilic Polymer Shell: A General Route to Water Soluble Nanocrystals. *Nano Letters* 2004, 4, (4), 703-707.

[71]. Hrelescu, C.; Stehr, J.; Ringler, M.; Sperling, R. A.; Parak, W. J.; Klar, T. A.; Feldmann, J., DNA Melting in Gold Nanostove Clusters. *Journal Of Physical Chemistry C* 2010, 114, (16), 7401-7411.

[72]. Huang, J.; Jackson, K. S.; Murphy, C. J., Polyelectrolyte Wrapping Layers Control Rates of Photothermal Molecular Release from Gold Nanorods. *Nano Lett.* 2012, 12, (6), 2982-2987.

[73]. Hühn, D.; Govorov, A.; Rivera Gil, P.; Parak, W. J., Photostimulated Au Nanoheaters in Polymer and Biological Media: Characterization of Mechanical Destruction and Boiling. *Advanced Functional Materials* 2012, 22, (2), 294-303.

[74]. Muñoz Javier, A.; del Pino, P.; Bedard, M. F.; Skirtach, A. G.; Ho, D.; Sukhorukov, G. B.; Plank, C.; Parak, W. J., Photoactivated Release of Cargo from the Cavity of Polyelectrolyte Capsules to the Cytosol of Cells. *Langmuir* 2008, 24, 12517-12520.

[75]. Zelikin, A. N.; Breheney, K.; Robert, R.; Tjipto, E.; Wark, K., Cytotoxicity and Internalization of Polymer Hydrogel Capsules by Mammalian Cells. *Biomacromolecules* 2010, 11, (8), 2123-2129.

[76]. O'Brien, J.; Wilson, I.; Ortaon, T.; Pognan, F., Investigation of the Alamar blue (Resazurin) fluorescent dye for the assessment of mammalian cell cytotoxicity. *TOXICOLOGY* 2001, 164, (1-3), 132-132.

[77]. Kastl, L.; Sasse, D.; Wulf, V.; Hartmann, R.; Mircheski, J.; Ranke, C.; Carregal-Romero, S.; Martínez-López, J. A.; Fernández-Chacón, R.; Parak, W. J.; Elsaesser, H.-P.; Rivera Gil, P., Multiple internalization pathways of polyelectrolyte multilayer capsules into mammalian cells. *ACS Nano* 2013, 7, (8), 6605-6618.

[78]. Yang, Q.; Wang, S.; Fan, P.; Wang, L.; Di, Y.; Lin, K.; Xiao, F.-S., pH-Responsive Carrier System Based on Carboxylic Acid Modified Mesoporous Silica and Polyelectrolyte for Drug Delivery. *Chem. Mater.* 2005, 17, (24), 5999-6003.

[79]. Zhu, C.-L.; Song, X.-Y.; Zhou, W.-H.; Yang, H.-H.; Wen, Y.-H.; Wang, X.-R., An efficient cell-targeting and intracellular controlled-release drug delivery system based on mesoporous silica nanoparticle-polyelectrolyte multilayer-aptamer conjugates. *J. Mater. Chem.* 2009, 19, (41), 7765-7770.

[80]. Buckler, K. J.; Vaughan-Jones, R. D., Application Of A New Ph-Sensitive Fluoroprobe (Carboxy-Snarf-1) For Intracellular Ph

Measurement In Small, Isolated Cells. ***Pflügers Archiv-European Journal Of Physiology*** **1990, 417, (2), 234-239.**

[81]. Pankhurst, Q. A.; Connolly, J.; Jones, S. K.; Dobson, J., Applications of Magnetic Nanoparticles in Biomedicine. ***Journal of Physics D: Applied Physics*** **2003, 36, (13), R167-R181.**

[82]. Colombo, M.; Carregal-Romero, S.; Casula, M. F.; Gutiérrez, L.; Morales, M. P.; Böhm, I. B.; Heverhagen, J. T.; Prosperi, D.; Parak, W. J., Biological Applications of Magnetic Nanoparticles. ***Chemical Society Reviews*** **2012, 41, 4306-4334.**

[83]. Fortin, J. P.; Wilhelm, C.; Servais, J.; Menager, C.; Bacri, J. C.; Gazeau, F., Size-sorted anionic iron oxide nanomagnets as colloidal mediators for magnetic hyperthermia. ***J. Am. Chem. Soc.*** **2007, 129, (9), 2628-35.**

[84]. Angelatos, A. S.; Radt, B.; Caruso, F., Light-Responsive Polyelectrolyte/Gold Nanoparticle Microcapsules. ***J. Phys. Chem. B*** **2005, 109, 3071-3076.**

[85]. Zhang, F.; Ali, Z.; Amin, F.; Feltz, A.; Oheim, M.; Parak, W. J., Ion and pH sensing with colloidal nanoparticles: influence of surface charge on sensing and colloidal properties. ***ChemPhysChem*** **2010, 11, 730-735.**

[86]. Hunter, R. C.; Beveridge, T. J., Application of a pH-sensitive fluoroprobe (C-SNARF-4) for pH microenvironment analysis in Pseudomonas aeruginosa biofilms. ***Applied and Environmental Microbiology*** **2005, 71, (5), 2501-2510.**

[87]. Muñoz_Javier, A.; Kreft, O.; Semmling, M.; Kempter, S.; Skirtach, A. G.; Bruns, O.; Pino, P. d.; Bedard, M. F.; Rädler, J.; Käs, J.; Plank, C.; Sukhorukov, G.; Parak, W. J., Uptake of colloidal polyelectrolyte coated particles and polyelectrolyte multilayer capsules by living cells. ***Advanced Materials*** **2008, 20, (22), 4281-4287.**

[88]. Holmberg, K., Surface Chemistry of Paper. In ***HANDBOOK OF APPLIED SURFACE AND COLLOID CHEMISTRY*****, ed.; Shah, D. O.; Schwuger, M. J., 'Ed.'^'Eds.' Wiley-VHC: Chichester, 2002; 'Vol.' 1, p^pp 123-174.**

[89]. Hermansson, M., The DLVO theory in microbial adhesion. ***Colloids and Surfaces B-Biointerfaces*** **1999, 14, (1-4), 105-119.**

[90]. Myers, D., ***Surfaces, Interfaces, and Colloids: Principles and***

***Applications*. ed.; John Wiley & Sons, Inc: 1999; 'Vol.' p 519.**

[91]. Rivera Gil, P.; Jimenez de Aberasturi, D.; Wulf, V.; Pelaz, B.; del Pino, P.; Zhao, Y.; de la Fuente, J.; Ruiz de Larramendi, I.; Rojo, T.; Liang, X.-J.; Parak, W. J., The Challenge to Relate the Physicochemical Properties of Colloidal Nanoparticles to Their Cytotoxicity. *Accounts of Chemical Research* 2013, 46, (3), 743-749.

Acknowledgement

I would like to address my great thanks to Professor Wolfgang J. Parak offer me the opportunity to work in his group and to supervise me in a free atmosphere. Here, I want to express my special thanks to my friend and supervisor Dr. Susana Carregal-Romero for many constructive discussions and advices since I arrived here.

I want to thanks our whole friendly group, special thanks to Abbasi, Faheem, Raimo, Moritz, Christian, José Maria, Bea, Pablo, Dani for many nice memory during these years besides working together, and thanks our special office member Prof. Bauer for his seasonal fresh fruit from his garden.

Further thanks to Dr. Andreas Schaper and Mr. Micheale Hellwig for their assistants about the TEM works. Thanks Andreas and Stefanie always help me to handle with a lot documents and computer affairs. Thanks Raimo again for his RDF analysis works.

Thanks Susana again for proofreading the manuscript, thanks Moritz again and thanks Jonas for translate the abstract in German.

Here, I am very glad to address my thanks to my Chinese friends past and current in Marburg, thanks Fang, Xiaowei, Tianqiang for your constructive discussions in the lab and so many nice Chinese food parties with you, also thanks some other friends I forget mention here.

Thanks the financial support from China Scholarship Council (CSC).

At last, I want to thanks whole of my family for your mental supporting, especially my parents, your encouragement make me face one by one challenges bravely. To my dear Qian, I have no proper word to describe my thanks for your warmly company during these years, thank you always standing with me in our daily life and my lab works, you make my life become more colorful and more meaningful.

Appendix

Wissenschaftlicher Werdegang

Persönliche Daten

Name: Yu, Xiang
Geburtsdatum: 30.09.1985
Geburtsort: Sichuan, China
Staatsangehörigkeit: Chinesisch

Ausbildung

09/2010 – 09/2014 Doktorarbeit, Philipps-Universität Marburg
Thema: Synthesis and characterization of colloidal particles fabricated by layer-by-layer assembly
Betreuer: Prof. Dr. Wolfgang. J. Parak

09/2007 – 06/2010 Master degree of Biochemistry and molecular biology, Sichuan Agriculture University, China
Thema: Self-assembled bilayer membrane structure based on hydrophobic bilayer theory
Betreuer: Prof. Dr. Wanshen Yang

09/2003 – 06/2007 Bachelor degree of agriculture science, Sichuan Agriculture Universtiy, China

09/2000 – 06/2003 Yan'feng high school, Sichuan, China

Wissenschaftliche Veröffentlichungen

[A1] S. Carregal-Romero, P. Rinklin, S. Schulze, M. Schäfer, A. Ott, D. Hühn, X. Yu, B. Wolfrum, K. M. Weitzel, W. J. Parak, "Ion transport through polyelectrolyte multilayers", *Macromolecular Rapid Communications* **34**, 1820–1826 (2013).

[A2] S.Carregal-Romero, P. Guardia, X. Yu, R. Hartmann, T. Pellegrino, W. J. Parak, "Magnetically triggered release of molecular cargo from iron oxide nanoparticle loaded microcapsules", *Nanoscale*, submitted.

[A3] A. Ott, X. Yu, R. Hartmann, J. Rejman, A. Schütz, M. Ochs, W. J. Parak, S. Carregal-Romero, "Light-Addressable and Degradable Silica Capsules for Delivery of Molecular Cargo to the Cytosol of Cells", *Chemistry of Materials*, submitted.

[A4] X. Yu, D. Y. Lei, F. Amin, R. Hartmann, G. P. Acuna, A. Guerrero-Martínez, S. A. Maier, P. Tinnefeld, S. Carregal-Romero, W. J. Parak, "Distance control in-between plasmonic nanoparticles via biological and polymeric spacers", *Nano*

Today **8**, 480 - 493 (2013).

[A5] R. Fenollosa, E. Garcia-Rico, S. Alvarez, R. Alvarez, X. Yu, I. Rodriguez, S. Carregal-Romero, C. Villanueva, P. Rivera-Gil, A. R. de Lera, W. J. Parak, F. Meseguer, Ramon A. Alvarez-Puebla, "Silicon nanoparticles as Trojan horses for potential cancer immunotherapy", *Journal of Nanobiotechnology*, submitted.

Patente

R. Fenollosa, E. Garcia-Rico, S. Alvarez, R. Alvarez, X. Yu, I. Rodriguez, S. Carregal-Romero, C. Villanueva, P. Rivera-Gil, A. R. de Lera, W. J. Parak, F. Meseguer, Ramon A. Alvarez-Puebla, "Silicon nanoparticles as Trojan horses for potential cancer immunotherapy", submitted.

*Gleichberechtigte Erstautorenschaft
Marburg, 01.09.2014

Erklärung

Hiermit versichere ich, dass ich meine Dissertation

Synthesis and characterization of particles fabricated by layer-by-layer assembly

selbständig ohne unerlaubte Hilfe angefertigt und mich dabei keiner anderen als der von mir ausdrücklich bezeichneten Quellen und Hilfen bedient habe.

Die Dissertation wurde in der jetzigen oder einer ähnlichen Form noch bei keiner Hochschuleeingereicht und hat noch keinem sonstigen Prüfungszweck gedient.

Name, Vorname: Yu, Xiang

Marburg, 01.09.2014 .....

Unterschrift

Ion Transport Through Polyelectrolyte Multilayers

Susana Carregal-Romero, Philipp Rinklin, Susanne Schulze, Martin Schäfer, Andrea Ott, Dominik Hühn, Xiang Yu, Bernhard Wolfrum,* Karl-Michael Weitzel,* Wolfgang J. Parak*

Polyelectrolyte multilayer (PEM) films and capsules loaded with ion-sensitive fluorophores can be used as ion-sensors for many applications including measurements of intracellular ion concentration. Previous studies have shown the influence of the PEM films/shells on the specific response of encapsulated ion-sensitive fluorophores. PEM shells are considered as semipermeable barriers between the environment and the encapsulated fluorophores. Parameters such as the time response of the encapsulated sensor can be affected by the porosity and charge of the PEM shell. In this study, the time response of an encapsulated pH-sensitive fluorophore towards pH changes in the surrounding environment is investigated. Furthermore, the conductance of PEM films for potassium ions is determined.

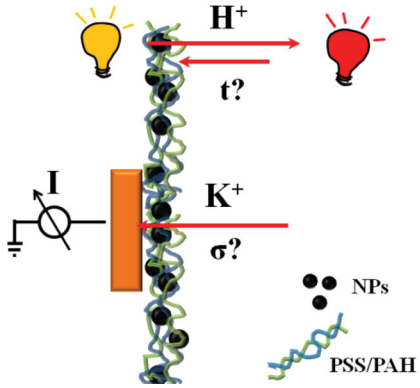

1. Introduction

Polyelectrolyte multilayer (PEM) films (i.e., planar geometry) and capsules (i.e., spherical geometry) produced by layer-by-layer (lbl) self assembly methods have become popular materials in applications such as filtration,[1] drug delivery,[2,3] and sensors.[4,5] Concerning sensing, one strategy is based on embedding analyte-sensitive fluorophores in the cavity of PEM capsules. In particular, this can be achieved by linkage of the analyte-sensitive fluorophores to big macromolecules such as dextran, which can be entrapped in the inner cavities of the capsules.[5] Upon encapsulation of the modified analyte-sensitive fluorophore, the fluorescence emission of the capsules will change depending on the analyte concentration. Thus, the analyte concentration can be determined via fluorescence read-out.[5] The PEM shell hereby acts as a semi-permeable membrane. PEM capsules must be porous enough to allow free diffusion of analyte molecules into the capsules where they can be detected. In contrast, their pores must be small enough to prevent the leakage of the analyte-sensitive fluorophores bound to macromolecules out of the capsules. Thus this detection principle is limited to small analytes, such as ions or small molecules like urea or CO_2, which can traverse the PEM shell.[6,7] Diffusion of ions or small molecules in a porous medium depends on the permeability.[8] The permeability of PEM shells can be tuned by

S. Carregal-Romero, A. Ott, D. Hühn, X. Yu, W. J. Parak
Fachbereich Physik, Philipps Universität Marburg, Marburg, Germany
E-mail: wolfgang.parak@physik.uni-marburg.de
S. Carregal-Romero
BIONAND, Centro Andaluz de Nanomedicina y Biotecnología, Málaga, Spain
P. Rinklin, B. Wolfrum
Institute of Bioelectronics PGI-8/ICS-8, JARA-FIT, Forschungszentrum, Jülich, Jülich, Germany
E-mail: b.wolfrum@fz-juelich.de
S. Schulze, M. Schäfer, K.-M. Weitzel
Fachbereich Chemie, Philipps Universität Marburg, Marburg, Germany
E-mail: weitzel@chemie.uni-marburg.de
W. J. Parak
CIC Biomagune, San Sebastian, Spain

DOI: 10.1002/marc.201300571

modification of several parameters during their assembly: i) Porosity of PEM shells depends on the chemical structure of the polyelectrolytes.[9] ii) The increase of the number of polyelectrolyte layers decreases the permeability of the shell.[10] iii) The introduction of additional building blocks such as nanoparticles (NPs) in-between the polyelectrolyte layers changes permeability of the PEM shells.[11] iv) Parameters such as temperature and ionic strength during the lbl assembly process also affect the final pore size of the PEM shell.[12,13] Furthermore, besides the assembly process, changes in the environment of already assembled PEM shells are also of importance and can temporarily or permanently modify their permeability due to the shrinking or swelling of the capsule. The swelling/shrinking of capsules depends on the nature of the polyelectrolytes, the number of bilayers, and the charge of the terminating layer. The environmental parameters that can affect the permeability are: i) temperature,[14,15] ii) changes of pH,[16–18] iii) changes of the redox state,[19] iv) changes in the polarity of the solvent,[20] and v) changes of the ionic strength.[21,22]

In the following, the transport of small ions as example of analyte molecules through PEM shells will be discussed. Due to their charge, ions can interact electrostatically with the PEM shell, in contrast to uncharged analytes. Understanding the ion transport through PEM shells is important for several applications especially for PEM capsules based ion-sensors. As already mentioned PEM capsules based on ion-sensitive fluorophores entrapped in the inner cavity have been successfully used as ion-sensors for Na^+, K^+, Cl^- and H^+ "in test tube"[5,23] and in vitro.[23–26] In this context, even multiplexed ion-sensing was demonstrated by using quantum dots (QDs) acting as barcodes.[27] These sensors can only work in case ions from the analyte solution or cellular environment can diffuse through the PEM shell and thus reach the encapsulated ion-sensitive fluorophores. Therefore, for further applications it is necessary to gain a better understanding of the parameters that affect the ion transport in these systems. Here in particular the temporal resolution, i.e., how fast ions can traverse the PEM shells and the possibility to determine absolute ion concentrations, i.e., if the ion concentration inside and outside the PEM shells is the same, are of importance. Concerning static equilibria and due to effects related to the Donnan potential, the ion concentration inside capsules in general differs from the bulk concentration.[22,28–31] Dynamic equilibria (transport processes) have been described in terms of ion diffusion and ion conductance. Ghostine et al. for example calculated diffusion coefficients of ferricyanide through a PEM shell using steady-state electrochemistry.[32] They observed an increase of the ion mobility as the temperature and the charge increased. Currently established concepts for determining ion conductivity of solid materials include impedance spectroscopy (IS),[33–35] the radiotracer diffusion technique (RD),[36] and pulsed field gradient nuclear magnetic resonance (PFG-NMR).[37–39] IS relies on the ability to have two electrodes in contact with the sample, which in the case of nanoscale samples raises the problem of electrical short circuits. RD and PFG-NMR do not use electrodes but cannot be easily applied to nanoscale samples either. The ideal technique for measuring ion transport through ultra-thin samples would be based on a setup with a single sample electrode contact. Such a new technique, termed low energy bombardment induced ion transport (BIIT) has been recently developed and demonstrated to be widely applicable.[40–42]

This work first tries to address the question how fast ions from the bulk can reach the ion-sensitive fluorophores embedded in the capsule cavity. For this purpose we measured the time response of encapsulated pH-sensitive fluorophores, which gives an upper limit for the response time of ion-sensitive dyes entrapped within PEM capsules. Second ion conductivity (in the case of potassium) through PEM membranes has been investigated experimentally. As the presence of NPs within the PEM shells is an important tool for adding new functionalities to the capsules such as magnetic guidance and barcoding,[27,43] we have also studied the influence of the presence of gold NPs in PEM films on their ion conductivity.

2. Results and Discussion

2.1. Synthesis of PEM Capsules with Embedded pH-sensitive Fluorophores

PEM capsules with the pH indicator seminaphtharhodafluor (SNARF) in their cavity and with and without polymer coated magnetic NPs (γ-Fe_2O_3, 31 ± 6 nm core diameter)[44,45] in their shell were synthesized according to standard procedures by lbl assembly of poly(sodium 4-styrenesulfonate) (PSS) and poly(allylamine hydrochloride) (PAH).[26,45] Some characterization data of the capsules are reported in Figure 1. SNARF is a pH-sensitive fluorophore which emits at two different wavelengths.[46] The ratio of the intensities of the two emission peaks depends on the pH value of the environment. In acidic media SNARF emits light more in the yellow at 583 nm and in alkaline ones more in the red at 627 nm.

2.2. Estimation of the Diffusion Time of Ions into PEM Capsules

For the study of the time response of encapsulated SNARF as pH-sensitive fluorophore the PEM capsules were modified with magnetic NPs. The PEM capsules were exposed to a time-dependent pH concentration profile, while meas-

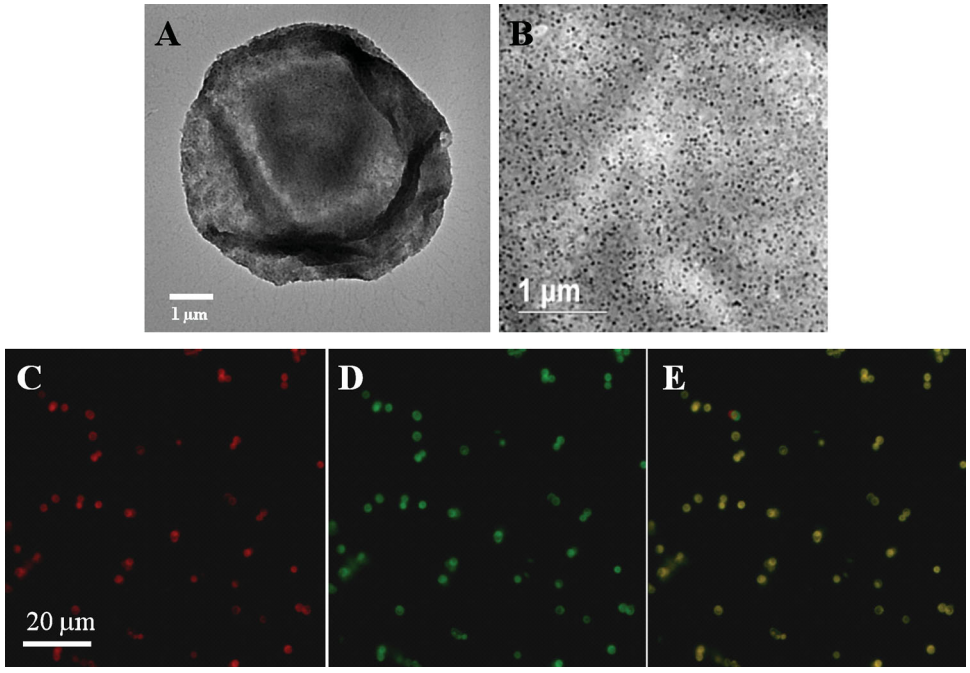

Figure 1. (A) Transmission electron microscopy (TEM) image of a PEM capsule loaded with γ-Fe_2O_3 NPs in its PEM wall (without SNARF in its cavity). (B) Image of the same capsule with higher resolution in order to demonstrate the distribution of the magnetic NPs. (C-E) Confocal microscopy images (red, "green" channel + overlay) of PEM capsules with magnetic NPs in their walls, and with the ratiometric dye SNARF in their cavity. Please note that SNARF actually emits in the red and in the yellow. However, for presentation purposes the yellow emission is depicted in green in false color mode. The composition of the walls of these magnetic PEM capsules was $(PSS/PAH)_2$γ-Fe_2O_3 $(PSS/PAH)_2$. SNARF was linked to dextran (M_w = 10 kDa) in order to prevent leakage of the dye from the capsule cavity.[26] The ratio of the emission intensities in the "green" and red channel can be used to calculate the local pH value.[23]

uring the fluorescence response (I_y) in real-time. We used a microfluidic channel with two inlets and a single outlet to generate a dynamic pH gradient (see Figure 2). The channel was molded using polyolefin polymer (POP). To load the channel with magnetic pH-sensitive PEM capsules, a suspension of the capsules (≈7×10^4 mL^{-1}) was flushed through the channel and capsules (with embedded magnetic NPs) were trapped at the top of the channel via a magnetic field.[47] The capsules did not deform during the magnetic trapping and kept their spherical shape (see the Supporting Information). Afterwards, two different pH-buffered solutions (10 mM of 2-(*N*-morpholino)ethanesulfonic acid

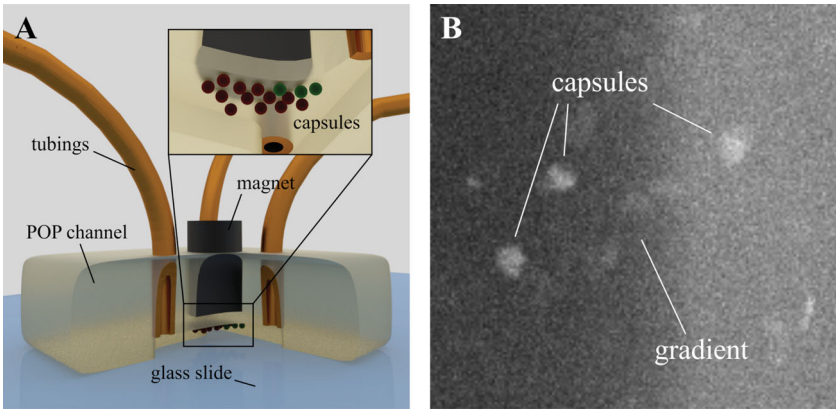

Figure 2. A) Microfluidic channel coupled to a fluorescence microscope where the PEM capsules are magnetically trapped at the top of the channel. Two solutions (1, 2) with different concentrations of protons (c_1, c_2) and pressure (p_1, p_2) are mixed producing a gradient that can be moved perpendicular to the direction of the gradient plane by (p_1, p_2) modification. B) Fluorescence image of $(PSS/PAH)_2$γ-Fe_2O_3 $(PSS/PAH)_2$ capsules trapped in the microfluidic channel in the vicinity of a static gradient (TRIS buffer adjusted to pH 9 on the left and MES buffer adjusted to pH6 labeled with TRITC on the right).

(MES) and 1 mM of tris(hydroxymethyl)aminomethane (TRIS) adjusted to pH 6 and pH 9, respectively) were pumped into the individual microchannel inlets using a pressure controlled fluidic system. By applying alternating pressures of 100 and 300 mbar at each inlet, the pH gradient could be rapidly moved from one side of the fluidic chamber to the other. The change in fluorescence of the SNARF in the capsules induced by the gradient's switching was recorded with an emCCD camera mounted to an inverted fluorescence microscope. The interframe time for the recording was set to 26.6 ms. For each measurement two pulses of pH 6 and pH 9 (duration: 10 s each) were applied and the intensity traces of individual capsules were extracted from the recorded image sequence. In order to increase the time resolution of the set-up, only one filter was used and thus the microscope registered intensity changes only of the yellow emission channel (I_y). In this way, at acidic pH = 6 the emission I_y of the capsules is higher than at basic pH = 9. The increase/decrease of such emission was measured while pH buffers (pH = 6 and 9) were exchanged. To correlate the capsules' switching behavior with that of the gradient, control measurements were performed using the above mentioned solutions and pressure protocols with tetramethylrhodamine isothiocyanate (TRITC) added to the pH 6 buffer.

The time it takes for ions (in this case H^+) to diffuse into the PEM capsules was estimated from the temporal change in fluorescence during exposure to the switching pH gradient in the microfluidic system. Therefore, we analyzed the recorded fluorescence intensity traces $I_y(t)$ of each capsule after switching from pH 6 to pH 9 and vice versa. Figure 3 shows a typical response after switching the concentration from pH 6 to pH 9. An offset was added to set the lower average steady-state fluorescence signal to 0. The horizontal lines indicate the levels at which 25%, 50% and 75% of the expected intensity change had occurred. To evaluate the response speed we derived the time it takes for the fluorescence change to reach a 25% threshold of the target value (at least 3 standard deviations of the root mean square (RMS) noise). This can be seen as the onset of unambiguous detection for the pH concentration measurements. To obtain a full response curve, the recorded intensity signal has to be deconvoluted with the concentration profile of the gradient. However, this would require exact knowledge of the time-dependent concentration distribution, for example by solving the combined Navier-Stokes and convection diffusion equations with the proper boundary conditions. Thus only an upper limit for the response time can be derived by assuming a step-like concentration profile of the gradient. From the recorded intensity traces of the individual capsules, we thus obtain a half time response of 163 ± 64 ms for the switch from pH 6 to pH 9 and 213 ± 114 ms for the switch from pH 9 to pH 6 (n = 8). The discrepancy for the two switching directions could be explained by inhomogeneities and the finite width of the actual concentration gradient at the channel surface. Another possible explanation could be related with the degree of ionization of the PAH layer. At pH 9 the ammonium groups of PAH are more deprotonated than at pH 6 and the loopy conformation of PAH in this conditions could decrease the permeation of H^+ through the capsule shell. In this way, the time response of the sensor capsule would be higher when the shift is from higher to lower pH than the contrary as it was observed in our experiment. It is known that the pH can affect the permeation of different ions such as Na^+, therefore it could also affect the permeation of H^+.[22] Nevertheless, the results yield a good estimate for an upper boundary of the response time of encapsulated SNARF to pH. The half time response of SNARF free in solution has been studied by fluorescent spectrophotometry using a stopped-flow mixing accessory that decreases the response time of the fluorescent spectrophotometer to 1 ms and the mixing time up to 8 ms. Chen et al. reported a response time of around 50 ms for SNARF free in solution and for switching from pH 2 to pH 10.[48] Therefore, the charged PEM shell increases the upper limit of the half time response for encapsulated SNARF as pH-sensor to 100-150 ms. Chen et al. also observed an increase of 10 ms in the time response of SNARF encapsulated in a nanoreactor made of calcium phosphate and phosphatidylcholine liposomes. The different nature of the SNARF carriers could explain the discrepancies. Nevertheless, the time response of SNARF encapsulated in PEM capsules is enough for many in vitro pH detection applications.[25,49] The effect of the PEM shell needs to be taken into account when using techniques that require higher temporal resolution.[50] It should be considered that proton transport or even diffusional transport of small ions in water occurs on a much faster time scale (*e.g.* 0.5 ms for a typical diffusion constant of $1.0 \cdot 10^{-9}$ m^2/s at a diffusion length of 1 μm considering 1D diffusion),[51] which is the size range of one PEM capsule.

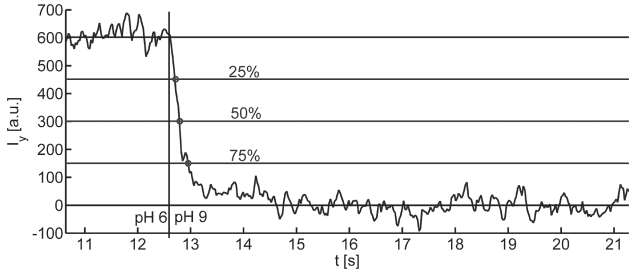

Figure 3. Fluorescence response measurements of PEM capsules loaded with 10 kDa SNARF-dextran in real-time. The selected filter set (excitation 440-490 nm, beam splitter 510 nm and emission 525-625 nm) records the emission $I_y(t)$ of the acidic form (pH 6) of SNARF. The vertical line indicates the time at which pH was switched from pH = 6 to pH = 9.

2.3. Estimation of the Ion Conductivity of Planar PEM Films

Finally, we studied the ion conductivity of planar PEM films, first without NPs trapped in between the polyelectrolyte layers. In a second measurement, the influence of the NPs on the ion conductivity was investigated. Application of PFG-NMR to the PEM films as investigated in this work is not straight forward, since the layers are in general prepared on a substrate. As it was mentioned, trying to detect the ion conductivity through these films with the help of impedance spectroscopy requires contact with two electrodes, which can easily induce short-circuits in the case of ultra-thin layers. As a consequence, we employ another technique, the recently developed bombardment induced ion transport (BIIT).[40–42] The pivotal aspect of this approach is that there is only the contact between one single electrode and the sample of interest needed for measuring the direct ion current through the film. The ion transport in the sample is induced by shining an ion beam on the front side of the sample, which leads to the adsorption of ions there. Adjusting the kinetic energy of the ions allowed us to create a well-defined surface potential and eventually gives rise to a potential and a concentration gradient across the sample. The ion transport was then detected by measuring the current induced on the backside electrode.

We have investigated the ionic conductivity of PEM films consisting of sixteen bilayers of (PAH/PSS) with and without gold NPs within the film, $(PAH/PSS)_{16}$ and $(PAH/PSS)(PAH/Au\ NPs/PSS)_{15}$ respectively, by means of the BIIT technique. The layers were prepared by the lbl technique according to a previously published protocol.[52] directly on a copper plate that was premodified with a monolayer of 3-mercaptopropionic acid, which at the same time served as the backside electrode required in BIIT (see the Supporting Information). The first layer of 3-mercaptopropionic acid was necessary to have a negative surface charge and start the lbl assembly.[53] The layers were bombarded by a continuous potassium ion beam with energies ranging between thermal conditions and about 10 eV. The current of the primary K^+ beam was typically 5 nA. In the experiment, the backside current was measured as a function of the ion beam potential which in turn determines the surface potential.

Our measurements indicate that the conductance of the $(PAH/PSS)_{16}$ membranes with and without Au NPs was of the order of $G = 1{\cdot}10^{-9}$ S; see Figure 4. Combined

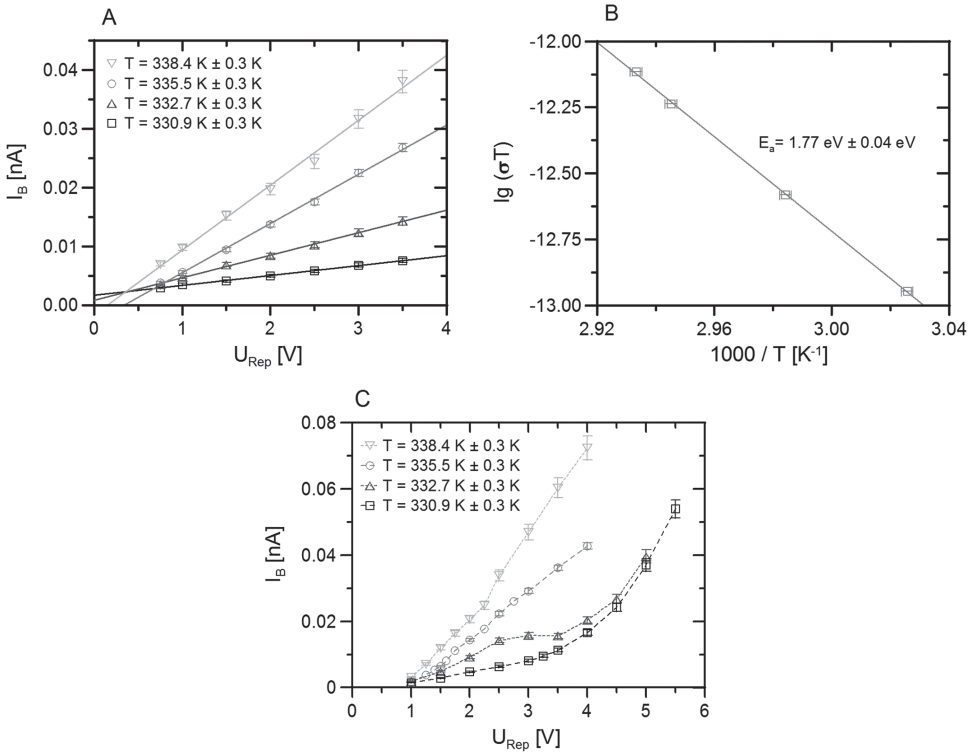

Figure 4. A) Backside current I_B in the PEM film based on $(PAH/PSS)_{16}$ without NPs as a function of the repeller voltage U_{Rep} at different temperatures. B) Arrhenius plot of the temperature dependence of the ionic conductivity σ in a polyelectrolyte multilayer film of PSS and PAH. The slope of the linear regression to the BIIT data is included, leading to the activation energy E_a. C) Backside current I_B of the PEM film based on $(PAH/PSS)(PAH/Au\ NPs/PSS)_{15}$ as a function of the repeller voltage.

with the area hit by the ion beam and the actual thickness of the membranes this leads to a conductivity of approximately 10^{-12} S/m. Much higher conductivities have been reported in the literature for e.g. protons in PEM films. However those measurements were carried out in aqueous conditions.[54,55] Here, the BIIT experiment was carried out under high vacuum conditions (10^{-9} mbar), so the membranes are most likely free of water. Our results agree with previously reported conductivities for similar PEM films of PSS/PAH in low hydration conditions. Direct current (DC) conductivities for (PSS/PAH) films were reported to be in the range of 10^{-12} S/m.[54,55] De et al. studied the dependence between humidity and ion conductivity in polyelectrolyte complexes for two different cations (Na^+ and Cs^+).[56] The water content within the PEM matrix was found to increase almost linearly while the DC ion conductivity increased exponentially with increasing humidity. Water molecules are responsible for the ion hydration as well as for the lowering of the energy barrier of the ion transport. Therefore, the conductivity and the activation energy for the ion transport obtained by the BIIT technique were expected to be lower and higher respectively than the ones obtained at higher ambient pressure.[57]

Despite the conductivities of both films with and without NPs being on the same order of magnitude, the current-voltage characteristics are fundamentally different (cf. Figure 4A,C). For the film without NPs, the observed backside current increased linearly with the applied voltage, indicating an Ohm's law like behavior. A similar behavior can be found for ion conducting glasses[41] and is most likely induced by the high number of mobile carriers inside the film prior to the ion bombardment. By contrast, the films with NPs clearly show a non-linear current-voltage characteristic indicating that more than one transport mechanism has to be considered. The presence of the NPs induces additional grains and thus grain boundaries such that competing conduction path ways arise. Depending on the given conditions such as the temperature and the applied voltage, the charge transport might work more efficiently either through the film material or along the grain boundaries. Finally one can probably not categorically rule out the possibility of electronic conductivity (as opposed to ionic conductivity) in the film with NPs. As a result, the current-voltage characteristics show linear and power law regimes as well as plateaus in the conductivity for one single temperature at different applied voltages. Thus, the temperature dependence of the conductivity is more complicated when NPs are present such that the activation energy in terms of an Arrhenius behavior cannot be derived. In contrast, the conductivity of the $(PAH/PSS)_{16}$ films made without NPs exhibits a simple Arrhenius behavior such that a well-defined activation energy of 1.77 ± 0.04 eV could be determined.

3. Conclusions

In conclusion, PEM shells around encapsulated ion-sensitive fluorophores act as semi-permeable barrier between the ion-sensitive fluorophores and the surrounding media. This barrier probably increases the response time of the ion-sensitive fluorophores. In the case of SNARF as example of a pH-sensitive fluorophore the response time was found to be below 500 ms, which is acceptable for many studies involving the analysis of the kinetics of cellular pH changes. Studies of the ion (here K^+) conductivity of PEM films have shown that films with and without NPs possess the same K^+ conductance in the order of $G = 1{\cdot}10^{-9}$ S meaning that the presence of gold NPs does not significantly affect the ion conductivity of the PEM shell. However the presence of gold NPs within the shell modified subtle details of the current-voltage characteristics of the PEM shell. The BIIT approach applied in this work has hardly any intrinsic thickness limitation. As such, the current experiment is considered to provide a proof of principle which paves the road to the investigation of even thinner films.

Supporting Information

Supporting Information is available from the Wiley Online Library or from the author.

Acknowledgements: This work was partly funded by the German Research Foundation (DFG grant PA 794/15-1 to WJP). X. Yu acknowledges a Chinese government scholarship (CSC).

Received: July 26, 2013; Revised: August 31, 2013; Published online: November 13, 2013; DOI: 10.1002/marc.201300571

[1] Z. Liu, Y. Yi, J. Gauczinski, H. Xu, M. Schönhoff, X. Zhang, *Langmuir* **2011**, *27*, 11806.
[2] S. Park, S. H. Bhang, W.-G. La, J. Seo, B.-S. Kim, K. Char, *Biomaterials* **2012**, *33*, 5468.
[3] M. Ochs, S. Carregal-Romero, J. Rejman, K. Braeckmans, S. C. De Smedt, W. J. Parak, *Angew. Chem. Int. Ed.* **2013**, *52*, 695.
[4] Z. Guanghong, X. Yibo, G. Jian, W. Zhiqiang, Z. Xi, *Langmuir* **2010**, *26*, 15022.
[5] L. L. del Mercato, A. Z. Abbasi, W. J. Parak, *Small* **2011**, *7*, 351.
[6] L. I. Kazakova, L. I. Shabarchina, G. B. Sukhorukov, *PhysChemChemPhys* **2011**, *13*, 11110.
[7] M. Wang, V. Janout, S. L. Regen, *Chem. Commun.* **2013**, *49*, 3576.

[8] K. Scott, S. Pilditch, M. Mamlouk, *J. Appl. Electrochem.* **2007**, *37*, 1245.
[9] L. L. del Mercato, G. Maruccio, P. P. Pompa, B. Bochicchio, A. M. Tamburro, R. Cingolani, R. Rinaldi, *Biomacromolecules* **2008**, *9*, 796–803.
[10] A. S. Angelatos, A. P. Johnston, Y. Wang, F. Caruso, *Langmuir* **2007**, *23*, 4554.
[11] W. Yuan, Z. Lu, C. M. Li, *J. Mater. Chem.* **2011**, *21*, 5148.
[12] C. Dejugnat, K. Kohler, M. Dubois, G. B. Sukhorukov, H. Mohwald, T. Zemb, P. Guttmann, *Adv. Mater.* **2007**, *19*, 1331.
[13] W.-F. Dong, S. Liu, L. Wan, G. Mao, D. G. Kurth, H. Möhwald, *Chem. Mater.* **2005**, *17*, 4992.
[14] K. Köhler, H. Möhwald, G. B. Sukhorukov, *J. Phys. Chem. B* **2006**, *110*, 24002.
[15] M. Prevot, C. Déjugnat, H. Möhwald, G. B. Sukhorukov, *ChemPhysChem* **2006**, *7*, 2497.
[16] P. M. Biesheuvel, T. Mauser, G. B. Sukhorukov, H. Möhwald, *Macromolecules* **2006**, *39*, 8480.
[17] T. Mauser, C. Déjugnat, G. B. Sukhorukov, *J. Phys. Chem. B* **2006**, *110*, 20246.
[18] D. Halozan, C. Déjugnat, M. Brumen, G. B. Sukhorukov, *J. Chem. Info. Modeling* **2005**, *45*, 1589.
[19] Y. Ma, W.-F. Dong, M. A. Hempenius, H. Möhwald, G. J. Vancso, *Nat. Mater.* **2006**, *5*, 724.
[20] A. A. Antipov, G. B. Sukhorukov, *Adv. Colloid Interface Sci.* **2004**, *111*, 49.
[21] K. Köhler, P. M. Biesheuvel, R. Weinkamer, H. Möhwald, G. B. Sukhorukov, *Phys. Rev. Lett.* **2006**, *97*, 188301/1.
[22] L. Krasemann, B. Tieke, *Langmuir* **2000**, *16*, 287.
[23] O. Kreft, A. Muñoz Javier, G. B. Sukhorukov, W. J. Parak, *J. Mater. Chem.* **2007**, *17*, 4471.
[24] M. Semmling, O. Kreft, A. Muñoz Javier, G. B. Sukhorukov, J. Käs, W. J. Parak, *Small* **2008**, *4*, 1763.
[25] P. Rivera Gil, M. Nazarenus, S. Ashraf, W. J. Parak, *Small* **2012**, *8*, 943.
[26] S. Carregal-Romero, M. Ochs, P. Rivera Gil, C. Ganas, A. M. Pavlov, G. B. Sukhorukov, W. J. Parak, *J. Controlled Release* **2012**, *159*, 120.
[27] L. L. del Mercato, A. Z. Abbasi, M. Ochs, W. J. Parak, *ACS Nano* **2011**, *5*, 9668.
[28] G. B. Sukhorukov, M. Brumen, E. Donath, H. Möhwald, *J. Phys. Chem. B* **1999**, *103*, 6434.
[29] D. Halozan, G. B. Sukhorukov, M. Brumen, E. Donath, H. Möhwald, *Acta Chimica Slovenica* **2007**, *54*, 598.
[30] D. Halozan, U. Riebentanz, M. Brumen, E. Donath, *Colloids Surf., A* **2009**, *342*, 115.
[31] H. Ohshima, *J. Colloid Interface Sci.* **2008**, *323*, 92.
[32] R. A. Ghostine, J. B. Schlenoff, *Langmuir* **2011**, *27*, 8241.
[33] B. Roling, C. Martiny, S. Bruckner, *Phys. Rev. B* **2001**, *63*, 214203/1.
[34] K. Funke, R. D. Banhatti, *Solid State Ionics* **2006**, *177*, 1551.
[35] J. C. Dyre, P. Maass, B. Roling, D. L. Sidebottom, *Rep. Prog. Phys.* **2009**, *72*, 046501/1.
[36] H. Mehrer, *Z. Phys. Chem.* **2009**, *223*, 1143.
[37] S. Arumugam, J. Shi, D. P. Tunstall, C. A. Vincent, *J. Phys.: Condens. Matter* **1993**, *5*, 153.
[38] A. R. Waldeck, A. J. Lennon, B. E. Chapman, P. W. Kuchel, *J. Chem. Soc., Faraday Trans.* **1993**, *89*, 2807.
[39] J. Kösters, M. Schönhoff, N. A. Stolwijk, *J. Phys. Chem. B* **2013**, *117*, 2527.
[40] M. Schäfer, K.-M. Weitzel, *PhysChemChemPhys* **2011**, *13*, 20112.
[41] P. V. Menezes, J. Martin, M. Schäfer, H. Staesche, B. Roling, K.-M. Weitzel, *PhysChemChemPhys* **2011**, *13*, 20123.
[42] S. Schulze, M. Schäfer, A. Greiner, K.-M. Weitzel, *PhysChemChemPhys* **2013**, *15*, 1481.
[43] B. Zebli, A. S. Susha, G. B. Sukhorukov, A. L. Rogach, W. J. Parak, *Langmuir* **2005**, *21*, 4262.
[44] T. Hyeon, S. S. Lee, J. Park, Y. Chung, H. Bin Na, *J. Am. Chem. Soc.* **2001**, *123*, 12798.
[45] A. Z. Abbasi, L. Gutierrez, L. L. del Mercato, F. Herranz, O. Chubykalo-Fesenko, S. Veintemillas-Verdaguer, W. J. Parak, M. P. Morales, J. M. Gonzalez, A. Hernando, P. de la Presa, *J. Phys. Chem. C* **2011**, *115*, 6257.
[46] K. J. Buckler, R. D. Vaughan-Jones, *Pflügers Arch. Euro. J. Physiol.* **1990**, *417*, 234.
[47] P. del Pino, A. Munoz-Javier, D. Vlaskou, P. Rivera Gil, C. Plank, W. J. Parak, *Nano Lett.* **2010**, *10*, 3914.
[48] Y.-C. Chen, A. Ostafin, H. Mizukami, *Nanotechnology* **2010**, *21*, 215503/1.
[49] D. Morgan, M. Capasso, B. Musset, V. V. Cherny, E. Rios, M. J. S. Dyer, T. E. DeCoursey, *Proc. Natl. Acad. Sci. USA* **2009**, *106*, 18022.
[50] F.-M. Boldt, J. Heinze, M. Diez, J. Petersen, M. Börsch, *Anal. Chem.* **2004**, *76*, 3473.
[51] E. Kätelhön, K. J. Krause, P. S. Singh, S. G. Lemay, B. Wolfrum, *J. Am. Chem. Soc.* **2013**, *135*, 8874.
[52] D. Hühn, A. Govorov, P. Rivera Gil, W. J. Parak, *Adv. Funct. Mater.* **2012**, *22*, 294.
[53] M. M. Sung, K. Sung, C. G. Kim, S. S. Lee, Y. Kim, *J. Phys. Chem. B* **2000**, *104*, 2273.
[54] M. F. Durstock, M. F. Rubner, *Langmuir* **2001**, *17*, 7865.
[55] Y. Akgöl, C. Hofmann, Y. Karatas, C. Cramer, H.-D. Wiemhöfer, M. Schönhoff, *J. Phys. Chem. B* **2007**, *111*, 8532.
[56] S. De, C. Cramer, M. Schönhoff, *Macromolecules* **2011**, *44*, 8936.
[57] C. Cramer, S. De, M. Schönhoff, *Phys. Rev. Lett.* **2011**, *107*, 028301/1.

Supporting Information

for *Macromol. Rapid Commun.*, DOI: 10.1002/marc. 201300571

Ion Transport Through Polyelectrolyte Multilayers

Susana Carregal-Romero, Philipp Rinklin, Susanne Schulze, Martin Schäfer, Andrea Ott, Dominik Hühn, Xiang Yu, Bernhard Wolfrum,* Karl-Michael Weitzel,* Wolfgang. J. Parak*

Susana Carregal-Romero[1,2], Philipp Rinklin[3], Susanne Schulze[4], Martin Schäfer[4], Andrea Ott[1], Dominik Hühn[1], Xiang Yu[1], Bernhard Wolfrum[3*], Karl Michael Weitzel[4*], Wolfgang J. Parak[1,5*]

[1] Fachbereich Physik, Philipps Universität Marburg, Marburg, Germany
[2] BIONAND, Centro Andaluz de Nanomedicina y Biotecnología, Málaga, Spain
[3] Forschungszentrum Jülich, Jülich, Germany
[4] Fachbereich Chemie, Philipps Universität Marburg, Marburg, Germany
[5] CIC Biomagune, San Sebastian, Spain
[*] corresponding authors: b.wolfrum@fz-juelich.de, weitzel@chemie.uni-marburg.de, wolfgang.parak@physik.uni-marburg.de

Ion transport through polyelectrolyte layers

SUPPORTING INFORMATION

I) Synthesis of spherical polyelectrolyte multilayers
II) Synthesis of planar polyelectrolyte multilayers
III) Estimation of the diffusion time of ions into spherical polyelectrolyte multilayers
IV) Estimation of the ion conductivity of planar polyelectrolyte multilayers
V) References

I) Synthesis of spherical polyelectrolyte multilayers

Polyelectrolyte multilayer (PEM) capsules have been synthesized using the layer-by-layer (lbl) self-assembly technique on calcium carbonate microspheres acting as templates. The $CaCO_3$ cores (20 mg) were prepared by mixing solutions of 0.33 M calcium chloride ($CaCl_2$, Sigma #223506) and 0.33 M sodium carbonate (Na_2CO_3, Sigma #S7795) under magnetic stirring.[1] The mean diameter of the microspheres was 2.6 ± 0.3 μm. The $CaCO_3$ cores were slightly positively charged (zeta potential around + 3 mV). Thus, the first layer of polyelectrolyte used for coating was negatively charged poly(sodium 4-styrenesulfonate) (PSS, $M_w \approx$ 70 kDa, Sigma #243051). The first layer was followed by a second layer made out of the positive polyelectrolyte poly(allylamine hydrochloride) (PAH, $M_w \approx$ 56 kDa, Sigma #283223). By repeating this sequence, two more bilayers of polyelectrolytes were added. Subsequently, maghemite nanoparticles (γ-Fe_2O_3 NPs) were adsorbed to the polyelectrolyte coated $CaCO_3$ cores. The magnetic NPs with a mean core diameter of 31.3 ± 6.3 nm had been synthesized following the procedure reported by Hyeon *et al.*{Hyeon, 2001 #7474} and had been consecutively coated with an amphiphilic polymer (poly(isobutylene-*alt*-maleic anhydride)) to render them hydrophilic and negatively charged.[2-4] Figure SI.I.1 shows the absorption spectra of the maghemite NPs dissolved in water after polymer coating.

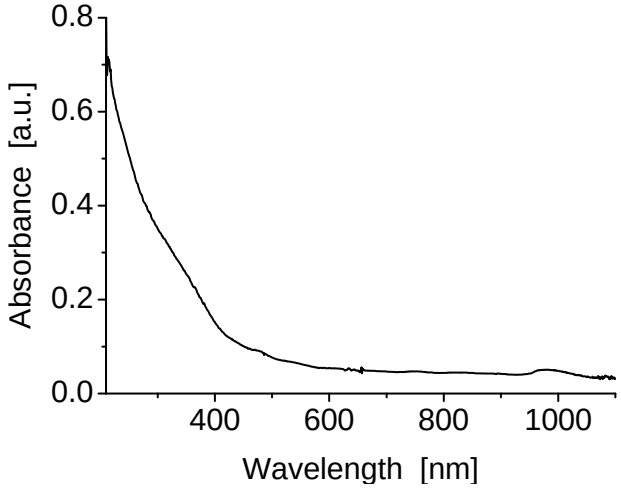

Figure SI.I.1. *UV/vis absorption of γ-Fe_2O_3 nanoparticles dissolved in milli-Q water.*

For adsorption of the magnetic NPs the $CaCO_3$@$(PSS/PAH)_2$ particles and the NPs (0.2 μM, 0.1 mL) were mixed in 1 mL of milli-Q water overnight under mechanical shaking. The sample was then washed twice and two more polyelectrolyte bilayers were added. Upon dissolution of the $CaCO_3$ cores with ethylenediaminetetraacetic acid disodium salt dihydrate (EDTA disodium salt, Sigma #E5134) the final capsule architecture was $(PSS/PAH)_2$ γ-Fe_2O_3 $(PSS/PAH)_2$. In order to make the pH-sensitive capsules, the cavities of the capsules were loaded with SNARF-dextran ($M_w \approx$ 10 kDa, Invitrogen #D-3303) with a postloading procedure as recently published.[1]

II) Synthesis of planar polyelectrolyte multilayers

On previously cleaned copper plates (*cf.* Figure SI.II.1) a self-assembled monolayer of 3-mercaptopropionic acid was deposited following methods from literature.[5] The outer carboxylic groups are believed to ensure a negative surface charge at neutral pH. Afterwards, the plates were dipped into an aqueous solution of the positively charged polyelectrolyte PAH (0.1872 g PAH in 100 mL of 0.5 M sodium chloride, pH = 6.5) (NaCl, Carl Roth #HN00) for 30 minutes to obtain a positively charged surface. After rinsing with water for removal of excess PAH the samples were dipped into a solution of the negatively charged polyelectrolyte PSS (0.4124 g PSS in 100 mL of 0.5 M NaCl, pH = 6.5) for 30 minutes. After an additional washing step for the removal of excess PSS, the sample architecture was (PAH/PSS). After the deposition of the first bilayer of polyelectrolytes the incubation time was reduced to 10 minutes. The first bilayer was assembled within 30 min per layer and without Au NPs to ensure high stability in the bottom region of the lbl matrix. Two types of planar PEM films were prepared: One without Au NPs and another one with Au NPs. The PEM film without Au NPs had a final architecture comprising 32 layers of polyelectrolytes, $(PAH/PSS)_{16}$. The PEM film containing Au NPs was produced with commercial 10 nm Au NPs (BBI, #EMGC10). Au NPs could be assembled in-between the PEMs as another building block because they are negatively charged. The final architecture of the PEM film loaded with Au NPs was $(PAH/PSS)(PAH/Au\ NPs/PSS)_{15}$. Both PEM films were dried under a nitrogen stream. The thickness of each polyelectrolyte layer of PAH or PSS was reported to be between 0.5 to 2 nm.[6-8] Thus, it can be assumed that the maximum thickness of the samples modified without Au NPs was approximately 200 nm.

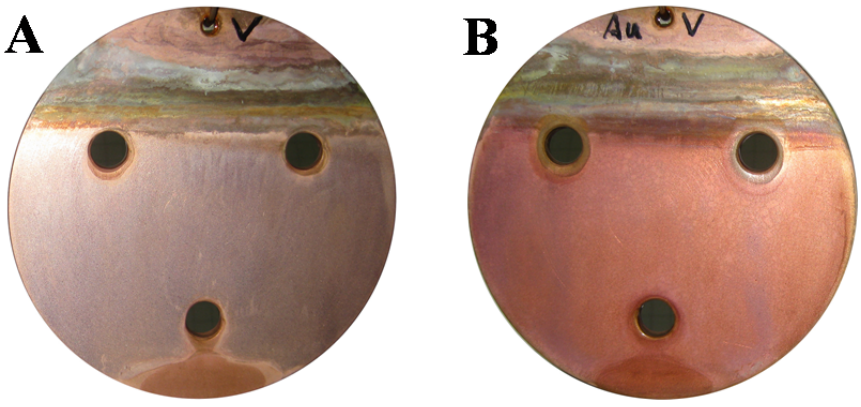

Figure SI.II.1. *Image of the copper plates where different PEM layers were assembled: (A)* $(PAH/PSS)_{16}$ *and (B)* $(PAH/PSS)(PAH/Au\ NPs/PSS)_{15}$.

III) Estimation of the diffusion time of ions into spherical polyelectrolyte multilayers

The pH response the aforementioned magnetic PEM capsules loaded with SNARF-dextran was characterized with fluorescence spectroscopy. Figure SI.III.1 shows the higher fluorescent emission at 583 nm for pH 6 compared with the low emission intensity at pH 9. The ratio between the fluorescent emissions at 627 nm (I_r) and at 583 nm (I_y) shows the pH response of the magnetic capsules.

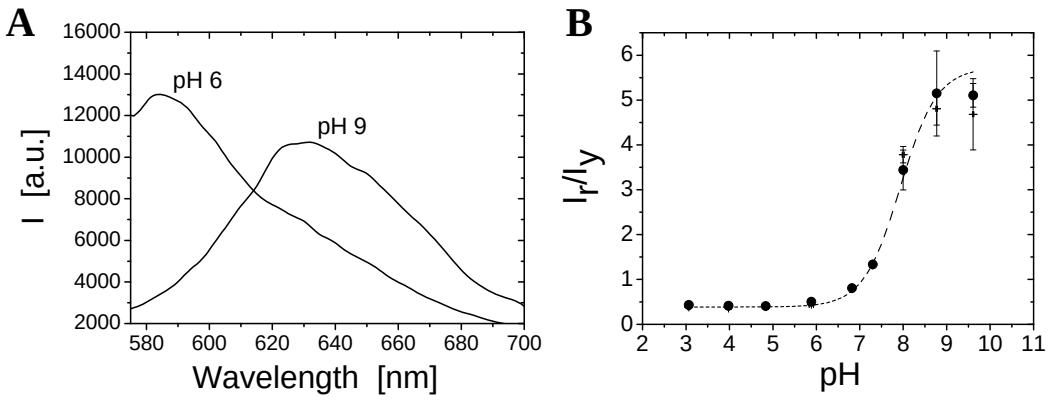

Figure SI.III.1. *Changes of fluorescence emission intensity of* $(PSS/PAH)_2$ γ-Fe_2O_3 $(PSS/PAH)_2$ *capsules loaded with SNARF-dextran. (A) Fluorescent spectra of the magnetic capsules at pH 6 and pH 9. (B) pH influence on the ratio* I_r/Iy *measured at 627 nm (*I_r*) and at 583 nm (*I_y*).*

PEM capsules were exposed to a time-dependent pH concentration profile, while measuring the fluorescence response in real-time. A microfluidic channel coupled to a fluorescence microscope, where the capsules were magnetically trapped, was used for this purpose. The magnetic PEM capsules that were trapped in the channel kept their spherical shape and did not fold in the presence of the magnetic field, *cf.* Figure SI.III.2.

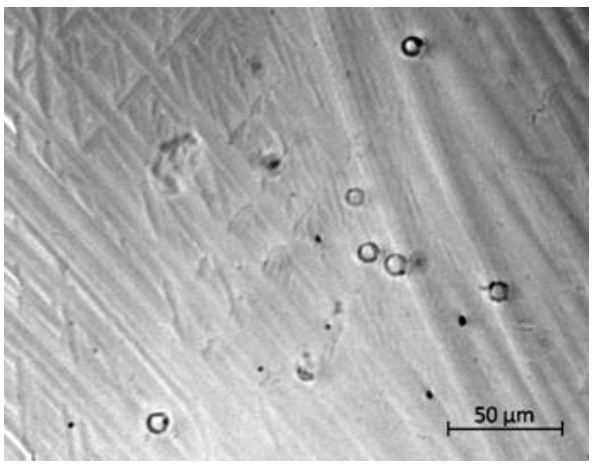

Figure SI.III.2. *Image of PEM capsules magnetically trapped in a microfluidic channel.*

In order to study the influence of the magnetic field on the distribution of magnetic NPs within the polyelectrolyte shell we exposed the PEM capsules to the magnetic field of a magnet for ten minutes (*cf.* Figure SI.III.3) and then we performed TEM images of the capsules. We did not observe an evident uneven distribution of the magnetic NPs after magnetic field exposure.

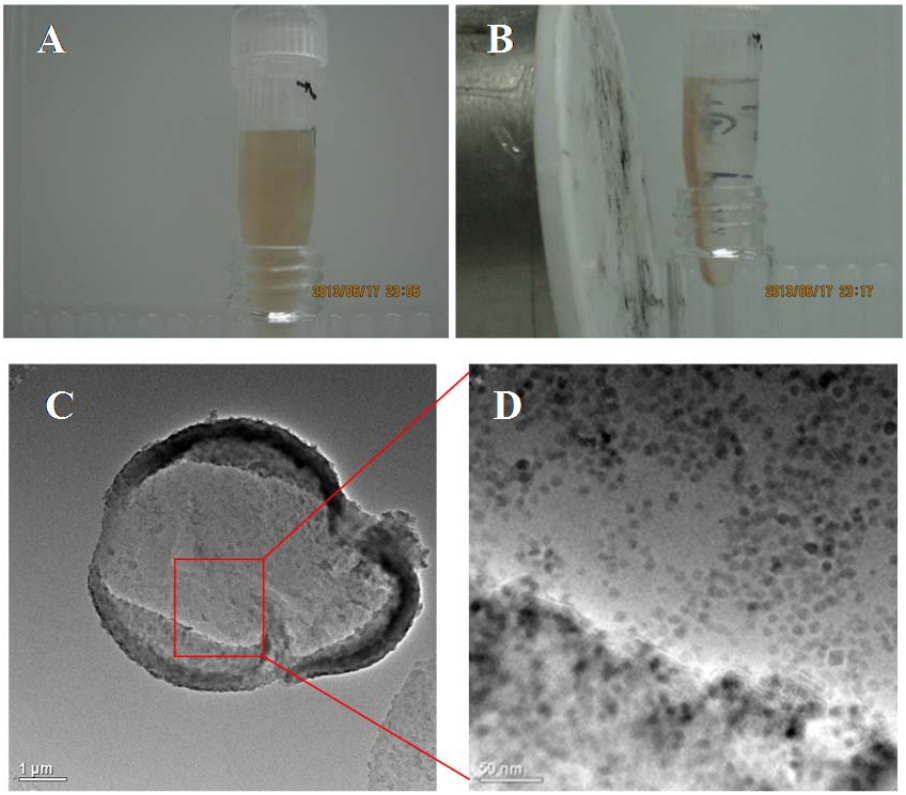

Figure SI.III.3. *Image of magnetic PEM capsules in aqueos solution in the absence (A) and presence of a magnetic field (B). Close to the magnet the capsules accumulated on the wall of the tube due to the presence of the magnetic field which had been applied for (B) 10 minutes. TEM images (C, D) of one of the capsules exposed to the magnetic field of the magnet for 10 minutes. (D) Detailed zoom in of the TEM image depicted in (C) showing the distribution of magnetic NPs within the capsule. Scale bars correspond to 1 µm and 50 nm, respectively.*

Two commercial buffers were used to shift the pH from 6 to 9 and *vice versa*: 10 mM of 2-(*N*-morpholino)ethanesulfonic acid (MES, Sigma #M3671) adjusted to pH 6 and 1 mM of tris(hydroxymethyl)aminomethane (TRIS, Carl Roth,#4855) adjusted to pH 9. The change in fluorescence of the capsules induced by the gradient's switching was recorded with an emCCD camera (C9100-13, Hamamatsu Photonics, Japan) mounted to an inverted fluorescence microscope (Axiovert 200 M, Carl Zeiss; Filters: ex 470/20BP, BS 510, em 575/50BP). The interframe time for the recording was set to 26.6 ms. For each measurement two pulses of pH 6 and pH 9 (duration: 10 s each) were applied and

the intensity traces of individual capsules were extracted from the recorded image sequence as shown in Figure SI.III.4.

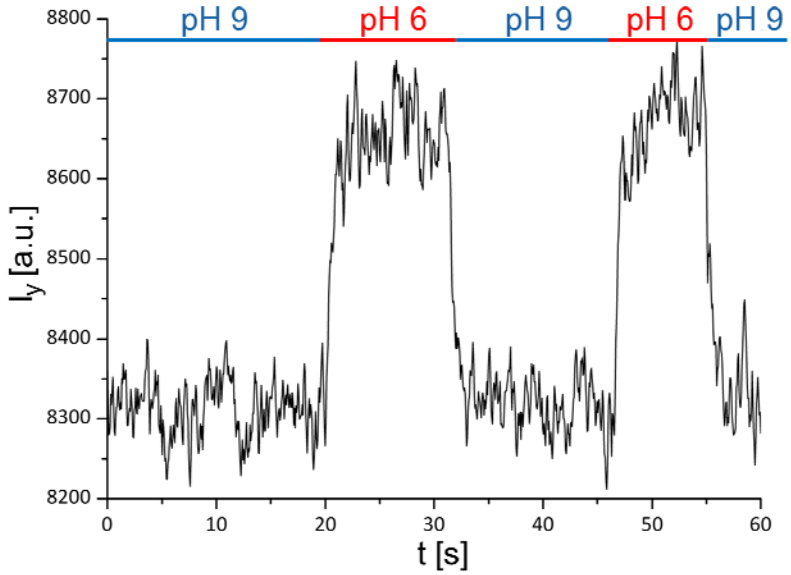

Figure SI.III.4. *Changes of fluorescence emission intensity of individual capsules loaded with SNARF in a microfluidic chamber upon pH change from 9 to 6. The selected filter set (excitation 440-490 nm, beam splitter 510 nm and emission 525-625 nm) records the emission $I_y(t)$ of the acidic form (pH 6) of SNARF. The vertical line indicates the time at which pH was switched from pH = 6 to pH = 9.*

To correlate the capsules' switching behavior with that of the gradient, control measurements were performed using the above mentioned solutions and pressure protocols with tetramethylrhodamine isothiocyanate (TRITC) added to the pH 6 buffer.

IV) Estimation of the ion conductivity of planar polyelectrolyte multilayers

The ionic conductivity of the planar PEMs (PAH/PSS)(PAH/Au NPs/PSS)$_{15}$ and (PAH/PSS)$_{16}$ was investigated by means of the bombardment induced ion transport (BIIT) technique.[9, 10] Here, the PEM layers were prepared as described above directly on a copper plate, which at the same time served as the backside electrode required in BIIT. The layers were bombarded by a continuous potassium ion beam with energies ranging between thermal conditions and about 10 eV. The current of the primary potassium ion beam was typically 5 nA. In the experiment, the backside current was measured as a function of the ion beam potential which in turn determines the surface potential. Further details of the BIIT technique have been described elsewhere.[11]

V) References

[1] S. Carregal-Romero, M. Ochs, P. Rivera_Gil, C. Gana, A. M. Pavlov, G. B. Sukhorukov, W. J. Parak, *J. Controlled Release* **2012**, *159*, 120.
[2] C.-A. J. Lin, R. A. Sperling, J. K. Li, T.-Y. Yang, P.-Y. Li, M. Zanella, W. H. Chang, W. J. Parak, *Small* **2008**, *4*, 334.
[3] M. T. Fernández-Argüelles, A. Yakovlev, R. A. Sperling, C. Luccardini, S. Gaillard, A. S. Medel, J.-M. Mallet, J.-C. Brochon, A. Feltz, M. Oheim, W. J. Parak, *Nano Lett.* **2007**, *7*, 2613.
[4] T. Pellegrino, L. Manna, S. Kudera, T. Liedl, D. Koktysh, A. L. Rogach, S. Keller, J. Rädler, G. Natile, W. J. Parak, *Nano Lett.* **2004**, *4*, 703.
[5] M. M. Sung, K. Sung, C. G. Kim, S. S. Lee, Y. Kim, *J. Phys. Chem. B* **2000**, *104*, 2273.
[6] G. Schneider, G. Decher, N. Nerambourg, R. Praho, M. H. Werts, M. Blanchard-Desce, *Nano Lett* **2006**, *6*, 530.
[7] G. Schneider, G. Decher, *Langmuir* **2008**, *24*, 1778.
[8] Z. Poon, J. B. Lee, S. W. Morton, P. T. Hammond, *Nano Lett.* **2011**, *11*, 2096.
[9] M. Schaefer, K. M. Weitzel, *PCCP* **2011**, *13*, 20112.
[10] P. V. Menezes, J. Martin, M. Schaefer, H. Staesche, B. Roling, K. M. Weitzel, *PCCP* **2011**, *13*, 20123.
[11] K. Schroeck, S. Schulze, A. Schlemmer, K.-M. Weitzel, *J. Phys. D: Appl. Phys.* **2010**, *43*, 025501/1.

Magnetically triggered release of molecular cargo from iron oxide nanoparticle loaded microcapsules

Susana Carregal-Romero[1#], Pablo Guardia[2#], Xiang Yu, Raimo Hartmann, Teresa Pellegrino[2*], Wolfgang J. Parak[2,3*]

[1] *Fachbereich Physik, Philipps Universität Marburg, Marburg, Germany*

[2] *Italian Institute of Technology, Genova, Italy*

[3] *CIC Biomagune, San Sebastian, Spain*

[#] *both authors contributed equally to this work*

[*] *corresponding authors: teresa.pellegrino@iit.it, wolfgang.parak@physik.uni-marburg.de*

Abstract

Photothermal release of cargo molecules has been extensively studied and microcapsules decorated with plasmonic nanoparticles have been widely used for this purpose in *in vitro* assays. However, some concerns about their suitability for some *in vivo* application cannot be easily overcome, in particular the problem of limited penetration depth of (even infrared) light. Magnetic nanoparticles are an alternative source for local heating, which can be triggered by applying alternating magnetic fields. Alternating magnetic fields are much less absorbed by tissue than light and thus can penetrated deeper. Here we present iron oxide nanocube modified microcapsules as platform for magnetically triggered molecular release. Layer-by-layer assembled polyelectrolyte microcapsules with 4.6 μm diameter, which had 18 nm diameter iron oxide nanocubes integrated in their walls, were loaded with an organic fluorescent polymer (Cascade Blue-labelled dextran), which was used as model of a molecular cargo. Through an alternating magnetic field the magnetic nanoparticles were able to heat their surroundings, thus destroying the microcapsule walls, leading to a final release of the embedded cargo to the surrounding solution. The cargo release was monitored in solution by measuring the increase in absorbance and fluorescence further to the exposure to AMF. Our results demonstrate that magnetothermal release of encapsulated material is possible.

Introduction

For the *in vitro* and *in vivo* delivery of functional molecular cargo (such as drugs or enzymes) it is often beneficial to encapsulate the cargo. Encapsulation can protect the cargo from enzymatic degradation {Rivera_Gil, 2009 #13984}, alter the intracellular distribution of the cargo within cells or the biodistribution within animals {De Koker, 2007 #12389; Shen, 2013 #24943}, as it can be also used for controlled release of the cargo {Johnston, 2010 #16071; Ochs, 2013 #23479}. Polyelectrolyte capsules as fabricated with layer-by-layer (LbL) assembly are one approach for encapsulation cargo {Sukhorukov, 2005 #9685}. This approach has been in particular optimized for cellular *in vitro* assays, in particular regarding the large micrometer size and the choice of material of the capsules. However, also *in vivo* applications, in particular concerning vaccination, have been reported {Sexton, 2009 #16073; De Koker, 2010 #15190}. So far, controlled release from such microcapsules has been obtained using a large variety of different stimuli, including pH {Sukhorukov, 2001 #12041}, redox potential {Liang, 2012 #24945}, enzymatic degradation {Rivera_Gil, 2009 #13984}, ultrasound {Pavlov, 2011 #19139}, microwaves {del Mercato, 2011 #19041}, and local photothermal local heating {Radt, 2004 #10070; Angelatos, 2005 #10223; Skirtach, 2006 #10665; Muñoz Javier, 2008 #12916; Carregal-Romero, 2012 #20105}. For externally triggered release in particular photothermal heating is of great interest, as it can be remotely controlled.

Photothermal heating, *i.e.* the local generation of heat upon optical resonant excitation of plasmonic nanoparticles (NPs) {Baffou, 2013 #24694} has nowadays reached a high level of maturity and is used in a variety of biologically motivated applications. Photothermal therapy preferentially induces apoptosis in cells by local heating (hyperthermia) {Huang, 2006 #13478; Hirsch, 2003 #9911; O'Neal, 2004 #9912}. This is a delicate process, as production of too much heat will lead to formation bubbles of evaporated water {Hühn, 2012 #20252}, which destroys cells by mechanical effects {Muñoz Javier, 2008 #12916} instead of controlled apoptosis. In addition, also other intracellular effects triggered by light activation of plasmonic NPs have been suggested, which are not based on creation of heat {Krpetic, 2010 #17324}. Photothermal heating also has been used for light-triggered destruction of carrier matrixes in which plasmonic NPs are embedded, which can be used for release of encapsulated molecular materials. Besides polymer capsules, carrier matrixes involve for example also liposomes. This technique has reached a degree of control that it even allows for opening of individual capsules *in vitro* {Carregal-Romero, 2012 #20105} and thus the subsequent release of different molecular cargo inside cells {Ochs, 2013 #23479}. However, concerning potential *in vivo* applications, photothermal heating of plasmonic

NPs by optical excitation shows a drawback due to the strong absorption of light by tissues, though absorption is reduced in the so-called biological window in the near infrared {Weissleder, 2001 #11748; Vogel, 2003 #12127}.

Besides optical heating of plasmonic NPs in literature also the heating of magnetic NPs with radiofrequencies (RF) has been reported {Pankhurst, 2003 #14246; Huang, 2010 #23501; Colombo, 2012 #20270}. Technically magnetothermal excitation is done *via* alternating magnetic fields (AMF). There is a striking analogy of heating plasmonic and magnetic NPs with light and RF radiation, respectively. Similar to plasmonic NPs the capability of magnetic NPs to act as heat mediators {Rosensweig, 2002 #25043; Hiergeist, 1999 #9883} has been exploited for magnetic mediated hyperthermia treatment {Hergt, 2006 #25049; Pankhurst, 2009 #25042; Fortin, 2007 #18645; Ling, 2013 #183} or for controlled drug delivery associated to the nanoparticles *via* thermo-sensitive linkers {Riedinger, 2013 #25053; N'Guyen, 2013 #25054}. Magnetic NPs however, have been so far less exploited to trigger release from carrier matrixes such as polyelectrolyte capsules. Probably the low heat performance shown by magnetic NPs as synthesized by conventional methods has set aside this promising approach {Hergt, 2007 #25052}. Recent advances on the synthesis of novel magnetic NPs {Lee, 2011 #18650} have pointed out than iron oxide nanocubes are very efficient heat-mediators for magnetic induced hyperthermia {Guardia, 2012 #25045}. Whereas such iron oxide nanocubes are preferentially prepared in organic solvents, they can be transferred to polar solvents as has been recently reported {Guardia, submitted #25050}, which also allows for their integration into polyelectrolyte capsules. Owing the heating capability of these magnetic NPs, they could be used to trigger release of molecular cargo from polyelectrolyte capsules or other carrier matrixes. Indeed, this concept has been demonstrated recently by Katagiri*et al.* for liposomes and hybrid capsules containing a fluorescent probe within the lipidic layer of the capsule shell {Katagiri, 2011 #25041; Katagiri, 2010 #15578}.

Here we present a proof of concept study of this technology where a model molecule (Cascade Blue-labelled dextran) was encapsulated and released from the inner cavity of polyelectrolyte microcapsules, which had magnetic NPs in their walls, as triggered by an AMF.

Materials and Methods

Magnetic nanoparticles synthesis:Synthesis of water-soluble iron oxide nanocubes with core size of 18 ± 2 nm were synthesized according to a previously published protocol {Guardia, submitted #25050}.Iron (III) acetylacetonate (99%), decanoic acid (99%) and dibenzyl ether (99%) were purchased from Acros. Squalane (98%) was purchased from Alfa Aesar. Milli-Q water (18.2 MΩ, filtered with filter pore size 0.22 μM) was from Millipore. All solvents used were of analytical grade and were purchased from Sigma-Aldrich. All chemicals were used as received. In brief, in a 50 mL three neck round bottom flasks equipped with a water cooled Allhin-condensers connected to a standard Schlenk line 0.353 g (1 mmol) of iron (III) acetylacetonate and 0.78 g (4.5 mmols) of decanoic acid were dissolved in 18 mL of dibenzyl ether (DBE) and 7 mL of squalane. After degassing for 120 minutes at 65 °C, the mixture was heated up to 200 °C (3 °C/min) and kept at this value for 2.5 h. Finally the temperature was increased at a heating rate of 7 °C/min up to 310 °C and maintained at this value for 1 h. After cooling down to room temperature, 60 mL of acetone were added and the solution was centrifuged at 8500 rpm. The collected black NP precipitate was dispersed in 2-3 mL of chloroform and the washing procedure was repeated for at least two more times. Finally the collected particles were dispersed in 15 mL of chloroform. For the water transfer, 15 mL of gallol-modified polyethylene glycol, GA-PEG {Riedinger, 2013 #25051} solution (0.1 M in chloroform containing 1 mL triethylamine) were added to a solution of the NPs in chloroform and stirred over night at room temperature. Then, 10 mL of de-ionized water were added resulting in the formation of two phases. After emulsification by means of shaking, the phases were allowed to separate and the aqueous phase containing the GA-PEG coated magnetic NPs was collected. This step was repeated until all NPs were transferred to water. The excess of GA-PEG was removed by dialysis over night at room temperature in de-ionized water bath using a cellulose membrane tubing (Molecular Weigth Cut Off, MWCO of 50 kDa). This step was repeated 5 times. Finally, the aqueous solution containing the NPs was concentrated by centrifugation by using a centrifuge filter (MWCO of 100 kDa) to a iron concentration of about 15-16 g/L (as determined by Induced Coupled Plasma -Atomic Emission Spectroscopy, ICP-AES, Thermo Fisher).

Synthesis of capsules:Template microparticles of $CaCO_3$ were obtained by mixing aqueous solutions of $CaCl_2$ (5 mL, 0.33 M) and Na_2CO_3(5 mL, 0.33 M) under magnetic stirring at room temperatur {Carregal-Romero, 2012 #20105}. Polyelectrolyte shells were assembled around the $CaCO_3$ template cores (~ 4 μm diameter, 10 mL, 165 mg) by LbL coating of alternating layers of poly(allylamine hydrochloride) (PAH, M_w ≈ 56 kDa) as positive polyelectrolyte, and poly(styrene sulfonate) (PSS, M_w ≈ 70 kDa) as negative polyelectrolyte. However, as 4th layer instead of PAH the strong positively charged polymer poly(acrylamide-co-diallyl-dimethylammonium chloride) (P(Am-DDA)) was assembly to the LbL shell.

P(Am-DDA) instead of PHA helped to increase the attachment attachment of magnetic NPs. For this 1 mL containing NP solution ([Fe] = 15.65 g/L) added to the capsule solution. Hereby the magnetic NPs were attached to the capsule shell on the positive layer of P(Am-DDA) *via* their negative charge (zeta potential of the magnetic NPs ζ = -24.2 ± 8 mV) , as it was previously reported {Abbasi, 2011 #17341}. The final architecture of the LbL shell was (PSS/PAH)(PSS/P(Am-DDA) NPs (PAH)$(PSS/PAH)_2$. After dissolution of the $CaCO_3$ core with ethylenediamine-tetraacetic acid disodium salt (0.2 M, pH 7) the capsules were filled with Cascade Blue-labelled dextran (10 kDa) *via* post-loading {Carregal-Romero, 2012 #20105} and further temperature shrinking of the LbL shell {Carregal-Romero, 2012 #20105}. The final concentration was $3.3 \cdot 10^8$ capsules/mL (in 5 mL). The capsules were characterized with optical microscopy, transmission electron microscopy (TEM), and dynamic light scattering (DLS) (*cf.* Figure 1). The capsule diameter was obtained by analysing optical microscopy images with the software UTHSCSA Image Tool (version 3.0).

Cargo release *via*magnetothermal heating: For the magnetothermal heating experiments a commercially available set-up was used (DM100 Series, nanoScaleBiomagnetics Corp.). Experiments were performed on a capsule solution with an iron content of 4.8 g/L. For a more detailed explanation about the used iron concentration we refer to the Supporting Information. Before heating experiments the capsule solution was purified from Cascade Blue-labelled dextran, which has leaked out the capsules. For this purpose 350 µL of capsule solution were placed on top of a magnet (0.2 T) for 20 minutes and the capsules were collected (due to the magnetic NPs in their walls) at the bottom, while the supernatant was discarded. Then 350 µL of fresh Milli-Q water was added to the precipitate, followed by careful shaking, in order to redisperse the capsules in solution. In order to quantify the possible presence of free Cascade Blue-labelled dextran, after adding fresh MQ-water, the solution was again placed on top of a magnet for 20 minutes, capsules were collected, and the absorption spectrum of the supernatant was recorded, which did not show significant leaching of Cascade Blue-labelled dextran. The sample was then split in two aliquots: 250 µL of test-sample to be treated and 100 µL control sample. The test-sample was placed under an AMF (300 kHz, 24 kAm^{-1}) for 90 minutes and the temperature of the solution under heating was monitored (*cf.* Figure 2). The control sample was kept at room temperature for 90 minutes. Both samples were then placed again on a magnet for 20 minutes to collect the capsules. The supernatants were then collected and filtered by using Microcentrifuge Spin Cups and Columns (MWCO cut-off 100 kDa), in order to remove capsule fragments from the supernatant which may not have precipitated. Absorption and fluorescence emission spectra of the supernatants were recorded using

quartz cuvettes (*cf.* Figure 3). In addition TEM images of the precipitate containing the capsules were recorded, *cf.* the Supporting Information.

Results and Discussion

Casules of 4.6 ± 0.4 µm diameter with a zeta potential of ζ = 12.05 ± 0.5 mV were successfully synthesized using aLbL approach (Figure 1A). Due to the presence of iron oxide nanocubes (18 ± 2 nm NP size) the capsules could be attracted by a magnet (after less than 5 minutes most of the sample was collected when placed under a magnet of 0.2 T). Despite the incorporation of the magnetic NPs at high concentration the geometry of the capsules was rather spherical. Presence of the magnetic NPs could be observed in optical microscopy and TEM images (*cf.* Figure 1). The loading of the capsules with Cascade Blue-labelled dextran could be confirmed by optical microscopy (*cf.* Figure 1).

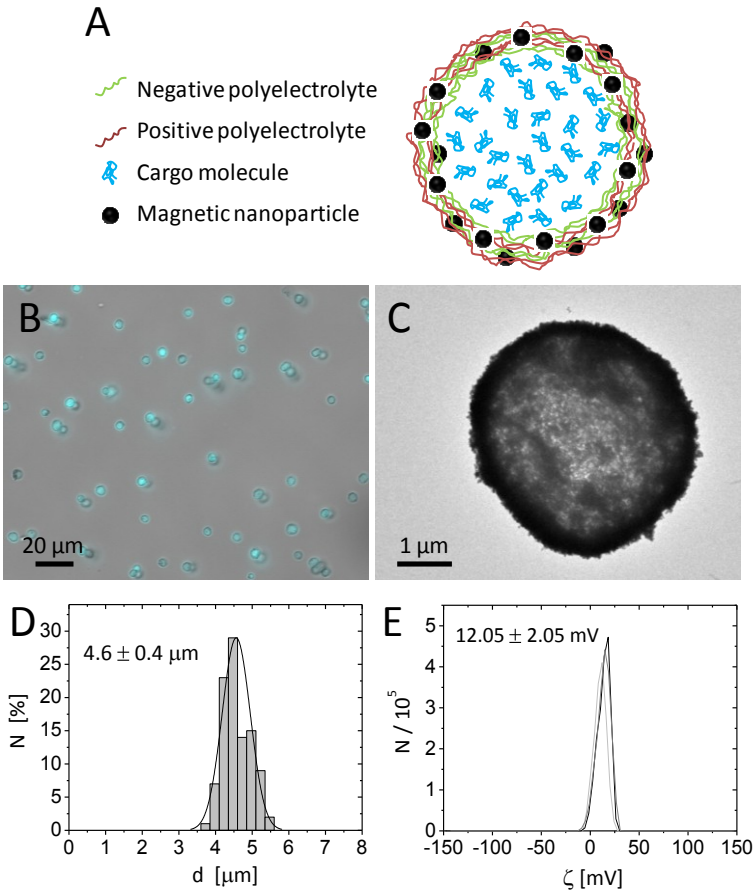

Figure 1: A) Sketch of one polyelectrolyte capsule comprising Cascade Blue-labelled dextran as fluorescent cargo in the cavity and magnetic NPs in the wall. B) Optical microscopy image of capsules dispersed in water, showing the bright field and blue fluorescence channel (excitation 365/50 nm, beam splitter 395 nm and emission 445/50 nm) corresponding to the emission of Cascade Blue-labelled dextran. The scale bar corresponds to 20 μm. C) TEM image of dried capsules. The scale bar corresponds to 1 μm. D) Histogram of the size distribution fitted with a Gaussian curve. E) ζ-potential measurements of the polyelectrolyte capsules in water. The values are the results of three independent measurements.

As iron oxide nanocubes have shown very efficient heating performances {Guardia, submitted #25050}, it should be possible to trigger the release of Cascade Blue-labelled dextran encapsulated inside capsules with these NP in their wall by an AMF. In order to demonstrate magnetothermal heating a solution containing capsules with a resulting iron concentration of 4.8 g/L was exposed to an AMF for 90 minutes. Upon exposure to the AFM, the used capsule concentration ensured a final temperature of about 90 °C in dynamic equilibrium, *cf.* Figure 2. In fact, under the same exposure conditions the finally reached temperature clearly depended on the capsules (*i.e.* iron) concentration and lower concentrations lead to lower final temperatures (cf. the Supporting Information). A capsule solution with a Fe content of only 1.5 g/L raised the temperature only to 40 °C. Thus control of capsules / iron concentration is of paramount importance, as the final temperature plays an important role on the opening of the capsules.

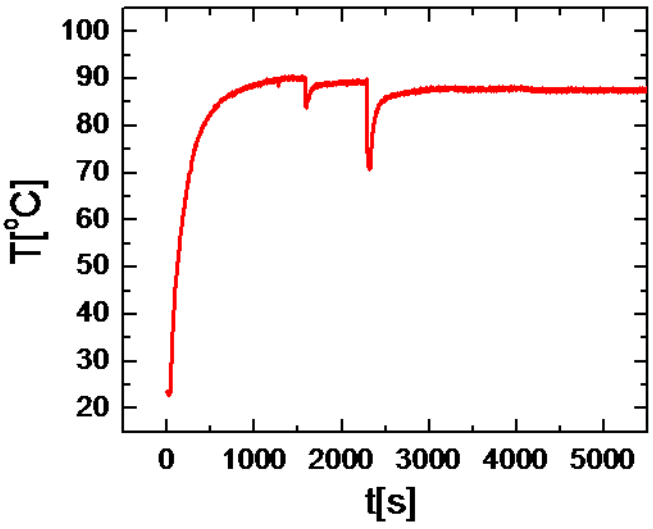

Figure 2: Bulk temperature T(t) as a function of time for a solution of capsules with 4.8 g/L of Fe, which has been placed under an AMF (300 kHz and 24 kAm^{-1}) for 90 minutes. During the experiment the solution was removed

from the cavity were the AMF was applied (dips in the curve at 1500 s and 2250 s) in order to control and shake the solution.

In order to evaluate the influence that the AMF, and hence the temperature increase, had on the capsules, TEM images from aliquots of the solution with AMF exposed capsules and the control sample were compared (*cf.* the Supporting Information). In the AMF treated capsules some damage in form of partially broken walls could be observed, together with the presence of some free magnetic NPs which had been released from the capsule walls. Both effects could not be found in the control capsules. However, even if some evidence of the effect of AFM exposure were observed, these result are clearly purely qualitative and the observable difference between both samples at best is relatively small. We thus performed an additional study based on recording the absorption and fluorescence spectra of the supernatant, in order to probe for CascadeBlue-labelled dextran released from the capsules upon AMF exposure (*cf.* Figure 3). Note that before experiments eventually leached dye had been removed and in an additional control no significant further leaching was observed on the time scale of experiments. For the control sample, after 90 minutes at room temperature (no AMF) a rather small enhancement in the absorption and fluorescence spectra was observed, which is likely ascribed to a slow leakage of CascadeBlue-labelled dextran from the capsules (Figure 3). On the other hand, in the case of AMF exposure remarkable changes in the absorption and fluorescence signals of the supernatant were observed. The fluorescence peak was centred at 420 nm, corresponding to the spectral feature of the fluorescence signal of free CascadeBlue-labelled dextran. In absorption however, for the AMF exposed sample, there was a strong and broad signal with a peak at 270 nm, and the characteristic absorption peaks of the free CascadeBlue-labelled dextran were partially hidden under this signal. This signal was clearly not present in the spectra of the control sample and of the initial supernatant. The absorption peak at 270 nm might be attributed to the presence of small polymeric fragments derived from the broken capsule walls, which absorbin the UV region, and which stronger absorb than the released CascadeBlue-labelled dextran. Indeed, this hypothesis is supported by the TEM images of AMF treated capsules in which a surface damage was observed. We thus conclude that, besides the release of CascadeBlue-labelled dextran as observed by the fluorescence spectra, the heat generated under AMF by the magnetic NPs in the capsules walls might also partially damage the polymeric shell in a way that polymer fragments, which absorb in the UV region are released.

Finally, the fluorescence intensities of the capsules before and after treatment of AMF irradiation were recorded with confocal microscopy. In a population of over 400 capsules an evident decrease of the

mean fluorescence intensity was observed for the AMF treated capsules as compared to the control sample (*cf.* the Supporting Information). This is an additional indication that upon AFM exposure the capsules get destroyed and release their cargo, fluorescent CascadeBlue-labelled dextran, is released to the environment.

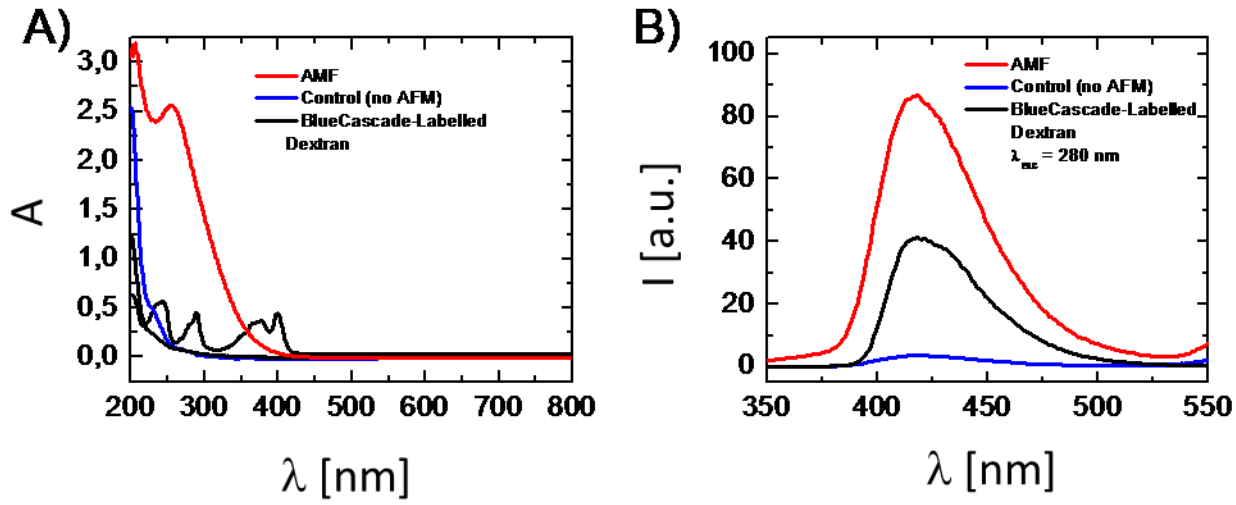

Figure 3. A) UV-vis absorption spectra, and B) fluorescence emission spectra (at λ_{exc} = 280 nm excitation) of i) free Cascade Blue-labelled dextran (black line), ii) the supernatant of a capsule solution which had been treated for 90 minutes under an AMF (300 kHz and 24 kAm^{-1}) (red line), and iii) the supernatant of a control sample of capsules which had been kept at room temperature for 90 minutes and thus had not been exposed to an no AMF (blue line).

Conclusions

The proof-of-concept experiment as shown in this study suggests that release of molecular cargo from polyelectrolyte capsules by NP-mediated heating is not only possible by light-irradiation of plasmonic NPs as reported before in literature, but also by AFM-irradiation of magnetic NPs. Owing the high heating performance of iron oxide nanocubes, damages in the polymer shell were prompted thorough an AMF, which allowed for release of the encapsulated molecular cargo. For successful remotely controlled release of cargo by magnetothermal heating the content of magnetic NPs has to be carefully tuned, as in our case only iron concentrations of 4.8 g/L but not of 1.5 g/L allowed for a sufficiently strong increase in temperature for opening the shell of the capsules. In comparison to optical excitation,

AMF excitation is barely absorbed by tissue, and thus an externally triggered release can be conveniently induced. This issue, opens new and exciting possibilities of cargo release for *in vivo* applications, though the geometry of the capsules would need to be optimized towards such applciations. In this regard, the future direction of this research should deal with the requirement of in vivo applications, which preferentially will involve smaller capsules.

Acknowledgements

The authors are grateful to Dr. Pablo delPino and Prof. Heinz Jänsch for helpful discussions, and to Simone Nitti and GiammarinoPugliese for helping with sample preparation. This work was supported by HSFP (project RGP0052/2012 to WJP), by the European project Magnifyco (Contract NMP4-SL-2009-228622 to TP) and by the Italian FIRB project (Nanostructured oxides, contract no.588BAP115AYN to TP). XY acknowledges support by the Chinese government (CSC, Nr. 2010691036).

References

Magnetically triggered release of molecular cargo from iron oxide nanoparticle loaded microcapsules

Susana Carregal-Romero[1#], Pablo Guardia[2#], Xiang Yu[1], Raimo Hartmann[1], Teresa Pellegrino[2*], Wolfgang J. Parak[1,3*]

[1] Fachbereich Physik, Philipps Universität Marburg, Marburg, Germany
[2] Italian Institute of Technology, Genova, Italy
[3] CIC Biomagune, San Sebastian, Spain
[#] both authors contributed equally to this work
[*] corresponding authors: teresa.pellegrino@unisalento.it, wolfgang.parak@physik.uni-marburg.de

SUPPORTING INFORMATION

Contents

I) Characterization of magnetic nanoparticles
II) Characterization of polyelectrolyte capsules loaded with magnetic nanoparticles and Cascade Blue-labelled dextran
III) TEM images of polyelectrolyte capsules before and after AMF treatment
IV) Absorption spectra of the polyelectrolyte capsule components
V) Confocal microscopy analysis of Cascade Blue-labelled dextran release
VI) Hyperthermia experiments

I) Characterization of magnetic nanoparticles

In Figure S-I.1 and Figure S-I.2 transmission electron microscopy (TEM) images of iron oxide nanoparticles (NPs) with hydrophobic capping, as yielded directly from the synthesis in organic solvents, and of the same NPs after a phase transfer to aqueous solution, respectively, are shown. Figure S-I.3 shows the hydrodynamic diameter and the zeta potential of the NPs in water obtained with dynamic light scattering (DLS) and Laser Doppler Velocimetry (LDV), respectively.

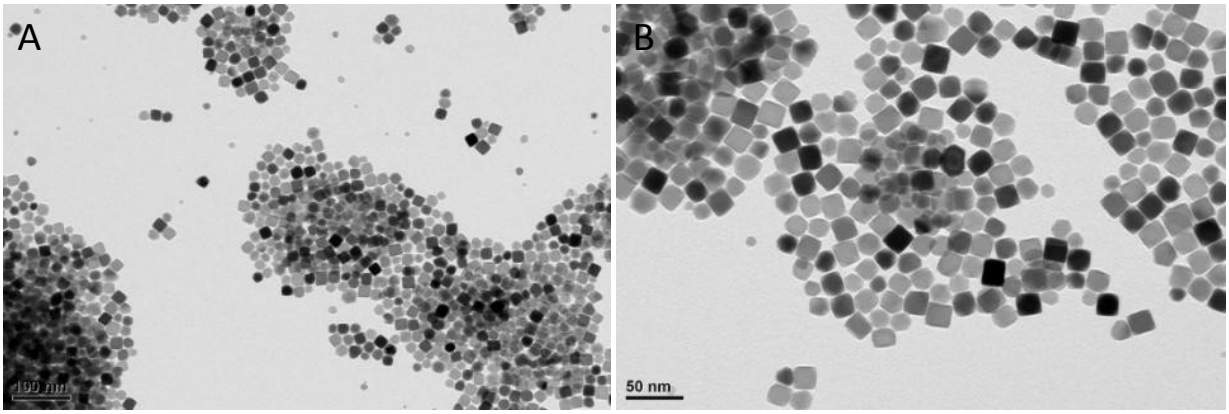

Figure S-I.1. *TEM images (A, B) of the hydrophobically capped magnetic nanoparticles in chloroform. The scale bars correspond to 100 nm (A) and 50 nm (B).*

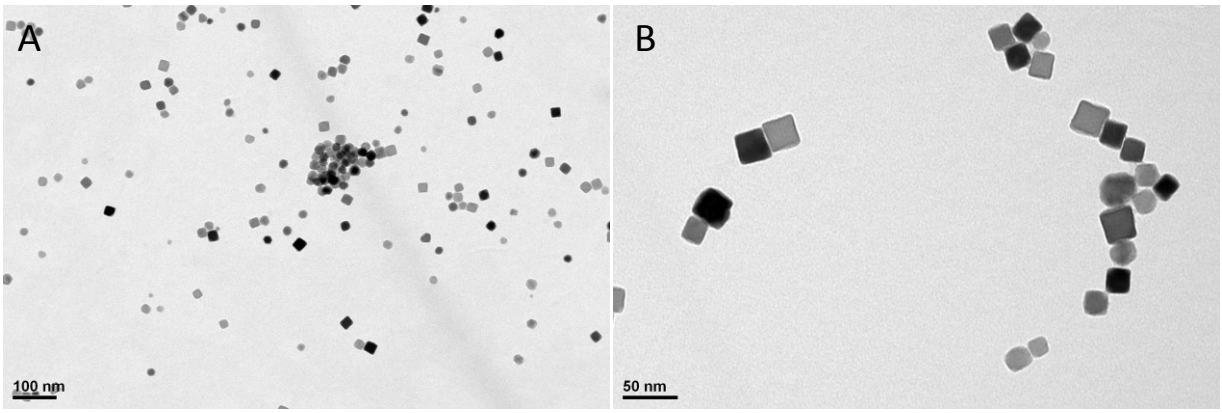

Figure S-I.2. *TEM images (A, B) of the water-soluble magnetic nanoparticles (i.e. after phase-transfer to water) used to produce the polyelectrolyte capsules sensitive to AMF. The scale bars correspond to 100 nm (A) and 50 nm (B).*

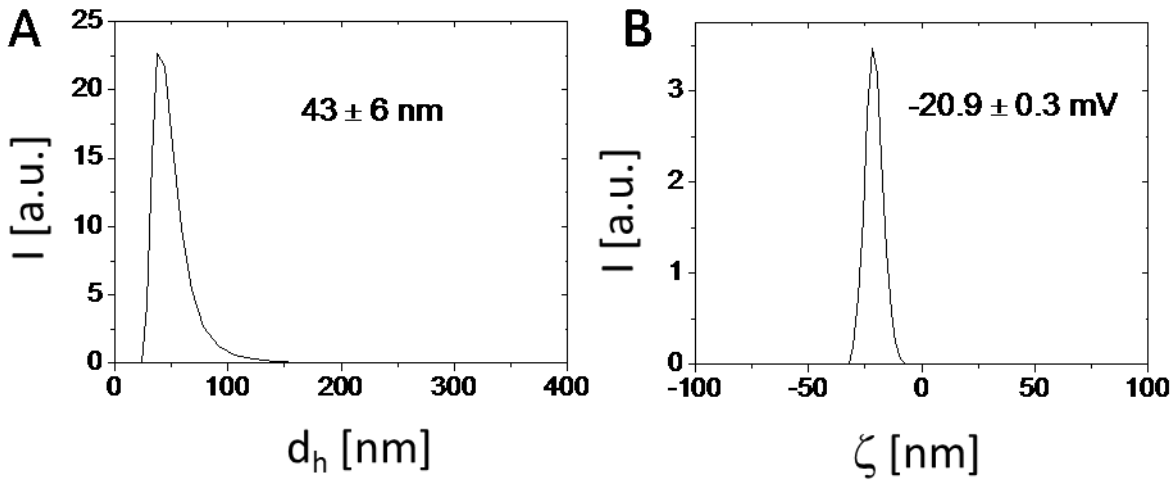

Figure S-I.3. *Distributions of the hydrodynamic diameter d_h (A) and ζ-potential (B) of the iron oxide NPs, as determined in Milli-Q water. The shown values are the result of three independent measurements.*

II) Characterization of polyelectrolyte capsules loaded with magnetic nanoparticles and Cascade Blue-labelled dextran

TEM images of polyelectrolyte capsules decorated with magnetic NPs in the shell at different magnifications are shown in Figure S-II.1.

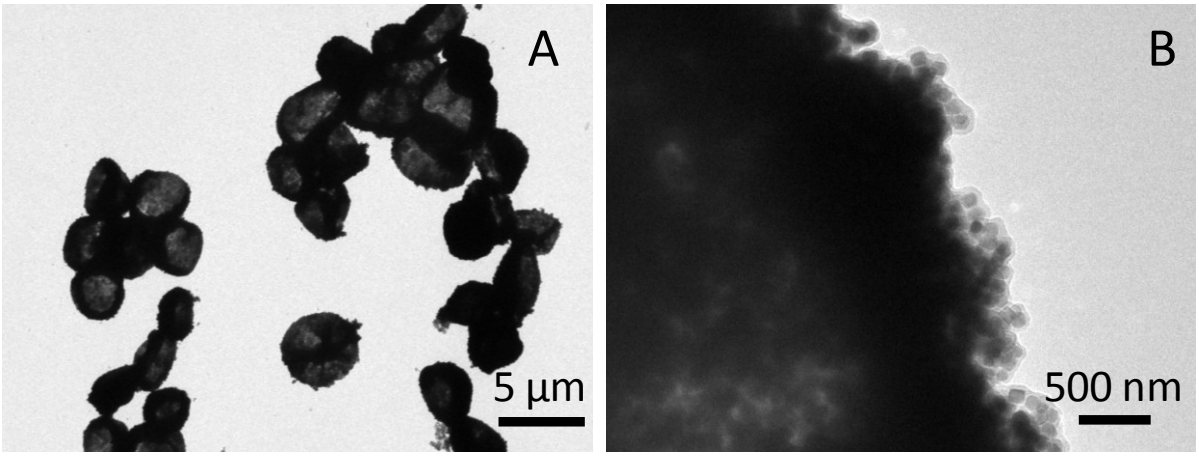

Figure S-II.1. *TEM images (A, B) at different magnifications of polyelectrolyte capsules decorated with magnetic NPs. The scale bars correspond to 5 µm (A) and 500 nm (B).*

The concentration of capsules was obtained by counting with a hemocytometer, which was possible due to their micrometre size. Induced Coupled Plasma -Atomic Emission Spectroscopy (ICP-AES) was used to obtain a concentration of 4.8 g/L of Fe in the polyelectrolyte capsule sample ($1.6 \cdot 10^7$ capsules/mL).

III) TEM images of polyelectrolyte capsules before and after AMF treatment

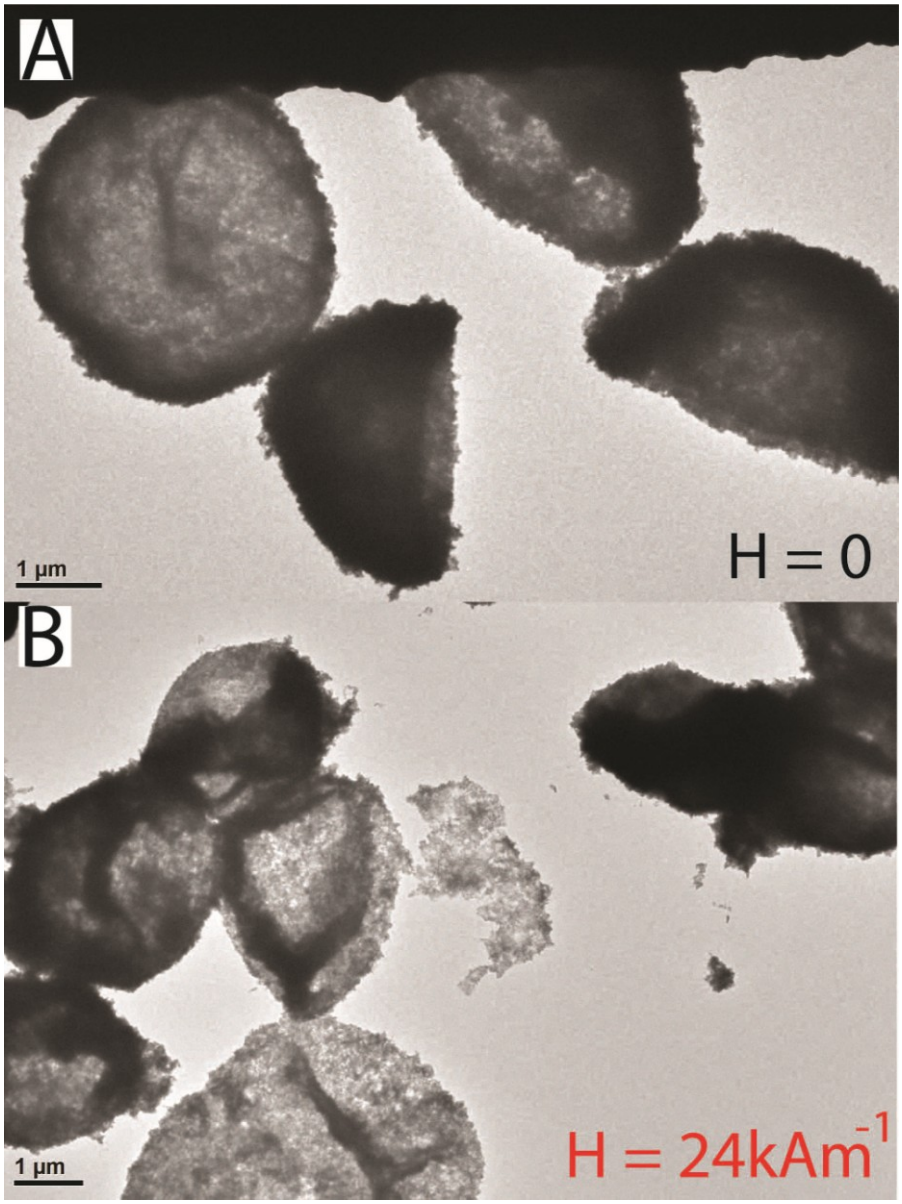

Figure S-III.1. *TEM images of iron oxide NPs decorated polyelectrolyte microcapsules after (A) and before (B) being exposed to alternaning magnetic fields (AMF, 300 kHz, 24 kAm^{-1}) for 90 minutes. Notice the free/detached NPs on panel B.*

IV) Absorption spectra of the polyelectrolyte capsule components

UV-Vis absorption spectra of all the components present in the polyelectrolyte capsules were measured in Milli-Q water and they are shown in Figure S-IV.1.

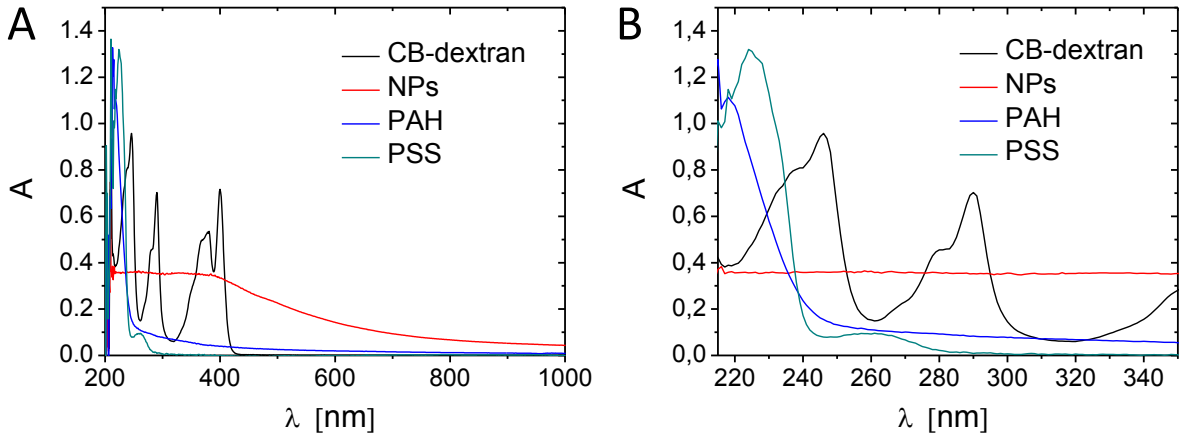

Figure S-IV.1. *Absorption spectra of the polyelectrolyte capsule components: Cascade Blue-labelled dextran (CB-dextran), magnetic NPs (NPs), poly (allylamine hydrochloride) (PAH), and poly (styrene sulfonate) (PSS). (A) Shows the obtained spectra ranging from 200 to 1000 nm and (B) is an enlargement showing only the absorption peaks between 215 and 350 nm.*

V) Confocal microscopy analysis of Cascade Blue-labelled dextran release

The release of Cascade Blue-labelled dextran was studied also by confocal microscopy, which was used to compare the amount of Cascade Blue-dextran still encapsulated in the polyelectrolyte capsules after AMF irradiation. For this, the irradiated and non-treated capsules were separated from their corresponding supernatant and were further washed two times with Milli-Q water. Then confocal images were taken. The analyzing toolbox was programmed in MATLAB R2010a and it was programmed to recognize circular objects in the images. The toolbox calculated the size or the mean fluorescence intensity value inside these circles in one or more channels.

A sample of polyelectrolyte capsules loaded with Cascade Blue-labelled dextran was irradiated with an alternating magnetic field (AMF) for 90 min (300 kHz, 24 kAm^{-1}) and its fluorescence intensity was compared with capsules that were not irradiated as control. Figure S-V.1 shows the results of the analysis of at least 400 different capsules of each sample (AMF treated and control). The fluorescence intensity was normalized. As it can be seen, the intensity of the capsules that were irradiated decreased compared to the control sample. This corresponds with the presence of Cascade Blue-labelled dextran released in the supernatant of the sample after AMF irradiation as detected by fluorescence spectroscopy. The capsules did not release the Cascade Blue-labelled dextran completely however.

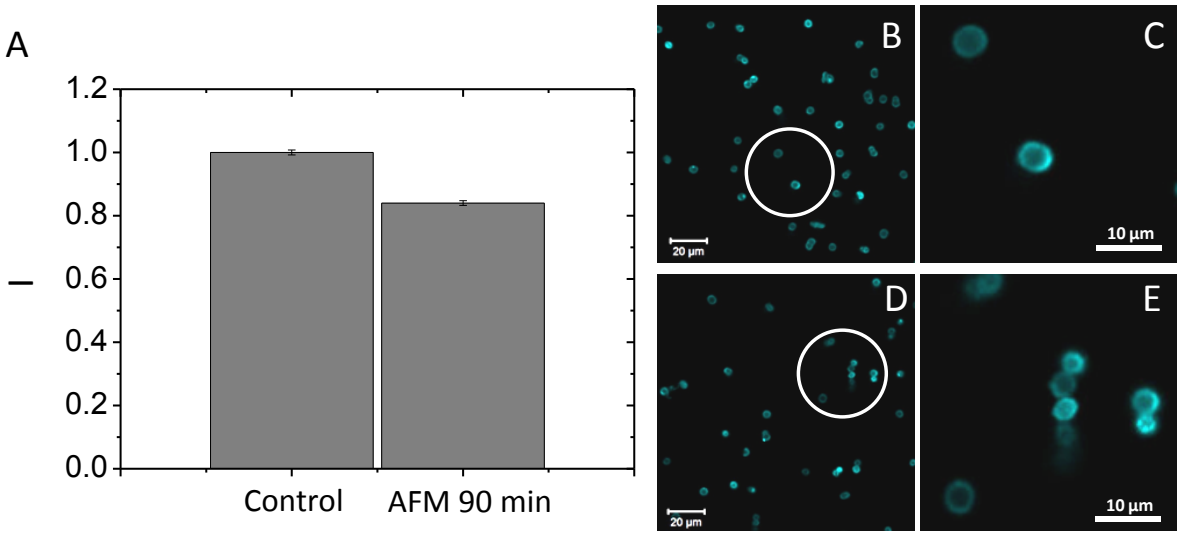

***Figure S-V.1**. A) Normalized fluorescence intensity of polyelectrolyte capsules loaded with Cascade Blue-labelled dextran after RF irradiation for 90 min (24 kAm^{-1}, 300 kHz) compared with a control sample that was not irradiated. (B, C) Confocal images (blue channel) of the control sample. The white circle in B corresponds to the area shown in image C. (D, E) Confocal images (blue channel) of the polyelectrolyte capsules irradiated for 90 min. The white circle in D corresponds to the area shown in image E. The scale bar corresponds to 20 µm for (B, D) and 10 µm for (C, E).*

VI) Hyperthermia experiments

For the AMF experiments different concentrations of iron were used. We observed that for low concentration of iron (below 4.8 g_{Fe}/L) the temperature achieved was below 80 ℃ (see Figure S-VI.1). Absorption spectra for these samples were recorded (Figure S-VI.2) showing a strong increase in the absorption at 270 nm, a feature also observed for the samples with an iron concentration of about 4.8 g_{Fe}/L. However the signal-to-noise ratio was rather low together with a strong contribution of the absorption at low energy/high wave lengths which were attributed to the presence of some polymer capsules with integrated magnetic NPs (Figure S-VI.2).

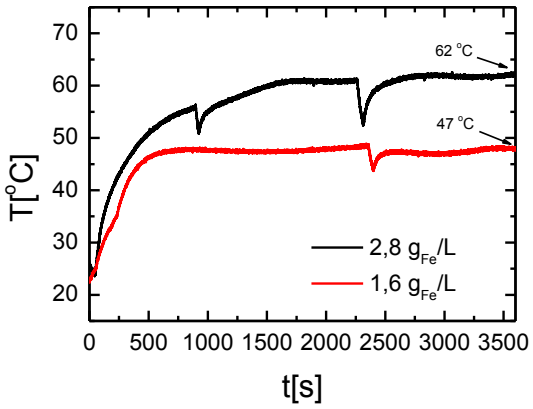

Figure S-VI.1. *Temperature as a function of time for 1.6 g/L (red line) and 2.7 g/L (black line) of a solution of polyelectrolyte capsules with integrated magnetic NPs placed under an AMF (300 kHz and 24 kAm^{-1}) for 60 minutes. During the experiment the solutions were removed from the cavity were the AMF was applied (dips in the curve at 900 s, 2350 s and 2450 s) in order to control and shake the solutions.*

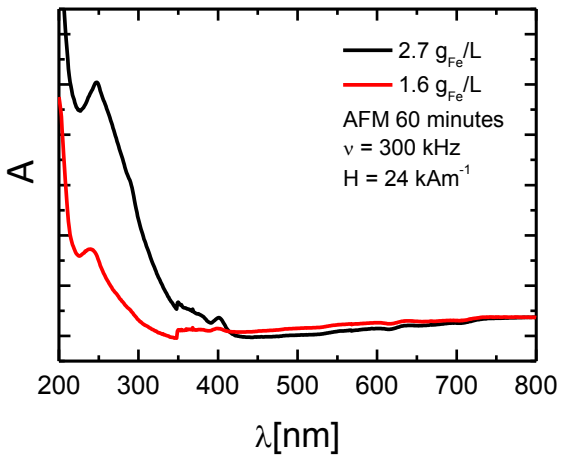

Figure S-VI.2. *UV-vis absorption spectra of the supernatant of two solutions of capsules with integrated magnetic NPs with iron content of 2.7 g/L (black line) and 1.6 g/L (red line) treated for 60 minutes under an AMF (300 kHz and 24 kAm^{-1}).*

The above shown results lead to two main conclusion: First, samples need to be filtered in order to remove the contribution of free magnetic NPs, and second the amount of magnetic NPs in the capsules needs to be as high as much in order to get a better signal-to-noise ratio. In this regard a solution with 4.8 g_{Fe}/L was used and treated for 90 minutes to ensure a better release of the Cascade Blue-labelled dextran. In addition the supernatant was filtered by using Microcentrifuge Spin Cups and Columns (cut-off 100K).

As reported in the main manuscript, after collecting the capsules with integrated magnetic NPs with a magnet and adding fresh MilliQ-Water, the capsules with integrated magnetic NPs were again collected and the supernatant was analyzed in order to ensure that no free Cascade Blue-labelled dextran was present in the initial solution.

Light-Addressable and Degradable Silica Capsules for Delivery of Molecular Cargo to the Cytosol of Cells

Andrea Ott,[1] Xian Yu,[1] Raimo Hartmann,[1] Joanna Rejman,[1] Adrian Schütz,[1] Markus Ochs,[1] Wolfgang J. Parak,[1,2] Susana Carregal-Romero*[1]

[1] Fachbereich Physik, Philipps-Universität Marburg, Marburg, Germany.

2 CIC Biomagune, San Sebastian, Spain

* Contact details: susana.carregalromero@physik.uni-marburg.de

Abstract

Degradable and light addressable silica capsules have been prepared based on $CaCO_3$ template particles. It was possible to load these capsules with an array of molecules such as anti-cancer drugs (doxorubicin), proteins (bovine serum albumin) and nucleic acids (messenger RNA encoding green fluorescent protein). *In vitro* degradation and release of these molecules was demonstrated and quantitatively compared with several kinds of polyelectrolyte multilayer capsules as examples of other delivery vehicles. The data suggests hydrolysis as a mechanism involved on intracellular degradation of silica capsules. Photothermal heating (by integrating plasmonic nanoparticles in the silica shell) was further used to induce remote molecular release.

Introduction

Silica (SiO_2) particles and capsules (*i.e.* hollow particles comprising only a shell) are among the most abundant and widely used synthetic materials applied in catalysis, sensing, imaging, and drug delivery.[1-6] Amorphous silica has been used as a pharmaceutical excipient acting as anticaking agent or as carrier for drug delivery.[7,8] Depending on the degree of porosity amorphous silica can be loaded with active molecules by a variety of different approaches. If the drug delivery system is based on mesoporous silica, both hydrophilic and hydrophobic drugs can be hosted inside the pores because they are generally homogenous and have a diameter ranging from 2 to 10 nm.[9-11] If the porosity of the silica is low, it can carry drugs or active molecules, such as DNA, predominantly on its surface.[12] The silica surface absorbs molecules mainly by formation of H-bonds or by means of London dispersion interaction.[13] In both cases the release of drugs can be triggered by applying an external stimulus such as a change of temperature or pH.[14-16] However, the active molecules can be also released by slow permeation or by particle degradation.[17-19] Silica can be degraded in biological environments.[20] The product of silica degradation is the non toxic silicic acid, which can even act as a source of Si, and which is useful in the formation of connective tissue (*e.g.* tendons and bones).[21] Therefore, there is an increasing interest in the synthesis and application of degradable silica.[22-25] In this context, different strategies to facilitate the degradation of silica, such as the incorporation of iron (III) or calcium have been reported recently. The removal of these ions from ion chelators present in the intracellular space increased the degradation rate of doped silica compared with regular silica.[22,26]

Our work explores firstly the possibility of forming degradable capsules based on amorphous silica, where a large amount of active molecules can be hosted in their hollow cavity. Calcium carbonate

particles were used as templates since they can be loaded with different types of molecules and easily dissolve under mild conditions.[27,28] Within this context, we studied the degradability of the silica shells which had been form on top of the calcium carbonate particles. We compared their degradability with the one of polymeric polyelectrolyte capsules made by the layer-by-layer (LbL) approach.[29] After internalization by cells, capsule degradation may lead to the release of the embedded molecular cargo to the cytosol. In particular we studied the delivery of encapsulated DQ-ovalbumine (DQ-OVA), and messenger RNA (mRNA) encoding green fluorescent protein (mGFP). We show that the encapsulation procedure did not affect the activity of these two types of molecules. Furthermore, we demonstrated the release of molecules from the lysosomes, where the silica capsules are first located,[30] to the cytosol. In addition to degradable silica capsules we also synthesized non-degradable silica capsules functionalized with plasmonic nanoparticles (NPs) as light-responsive elements. Au NPs (of certain size, shape, and degree of agglomeration) are able to absorb IR-light and transform it into heat.[31-35] Cytosolic release triggered *via* light irradiation was in this way achieved by illuminating the gold NPs in the silica shell. The light-responsive silica capsules were deliberately made to be intrinsically non-degradable. Thus cytosolic release could be achieved in a controlled way only upon irradiation.[28,36-39] The two different *in vitro* release mechanisms of cargo molecules from degradable and light-responsive silica capsules are discussed in this work.

Experimental Section

Materials and Methods

Tetraethyl orthosilicate (TEOS, $Si(OC_2H_5)_4$, #86578), ammonium hydroxide solution (NH_4OH,

#320145), ethylenediamine-tetraacetic acid disodium salt (EDTA, $C_{10}H_{14}N_2Na_2O_8 \cdot 2H_2O$, #E5134), calcium chloride ($CaCl_2 \cdot 2H_2O$, #223506), sodium carbonate (Na_2CO_3, #S7795), poly(allylamine hydrochloride) (PAH, M_w= 56 kDa, #283223), poly(sodium 4-styrenesulfonate) (PSS, M_w = 70 kDa, #243051), poly-L-arginine hydrochloride (PARG, M_w > 70 kDa, #P3892), dextran sulfate sodium salt (DEXS, M_w= 10 kDa, #D4911), doxorubicin hydrochloride (DOX, $C_{27}H_{29}NO_{11} \cdot HCl$, #D1515), dextran-tetramethylrhodamine isothiocyanate (dextran-TRICT, M_w = 155 kDa, # T1287), Resazurin solution (#TOX8), and the 96-well plates for cell culture (#CLS3603) in which the toxicology assay was carried out were obtained from Sigma-Aldrich. DQ™ Ovalbumin (M_w = 45 kDa, #D12053), bovine serum albumin-FITC (FITC-BSA, #A23015), and SNARF-dextran (M_w ~ 10 kDa, #D-3303) were purchased from Fisher Scientific. Pronase (#10165921001) was obtained from Roche Applied Science. Absolute ethanol (#9065.2) and methanol (#8388.6) were obtained from Roth. The fluorophore Dy634 (NHS-ester, #634-00) was purchased from Dyomics, and methoxy-polyethyleneglycol with thiol terminus (mPEG-SH, #125000-40) from Rapp Polymere GmbH. mRNA encoding green fluorescent protein (GFP) was produced as previously reported.[40]

Transmission electron microscopy (TEM) imaging was performed using a JEOL Model JEM 3010 operating at an acceleration voltage of 300 keV. The software ImageTool (version 3.0) was used to derive the diameters of the template cores and silica capsules from the TEM images. Fluorescence spectra of capsules were recorded with a fluorometer (Fluorolog-3 from Horiba JOBIN YVON). Confocal fluorescent microscopy images of cells, which had been incubated with capsules, were acquired using a LSM 510 META microscope (Zeiss, Germany). From these images intracellular fluorescence intensities were analyzed with the software Image J. The basic setup for opening of capsules triggered with infrared light consisted of a wide-field fluorescence microscope (Axiovert

200M, Zeiss, Germany), which was coupled to an 830 nm IR laser diode (130 mW maximum output) *via* fiber optics and a beam-coupling device (Rapp-Opto DL-830 CV laser and fixed spot illumination coupling). The maximum light power reaching the sample plane for the used 63x/1.4 oil immersion Plan-Apochromat objective was ~30 mW (continuous output). In the light focus the energy is dispersed across an oval spot of about 6 μm^2 diameter.[28] With a tunable power supply, the output power of the laser could be varied continuously from 0 to 30 mW on the sample plane. Capsules were opened upon irradiation with laser intensities between 2.5 and 3 $mW/\mu m^2$ upon illumination for 1-2 seconds. Detailed protocols are described in the Supporting Information.

Silica Capsule Synthesis

$CaCO_3$ cores were prepared as reported elsewhere.[41] They were used as templates during the formation of the silica capsule and employed to encapsulate different molecules. Briefly, 615 µL of a 0.33 M $CaCl_2$ solution were mixed under magnetic stirring with 615 µL of a 0.33 M Na_2CO_3 solution.[28,42] After 30 s the solution was transferred to a tube and further incubated for 2 min. The $CaCO_3$ particles were then washed three times with 1 mL Milli-Q water, followed by centrifugation at low speed (110×g for 1 min). The encapsulation of proteins (FITC-BSA and DQ-OVA), messenger RNA and SNARF-dextran was carried out similar as described above for the synthesis of plain $CaCO_3$ particles by co-precipitation of the macromolecules with the $CaCO_3$ during the particle formation.[43,44] The encapsulation of DOX was achieved by co-precipitation of polystyrene-block-poly(acrylic acid) (PS-b-PAA) micelles and further post-loading as reported by Tong *et al.*[28,45] For synthesizing degradable silica capsules after co-precipitation, a stabilization of the $CaCO_3$ cores (with embedded molecules) was performed in ethanol as second step of the synthesis. This was achieved by wrapping the $CaCO_3$ cores with mPEG-SH. Briefly, 3 mg of mPEG-SH in 1 mL Milli-Q water were added to the $CaCO_3$ cores and shaken for at least 30 min.

Assuming that the number of $CaCO_3$ particles was 10^8 in 1 mL and a $CaCO_3$ radius of about 2.5 μm, this corresponded to 40 mPEG-SH molecules added per nm^2 of $CaCO_3$ surface. This is in the range of concentrations reported to stabilize other surfaces such as gold nanospheres and nanorods.[46] After shaking, the $CaCO_3$ particles were washed twice with 1 mL Milli-Q water and once with ethanol. Then, they were transferred with 4.5 mL of ethanol to a 40 mL glass vial. 4 mL Milli-Q water, 13.6 mL ethanol, and 230 μL ammonium hydroxide solution were added. Under fast stirring at 750 rpm, 90 μL of tetraethyl orthosilicate were added. The solution was stirred at a steady speed of 400 rpm for 3 h. After this process a silica shell had formed around the $CaCO_3$ particles (with the integrated molecular cargo). The particles were then washed twice with ethanol and once with Milli-Q water before adding 1 mL of 0.2 M EDTA at pH 5.5 to dissolve the $CaCO_3$ cores as it has been reported elsewhere.[47,48] The resulting silica capsules with embedded molecular cargo were washed three more times before adding 1 mL of 1 mg/mL (in 0.5 M of NaCl) PARG solution to the capsules. The capsules were left shaking in the PARG solution for 12 min and were then washed three times with Milli-Q water. The capsules were re-dispersed in Milli-Q water. The last layer of PARG was added to provide the capsules with positive surface charge. In case 10 kDa SNARF-dextran was used as molecular cargo (pre-loading of the $CaCO_3$ particles), after silica shell formation and dissolution of the $CaCO_3$ template cores the capsules were further dispersed in 150 μL of a 0.5 mg/mL 10 kDa SNARF-dextran solution (post-loading) and shaken for 1 h, before adding the last layer of PARG (1 mL, 1 mg/mL). In contrast, for the synthesis of non-degradable (light-responsive) silica capsules the $CaCO_3$ template cores were coated with a monolayer of poly(sodium 4-styrenesulfonate) (2 mg/mL in 0.5 M of NaCl and pH 6.5) and then with a positively charged layer of poly(allylamine hydrochloride) (2 mg/mL in 0.5 M of NaCl and pH 6.5).[49] After addition of this PSS/PAH bilayer, aggregates of Au NPs were assembly *via* electrostatic interactions on top of the bilayer as reported previously.[41] Subsequently functionalization with mPEG-SH and the SiO_2

coating was carried out as described above for the degradable capsules. In the synthesis procedure for the nondegradable capsules the thiol groups bound strongly to the surface of the Au NPs, providing the particles stability in the ethanol/water mixture which is used for the SiO_2 coating. The final architectures of the capsules were mPEG-SH@SiO_2@PARG and (PSS/PAH)Au@mPEG-SH@SiO_2@PARG for the degradable and non-degradable (light-responsive) silica shells, which in the following will be referred to as 1-SiO_2 and 1-Au-SiO_2 capsules, respectively.

Polyelectrolyte Capsule Synthesis

Positively charged $CaCO_3$ particles were also used as templates to prepare LbL capsules [28]. The preparation of these cores was carried out as described previously for the synthesis of silica capsules. The formation of the polyelectrolyte shell for LbL capsules is based on the electrostatic self-assembly of layers of polyelectrolytes with alternating charge on the surface of a template.[50,51] Enzymatically degradable LbL capsules were made with dextran sulfate (DEXS, negatively charged) and poly-L-arginine hydrochloride (PARG, positively charged), as reported previously.[29,41,52,53] Five bilayers of polyelectrolytes were assembled, resulting in $(DEXS/PARG)_5$ capsules. Nondegradable capsules $(PSS/PAH)_5$ were made by assembling 5 bilayers of poly(sodium 4-styrenesulfonate) (PSS, negatively charged) and poly(allylamine hydrochloride) (PAH, positively charged). Also degradable and nondegradable light-responsive capsules were synthesized. They were prepared as described by LbL assembly of DEXS/PARG and PSS/PAH, but with addition of agglomerated Au NPs (15 nm core diameter) after the third bilayer of polyelectrolytes, leading to $(DEXS/PARG)_3Au(DEXS/PARG)_2$ and $(PSS/PAH)_3Au(PSS/PAH)_2$ capsules, respectively.[41] After LbL assembly of the polyelectrolyte shells the template cores were dissolved by adding 1 mL of 0.2 M EDTA at pH 5.5. Concerning embedded molecular cargo, capsules loaded with 10 kDa SNARF-dextran were prepared using the $CaCO_3$ cores

loaded with the SNARF-dextran (preloading). However, after dissolution of the $CaCO_3$ cores the capsules were additionally postloaded and shrank in a water bath at 70 °C for one hour.[43] Postloading of the LbL capsules was necessary in case of 10 kDa SNARF-dextran because the porosity of the polyelectrolyte multilayer shell is high. Shrinking of the shell reduces the pore size.[54] We hereby followed previously published protocols.[28,41] The final architectures of the LbL capsules were $(DEXS/PARG)_5$, $(DEXS/PARG)_3Au(DEXS/PARG)_2$, $(PSS/PAH)_5$, and $(PSS/PAH)_3Au(PSS/PAH)_2$ and will be further referred as 2-(DEXS/PARG), 2-Au(DEXS/PARG), 3-(PSS/PAH), and 3-Au(PSS/PAH), respectively.

Cell Culture

Human cervical cancer cells (HeLa) were seeded and grown in Eagle´s Minimal Essential Medium supplemented with 10% fetal bovine serum (FBS), L-glutamine and 1% penicillin/streptomycin. Human breast adenocarcinoma cells (MDA-MB-231) were seeded and grown in Dulbecco´s Modified Eagle Medium (DMEM) with 4.5 g/L glucose supplemented with 10% FBS, L-glutamine and 1% penicillin/streptomycin. The cells were incubated at 37 °C in an atmosphere of 95 % air and 5 % CO_2. For *in vitro* capsule degradation experiments µ-Slides with 8 wells (Ibidi #80826) were used. 20000 cells were seeded in 300 µL of cell medium to a growth area of 1.0 cm^2 of each well. 5 capsules were added per seeded cell. For experiments involving light-mediated *in vitro* opening of capsules one day prior to the experiments, 100000 cells were plated in 2 mL medium on standard cell culture µ-Dishes (Ibidi #81156) to a growth of 3.5 cm^2 of each dish. The cells were incubated with 5 capsules per cell overnight.

Calibration Curves of pH-Sensitive Capsules

Calibration curves for the pH-dependent fluorescence emission of capsules loaded with SNARF-dextran were obtained by incubating the capsules in buffer solutions of different pH and imaging their fluorescence with fluorescence microscopy. Analysis of the images was done using the software Matlab. The evaluation of the response of encapsulated SNARF to different pH was performed as published previously.[41] However, in contrast to previous reports the pH values were recorded in high potassium buffers of different pH in the presence of the ionophore nigericin.[55]

Cytotoxicity Assays

The cytotoxicity assay was done using a fluorescence-based approach employing resazurin. Resazurin is a non-toxic non-fluorescent compound, which in living cells is converted into fluorescent resorufin.[56] Two different cell lines were tested: 15000 MDA-MB-231 cells or 10000 HeLa cells were seeded per well in a 96-well plate (360 μL medium/well, 0.32 cm^2/well surface area, Corning #3603) and incubated for 48 h. Subsequently different concentrations of 1-SiO_2, 1-Au-SiO_2, 2-(DEXS/PARG), 2-Au(DEXS/PARG), 3-(PSS/PAH) and 3-Au(PSS/PAH) capsules were added to the cells and incubated for 48 h. The experiments were repeated three times for each capsule concentration. Control experiments were done with cells that were not incubated with capsules. Before adding 10% of resazurin, the cells were washed with phosphate buffered saline (PBS). After 3 h of incubation with resazurin (37 °C and 5% CO_2) the samples were analyzed with a fluorometer (excitation 560 nm, emission between 572 and 650 nm). The background emission was subtracted from each value of fluorescence emission. For evaluation the fluorescence emission intensity at 584 nm was used, which is assumed to correlate with the viability of the cells. Previously described protocols.[30]

Results and Discussion

Silica Capsule Formation

$CaCO_3$ particles were used as templates for the formation of two different types of silica capsules, which were either degradable (1-SiO_2) or non-degradable, but light-responsive (1-Au-SiO_2) (Figure 1). Concerning the degradable capsules, in order to make the $CaCO_3$ template cores stable in the medium required for the coating reaction for the assembly of the silica shell we grafted the particles with 5 kDa mPEG-SH. The mPEG-SH molecules adsorbed *via* their thiol termini to the $CaCO_3$ cores, most likely driven by their nucleophilic character and the positive charge of the $CaCO_3$ particles.[41] In this way the $CaCO_3$ particles could be transferred into a solution of ammonia in ethanol/water. Inthis solution they could be directly coated with silica upon addition of tetraethyl orthosilicate (TEOS) which then hydrolyzed and condensed, forming a shell. This typical Stöber silica coating[57] produced a homogeneous and smooth shell of SiO_2 as shown in Figure 1C. An alternative degradable silica coating was produced by using poly(vinyl pyrrolidone) (PVP) instead of mPEG-SH. Polymers in general have been used extensively to stabilize particles for further silica coating.[58] The most popular polymer in this connection is PVP, and therefore we also studied the formation of SiO_2 *via* PVP wrapping of $CaCO_3$ particles. The results obtained showed slight aggregation of the $CaCO_3$ cores after PVP functionalization and the formation of a rough surface after SiO_2 coating. The capsules obtained after the dissolution of the core were not spherical (data shown in the Supplementary Information). Thus preference was given to using mPEG-SH as priming layer for silica coating. The non-degradable, light-responsive silica capsules were prepared by taking advantage of the optothermal properties of Au NPs embedded in the silica shell. The final Au-modified silica capsules were responsive to infrared (IR) light. Figure 1A and 1E show a schematic representation of the steps followed during the preparation of both silica capsules

(degradable and non-degradable, light-responsive). The final step in the preparation was in both cases the addition of one last layer of poly-L-arginine to render the capsule surface positively charged. This was done in view of the fact that the uptake of positively charged capsules by cells is faster than that of negatively charged ones.[59] Whereas the diameter of the 1-SiO_2 and 1-Au-SiO_2 capsules was found to be 6.6 ± 0.6 μm and 6.5 ± 0.4 μm, the shell thickness (silica and PARG) was 0.6 ± 0.2 μm for 1-SiO_2 and 0.6 ± 0.3 μm for 1-Au-SiO_2 capsules, as measured with the software UTHSCSA Image Tool. The high standard deviation is mainly due to the low monodispersity of the $CaCO_3$ template cores (data included in the Supplementary Information).

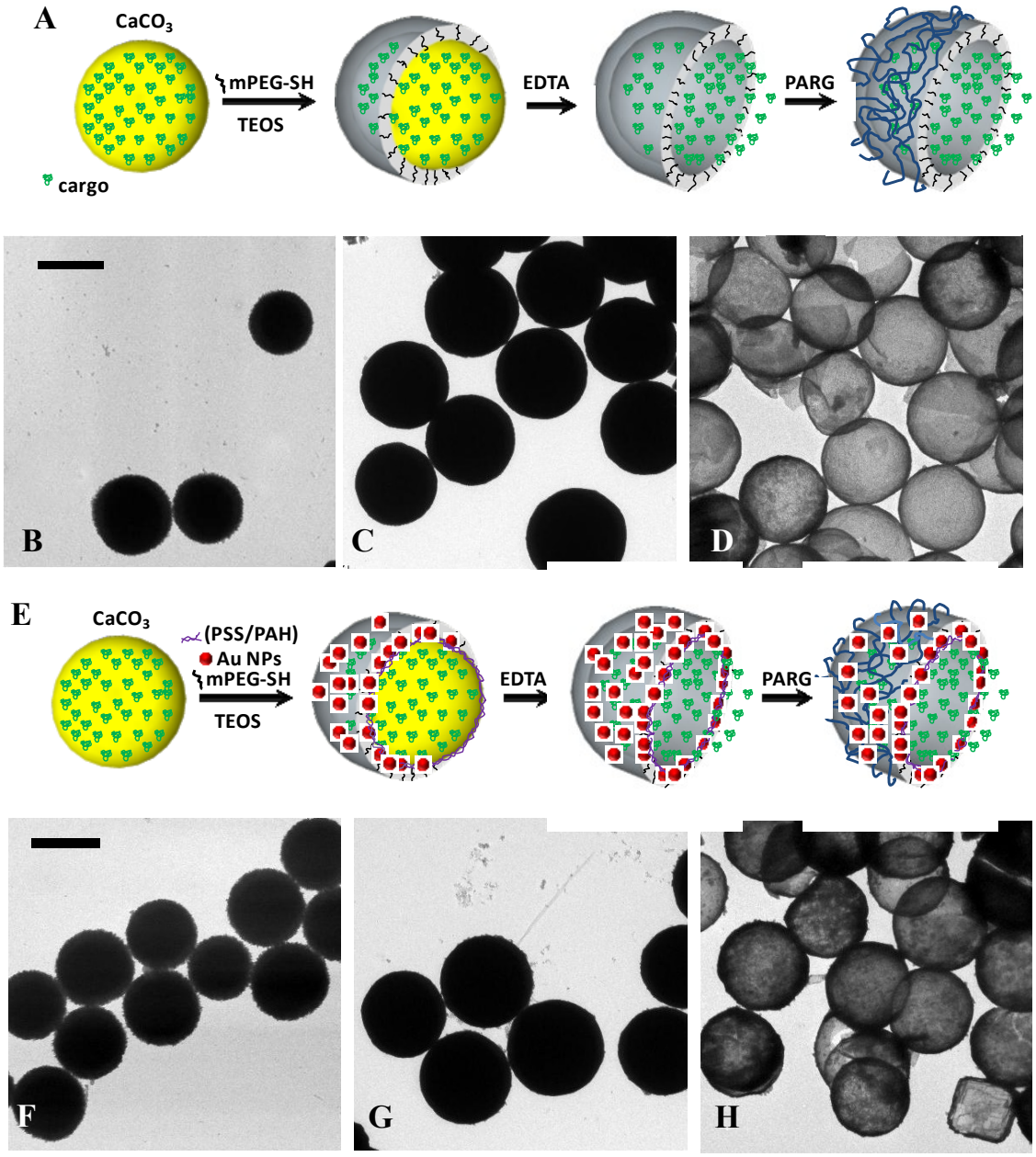

Figure 1. Synthesis of SiO_2 capsules: (A) degradable (1-SiO_2) and (E) non-degradable, light responsive (1-Au-SiO_2) capsules. TEM images of: (B, F) $CaCO_3$ cores (the same sample was used for both types of capsules), (C) $CaCO_3$@SiO_2 particles, (D) 1-SiO_2 capsules, (G) (PSS/PAH)Au@SiO_2 particles, and (H) 1-Au-SiO_2 capsules. The scale bars correspond to 5 μm.

TEM images of all six different types of capsules (including the polyelectrolyte capsules as controls) based on silica, (DEXS/PARG), and (PSS/PAH) are shown in Figure 2. The images of the capsules as dried on TEM grids show that the silica capsules are rigid while the polyelectrolyte capsules folded on the TEM grid. The gold NP agglomerates are also visible in these images.

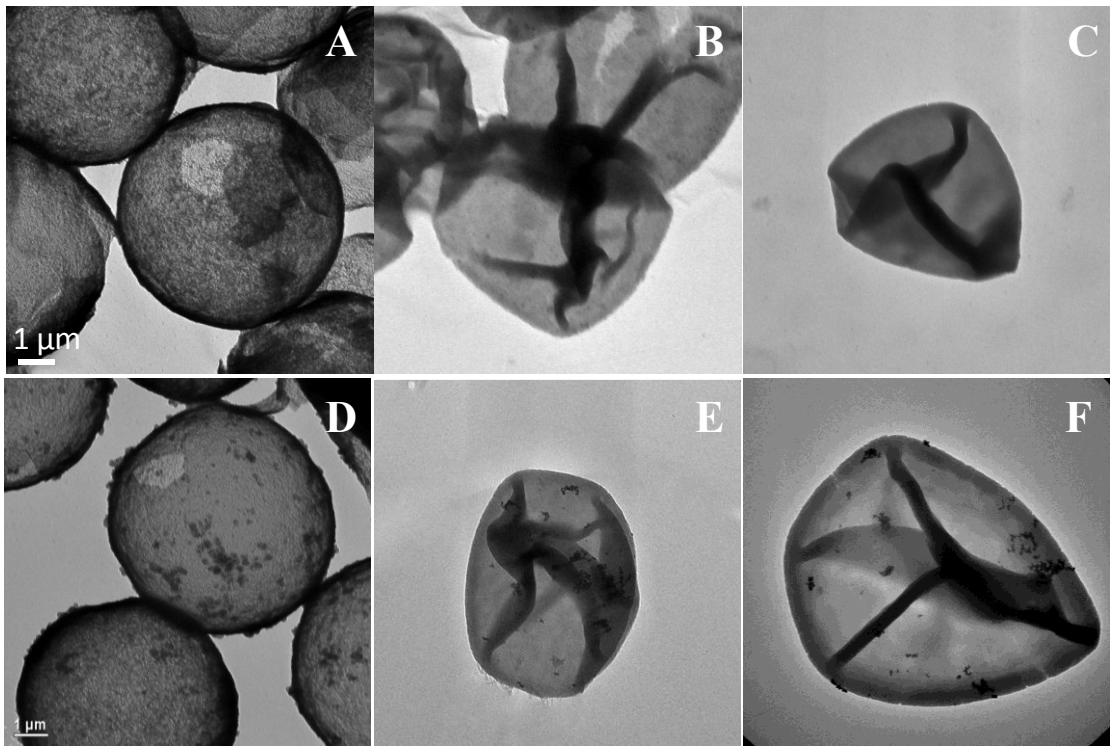

Figure 2. TEM images of the six different types of capsules: (A) 1-SiO_2, (B) 2-(DEXS/PARG), (C) 3-(PSS/PAH), (D) 1-Au-SiO_2, (E) 2-Au(DEXS/PARG), and 3-(PSS/PAH). All images were made with the same magnification. The scale bar corresponds to 1 µm.

The encapsulation of different molecules in the inner cavity of these silica capsules (*i.e.* 1-SiO_2 and 1-Au-SiO_2), was carried out in a similar way as the loading of polyelectrolyte multilayer (PEM) capsules made with similar $CaCO_3$ cores.[44,49] It is possible to encapsulate large molecules like proteins by their co-precipitation during the formation of $CaCO_3$. Due to the large size of such molecules they cannot

diffuse out of the capsule during the $CaCO_3$ dissolution by EDTA. Smaller molecules can be incorporated when the $CaCO_3$ particles contain polystyrene-block-poly(acrylic acid) (PS-b-PAA) micelles and the capsules are post-loaded after core dissolution, as reported by Tong *et al.*[45] The size of the capsules depends mainly on the size of the $CaCO_3$ template cores, and therefore capsules can be synthesized in a large range of sizes from typically 0.5 to 10 µm.[60,61] Figure 3 shows differently sized 1-SiO_2 and 1-Au-SiO_2 capsules (~3 and ~7 µm) loaded with a variety of molecules. The capsules were loaded with doxorubicin (DOX, 0.58 kDa) being an anti-cancer drug and the fluorescently labeled protein bovine serum albumin (BSA-FITC, 66 kDa), in order to demonstrate that molecules with different sizes and chemical properties can be easily incorporated within the silica cavity. The amount of encapsulated DOX was spectroscopically estimated for each capsule with a diameter of around 3 µm to be 0.6 - 2×10^9 molecules. More information about the loading of cargo molecules can be found in the Supplementary Information.

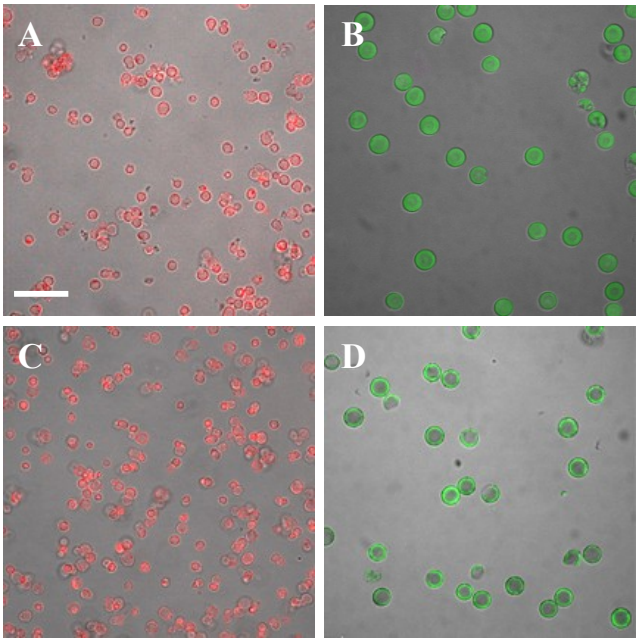

Figure 3. Confocal microscopy images of 1-SiO_2 capsules loaded with (A) doxorubicin hydrochloride (0.58 kDa) and (B) bovine serum albumin-FITC (~ 66 kDa). The size of the capsules was 3.1 ± 0.7 μm (A) and 7.1 ± 0.7 μm (B). (C) and (D) are confocal images of non-degradable 1-Au-SiO_2 capsules loaded with doxorubicin hydrochloride (3.2 ± 0.6 μm) and bovine serum albumin (7.3 ± 0.5 μm) respectively. The scale bar corresponds to 20 μm.

Degradation of Silica Capsules

In order to study the *in vitro* degradation of both types of silica capsules we employed labeled ovalbumine (DQ-OVA) (~ 45 kDa) as model of an inactive compound that is activated by enzymatic cleavage.[29,62] This molecule is composed of the protein ovalbumine labeled with green BODIPY dyes (excitation/emission maxima ~ 503 nm/512 nm). The dye molecules self-quench due to their close proximity within the protein. Upon enzymatic degradation by proteases the protein is cleaved into peptide fragments, self-quenching is revoked, and the green fluorescence emission rapidly increases.[63] DQ-OVA presents also red fluorescence at high concentrations. This has been explained by the formation of protein dimers that absorb light around 570 nm and emit light around 630 nm.[64,65] However, there are several dimer conformations whose fluorescence is different and therefore the ultimately observed red fluorescence intensity cannot be used to estimate the concentration of protein or dye. Nevertheless, the mixture of both fluorescence emissions (*i.e.* in the green and in the red) provides an indicator of the onset of the enzymatic degradation, since the capsules appear orange colored before uptake by the cells and yellowish after their internalization and intracellular degradation. The presence of only green fluorescence indicates that DQ-OVA has been degraded. As this involves a distance increase between the dyes the red fluorescence disappears over time. Figure 4 shows the gradual degradation of 1-SiO_2 and 1-Au-SiO_2 capsules loaded with DQ-OVA. These data clearly point out that the 1-SiO_2 capsules are intrinsically degradable, whereas the 1-Au-SiO_2 capsules (without light-

stimulation) are non-degradable, *i.e.* the proteolytic enzymes present in the lysosome cannot degrade the capsule walls and thus cannot reach the DQ-OVA. 1-SiO_2 capsules degraded spontaneously which resulted in the onset of green fluorescence. The biodistribution of the green fluorescent spots also indicates release of the peptide fragments originating from DQ-OVA out of the lysosomes in which the capsules reside. Confocal microscopy images recorded after 8h demonstrate the initial homogeneous distribution of the green fluorescent DQ-OVA fragments in the cytosol (additional data are shown in the Supplementary Information). The images acquired at later time points demonstrate granular intracellular distribution pattern of the green spots suggesting that the peptide fragments have been eventually enclosed in smaller intracellular vesicles (possibly exosomes). The fact that the nuclei were not stained at any time point indicates that the peptide fragments cannot cross the nuclear membrane. In contrast 1-Au-SiO_2 capsules showed no degradation or release during 80 hours of observation. The presence of 2 bilayers of non-degradable polyelectrolytes together with the Au NPs blocked the capsule degradation, which makes these capsules interesting for remotely controlled light-mediated drug release, in which no spontaneous but only triggered release occurs.

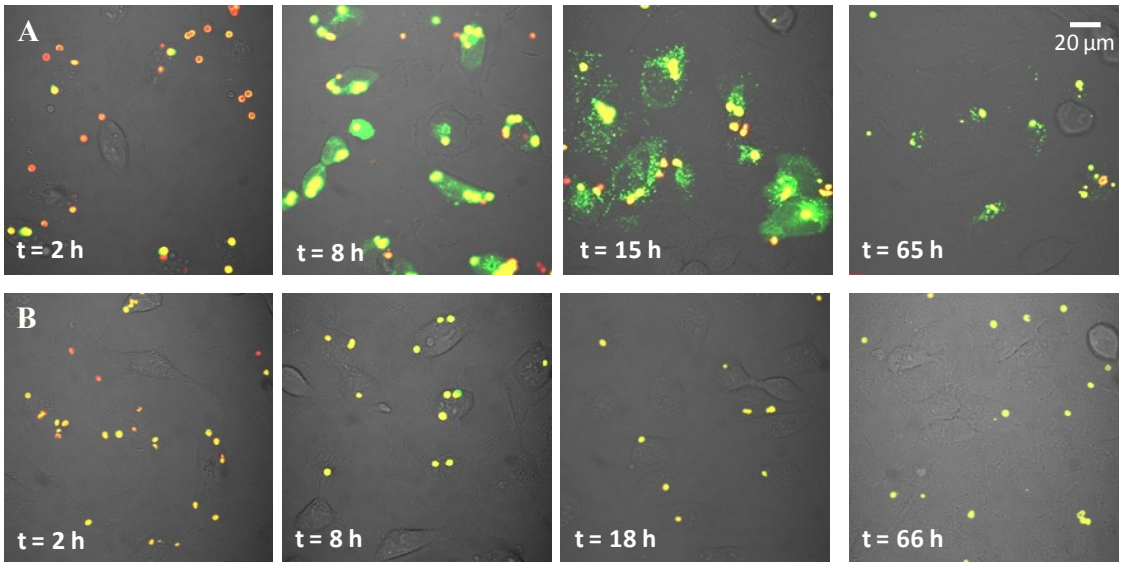

Figure 4. Degradation of internalized SiO_2 capsules in HeLa cells. (A) Degradable 1-SiO_2 capsules and (B) non-degradable 1-Au-SiO_2 capsules loaded with the fluorogenic protein DQ-OVA as cargo. Confocal images were taken at different time points after adding the capsules to the cells. An overlay of the red and green fluorescence and the transmission channels are presented. For additional information including 3D, we refer the reader to the Supplementary Information). The scale bar corresponds to 20 μm.

In order to compare the release of proteins from 1-SiO_2 and 1-Au-SiO_2 capsules and other carrier systems polyelectrolyte capsules were produced. Starting from the same $CaCO_3$ cores preloaded with DQ-OVA, six different types of capsules were produced: two based on silica (*i.e.* 1-SiO_2 and 1-Au-SiO_2), two based on degradable polyelectrolytes (*i.e.* 2-(DEXS/PARG) and (2-Au(DEXS/PARG)),[29] and two based on non-degradable polyelectrolytes (*i.e.* 3-(PSS/PAH) and 3-Au-(PSS/PAH)).[41] Figure 5 shows HeLa cells after 18 hours of incubation with the polyelectrolyte capsules used as control. Only 1-SiO_2 (Figure 5A in agreement with Figure 4A) and 2-(DEXS/PARG) capsules (Figure 5C) were degraded and released the cleaved DQ-OVA fragments. The released fragments in Figure 5C however seem to have a more granular intracellular distribution in comparison to the ones shown in Figure 5A, and thus release to the cytosol might be lower. Surprisingly, the degradable polyelectrolyte capsules based on DEXS and PARG containing Au NPs were not degraded within 80 h (Figure 5D). The TEM image of the capsules in Figure 2E demonstrates the low amount of embedded Au NPs, which apparently is already sufficient to block capsule degradation. This suggests that Au NPs in the capsule walls affect the degradation of the polyelectrolytes which otherwise would be enzymatically cleaved.[53] Whether this is due to deactivation of enzymatic activity upon the presences of Au NPs or due to physicochemical reasons remains a subject of future investigations. From our data also long-term degradation of these capsules cannot be excluded. In Figures 4B and 5B we observed that silica capsules containing Au NPs did not release the cleaved DQ-OVA fragments. In this case there were two reasons

why the capsule did not degrade: the presence of Au NPs and the employment of non-degradable polyelectrolytes (PSS and PAH).

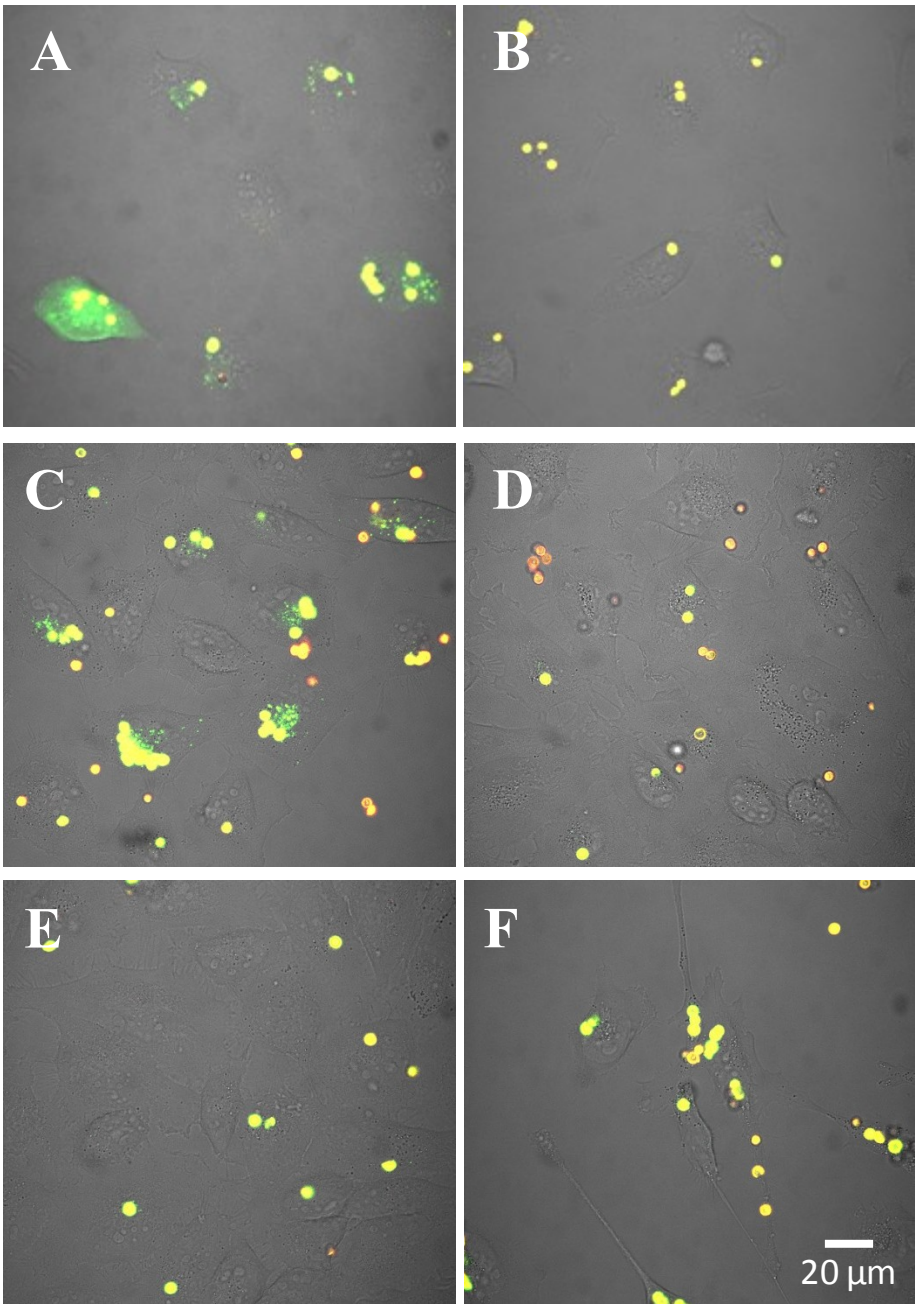

Figure 5. Confocal microscopy images demonstrating degradation of differently composed capsules incubated with HeLa cells for 18 h. All the capsules were loaded with the fluorescent protein DQ-OVA. (A) Degradable 1-SiO_2 capsules, (B) non-degradable 1-Au-SiO_2 capsules, (C) degradable 2-(DEXS/PARG) capsules, (D) 2-Au-

(DEXS/PARG) capsules, (E) non-degradable 3-(PSS/PAH) capsules, and (F) non-degradable 3-Au(PSS/PAH) capsules. The scale bar corresponds to 20 μm.

The kinetics of the DQ-OVA release from the six differently composed capsules were analyzed to compare their efficiency as delivery vehicles. The degradation of all types of capsules was studied by recording confocal images at different time points, starting immediately after adding the capsules to the cells (t = 0 h) and followed up to 80 h. From these images the different kinetics of DQ-OVA release were determined. In order to avoid erroneous results only cells which had internalized one single capsule were considered in this evaluation. As presented in Figure 6 1-SiO_2 and 2-(DEXS/PARG) capsules released the cleaved DQ-OVA fragments to the cytosol in less than 24 h. During this time the increase of fluorescence in the cytosol grew exponentially (see the inset in Figure 6). After that time, emission decreased slightly, probably due to the partial exocytosis of the cleaved protein fragments, or due to label dilution upon cell division. Release of cleaved DQ-OVA fragments was found to be slightly higher for 1-SiO_2 capsules than for the degradable polyelectrolyte capsules. In contrast, the mean fluorescence intensity (per cell) was constant for 1-Au-SiO_2, 2-Au(DEXS/PARG), 3-(PSS/PAH) and 3-Au(PSS/PAH) capsules, indicating that their cargo was not released. The error bars shown in Figure 6 are substantial because the cellular volume varies per cell.

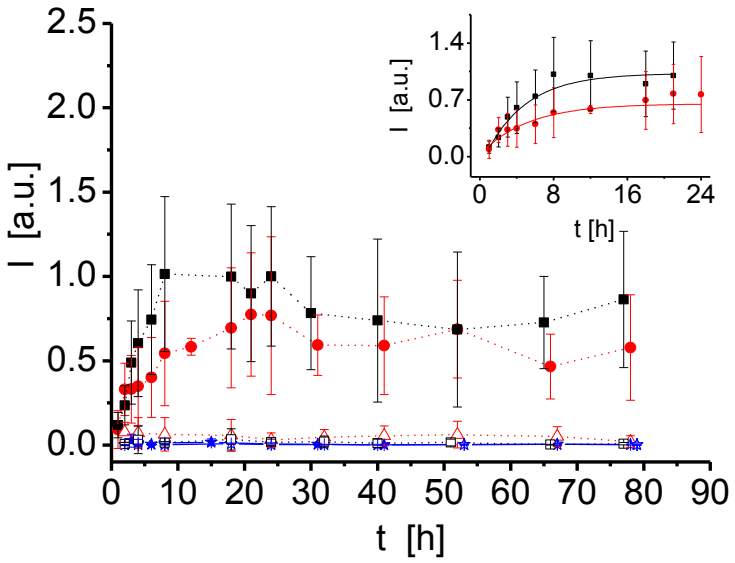

Figure 6. The mean fluorescence intensity of the enzymatically degraded DQ-OVA recorded over time. The increase in green fluorescence intensity per cell was evaluated only in those cells, which had internalized exactly one capsule. Dark squares correspond to the release from 1-SiO_2 and red circles to the release from 2-(DEXS/PARG) capsules. Blue stars, empty black squares, red triangles, and empty blue stars correspond to release from 3-(PSS/PAH), 1-Au-SiO_2, 2-Au-(DEXS/PARG), and 3-Au(PSS/PAH) capsules, respectively. It can be seen in the inset that only the data for the degradable capsules (1-SiO_2 and 2-(DEXS/PARG)) obtained within the first 10 h can be described with an exponential function $I(t)= I_0 + I_{max}(1-\exp(-k \cdot t))$. After around 10 h the curve reached a saturation level.

The cytosolic release of cargo encapsulated in silica capsules might be explained by the rupture of the lysosomes where capsules are eventually located after being internalized.[30,66] Similar phenomena were reported previously for other colloidal carrier systems.[67] A clear swelling of the lysosomes which contained the capsules could be seen, as presented in Figure 7. The membrane of the lysosomes acts as a non-permeable membrane for the proteins and the products of the capsule degradation that are released inside these compartments from 1-SiO_2 capsules upon their degradation. The large observed swelling is probably caused by the osmotic pressure established after the delivery of charged molecules that cannot

diffuse from this intracellular compartment. Most likely, water from the cytosol enters these compartments, which causes their swelling and final break. In consequence, the cleaved protein is delivered into the cytosol (*cf.* Figures 3 and 4). Because the capsules are internalized over time we observed this phenomenon during the first 32 h. Merdan *et al.* reported a similar process which resulted from the high osmotic pressure during the acidification of endosomes/lysosomes due to the presence of poly(ethylenimine) (PEI).[67]

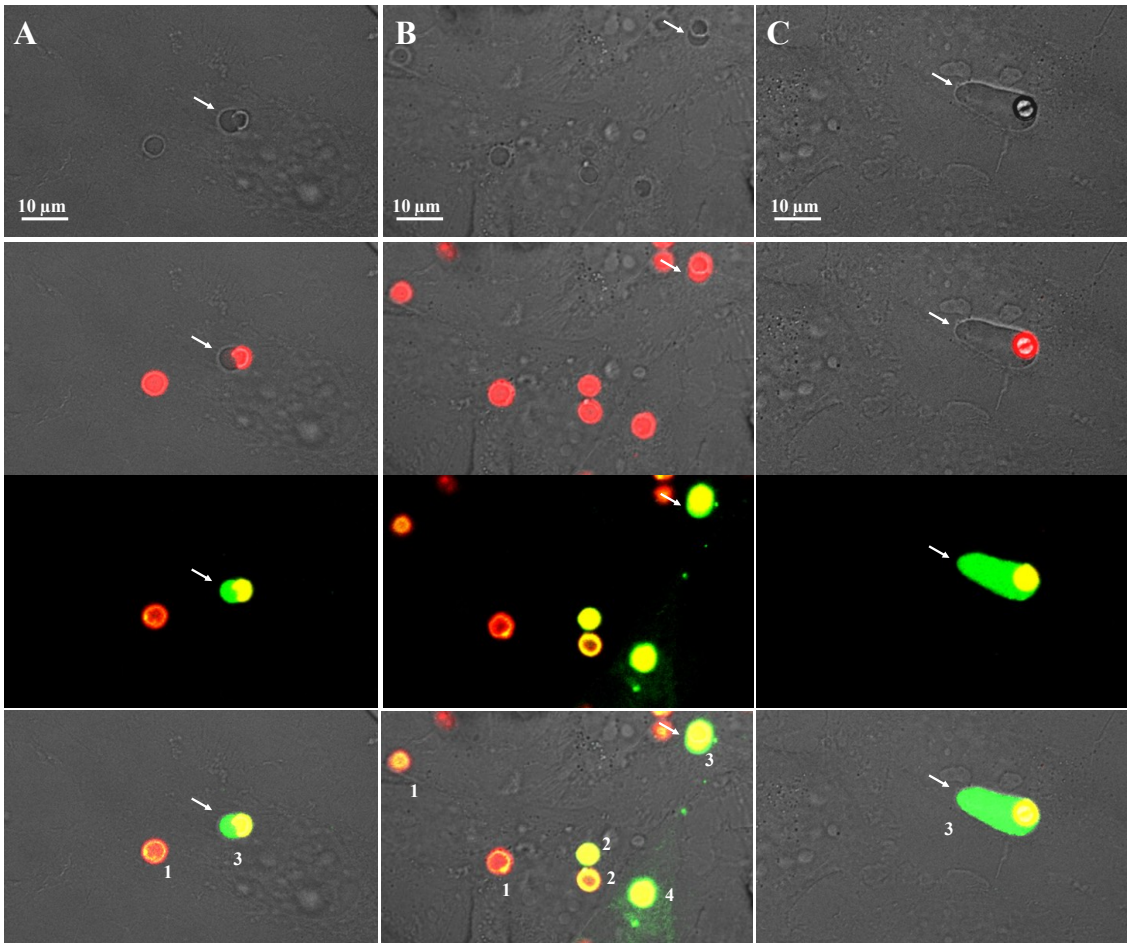

Figure 7. Confocal microscopy images demonstrating the swelling of the lysosomes upon the degradation of internalized 1-SiO_2 capsules loaded with DQ-OVA in HeLa cells. Images were taken after 2 h (A), 6 h (B) and 31 h (C). From top to bottom we show the transmission channel, the overlay of transmission and red fluorescent

channel, the overlay of red and green fluorescence channel, and finally, the overlay of transmission, red and green channels. The numbers indicate differently localized capsules: (1) Capsules that are not internalized, indicated by the red color of DQ-OVA and by their extracellular position. (2) Capsules that are localized in the lysosomes, as concluded from their intracellular position. (3) Capsules that are in swollen lysosomes, as indicated by their intracellular location and by the green color of DQ-OVA, which indicates enzymatic degradation. (4) Capsules that released the cleaved protein into the cytosol visualized by the green fluorescence distributed over the cell. The arrows indicate the swollen lysosomes. The size of the scale bars corresponds to 10 μm.

The reason why the silica capsules are degraded inside the lysosome is likely related to the presence of mPEG-SH on the surface on the $CaCO_3$ template cores which had been used for the assembly of the silica shell. To verify this we prepared capsules with PVP (10 kDa) instead of mPEG-SH as stabilizing agent and also loaded them with DQ-OVA. Only in a few cases a slight release was observed (data shown in the Supplementary Information). This indicates that mPEG-SH plays a roll not only in the formation of a smooth and homogeneous silica shell but also in the degradation mechanism.

It has been reported that amorphous silica dissolves due to the following overall reaction.[68]

$$SiO_{2\,(s)} + 2H_2O \rightarrow H_4SiO_{4\,(aq)} \qquad (1)$$

Therefore, we performed experiments in aqueous solution to study the parameters which may affect the degradation process. For simplicity we produced capsules loaded with dextran covalently bound to tetramethyl rhodamine isothiocyanate (TRICT). TRICT is not pH sensitive and has a high fluorescent intensity (see the Supporting Information).[69,70] We used the co-precipitation method to encapsulate 155 kDa dextran-TRICT (excitation/emission maxima ~ 557 nm/576 nm) in 1-SiO_2 and 1-Au-SiO_2 capsules. We used conditions mimicking the lysosome, namely acidic pH and the presence of hydrolytic enzymes. Both types of capsules were incubated in phosphate buffered saline (PBS) at pH 7.3 and 4.0. The effect

of the enzymes was studied by employing pronase (2 mg/mL in PBS at pH 7.3) which is a mixture of proteases (the maximum enzyme activity is at pH 6.0 - 7.5 and working concentration 0.5 - 2 mg/mL).[71] Capsules were incubated at 37 ºC for at least 50 h and the degradation was continuously monitored by recording spectra of the free dextran-TRICT release with a fluorometer. As shown in Figure 8 only the 1-SiO_2 capsules were degraded considerably, leading to release of dextran-TRICT. The presence of proteases caused slightly higher degrees of degradation. The degradation process was much more efficient at pH 7.3 than at pH 4. These results suggest that the presence of the enzymes may increase the capsule dissolution by degrading the PARG that is on the surface of the silica capsules. As expected, capsules containing Au NPs in the shell (1-Au-SiO_2) were not degraded. These results are in agreement with previously reported data about the dissolution of biogenic and synthetic colloidal silica at alkaline pH values,[68] and with our *in vitro* data (*cf.* Figure 5). Since the 1-SiO_2 capsules are more readily degraded at alkaline pH we speculate that the degradation of the silica shell starts already in the (slightly alkaline to neutral) cell medium. Thus, once the capsules are present in acidic intracellular vesicles, which pH is further reduced with time, the protease enzymes present in these compartments help to finally release the content of the capsules. As also the ionic strength and the nature of the ions could affect the dissolution of the shell we performed experiments with Tris-buffered saline at pH 7.6 and 4.4 and obtained similar results (*cf.* the data shown in the Supporting Information. Interestingly, we also observed that low temperatures (*e.g.*, 4 ºC) may decrease the degradation of 1-SiO_2.

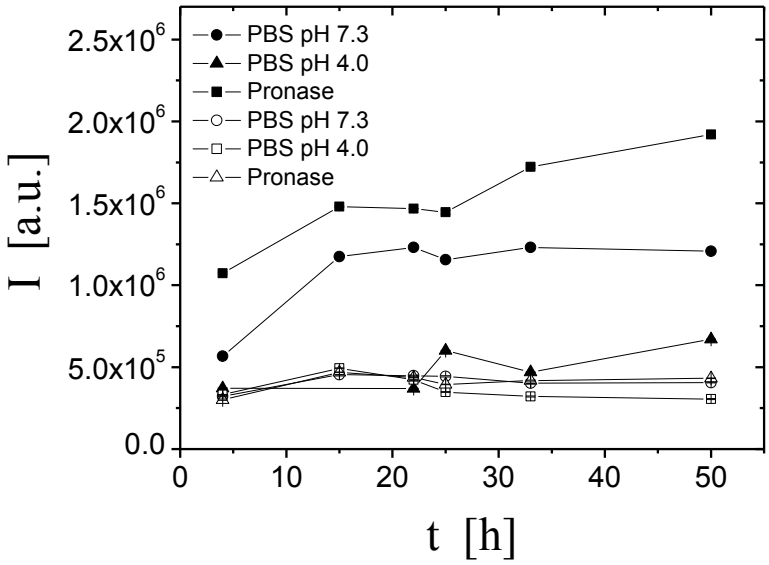

Figure 8. Degradation of silica capsules at 37 ºC. Fluorescent intensity I of free dextran-TRICT in solution which has been released from silica based capsules in different buffer solutions. Solid symbols correspond to 1-SiO_2 capsules in (•) PBS at pH 7.3, (▲) PBS at pH 4.0, and (■) pronase (2 mg/mL) in PBS at pH 7.3. Empty symbols correspond to 1-Au-SiO_2 capsules in (○) PBS at pH 7.3, (Δ) PBS at pH 4.0, and (□) pronase (2 mg/mL) in PBS at pH 7.3.

Release of messenger RNA from 1-SiO_2 capsules

The Stöber silica coating used to produce the degradable 1-SiO_2 capsules could be potentially harmful for the activity of some encapsulated biological molecules, since the hydrolysis of TEOS is carried out in an ammonia solution using a mixture of ethanol and water as a solvent. In order to determine if biologically active molecules retain their activity upon encapsulation we produced 1-SiO_2 capsules loaded with messenger RNA (mRNA) encoding green fluorescent protein (GFP). Therapies based on mRNA transfection are of high interest because, in contrast to plasmid DNA-based approaches, they do not introduce genetic modifications. Moreover, to be active mRNA does not need to enter the nucleus, and thus circumvents a serious obstacle that is encountered by the use of plasmid DNA.[40,72] In this set of

experiments, the PARG used as the outer layer was covalently labeled with Dy634 (excitation/emission maxima ~ 635 nm/658 nm). This enabled us to visualize the location of the capsule shell respect to the position of the synthesized GFP upon delivery of mRNA into the cytosol. Figure 9 shows HeLa cells with an intense green fluorescence spread all over the cytosol. This indicates that GFP was synthesized upon release of the mRNA from the capsule and from the lysosome in which the capsules were located after being internalized. The delivery of mRNA encoding GFP was also studied with another cell line (MDA-MB-231), yielding similar results (data shown in the Supplementary Information). The red fluorescence originating from the capsule shell decreased in time. This indicates that capsules were degraded and the parts of the shell carrying the red dye were diluted into the cytosol beyond the detection limit. Thus, 1-SiO_2 capsules represent a good alternative for mRNA delivery compared to polymers, such as PEI, that might bind mRNA too strongly to permit its translation in the cytosol.[40]

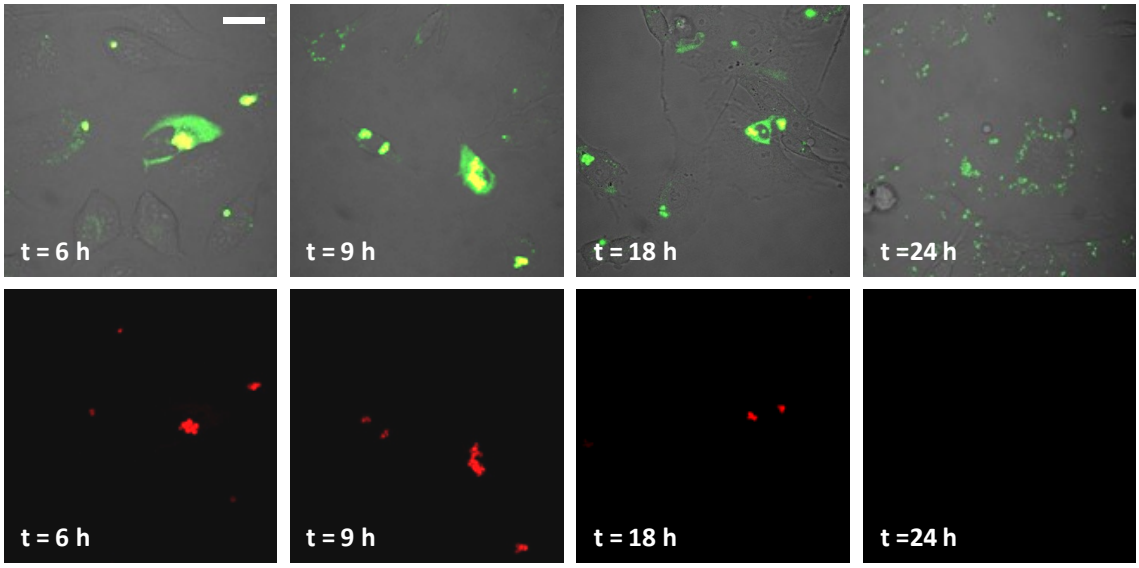

Figure 9. Fluorescence distribution in HeLa cells incubated with degradable 1-SiO_2-Dy634 capsules loaded with mRNA encoding GFP. The 1-SiO_2 capsules were also labeled with Dy634. The top images correspond to the overlay of the green (GFP), red (Dy634 labeled PARG) fluorescence and transmission

channels. The presence of GFP in the cytosol, due to the delivery of mRNA, could be detected already after 6 h. The scale bar corresponds to 10 μm.

Light-induced Delivery into the Cytosol

We evaluated the possibility to release cargo molecules from silica capsules containing Au NPs within their walls (*i.e.* 1-Au-SiO_2) and compared it with the light-mediated release from polyelectrolyte capsules.[41]. The capsules were loaded with seminaphtharhodafluor-dextran (SNARF-dextran). It is worth mentioning that several light-addressable materials based on silica have been already reported. Katagiri *et al.* produced hybrid capsules based on polyelectrolytes, lipids, SiO_2, and TiO_2, where controlled release was demonstrated in solution upon UV-light irradiation.[73] Recently, mesoporous silica particles functionalized with the photosensitive molecule spiropyran have also been used to demonstrate *in vitro* release of a dye following irradiation with 365 nm UV-light.[74] It should be mentioned, however, that since hemoglobin absorbs strongly light in the UV-Vis range,[75] particles or capsules having components that absorb light in the infrared (IR) region have more potential to be employed in future *in vivo* applications, such as remote controlled release or hyperthermia.[76-78] Therefore, an IR laser (830 nm) was employed in our experiments.

SNARF is a ratiometric pH indicator widely used for biological applications.[79,80] It is characterized by two emission bands at two different wavelengths which respective intensities depend on the pH value of the (local) environment.[81] In acidic environments SNARF has a yellowish emission (at 583 nm) while at alkaline pH, intensity shifts towards the red emission peak (at 627 nm). Thus, SNARF is a very useful tool to sense pH in different intracellular compartments.[82,83] After intracellular uptake encapsulated SNARF is located in lysosomes,[30] which are acidic.[84] When SNARF is released (*e.g.* upon light-

mediated heating) into the (neutral) cytosol this can be observed by a change in its emission color.[41] Here, we studied the possibility to release SNARF from 1-Au-SiO_2 capsules in a remote way *via* light illumination (with a power density around 3.5 $\mu W/\mu m^2$ for few seconds). Figure 10 shows that upon laser irradiation only capsules that had been irradiated changed their fluorescence emission, whereas non-irradiated capsules kept their fluorescence emission. This demonstrates that only the lysosome where the capsule was located had been permeabilized upon local heat-generation, which resulted in a change in the environment of the SNARF from acidic to alkaline pH. Only the cells where one capsule was opened showed red emission spreading along the cytosol, but other cells that had not been illuminated remained unaffected. These experiments demonstrate that photothermal release of encapsulated molecules from 1-Au-SiO_2 capsules to the cytosol is as efficient as the remote controlled release from polyelectrolyte capsules (2-Au(DEXS/PARG) and 3-Au(PSS/PAH)) that has been reported in previous work.[38] Although the opening mechanism was not studied in detail, pre-existing structural defects in the silica capsule may play a role in the opening upon local heat production.

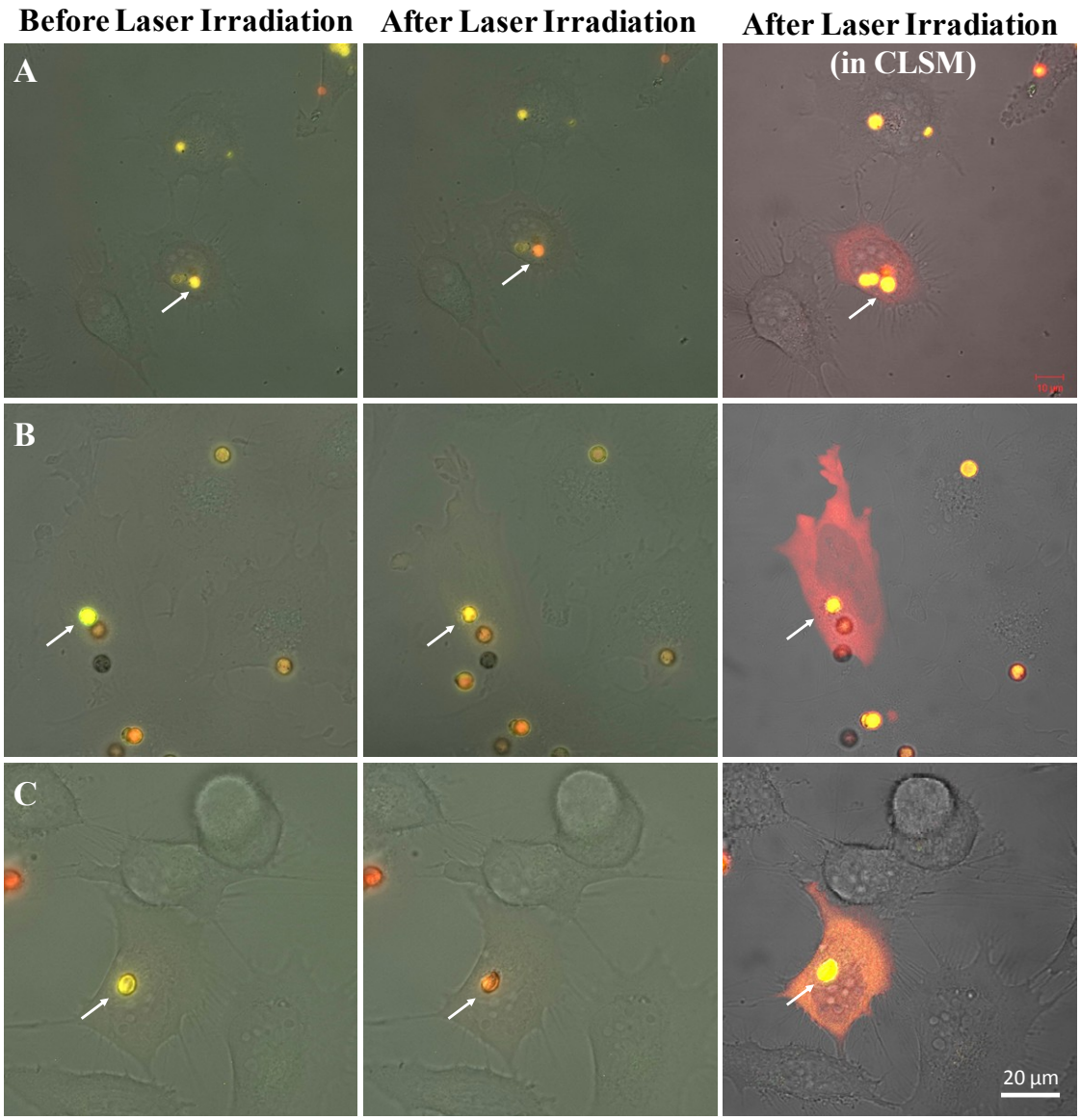

Figure 10. Capsule opening and subsequent cytosolic release of encapsulated 10 kDa SNARF-dextran upon light-mediated heating of Au NPs present in the capsule shell. (A) 1-Au-SiO_2 capsules, (B) 2-Au(DEXS/PARG) capsules, and (C) 3-Au(PSS/PAH) capsules. Confocal laser scanning microscopy (CLSM) was used to obtain clear images of the homogeneous cytosolic release of SNARF-dextran (images on the right) in HeLa cells. The irradiated (3.5 µW/µm^2 for a few seconds) capsule changed its fluorescence emission (from yellowish to orange-red) due to the pH change upon the permeation of the acidic compartment where it resided before illumination to the neutral cytosolic pH after irradiation. All images were acquired with the same magnification. The scale bar corresponds to 20 µm.

By using calibration curves as obtained in solutions potassium rich buffers and nigericin[55] the pH of capsules incorporated by cells before and after irradiation was estimated (*cf.* Supplementary Information). The results are shown in Table 1. The data clearly show the transition from an acidic (lysosome) to a slightly alkaline / neutral environment (cytosol) upon light-mediated release, in agreement to a previous reported for Au(PSS/PAH) capsules.[41]

	Before IR radiation	After IR radiation
1-Au-SiO_2	6.0 ± 1.1	8.0 ± 0.5
2-Au(DEXS/PARG)	< 6.5	7.8 ± 0.2
3-Au(PSS/PAH)	6.6 ± 0.5	7.9 ± 0.4

Table 1. Estimated pH values of capsules before and after opening of the silica capsules containing Au NPs with the calibration curve obtained with potassium rich buffers and nigericin.

Cytotoxicity of Silica Capsules

We studied viability of two different cell lines in the presence of different concentrations of (empty) capsules by employing a Resazurin assay (excitation/emission maxima ~ 560 nm/590 nm)[85,86]. By using empty capsules (*i.e.* without encapsulated molecular cargo) any potential spectral overlap of the cargo with the dye resazurin could be avoided and any observed change in viability would only be due to the shell composition, and not due to possible effects of the encapsulated cargo. The amount of capsules which were added *per* cell varied from 5 to 50 (5 capsules/cell was the concentration which was used for all the rest of experiments reported in this work). HeLa and MDA-MB-231 cell lines were incubated

with 5, 10, 25, and 50 capsules/cell for 24 h and then viability was assessed. Figure 11 shows that 1-SiO_2 and 1-Au-SiO_2 capsules have similar toxicity compared with LbL capsules. Reduction of viability in HeLa cells is negligible for the used concentrations. In MDA-MB-231 cells a reduction in viability for concentrations above 25 capsules/cell was found. Figure 11 B,C shows similar results obtained for 2-(DEXS/PARG), 2-Au(DEXS/PARG), 3-(PSS/PAH), and 3-Au(PSS/PAH) capsules. These results indicate that SiO_2 based capsules show similar toxicity as capsules based on degradable or synthetic polyelectrolytes.[87,88]

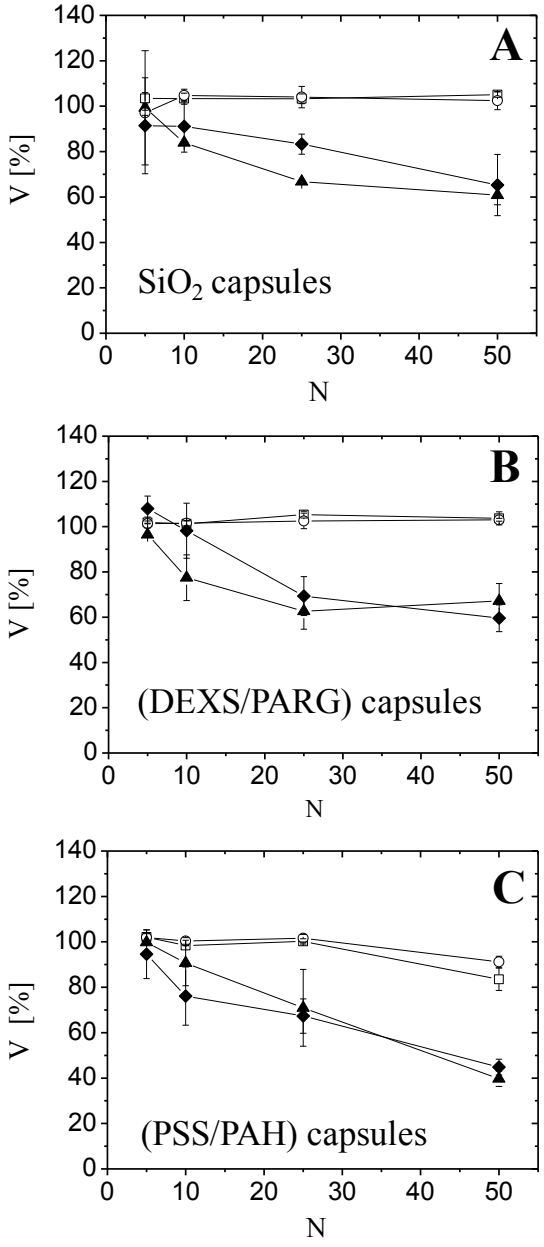

Figure 11. Viability of empty capsules as determined with a Resazurin assay for the six different types of capsules in HeLa cells (empty symbols: □, ○) and MDA-MB-231 cells (black symbols: ♦, ▲). Cells were incubated for 24 h with (A) 1-SiO_2 (□,♦), and 1-Au-SiO_2 (○, ▲), (B) 2-(DEXS/PARG) (□,♦) and 2-Au(DEXS/PARG) (○, ▲), and (C) 3-(PSS/PAH) (□,♦) and 3-Au(PSS/PAH) (○, ▲) capsules. V represents the percentage of viable cells and N the number of capsules that have been added per cell.

Conclusions

Silica capsules produced on $CaCO_3$ template particles can be used as efficient carrier systems for different molecules ranging from cancer drugs such as doxorubicin (0.58 kDa) to mRNA (~1000 kDa). The cargo molecules can be released in the cytosol as a result of silica capsule degradation and osmotic swelling of the lysosomes. We have shown that the silica shell is degraded *via* hydrolysis and that the rate of degradation is increased at alkaline pH. The presence of proteases can also increase the rate of degradation by cleaving the outer layer of poly-L-arginine present on the SiO_2 surface. We have demonstrated that degradable silica capsules are suitable to deliver intact mRNA (mGFP) able to serve as a template for the synthesis of proteins in the cytosol. Moreover, we showed that it is possible to form non-degradable and light-responsive silica shells by the addition of agglomerates of Au NPs. We delivered a pH sensor *via* IR light-triggered release into the cytosol, with similar efficiencies as reported for polyelectrolyte capsules.[41] Viability studies showed that the toxicity of silica capsules (with and without Au NPs) is similar to that of degradable polyelectrolyte capsules. The easy synthesis process, feasibility to be loaded with different molecules and NPs (within the hollow cavity and in/on the surface) and non-toxic products of silica capsule degradation make them an interesting system for drug delivery.

Acknowledgments

This work was supported by the Loewe project Synbiochem (grant to WJP). XY acknowledges a Chinese government scholarship (CSC).

References

(1) Halas, N. J. *ACS Nano* 2008, *2*, 179-183.

(2) Joo, S. H.; Park, J. Y.; Tsung, C.-K.; Yamada, Y.; Yang, P.; Somorjai, G. A. *Nat. Mater.* 2009, *8*, 126-131.

(3) (a) Sanles-Sobrido, M.; Exner, W.; Rodriguez-Lorenzo, L.; Rodriguez-Gonzalez, B.; Correa-Duarte, M. A.; Alvarez-Puebla, R. A.; Liz-Marzan, L. M. *J. Am. Chem. Soc.* 2009 *131*, 2699-2705. (b) Vazquez-Vazquez, C.; Vaz, B.; Giannini, V.; Perez-Lorenzo, M.; Alvarez-Puebla, R. A.; Correa-Duarte, M. A. *J. Am. Chem. Soc.* 2013, *135*, 13616-13619.

(4) Hwang, D. W.; Ko, H. Y.; Kim, S.-K.; Kim, D.; Lee, D. S.; Kim, S. *Chem.--Eur. J.* 2009, *15*, 9387-93.

(5) (a) Schlossbauer, A.; Schaffer, D.; Kecht, J.; Wagner, E.; Bein, T. *J. Am. Chem. Soc.* 2008, *130*, 12558-9. (b) Schlossbauer, A.; Dohmen, C.; Schaffer, D.; Wagner, E.; Bein, T. *Angew. Chem., Int. Ed.* 2011, *50,* 6828

(6) (a) Du , L.; Liao, S.; Khatib, H. A.; Stoddart, F.; Zink, J. I. *J. Am. Chem. Soc.* 2009, *131*, 15136-15142. (b) Xia, T.; Kovochich, M.; Liong, M.; Meng, H.; Kabehie, S.; George, S.; Zink, J. I.; Nel, A. E. *ACS Nano* 2009, *3*, 3273-3286.

(7) Ferrag, F.; Hadjadj-Aoul, O.; Belkadi, M.; Talamali, R.; Canselier, J. P. *Phys. Chem. News* 2006, *27*, 118-123.

(8) Villota, R.; Hawkes, J. G. *Crit. Rev. Food Sci. Nutr.* 1986, *23*, 289-321.

(9) Liong, M.; Lu, J.; Kovochich, M.; Xia, T.; Ruehm, S. G.; Nel, A. E.; Tamanoi, F.; Zink, J. I. *ACS Nano* 2008, *2*, 889-896.

(10) Li, Z.; Barnes, J. C.; Bosoy, A.; Stoddart, J. F.; Zink, J. I. *Chem. Soc. Rev.* 2012, *41*, 2590-2605.

(11) Wu, S.-H.; Hung, Y.; Mou, C.-Y. *Chem. Commun.* 2011, *47*, 9972-9985.

(12) Fuller, J. E.; Zugates, G. T.; Ferreira, L. S.; Ow, H. S.; Nguyen, N. N.; Wiesner, U. B.; Langer, R. S. *Biomaterials* 2008, *29*, 1526-32.

(13) Delle Piane, M.; Corno, M.; Ugliengo, P. *J. Chem. Theory Comput.* 2013, *9*, 2404-2415.

(14) Guo, J.; Yang, W.; Wang, C.; He, J.; Chen, J. *Chem. Mater.* 2006, *18*, 5554-5562.

(15) Yang, Q.; Wang, S.; Fan, P.; Wang, L.; Di, Y.; Lin, K.; Xiao, F.-S. *Chem. Mater.* 2005, *17*, 5999-6003.

(16) Aznar, E.; Marcos, M. D.; Martinez-Manez, R.; Sancenon, F.; Soto, J.; Amoros, P.; Guillem, C. *J. Am. Chem. Soc.* 2009, *131*, 6833-6843.

(17) Zhang, H.; Shahbazi, M.-A.; Makila, E. M.; da Silva, T. H.; Reis, R. L.; Salonen, J. J.; Hirvonen, J. T.; Santos, H. A. *Biomaterials* 2013, *34*, 9210-9219.

(18) Huo, Q.; Liu, J.; Wang, L.-Q.; Jiang, Y.; Lambert, T. N.; Fang, E. *J. Am. Chem. Soc.* 2006, *128*, 6447-6453.

(19) Zhu, C.-L.; Song, X.-Y.; Zhou, W.-H.; Yang, H.-H.; Wen, Y.-H.; Wang, X.-R. *J. Mater. Chem.* 2009, *19*, 7765-7770.

(20) Cauda, V.; Schlossbauer, A.; Bein, T. *Microporous Mesoporous Mater.* 2010, *132*, 60-71.

(21) Sripanyakorn, S.; Jugdaohsingh, R.; Dissayabutr, W.; Anderson, S. H. C.; Thompson, R. P. H.; Powell, J. J. *Br. J. Nutr.* 2009, *102*, 825-834.

(22) Pohaku Mitchell, K. K.; Liberman, A.; Kummel, A. C.; Trogler, W. C. *J. Am. Chem. Soc.* 2012, *134*, 13997-14003.

(23) Chen, K.; Zhang, J.; Gu, H. *J. Mater. Chem.* 2012, *22*, 22005-22012.

(24) Radin, S.; El-Bassyouni, G.; Vresilovic, E. J.; Schepers, E.; Ducheyne, P. *Biomaterials* 2005, *26*, 1043-1052.

(25) He, Q.; Shi, J.; Zhu, M.; Chen, Y.; Chen, F. *Microporous Mesoporous Mater.* 2009, *131*, 314-320.

(26) Li, X.; Zhang, L.; Dong, X.; Liang, J.; Shi, J. *Microporous Mesoporous Mater.* 2007, *102*, 151-158.

(27) Kazakova, L. I.; Shabarchina, L. I.; Sukhorukov, G. B. *Phys. Chem. Chem. Phys.* 2011, *13*, 11110.

(28) Ochs, M.; Carregal-Romero, S.; Rejman, J.; Braeckmans, K.; De Smedt, S. C.; Parak, W. J. *Angew. Chem., Int. Ed.* 2013, *52*, 695-699

(29) Rivera_Gil, P.; Koker, S. D.; De_Geest, B. G.; Parak, W. J. *Nano Lett.* 2009, *9*, 4398-4402.

(30) Kastl, L.; Sasse, D.; Wulf, V.; Hartmann, R.; Mircheski, J.; Ranke, C.; Carregal-Romero, S.; Martínez-López, J. A.; Fernández-Chacón, R.; Parak, W. J.; Elsaesser, H.-P.; Rivera Gil, P. *ACS Nano* 2013, *7*, 6605-6618

(31) Hrelescu, C.; Stehr, J.; Ringler, M.; Sperling, R. A.; Parak, W. J.; Klar, T. A.; Feldmann, J. *J. Phys. Chem. C* 2010, *114*, 7401-7411.

(32) Hühn, D.; Govorov, A.; Rivera Gil, P.; Parak, W. J. *Adv. Funct. Mater.* 2012, *22*, 294-303.

(33) Huang, J.; Jackson, K. S.; Murphy, C. J. *Nano Lett.* 2012, *12*, 2982-2987.

(34) Huschka, R.; Barhoumi, A.; Liu, Q.; Roth, J. A.; Ji, L.; Halas, N. J. *ACS Nano* 2012, *6*, 7681-7691.

(35) Agarwal, A.; MacKey, M. A.; El-Sayed, M. A.; Bellamkonda, R. V. *ACS Nano* 2011, *5*, 4919-4926.

(36) Skirtach, A. G.; Javier, A. M.; Kreft, O.; Köhler, K.; Alberola, A. P.; Möhwald, H.; Parak, W. J.; Sukhorukov, G. B. *Angew. Chem., Int. Ed.* 2006, *45*, 4612-4617.

(37) Radt, B.; Smith, T. A.; Caruso, F. *Adv. Mater.* 2004, *16*, 2184-2189.

(38) Muñoz Javier, A.; del Pino, P.; Bedard, M. F.; Skirtach, A. G.; Ho, D.; Sukhorukov, G. B.; Plank, C.; Parak, W. J. *Langmuir* 2008, *24*, 12517-12520.

(39) Palankar, R.; Skirtach, A. G.; Kreft, O.; Bedard, M.; Garstka, M.; Gould, K.; Möhwald, H.; Sukhorukov, G. B.; Winterhalter, M.; Springer, S. *Small* 2009, *5*, 2168-2176.

(40) Rejman, J.; Tavernier, G.; Bavarsad, N.; Demeester, J.; De Smedt, S. C. *J. Controlled Release* 2010, *147*, 385-91.

(41) Carregal-Romero, S.; Ochs, M.; Rivera Gil, P.; Ganas, C.; Pavlov, A. M.; Sukhorukov, G. B.; Parak, W. J. *J. Controlled Release* 2012, *159*, 120-127.

(42) Sukhorukov, G. B.; Volodkin, D. V.; Günther, A. M.; Petrov, A. I.; Shenoy, D. B.; Möhwald, H. *J. Mater. Chem.* 2004, *14*, 2073-2081.

(43) She, Z.; Antipina, M. N.; Li, J.; Sukhorukov, G. B. *Biomacromolecules* 2010, *11*, 1241-7.

(44) Petrov, A. P.; Volodkin, D. V.; Sukhorukov, G. B. *Biotechnol. Prog.* 2005, *21*, 918-925.

(45) Tong, W.; Zhu, Y.; Wang, Z.; Gao, C.; Möhwald, H. *Macromol. Rapid Commun* 2010, *31*, 1015-9.

(46) Fernandez-Lopez, C.; Mateo-Mateo, C.; Alvarez-Puebla, R. A.; Perez-Juste, J.; Pastoriza-Santos, I.; Liz-Marzan, L. M. *Langmuir* 2009, *25*, 13894-13899.

(47) Volodkin, D. V.; Larionova, N. I.; Sukhorukov, G. B. *Biomacromolecules* 2004, *5*, 1962-1972.

(48) Abbasi, A. Z.; Gutierrez, L.; del Mercato, L. L.; Herranz, F.; Chubykalo-Fesenko, O.; Veintemillas-Verdaguer, S.; Parak, W. J.; Morales, M. P.; Gonzalez, J. M.; Hernando, A.; de la Presa, P. *J. Phys. Chem. C* 2011, *115*, 6257-6264.

(49) del Mercato, L. L.; Abbasi, A. Z.; Parak, W. J. *Small* 2011, *7*, 351-363.

(50) Sukhorukov, G. B.; Donath, E.; Davis, S.; Lichtenfeld, H.; Caruso, F.; Popov, V. I.; Möhwald, H. *Polym. Adv. Technol.* 1998, *9*, 759-767.

(51) Donath, E.; Sukhorukov, G. B.; Caruso, F.; Möhwald, H. *Angew. Chem., Int. Ed.* 1998, *37*, 2202-2205.

(52) De_Geest, B. G.; Vandenbroucke, R. E.; Guenther, A. M.; Sukhorukov, G. B.; Hennink, W. E.; Sanders, N. N.; Demeester, J.; Smedt, S. C. *Adv. Mater.* 2006, *18*, 1005-1009.

(53) De Koker, S.; De Geest, B. G.; Cuvelier, C.; Ferdinande, L.; Deckers, W.; Hennink, W. E.; De Smedt, S.; Mertens, N. *Adv. Funct. Mater.* 2007, *17*, 3754-3763.

(54) Köhler, K.; Sukhorukov, G. B. *Adv. Funct. Mater.* 2007, *17*, 2053-2061.

(55) Bond, J.; Varley, J. *Cytometry, Part A* 2005, *64A*, 43-50.

(56) O'Brien, J.; Wilson, I.; Ortaon, T.; Pognan, F. *Toxicology* 2001, *164*, 132-132.

(57) Stöber, W.; Fink, A.; Bohn, E. *J. Colloid Interface Sci.* 1968, *26*, 62.

(58) Guerrero-Martinez, A.; Perez-Juste, J.; Liz-Marzan, L. M. *Adv. Mater.* 2012, *22*, 1182-1195.

(59) Muñoz Javier, A.; Kreft, O.; Piera Alberola, A.; Kirchner, C.; Zebli, B.; Susha, A. S.; Horn, E.; Kempter, S.; Skirtach, A. G.; Rogach, A. L.; Rädler, J.; Sukhorukov, G. B.; Benoit, M.; Parak, W. J. *Small* 2006, *2*, 394-400.

(60) Imai, H.; Tochimoto, N.; Nishino, Y.; Takezawa, Y.; Oaki, Y. *Cryst. Growth Des.* 2012, *12*, 876-882.

(61) Wang, Y.; Moo, Y. X.; Chen, C.; Gunawan, P.; Xu, R. *J. Colloid Interface Sci.* 2010, *352*, 393-400.

(62) Chanana, M.; Rivera Gil, P.; Correa-Duarte, M. A.; Parak, W. J.; Liz-Marzán, L. M. *Angew. Chem., Int. Ed.* 2013, *52*, 4179-4183.

(63) Mansour, M. K.; Latz, E.; Levitz, S. M. *J. Immunol.* 2006, *176*, 3053-3061.

(64) Bergstroem, F.; Mikhalyov, I.; Haeggloef, P.; Wortmann, R.; Ny, T.; Johansson, L. B. A. *J. Am. Chem. Soc.* 2002, *124*, 196-204.

(65) Mikhalyov, I.; Gretskaya, N.; Bergstroem, F.; Johansson, L. B. A. *Phys. Chem. Chem. Phys.* 2002, *4*, 5663-5670.

(66) Muñoz_Javier, A.; Kreft, O.; Semmling, M.; Kempter, S.; Skirtach, A. G.; Bruns, O.; Pino, P. d.; Bedard, M. F.; Rädler, J.; Käs, J.; Plank, C.; Sukhorukov, G.; Parak, W. J. *Adv. Mater.* 2008, *20*, 4281-4287.

(67) Merdan, T.; Kunath, K.; Fischer, D.; Kopecek, J.; Kissel, T. *Pharm. Res.* 2002, *19*, 140-146.

(68) Dove, P. M.; Han, N.; Wallace, A. F.; De Yoreo, J. J. *Proc. Natl. Acad. Sci. U. S. A.* 2008, *105*, 9903-9908.

(69) Geisow, M. J. *Exp. Cell Res.* 1984, *150*, 29-35.

(70) Kenmoku, S.; Urano, Y.; Kojima, H.; Nagano, T. *J. Am. Chem. Soc.* 2007, *129*, 7313-7318.

(71) https://www.roche-applied-science.com

(72) Rejman, J.; Bragonzi, A.; Conese, M. *Mol. Ther.* 2005, *12*, 468-474.

(73) Katagiri, K.; Koumoto, K.; Iseya, S.; Sakai, M.; Matsuda, A.; Caruso, F. *Chem. Mater.* 2009, *21*, 195-197.

(74) Chen, L.; Wang, W.; Su, B.; Wen, Y.; Li, C.; Zhou, Y.; Li, M.; Shi, X.; Du, H.; Song, Y.; Jiang, L. *ACS Nano* 2014, *8*, 744-751.

(75) Weissleder, R.; Mahmood, U. *Radiology* 2001, *219*, 316-333.

(76) Jain, P. K.; Huang, X. H.; El-Sayed, I. H.; El-Sayed, M. A. *Acc. Chem. Res.* 2008, *41*, 1578-1586.

(77) (a) Huschka, R.; Zuloaga, J.; Knight, M. W.; Brown, L. V.; Nordlander, P.; Halas, N. J. *J. Am. Chem. Soc.* 2011, *133*, 12247-12255. (b) Lal, S.; Clare, S. E.; Halas, N. J. *Acc. Chem. Res.* 2008, *41*, 1842-51.

(78) Zhou, W.; Shao, J.; Jin, Q.; Wei, Q.; Tang, J.; Ji, J. *Chem. Commun.* 2010, *46*, 1479-1481.

(79) Hunter, R. C.; Beveridge, T. J. *Appl. Environ. Microbiol.* 2005, *71*, 2501-2510.

(80) Sheldon, C.; Cheng, Y. M.; Church, J. *Pflügers Arch.* 2004, *449*, 307-318.

(81) Zhang, F.; Ali, Z.; Amin, F.; Feltz, A.; Oheim, M.; Parak, W. J. *ChemPhysChem* 2010, *11*, 730-735.

(82) Han, J.; Loudet, A.; Barhoumi, R.; Burghardt, R. C.; Burgess, K. *J. Am. Chem. Soc.* 2009, *131*, 1642-1643.

(83) Kreft, O.; Muñoz Javier, A.; Sukhorukov, G. B.; Parak, W. J. *J. Am. Chem. Soc.* 2007, *17*, 4471-4476.

(84) Rivera Gil, P.; Nazarenus, M.; Ashraf, S.; Parak, W. J. *Small* 2012, *8*, 943-948.

(85) Singh, M. P.; Atkins, T. M.; Muthuswamy, E.; Kamali, S.; Tu, C.; Louie, A. Y.; Kauzlarich, S. M. *ACS Nano* 2012, *6*, 5596-5604.

(86) Monteiro-Riviere, N. A.; Inman, A. O.; Zhang, L. W. *Toxicol. Appl. Pharmacol.* 2009, *234*, 222-235.

(87) De Geest, B. G.; Willart, M. A.; Hammad, H.; Lambrecht, B. N.; Pollard, C.; Bogaert, P.; De Filette, M.; Saelens, X.; Vervaet, C.; Remon, J. P.; Grooten, J.; De Koker, S. *ACS Nano* 2012, *6*, 2136-2149.

(88) Kirchner, C.; Javier, A. M.; Susha, A. S.; Rogach, A. L.; Kreft, O.; Sukhorukov, G. B.; Parak, W. J. *Talanta* 2005, *67*, 486-491.

Table of Contents

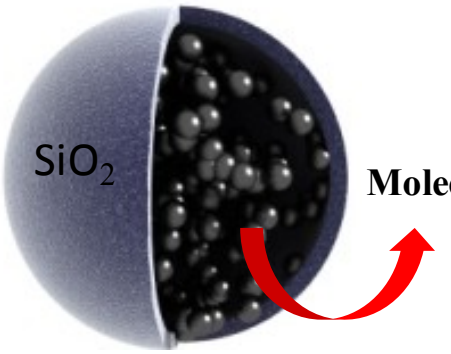

Molecule Release

$$SiO_{2\,(s)} + 2H_2O \rightarrow H_4SiO_{4\,(aq)}$$

Andrea Ott,[1] Xian Yu,[1] Raimo Hartmann,[1] Joanna Rejman,[1] Adrian Schütz,[1] Markus Ochs,[1] Wolfgang J. Parak,[1,2] Susana Carregal-Romero*[1]

[1] Fachbereich Physik, Philipps-Universität Marburg, Marburg, Germany.

[2] CIC Biomagune, San Sebastian, Spain

* Contact details: susana.carregalromero@physik.uni-marburg.de

Light-Addressable and Degradable Silica Capsules for Cytosolic Release

SUPPORTING INFORMATION

I) Characterization of SiO_2 capsules

II) Synthesis of SiO_2 capsules made with PVP as stabilizing agent

III) Synthesis of polyelectrolyte capsules.

IV) Loading efficiency of capsules

V) *In vitro* degradation of 1-SiO_2 capsules and cytosolic release

VI) Degradation of 1-SiO_2 capsules in aqueous solution

VII) Light-mediated release into the cytosol

VIII) References

I) Characterization of SiO_2 capsules

Two different types of silica capsules, named 1-SiO_2 and 1-Au-SiO_2, were prepared using $CaCO_3$ particles as sacrificial template and thiol-terminated polyethyleneglycol (mPEG-SH) as a stabilizing agent. In the main body of our manuscript we demonstrated the 1-SiO_2 capsules degradation. This process in turn could be employed to deliver different molecules into the cell cytosol. To the contrary, shells containing gold nanoparticles (*i.e.* 1-Au-SiO_2 capsules) were not degradable but responded to IR-light. This irradiation allowed delivery of molecules enclosed in these 1-Au-SiO_2 capsules. The 1-SiO_2 capsules were made by functionalizing $CaCO_3$ particles with mPEG-SH ($CaCO_3$@mPEG-SH). Since the thiol groups exert nucleophilic behavior, they can be adsorbed on the calcium carbonate surface. It has been reported that $CaCO_3$ surfaces can be functionalized with other nucleophiles such as hydroxide anions or water.[1] We observed that the $CaCO_3$ particles became soluble in ethanol after mPEG-SH functionalization. The silica coating was made in a mixture of water, ethanol, and ammonium hydroxide. The 1-Au-SiO_2 capsules were made differently than the 1-SiO_2 capsules. For the 1-Au-SiO_2 capsules first $CaCO_3$ particles were coated with one layer of poly(sodium 4-styrenesulfonate) (PSS), then with one layer of poly(allylamine hydrochloride) (PAH), and after that with gold nanoparticles (Au NPs). Before adding the silica shell, mPEG-SH was used again to stabilize the particles in ethanol. This time thiol groups could attach to the gold surface.[2] After adding the silica shell the 1-SiO_2 and the 1-Au-SiO_2 the core-shell particles had the structure $CaCO_3$@mPEG-SH@SiO_2 and $CaCO_3$@(PSS/PAH)Au@mPEG-SH@SiO_2, respectively. The last steps in the synthesis of both types of capsules were similar. The sacrificial template $CaCO_3$ core were dissolved with ethylenediamine-tetraacetic acid disodium salt (EDTA) and one last layer of the bio-degradable polyelectrolyte poly-L-arginine hydrochloride (PARG) was added. Therefore, the final architectures of the produced capsules

were mPEG-SH@SiO_2@PARG (termed 1-SiO_2) and (PSS/PAH)Au@mPEG-SH@SiO_2@PARG (termed 1-Au-SiO_2).

In order to determine the thickness of the silica shell in both types of capsules the size of the $CaCO_3$ particles before coating, after coating with SiO_2, and after $CaCO_3$ removal and PARG wrapping were analyzed and compared. The analysis was made with transmission electron microscopy (TEM, *cf.* Figure SI.I.1). The compared capsules did not carry any cargo (no dyes or drugs in the inner cavity) and were prepared from the same $CaCO_3$ particles with a diameter of 5.3 ± 0.4 μm. As it can be seen from the size distribution plots in Figure SI.I.1 the thickness of both 1-SiO_2 and 1-Au-SiO_2 was 0.6 μm, as determined by TEM analysis. The effect of the presence of Au NPs in the shell thickness was not considered since it was within the standard deviation of the initial $CaCO_3$ cores diameter.

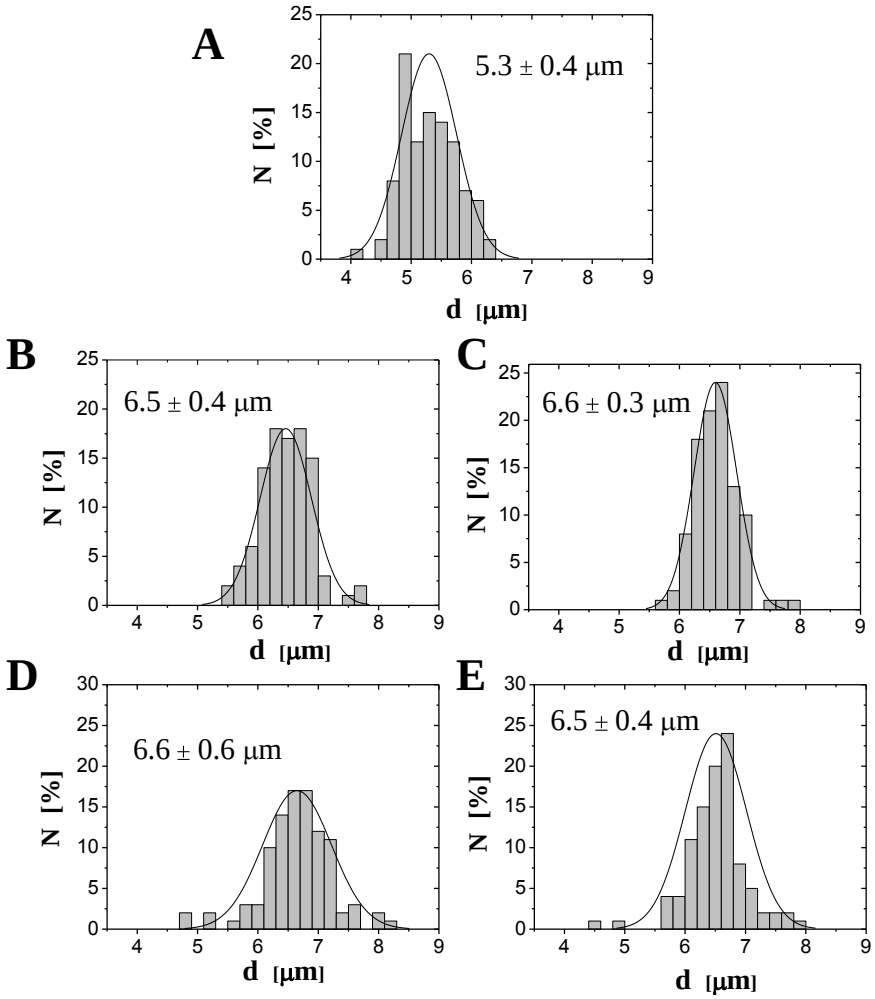

Figure SI.I.1. The particle diameter (d) obtained from TEM images. 1-SiO_2 (degradable) and 1-Au-SiO_2 (light-responsive) capsules were analyses at different stages of their synthesis. (A) $CaCO_3$. (B) $CaCO_3$@mPEG-SH@SiO_2. (C) mPEG-SH@SiO_2@PARG (*i.e.* 1-SiO_2). (D) $CaCO_3$@(PSS/PAH)Au@mPEG-SH@SiO_2@PARG. (D) (PSS/PAH)Au@SiO_2@PARG (*i.e.* 1-Au-SiO_2). The thickness of the shell for both capsule types was 0.6 ± 0.2 μm.

II) Synthesis of SiO_2 capsules with PVP as a stabilizing agent

In order to study whether it would be possible to form a silica shell on the $CaCO_3$ particles by using another polymer instead of mPEG-SH to stabilize the $CaCO_3$ template surface, we used poly(vinylpyrrolidone) (PVP). PVP is largely used to stabilize the surface of NPs that are later coated with silica shells.[3] This polymer can also exert nucleophilic behavior due to the lone pair of electrons of the N and O atoms.[4] Figure SI.II.1 shows the schematic representation of the synthesis of 1-SiO_2 capsules capped with PVP instead of mPEG-SH.

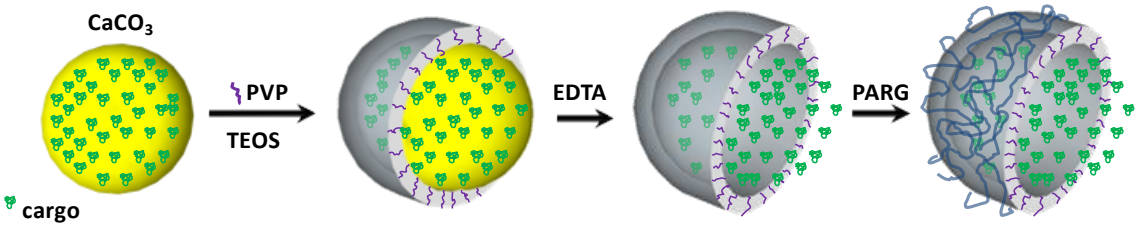

Figure SI.II.1. Synthesis of SiO_2 capsules using PVP as a capping agent of $CaCO_3$ templates. Cargo molecules could be incorporated in the cavity of these capsules by co-precipitation. PVP is used to functionalize the surface of $CaCO_3$ particles and TEOS is the precursor for the silica shell formation. EDTA is added to dissolve the core and PARG to make the capsule positively charged.

Two different sizes of PVP polymers (15 kDa and 55 kDa) were used (15 kDa, Fluka, #81390 and 55 kDa, Sigma, #85,656-8). Only the 55 kDa PVP was found to be suitable to produce silica shells on $CaCO_3$ cores through the Stöber method as described in the following. 21.3 mg of $CaCO_3$ were synthesized as described earlier.[5] The $CaCO_3$ cores were then functionalized with 14 mg of 55 kDa PVP in 1 mL Milli-Q water (19.5 molecules/nm^2 considering a $CaCO_3$ particle radius of 2.5 µm). The $CaCO_3$ particles slightly agglomerated after addition of PVP as it can be seen in Figure SI.II.2. However, the particles were sufficiently stable in the ethanol/water/ammonium hydroxide mixture which was used to

coat the $CaCO_3$ with SiO_2, as described in the following. The sample was washed twice with Milli-Q water and once with ethanol. The precipitate of PVP capped $CaCO_3$ particles was then transferred with 4.5 mL of ethanol to a 40 mL glass vial. 4 mL Milli-Q water, 13.6 mL ethanol and 230 µL ammonium hydroxide solutions were added. Under fast stirring at 750 rpm 90 µL of tetraethylorthosilicate (TEOS) were added. The solution was kept stirring at a steady speed of 400 rpm for 3 h. The particles were then washed twice with ethanol and once with Milli-Q water before adding 1 mL of 0.2 M ethylenediamine-tetraacetic acid disodium salt (EDTA) at pH 5.5 to dissolve the $CaCO_3$ cores. The capsules (particles with shell and empty cavity) were washed three more times before adding 1 mL of 1 mg/mL PARG solution to the capsules. The capsules were shaken in the PARG solution (1 mg/mL in 0.5 M of NaCl) for 12 min and then washed with Milli-Q water thrice. Finally, the capsules were re-dispersed in Milli-Q water. Figure SI.II.2(A,B,C) shows confocal images of the particles at different steps of the synthesis. Figure SI.II.2(D,E) shows TEM images of the core-shell structure ($CaCO_3$@PVP@SiO_2) and the capsules after core dissolution. The presence of PVP resulted in the formation of rough silica shells (in contrast to shells produced using mPEG-SH as a capping agent) and therefore capsules are not completely spherical. The capsules are named PVP-SiO_2. The degradability of these shells was studied and the results are shown in section (V).

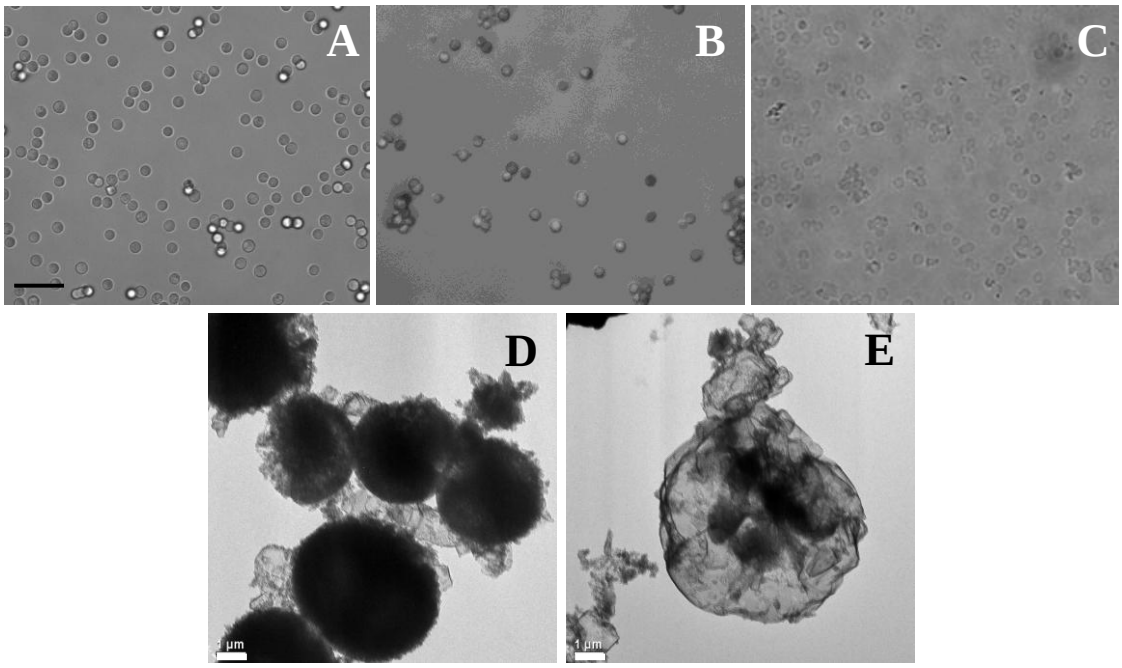

Figure SI.II.2. Confocal images of SiO_2 capsules made with 55 kDa poly(vinylpyrrolidone) (PVP) as an agent stabilizing $CaCO_3$ particles. (A) Image of $CaCO_3$ cores before coating with PVP. (B) $CaCO_3$ cores coated with PVP. (C) SiO_2 capsules after $CaCO_3$ dissolution (*i.e.* PVP-SiO_2). The scale bar corresponds to 10 µm and is the same in (A, B, C). TEM images of the silica shell formation: (D) $CaCO_3$ particles coated with PVP and SiO_2. (E) PVP-SiO_2 capsules. The scale bars in (D, E) correspond to 1 µm.

III) Synthesis of polyelectrolyte capsules

Polyelectrolyte multilayer capsules were synthesized in order to compare them with the aforementioned SiO_2 capsules (*i.e.* 1-SiO_2 and 1-Au-SiO_2) as carrier systems for *in vitro* release of molecules into the cytosol. We prepared 7 different shell compositions in total. 3 capsule types contained SiO_2 in their shell and 4 capsule types were prepared using polyelectrolytes as main building blocks. After that, we studied the loading efficiency, viability and degradation or light-triggered release of encapsulated molecules. We chose polyelectrolyte capsules for the comparison because they have been broadly studied for drug delivery.[6-9] Table SI.III.1 summarizes the results of the *in vitro* degradability of the different capsules.

name	shell architecture	release *in vitro*	
		degradable	light-responsive
1-SiO_2	mPEG-SH@SiO_2@PARG	YES	NO
1-Au-SiO_2	(PSS/PAH)Au@ mPEG-SH@SiO_2@PARG	NO	YES
$^{(1)}$PVP-SiO_2	PVP@SiO_2@PARG	NO	NO
2-(DEXS/PARG)	$(DEXS/PARG)_5$	YES	NO
2-Au(DEXS/PARG)	$(DEXS/PARG)_3Au(DEXS/PARG)_2$	NO	YES
3-(PSS/PAH)	$(PSS/PAH)_5$	NO	NO
3-Au(PSS/PAH)	$(PSS/PAH)_3Au(DEXS/PAH)_2$	NO	YES

Table SI.III.1. Names, shell architecture and properties of the capsules used in the study. Silica shells were compared with polyelectrolyte capsules. The names of the polymers: methoxy-polyethyleneglycol with thiol terminus (mPEG-SH), poly(vinylpyrrolidone) (PVP), poly-L-arginine hydrochloride (PARG), dextran sulfate sodium salt (DEXS), poly(allylamine hydrochloride) (PAH) and poly(sodium 4-styrenesulfonate) (PSS). [(1)]These capsules were not used to compare the loading efficiency and the cargo release.

PEM capsules were produced *via* the Layer-by-Layer (LbL) approach. Different polyelectrolyte pairs were employed: a) degradable polyelectrolytes: poly-L-arginine hydrochloride (PARG) and dextran sulfate sodium salt (DEXS) and b) synthetic and non-degradable polyelectrolytes: poly(allylamine hydrochloride) (PAH) and poly(sodium 4-styrenesulfonate) (PSS). The samples are named 2-(DEXS/PARG), 2-Au(DEXS/PARG), 3-(PSS/PAH) and 3-Au(PSS/PAH). As it can be seen in Table SI.III.1 all the LbL capsules contained 10 layers of polyelectrolytes (5 bilayers). Figure SI.III.1 shows the steps in the synthesis of the LbL capsules. $CaCO_3$ particles were prepared first (they could be optionally loaded with cargo molecules). Then the negatively charged polyelectrolyte was attached to the surface of the particles by electrostatic interaction. Subsequently a layer of positively charged polyelectrolyte was assembled on the core-shell particles ($CaCO_3$(PSS/PAH)). The process was repeated till the desired numbers of bilayers was achieved. Charged Au NPs were optionally incorporated in between the layers. This synthetic protocol has been largely used to produce differently composed capsules [5,10-13]).

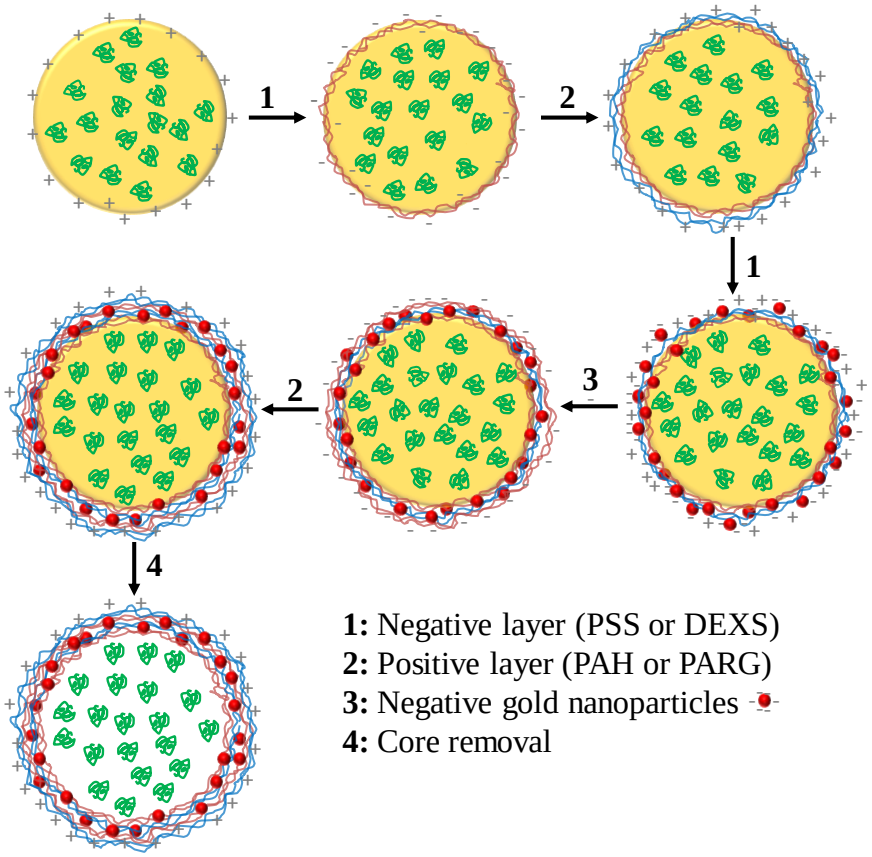

Figure SI.III.1. Schematic representation of the Layer-by-Layer (LbL) assembly applied in the synthesis of polyelectrolyte multilayer (PEM) capsules. $CaCO_3$ particles are in the scheme preloaded with cargo molecules (in brown) and the PEM capsules were loaded with negative charged NPs (red spheres). When the PEM capsules do not contain NPs the third step is skipped, but the rest of steps in the synthesis are similar.

In Figure SI.III.2 TEM images of the six different types of capsules are shown (PVP-SiO_2 capsules were already shown in Figure SI.II.2). As it can be seen, silica capsules are rigid while PEM capsules collapsed in the absence of water. We found broken capsules in all the samples. Note that this may be due to the TEM grid preparation and the imaging procedure, since we observed a lower amount of broken capsules in corresponding confocal microscopy images. However, most likely also the EDTA dissolution of the $CaCO_3$ core is responsible for the damage of the capsule shells, as it has been already reported for PEM capsules.[14]

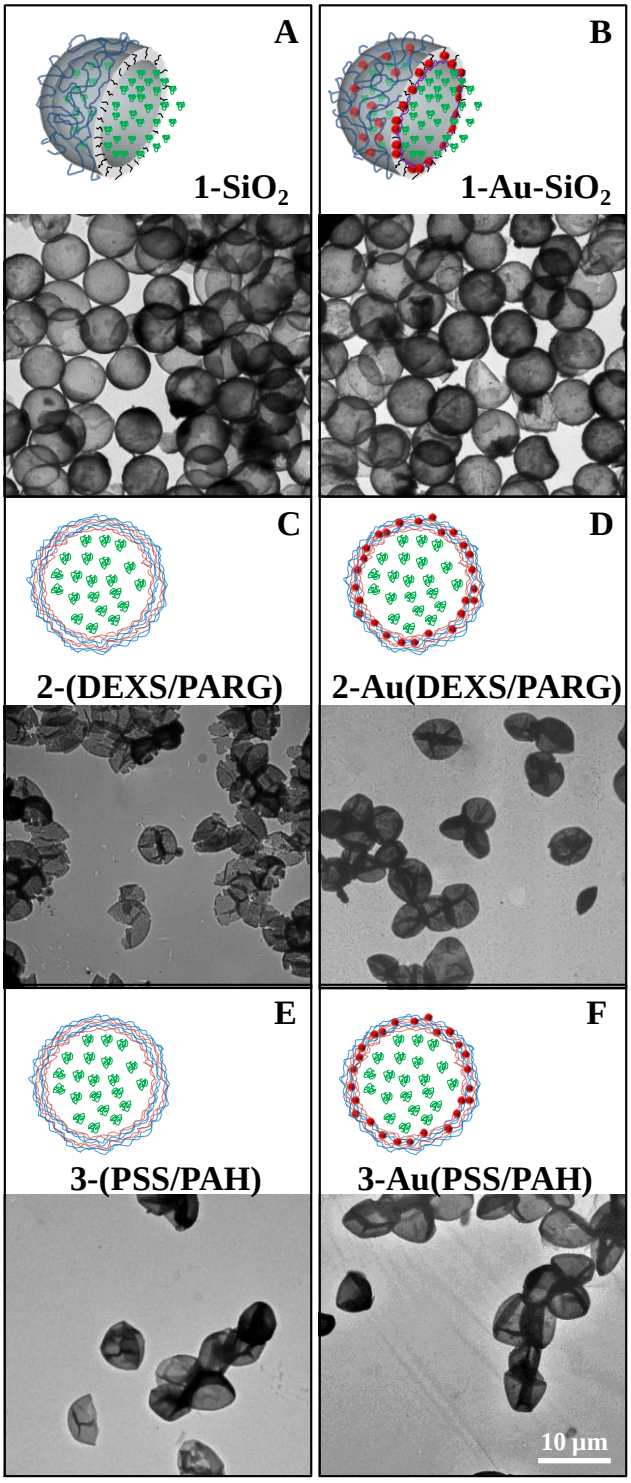

Figure SI.III.2. TEM images of six different types of capsules and their schematic representation: (A) 1-SiO_2, (B) 1-Au-SiO_2, (C) 2-(DEXS/PARG), (D) 2-Au(DEXS/PARG), (E) 3-(PSS/PAH) and (F) 3-Au(PSS/PAH). The scale bar corresponds to 10 µm.

IV) Loading efficiency of capsules

In this section we will discuss the efficiency of the 1-SiO_2 and 1-Au-SiO_2 silica shells to encapsulate high and low molecular weight molecules and made a comparison with capsules prepared by LbL assembly. We employed bovine serum albumin modified with fluorescein isothiocyanate (~ 66 kDa, FITC-BSA), a low molecular weight drug - doxorubicin (0.58 kDa) and DQ ovalbumin (DQ-OVA, ~45 kDa), which is a fluorescence-labeled protein (*cf.* Table SI.III.1).

First, to study the ability to encapsulate high molecular weight molecules in the cavity of the capsules FITC-BSAFITC-BSA was employed (~ 66 kDa,). This model-protein was incorporated in the capsules cavity by co-precipitation. To that end $CaCO_3$ cores were formed in the presence of a water solution of FITC-BSA (1.23 mL of 0.33 M $CaCl_2$, 1.23 mL of 0.33M Na_2CO_3 and 1.5 mL of 50 L of FITC-BSA were mixed). The shell assembly around the cores was carried out as described in Chapters I and III. It was followed by the cores dissolution. The same batch of $CaCO_3$ particles loaded with FITC-BSA was used to produce the six different types of capsules (*cf.*, Table SI.III.1). The average amount of fluorescently-labelled protein inside the capsules after core dissolution was evaluated by analyzing confocal micrographs with a software written for this purpose in Matlab (Mathworks). Quantitative evaluation was done by measuring the integrated fluorescent intensity of individual capsules in images made using the same acquisition parameters for all images. The intensity ratio of the FITC-BSA loaded capsules 1-SiO_2: 1-Au-SiO_2: 2-(DEXS/PARG): 2-Au-(DEXS/PARG): 3-(PSS/PAH): 3-Au(PSS/PAH) was 1: 0.61 : 0.08: 0.10: 0.98: 0.92. The loading of the capsules with embedded Au NPs compared to their analogues without Au NPs was very similar, except for the silica capsules. It has been reported for LbL capsules that the presence of NPs within the shells can increase their permeability due to the formation of defects in the shells.[15] We only observed this difference for silica shells prepared with and without gold NPs. In this case reduced loading of the silica shells with Au NPs could be attributed to the

presence of defects, though this would have to be further confirmed. The most noticeable result was the low loading of the biodegradable capsules based on DEXS/PARG, with a loading of only 8 % as compared to the degradable 1-SiO_2 capsules. Shells composed out of different materials may have quite different porosity,[16] which can lead to different encapsulation properties. Therefore, (degradable) 1-SiO_2 capsules could present an advantage *versus* (degradable) DEXS/PARG capsules in terms of encapsulation efficiency for certain molecules.

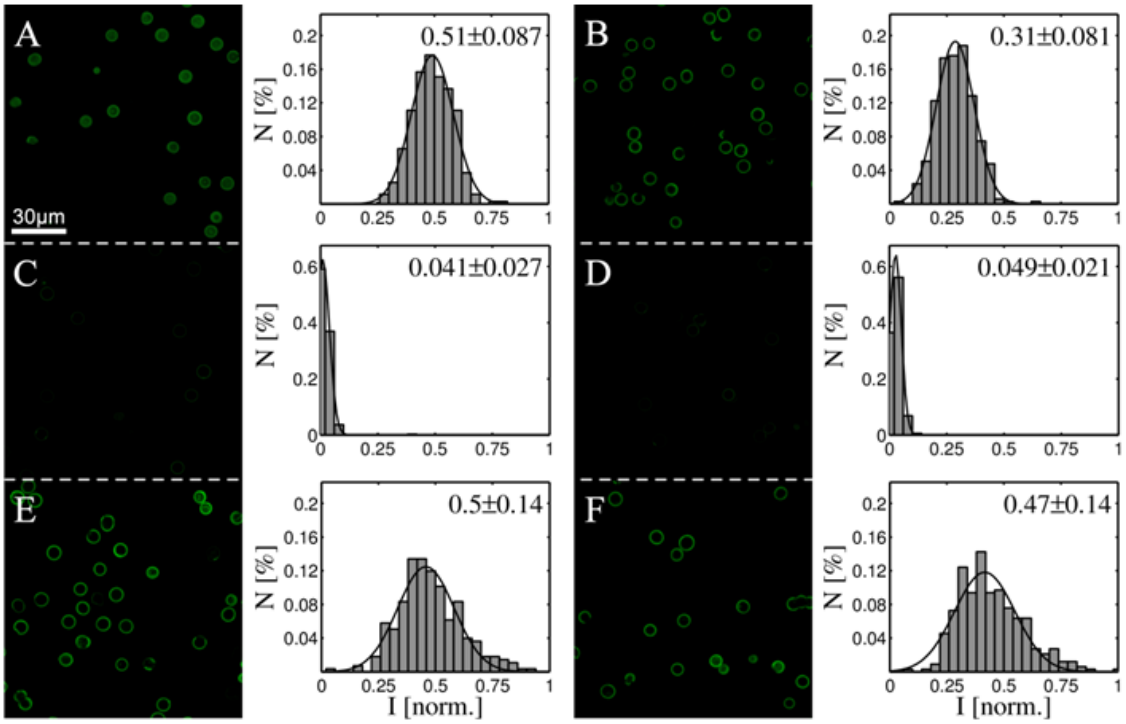

Figure SI.IV.1. Confocal images of the green channel and the corresponding intensity distribution of FITC-BSAFITC-BSA loaded capsules obtained from the analysis of confocal micrographs: (A) 1-SiO_2, (B) 1-Au-SiO_2, (C) 2-(DEXS/PARG)$_2$ (D) 2-Au(DEXS/PARG)$_2$ (E) 3-(PSS/PAH) and (F) 3-Au(PSS/PAH). I - the normalized integrated fluorescent intensity of individual capsules and N - the frequency at which such intensity values occurred. Note that in all cases the encapsulated FITC-BSA is not homogeneously distributed in the capsule cavity, but rather sticks to the inner capsules shells.

The loading ability of 1-SiO_2, 1-Au-SiO_2, 2-(DEXS/PARG), 2-Au(DEXS/PARG), 3-(PSS/PAH), and 3-Au(PSS/PAH) capsules was also studied for the model drug doxorubicin hydrochloride (DOXS). DOXS is a fluorescent cancer drug (excitation/emission maxima ~ 480 nm/560-590 nm). Since DOXS is only 0.58 kDa small, it was chosen to compare the encapsulation of low molecular weight molecules by the silica and LbL capsules. Post-loading was employed as the encapsulation technique.[17,18] To produce capsules as similar as possible the same batch of $CaCO_3$ particles was used as template in the formation of the six different types of capsules. In the first step of the synthesis, $CaCO_3$ particles were coprecipitated with micelles based on the block-copolymer poly(styrene)-block-poly(acrylic acid) (PSS-b-PAA, $M_n \approx 8700$, Sigma-Aldrich #735892). The encapsulation was performed after the dissolution of the core with EDTA as previously described.[18] To compare the loading efficiency of the six samples we kept the ratio DOXS molecules/number of capsules constant during the postloading process. For each type of capsules (*cf.* Table SI.III.1) we mixed $3.75 \cdot 10^7$ capsules (in water) with $2.2 \cdot 10^{-6}$ mol of DOXS dissolved in dimethyl sulfoxide (100 µL). The mixture was shaken mechanically for 30 min. After that, the samples were first washed once with ethanol and then thrice with Milli-Q water. The DOXS encapsulated efficiency was evaluated by employing absorption spectrophotometry. The amount of DOXS which was not encapsulated and thus remained free in solution was measured. The absorbance of DOXS was measured in each supernatant after each step of the encapsulation procedure. The concentration of DOXS was calculated based on the extinction coefficient of DOXS at 480 nm (ε_{480} = 11500 $M^{-1} \cdot s^{-1}$) and the known concentration of capsules as measured with a hemocytometer (which was possible due to the large size of the capsules).[19] In addition, the integrated fluorescent intensity of individual capsules was determined from confocal micrographs (see Figure SI.IV.2). Both results were compared. The results obtained with these two approaches are shown in Table SI.IV.1.

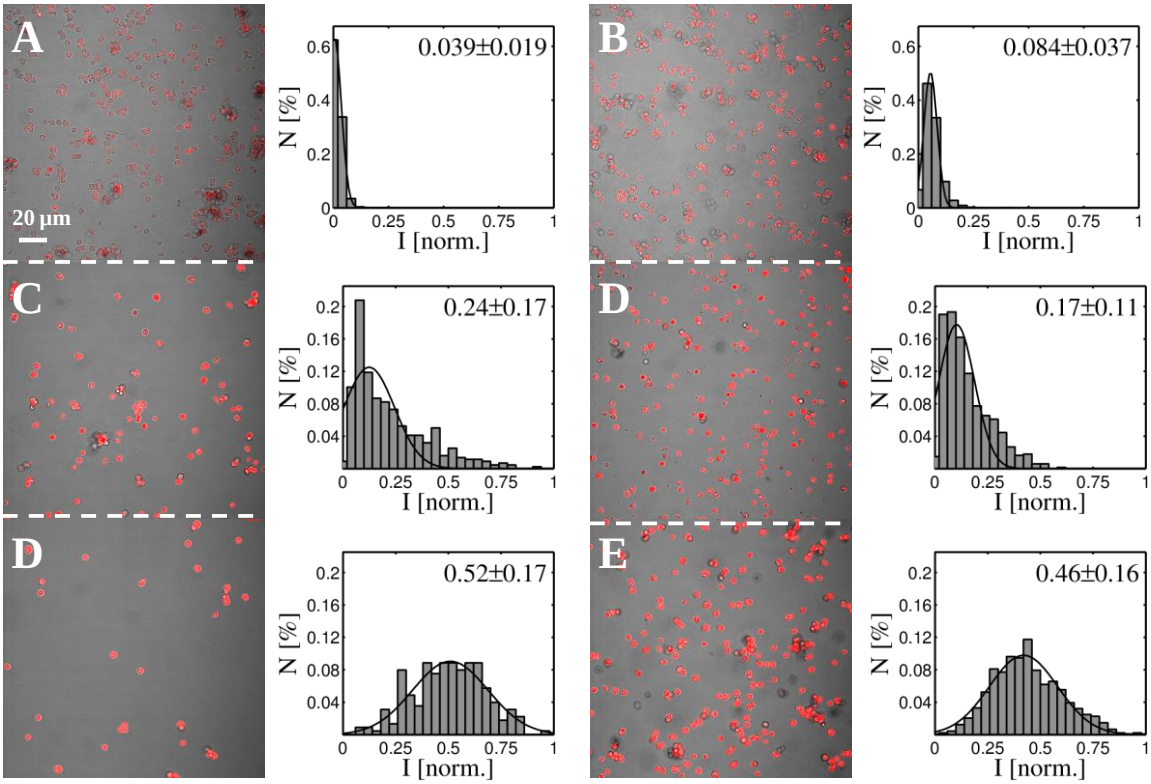

Figure SI.IV.2. Confocal microscopy images of the overlay of the red fluorescence and transmission channel of DOXS loaded capsules and the corresponding intensity distribution obtained from the analysis of confocal micrographs: (A) 1-SiO_2, (B) 1-Au-SiO_2, (C) 2-(DEXS/PARG)$_3$ (D) 2-Au(DEXS/PARG)$_3$ (E) 3-(PSS/PAH) and (F) 3-Au(PSS/PAH)$_3$ I - the normalized integrated fluorescent intensity of individual capsules; and N - the frequency at which such intensity values occurred. Note that in all cases the encapsulated DOXS is distributed rather homogeneously in the capsule cavity.

Capsule type	Molecules per capsule detected by absorption	Fluorescence intensity I [norm.]
1-SiO_2	$8.2 \cdot 10^8$	0.04 ± 0.02
1-Au-SiO_2	$20.2 \cdot 10^8$	0.08 ± 0.04
2-(DEXS/PARG)	$31.6 \cdot 10^8$	0.24 ± 0.17
2-Au(DEXS/PARG)	$13.8 \cdot 10^8$	0.17 ± 0.11
3-(PSS/PAH)	$15.7 \cdot 10^8$	0.52 ± 0.17
3-Au(PSS/PAH)	$18.7 \cdot 10^8$	0.46 ± 0.16

Table SI.IV.1. The number of doxorubicin (DOXS) molecules encapsulated per capsule evaluated by absorption spectrophotometry and the normalized integrated fluorescent intensity of individual capsules as obtained from the analysis of confocal micrographs of differently composed silica and LBL capsules.

As it can be seen in Table SI.IV.1 the information about the loading efficiency obtained by two different methods is not fully consistent. It must be taken into account that the calculation of molecules/capsule is subject to many experimental errors and it has to be regarded critically. Nevertheless, it offers an idea about the range of the number of DOXS molecules that can be encapsulated within one capsule (~1-$30 \cdot 10^8$ molecules/capsule). The intensity ratio of the DOXS loaded capsules 1-SiO_2: 1-Au-SiO_2: 2-(DEXS/PARG): 2-Au-(DEXS/PARG): 3-(PSS/PAH): 3-Au(PSS/PAH) was 1: 2 : 6: 4.2: 13: 11.5. The differences in the loading quantity compared with the coprecipitation method were bigger and silica

shells were not as efficient as LbL capsules in encapsulating the low molecular weight DOXS. These results and the results obtained for FITC-BSA could be the consequence of an expected lower porosity of silica shells compared with LbL capsules. In addition to the shell porosity the interaction between the shell and the respective cargo molecules will play a role in the number of molecules that remain encapsulated inside the hollow cavity and adsorbed to the inner shell of the capsule. In particular in the case of FITC-BSA the capsules seem to be empty in the inner cavity, but the shell present strong fluorescence. This means that an appreciable amount of cargo molecules is entrapped due to interaction with the capsule shell. The strong attachment of cargo molecules to the capsule shell can be for example seen in Figure SI.IV.1.

The results obtained for DQ-OVA capsules are shown in Figure SI.IV.3. The protein was encapsulated by a co-precipitation approach (100 µL of DQ-OVA 1 mg/mL, 615 µL of $CaCl_2$ 0.33 M, and 615 µL of Na_2CO_3 0.33 M). Six different types of capsules (*cf.*, Table SI.III.1) were produced from the same batch of $CaCO_3$ template particles. As it can be seen in Figure SI.IV.3 the capsules have different emission intensities at two different ranges of wavelengths. This is due to nature of the DQ-OVA, which is a protein conjugated with shelf-quenched BODIPY® FL dye.[20]

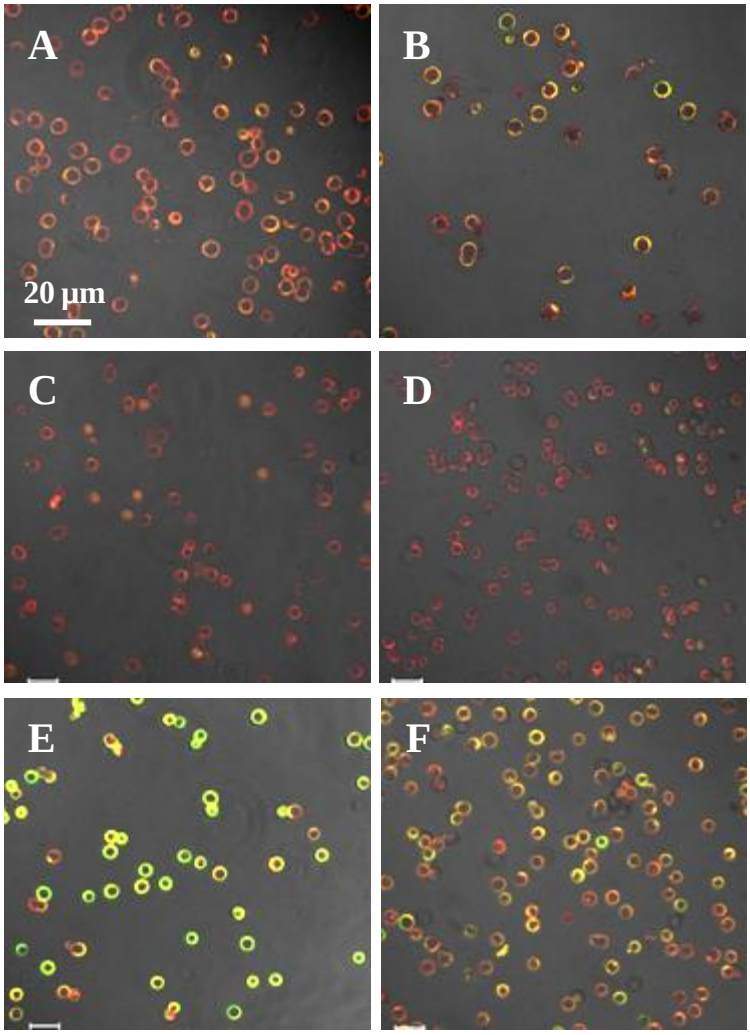

Figure SI.IV.3. Confocal images of the overlay of the red and green fluorescence and the transmission channels (left) and the transmission channel (right) of DQ-OVA loaded capsules: (A) 1-SiO_2, (B) 1-Au-SiO_2, (C) 2-(DEXS/PARG)$_3$, (D) 2-Au(DEXS/PARG)$_3$, (E) 3-(PSS/PAH) and (F) 3-Au(PSS/PAH).

BODIPY® FL has two emission peaks, the first one (green fluorescence) has an excitation maximum at 503 nm and an emission maximum at 512 nm. The green fluorescence emission is enhanced upon proteolytic digestion, which is observed when the cleaved fragments of DQ-OVA are released. The second emission peak has the excitation maximum at 570 nm and emission maximum at 630 nm (red

fluorescence emission) and it only appears when BODIPY® FL is highly concentrated due to the dimer formation.[212223] This second emission not only depends on the concentration of dye, but also on the orientation of the molecules that form dimers. This makes it very complicated to estimae the amount of encapsulated DQ-OVA in the six different types of capsules by fluorescence intensity measurements (*cf.*, Table SI.III.1). The different emission intensities shown in Figure SI.IV.3 may be explained by the different concentrations of BODIPY® FL monomers and dimers and the interaction of the dye with the different polyelectrolytes. Notwithstanding, we analyzed again confocal micrographs using the same acquisition parameters for all images and compared only the red emission of capsules containing DQ-OVA. The intensity ratio of the DQ-OVA loaded capsules 1-SiO_2: 1-Au-SiO_2: 2-(DEXS/PARG): 2-Au-(DEXS/PARG): 3-(PSS/PAH): 3-Au(PSS/PAH) was 1: 1.3 : 0.93: 0.75: 1.7: 1.2. These results are in agreement with the results obtained with the FITC-BSA loading. Silica shells (1-SiO_2 and 1-Au-SiO_2) were slightly more efficient in encapsulating high molecular weight proteins than capsules based on degradable polyelectrolytes (DEXS/PARG). However, the most efficient capsules in terms of loading efficiency were prepared with the non-degradable (PSS/PAH) polyelectrolytes.

V) *In vitro* degradation of 1-SiO_2 capsules and the cytosolic cargo release

In this section we present more evidences about the cytosolic cargo release from 1-SiO_2 capsules after their internalization by cells. In a first set of experiments 1-SiO_2 capsules loaded with Dextran-tetramethylrhodamine isothiocyanate (TRICT; molecular weight of Dextran-TRICT ≈ 155 kDa, Sigma-Aldrich, #T1287) were prepared by co-precipitation of this labelled polysaccharide with $CaCO_3$. 100 µL of 1 mg/mL of dextran-TRICT (in water) was mixed with 615 µL of $CaCl_2$ 0.33 M and 615 µL of Na_2CO_3 0.33 M to prepare the $CaCO_3$ template particles. A silica shell was formed using mPEG-SH as a

capping agent. PARG was added to the outer shell after core dissolution with EDTA. Dextran-TRICT capsules were incubated with HeLa cells and confocal micrographs were taken at different time points after the addition of the capsules to the cells (t = 0 h). Figure SI.V.1 shows the release of the red fluorescent dextran-TRICT into the cytosol, which is evident especially after 20 h of incubation. Besides the homogeneous release into the cytosol, dextran-TRICT was also present inside small vesicles that were observed as granular structures inside the cells. These vesicles might be exosomes.

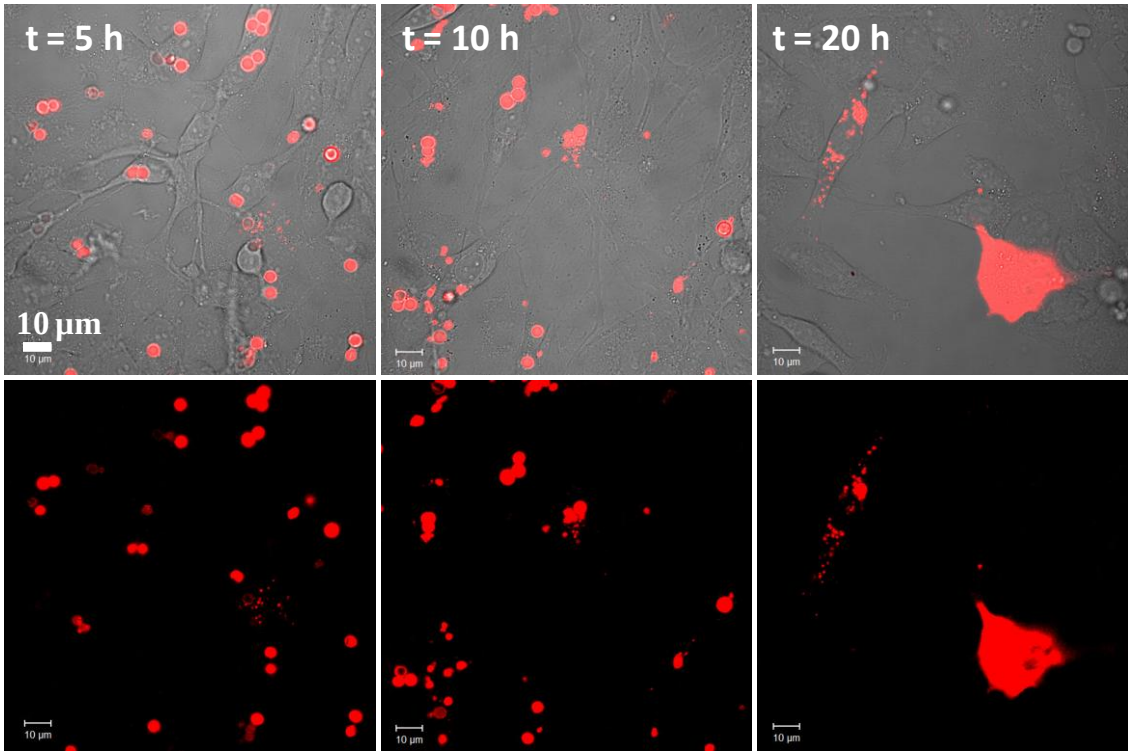

Figure SI. V.1. Confocal micrographs demonstrating the degradation of 1-SiO_2 capsules loaded with dextran-TRITC (155 kDa) in HeLa cells. The images were acquired at different time points. The images on the top correspond to the overlay of the transmission and the red fluorescence channels. The images on the bottom only show the red fluorescence channel. The scale bars corresponds to 10 µm.

PVP-SiO_2 capsules were produced to check whether different capping molecules (PVP *versus* mPEG-SH) influence the formation of silica shell. PVP-SiO_2 capsules loaded with DQ-OVA were prepared by co-precipitation, using 100 µL of DQ-OVA solution in Milli-Q water (1 mg/mL), 615 µL of $CaCl_2$ (0.33 M) and 615 µL of Na_2CO_3 (0.33 M). We confirmed that the produced shells are very inhomogeneous and rough (*cf.* Figure SI.II.2). The in-time degradation of these capsules *in vitro* was studied with HeLa cells. Figure SI.V.2 shows orthogonal views of HeLa cells incubated with DQ-OVA loaded 1-SiO_2 capsules. As it can be seen, the appearance of green fluorescence in the cells due to the DQ-OVA degradation is negligible, as compared with the release observed from DQ-OVA loaded 1-SiO_2 capsules (*cf.* Figure SI.V.2). This suggests that the polymer acting as a capping agent influences also the degradation of the silica shell. It points out that capsules produced using PVP as a capping agent are not suited as degradable capsules.

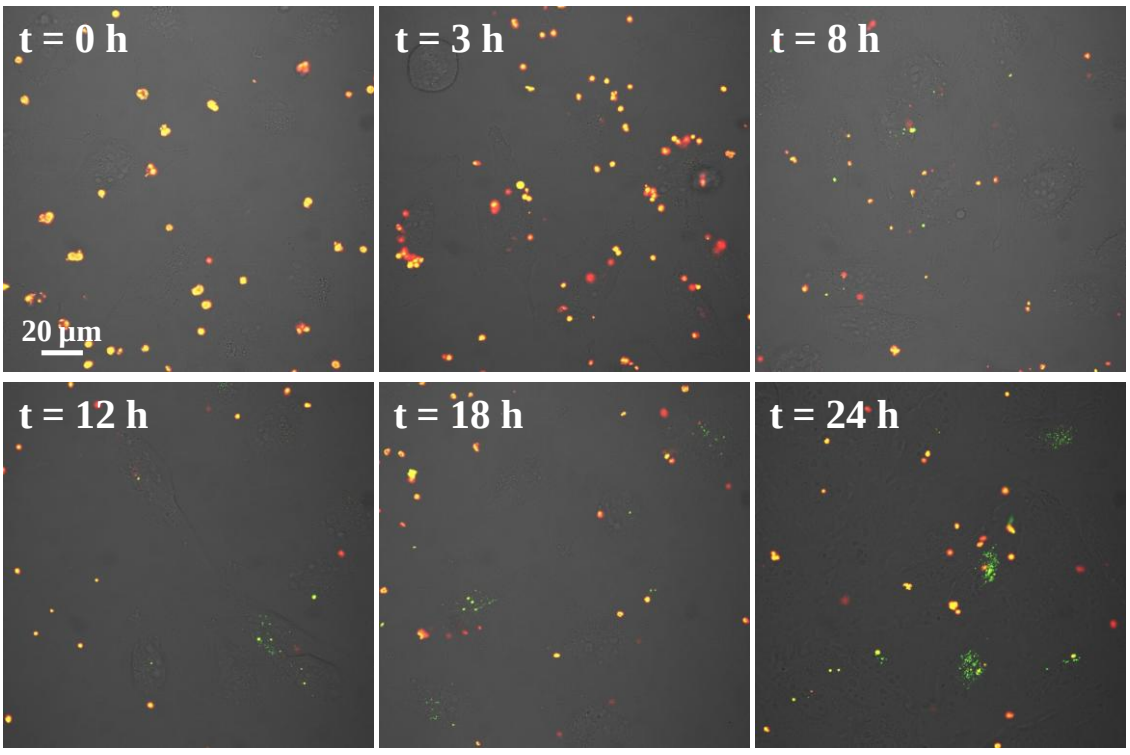

Figure SI.V.2. Degradation of PVP-SiO_2 capsules internalized by HeLa cells. These capsules were made with 55 kDa PVP as a stabilizing agent. They were loaded with DQ-OVA (*cf.* Table SI.III.1). The images were acquired at different time points. The scale bar corresponds to 20 μm.

Also orthogonal images made with confocal microscopy (based on recording z-stacks) were taken to point out the homogeneous distribution of released DQ-OVA in the cytosol when 1-SiO_2 capsules were used as carrier systems. The cytosolic release of DQ-OVA from 1-SiO_2 capsules is evident in the orthogonal view shown in Figure SI.V.3. Here the whole cellular cytosol is stained with the cleaved DQ-OVA fragments (in green). The release of DQ-OVA from LbL capsules prepared from DEXS and PARG) has been reported previously[13] However, in this case no homogeneous distribution of cleaved protein was evident and the green fluorescence was mostly observed in granular structures present in the cytosol. This suggests that most of the released protein may be located in exocytotic vesicles.[13] Thus, there is indication that 1-SiO_2 capsules are better suited for spontaneous release to the cytosol *via* biodegradation than 2-(DEXS/PARG) capsules.

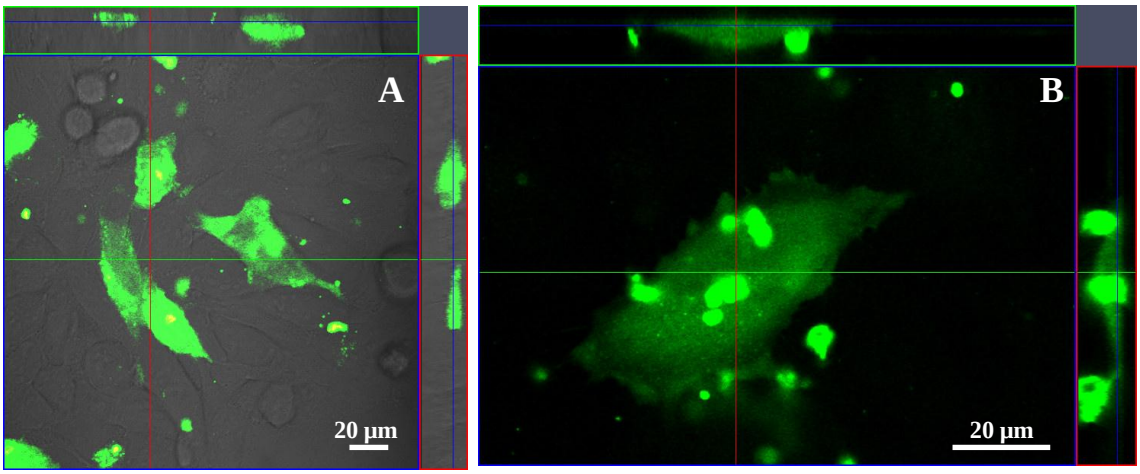

Figure SI.V.3. Degradation of 1-SiO_2 capsules loaded with DQ-OVA leads to cytosolic release of cleaved DQ-OVA (green). An orthogonal view of three perpendicular cross-sections of the cell recorded with a confocal

microscope is shown. (A) Overlay image of the transmission and the green fluorescence channels 9 h adding the capsules to HeLa cells. (B) Image of the green fluorescence channel made after 22 h of capsule incubation.

The nuclei of HeLa cells were stained with 4´,6-diamidino-2-phenylindole (DAPI; Life technologies # D21490) The cells were grown in µ-slide 8 wells (Ibidi # 80826); 10000 cells/well were plated and 5 capsules/cell were added. 1-SiO_2 and 1-Au-SiO_2 capsules loaded with DQ-OVA (as prepared as described in section SI.IV) were used to study the location of the released protein after 24 h. After this incubation time, cells were washed with 300 µL of Hank's balanced salt solution (HBBS, Life Technologies # 14025092) for 2 min. Then, the HBBS solution was removed and 150 µL of a 70 µM DAPI solution (in HBBS) was added in each well and the cells were incubated with this solution for 12 min. Afterwards, the cells were washed twice with HBBS and 300 µL of fresh cellular medium were added in each well, before imaging with confocal microscopy. Based on the fluorescence microscopy data the release of DQ-OVA from 1-SiO_2 and 1-Au-SiO_2 capsules was compared. Low magnification confocal micrographs (Figure SI.V.4) show the ability of 1-SiO_2 capsules to release DQ-OVA into the cytosol. This was not observed for the non-degradable 1-Au-SiO_2 capsules. Figure SI.V.4 shows that 1-Au-SiO_2 capsules are indeed not degradable and 1-SiO_2 capsules release cleaved DQ-OVA to the cytosol, but the protein fragments do not reach the cellular nuclei. The green fluorescence was observed mainly around the blue-stained nuclei.

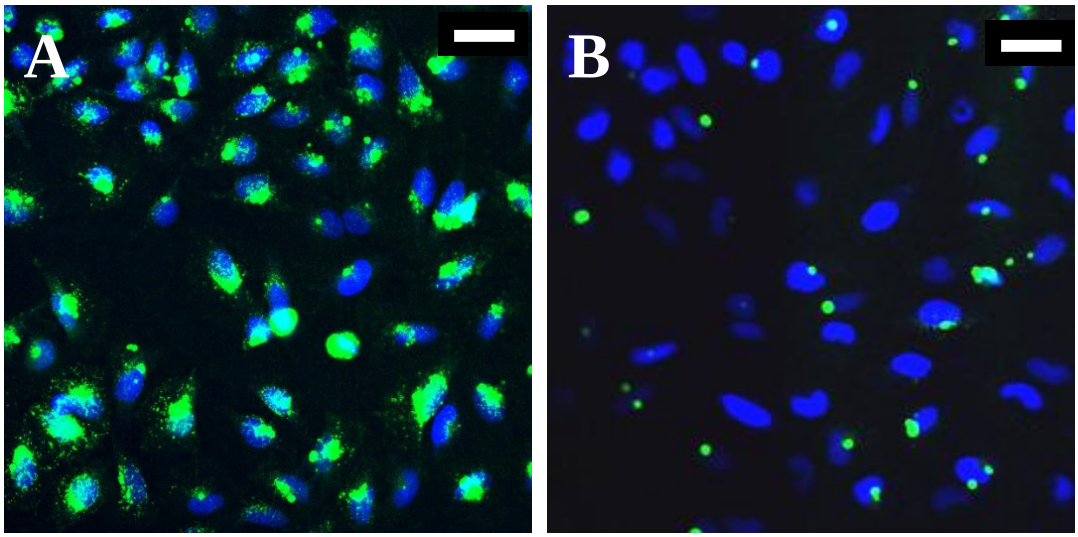

Figure SI.V.4. Confocal micrographs of HeLa incubated for 24 h with (A) 1-SiO_2 and (B) 1-Au-SiO_2 capsules loaded with DQ-OVA. The nuclei were stained with DAPI. For simplicity, only the blue and the green fluorescence channels are shown. The green fluorescence observed in (A) around the nuclei correspond to the cleaved DQ-OVA fragments. The scale bars correspond to 50 µm.

Figure SI.V.5 shows more confocal micrographs of swollen lysosomes where1-SiO_2 capsules loaded with DQ-OVA were internalized. After 2 h some swelling could be observed, this manifests by the fact that the red and the green emission do not co-localize entirely. As mentioned before the green fluorescence corresponds to the cleaved protein fragments and the red fluorescence is due to the presence of dimers of BODIPY® FL that are only formed at high concentrations and therefore are not observed when the protein is cleaved and diluted in the cytosol. The lack of co-localization of red and green emission could also mean that the release of the cleaved DQ-OVA fragments initially localize only around the capsule in which the protein was encapsulated. However, it was possible to observe a vesicle around the capsule where the green fluorescence is located in the transmission channel (*cf.*, Figure 6 in the main manuscript and SI.V.5B). In Figure SI.V.5B two such vesicles are nicely visible in the transmission channel. These two structures co-localize with the cleaved DQ-OVA fragments around

the capsules. The large size of these lysosomes in which the capsules are located [24] is likely caused by the entrance of water from the cytosol due to the degradation of the capsules.[25] After the burst of the lysosomes the release of DQ-OVA could be observed as it was shown in Figure SI.V.3, where the green fluorescence is homogeneously distributed in whole cytosol.

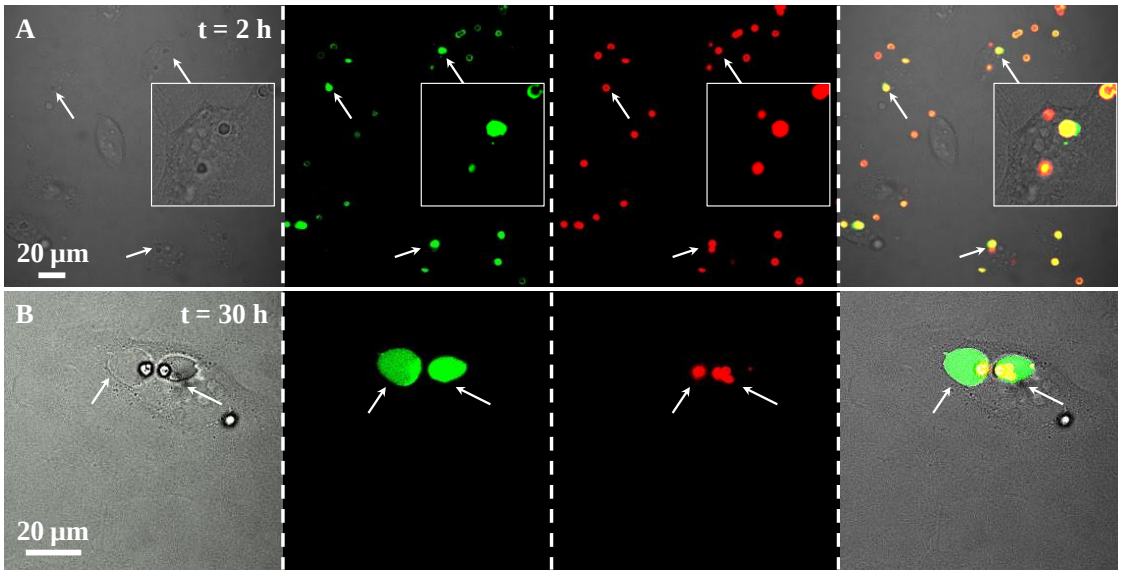

Figure SI.V.5. Confocal images of the swelling of lysosomes upon the internalization of 1-SiO_2 capsules loaded with DQ-OVA in HeLa cells. The cells were incubated for (A) 2 h and (B) 30 h with DQ-OVA loaded 1-SiO_2 capsules. Arrows point at the swollen vesicles. The scale bars correspond to 20 µm.

In Figure SI.V.6 we show the release of mRNA encoding the green fluorescent protein (GFP) that serves as a template to synthesize GFP in the cytosol in MDA-MB-231 cells. Typically, mRNA can be delivered to cells after being complexed with cationic lipids and polymers. It has been reported that the mRNA dissociation from cationic polymers is very inefficient, which prevents mRNA from being transcribed in the cytosol.[26] Recently, we demonstrated that it is possible to release mRNA by light mediated opening of LbL capsules functionalized with gold NPs (similar to 3-Au(PSS/PAH) capsules) while maintaining the biological activity of nucleic acids.[18] However, the release of mRNA from degradable LbL capsules

was not possible with capsules composed of DEXS/PARG. Here, 1-SiO_2 capsules with encapsulated mRNA encoding GFP were produced using the co-precipitation method as reported previously.[18] 15 μg of mRNA encoding GFP (synthesized from pGEM4Z/EGFP/A64 plasmid)[26] were diluted in 500 μL of RNase free water and mixed with 615 μL of $CaCl_2$ 0.33 M. Afterwards, 615 μL of Na_2CO_3 0.33 M were added while stirring at 1000 rpm. After 30 s of mixing the resulting $CaCO_3$ particles were left 3 min for ripening. Immediately afterward the cores were washed twice with RNase free water and wrapping with mPEG-SH was carried out. The coating with silica was done as described above. The PARG used as the last layer was labelled with the red dye Dy634 (Dyomincs # 634-1) (excitation/emission maxima ~ 635 nm/658 nm). Figure SI.IV.6A shows that after capsule uptake by MDA-MB-231 cells, GFP was synthesized in the cytosol. This can be seen by the onset of green fluorescence in the cytosol and by the fact that this emission did not co-localize with the emission of the shell of the 1-SiO_2 capsules (in red) from which the mRNA had been released. Figure SI.V.6B shows an orthogonal view of the green fluorescence originating from GFP.

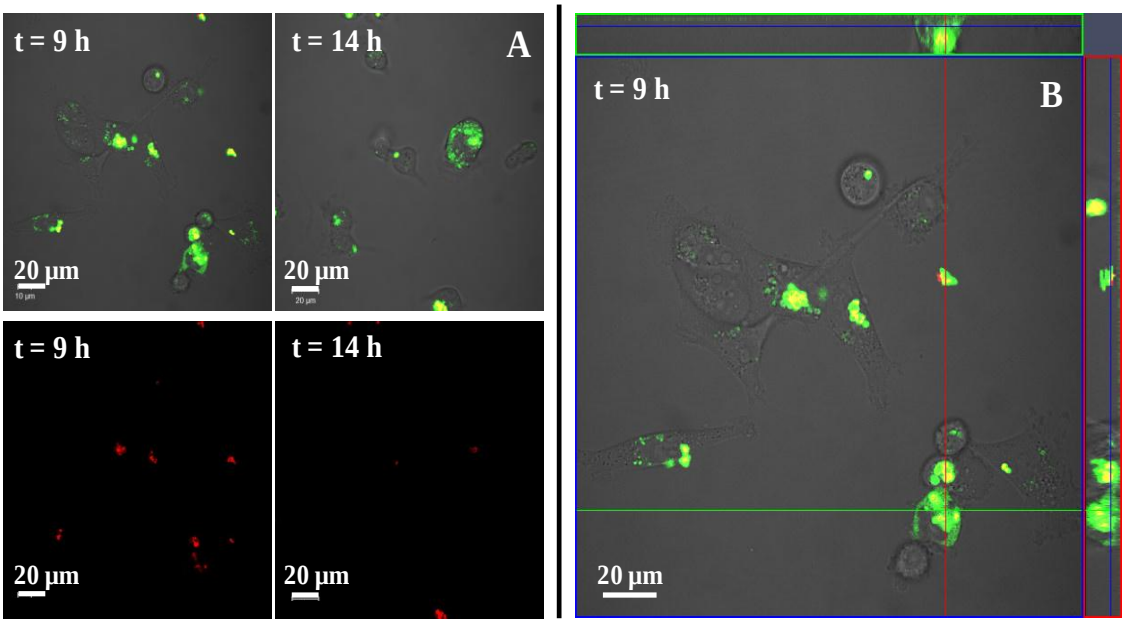

Figure SI.V.6. Fluorescence of MDA-MB-231 cells incubated with degradable 1-SiO_2 capsules loaded with mRNA encoding GFP and labeled with Dy634 (excitation/emission maxima ~ 635 nm/658 nm). The formation of GFP within the cytosol due to the delivery of mRNA encoding it could be observed after 9 hours. (A) The images on the top correspond to the overlay of the green and red fluorescence channels with the transmission channel. (B) Orthogonal view of three perpendicular cross-sections through the cell. The scale bars correspond to 20 µm.

VI) Degradation of SiO_2 capsules in aqueous solution.

It has been observed that the degradation of 1-SiO_2 capsules is related to the pH of the capsule environment and the presence of proteases (*cf.* Figure 7 of the main manuscript). In the main body of our manuscript we showed the results obtained with phosphate buffered saline (PBS). To show that these data did not depend on the constituents of the particular buffer, a study on the degradation of 1-SiO_2 capsules was done in a second buffer (at different pH). 1-SiO_2 capsules loaded with dextran-TRICT

(prepared as it was described in section SI.V) were used to analyze the release of dextran-TRICT in buffer solutions characterized by different pH values. The samples were characterized by fluorescence spectroscopy. To that end, 100 µL capsule solutions in water ($3.5 \cdot 10^7$ capsule/mL) were mixed with 200 µL of Milli-Q water or buffers at different pH. Tris(hydroxymethyl)aminomethane (TRIS, Sigma-Aldrich # 94158) was used as a buffer. The final pH was verified with a pH-meter. Release from capsules that were incubated with the buffer at 37 ºC to mimic physiological temperature was compared with the release from capsules that were stored at 4 ºC in Milli-Q water (pH 6.2). As it can be seen in Figure SI.VI.1 the release of dextran-TRICT from 1-SiO_2 capsules at 37 ºC in TRIS buffer was similar to the release obtained in PBS buffer. The capsules stored at 4 ºC were not degraded, even though the pH was close to 7. Probably the degradation is influenced by temperature and further studies need to be done in order to analyze the different parameters that influence the degradation of the silica shell.

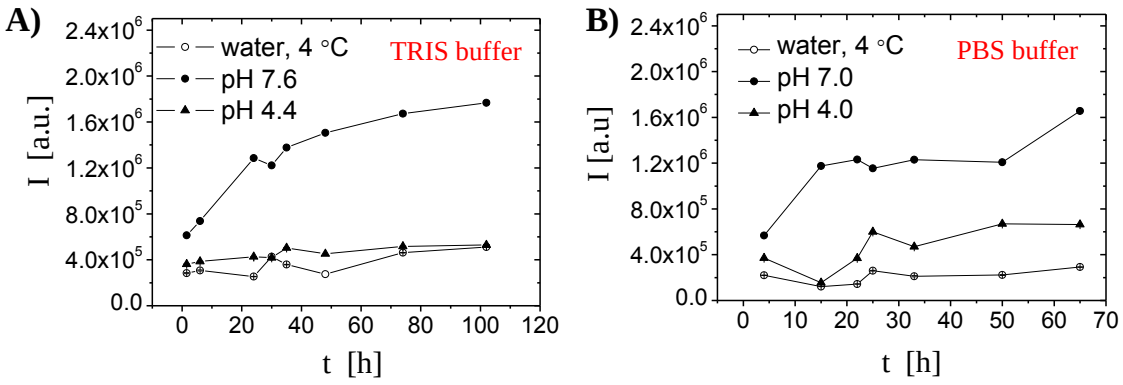

Figure SI.VI.1. Time-dependent degradation of 1-SiO_2 capsules loaded with dextran-TRICT (155 kDa) performed in TRIS and PBS buffers. I denotes the fluorescence of released dextran-TRICT in the supernatant, after different incubation times t. (A): (•) TRIS buffer at pH 7.6 and 37 ºC, (▲) TRIS buffer at pH 4.4 and 37 ºC, and (○) Milli-Q water at 4 ºC. (B): (•) PBS buffer at pH 7.0 and 37 ºC, (▲) TRIS buffer at pH 4.0 and 37 ºC, and (○) Milli-Q water at 4 ºC.

VII) Light-mediated release into the cytosol

In this section we present more images of the cytosolic release from light-responsive silica and polyelectrolyte capsules. The experimental set-up is described in detail in the main manuscript.

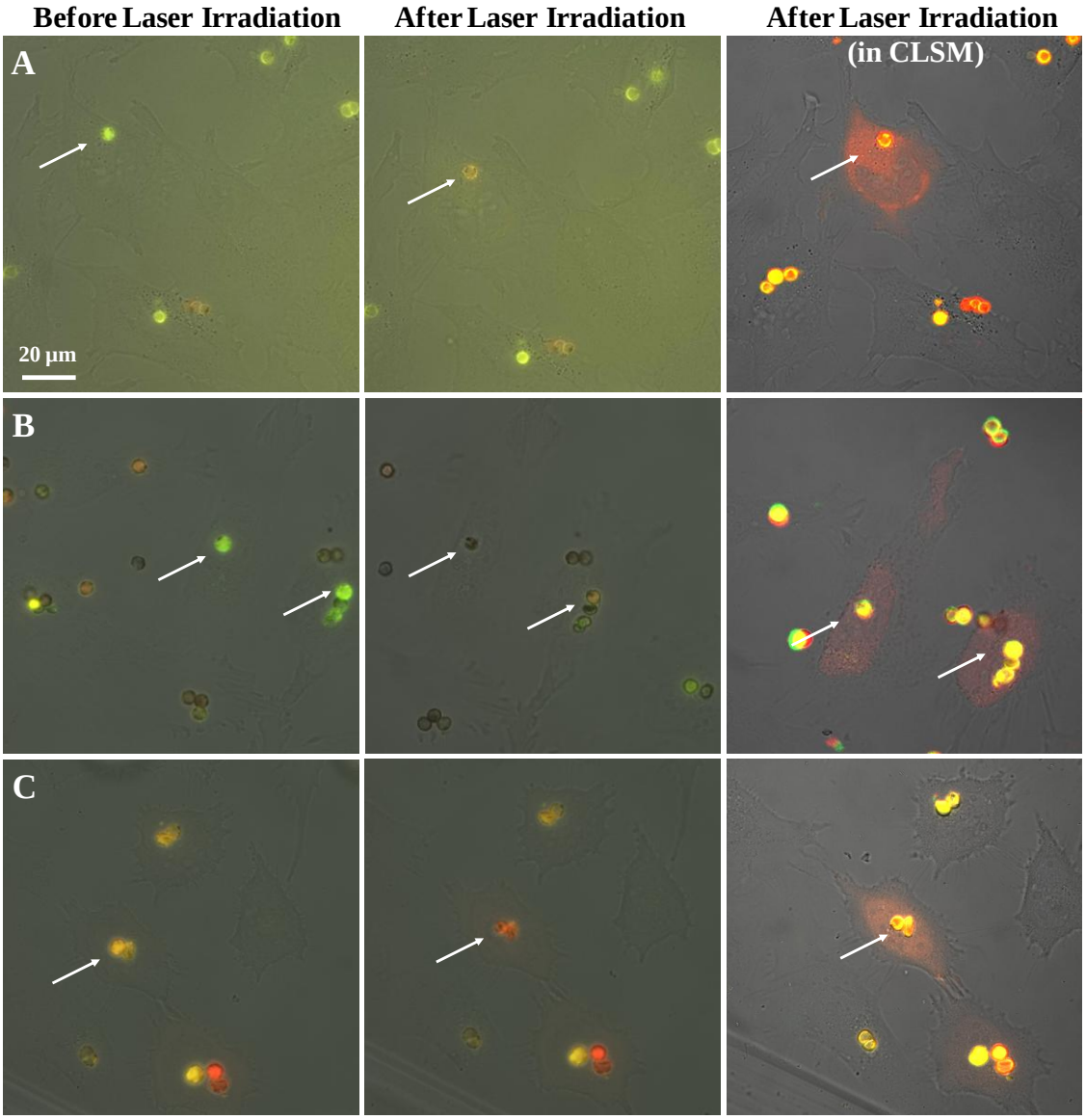

Figure SI.VII.1 Images demonstrating the opening and the cytosolic release of dextran-SNARF (10 kDa) encapsulated in the inner cavity of capsules functionalized with Au NPs. (A) 1-Au-SiO_2, (B) 2-Au(DEXS/PARG), and (C) 3-Au(PSS/PAH). In the images, the irradiated capsules changed the fluorescence emission (from

yellowish to orange-red) due to the pH change upon the rupture of the acidic compartment (lysosome) in which they are located after cellular internalization.[5] Confocal laser scanning microcopy (CLSM) was used to observe the homogeneous cytosolic release of SNARF-dextran. A laser power density of 3.5 $\mu W/\mu m^2$ had been applied for a few seconds for the opening of the capsules.[5] The scale bar corresponds to 20 μm.

VIII) References

(1) Okhrimenko, D. V.; Nissenbaum, J.; Andersson, M. P.; Olsson, M. H. M.; Stipp, S. L. S. *Langmuir* 2013, *29*, 11062-11073.

(2) Fernandez-Lopez, C.; Mateo-Mateo, C.; Alvarez-Puebla, R. A.; Perez-Juste, J.; Pastoriza-Santos, I.; Liz-Marzan, L. M. *Langmuir* 2009, *25*, 13894-13899.

(3) Guerrero-Martinez, A.; Perez-Juste, J.; Liz-Marzan, L. M. *Adv. Mater.* 2012, *22*, 1182-1195.

(4) Behera, M.; Ram, S. *Nano Lett.* 2013, *3*, 17/1-17/7.

(5) Carregal-Romero, S.; Ochs, M.; Rivera Gil, P.; Ganas, C.; Pavlov, A. M.; Sukhorukov, G. B.; Parak, W. J. *J. Controlled Release* 2012, *159*, 120-127.

(6) De Cock, L. J.; De Koker, S.; De Geest, B. G.; Grooten, J.; Vervaet, C.; Remon, J. P.; Sukhorukov, G. B.; Antipina, M. N. *Angew. Chem., Int. Ed.*2010, *49*, 6954.

(7) Muñoz Javier, A.; del Pino, P.; Bedard, M. F.; Skirtach, A. G.; Ho, D.; Sukhorukov, G. B.; Plank, C.; Parak, W. J. *Langmuir* 2008, *24*, 12517-12520.

(8) De Koker, S.; De Geest, B. G.; Cuvelier, C.; Ferdinande, L.; Deckers, W.; Hennink, W. E.; De Smedt, S.; Mertens, N. *Adv. Funct. Mater.* 2007, *17*, 3754-3763.

(9) De Geest, B. G.; Sanders, N. N.; Sukhorukov, G. B.; Demeester, J.; De Smedt, S. C. *Chem. Soc. Rev.* 2007, *36*, 636-649.

(10) Donath, E.; Sukhorukov, G. B.; Caruso, F.; Davis, S. A.; Möhwald, H. *Angew. Chem., Int. Ed.* 1998, *37*, 2202-2205.

(11) Caruso, F. *Chem.- Eur. J.* 2000, *6*, 413-419.

(12) Rivera_Gil, P.; del Mercato, L. L.; del Pino, P.; Muñoz-Javier, A.; Parak, W. J. *Nano Today* 2008, *3*, 12-21.

(13) Rivera_Gil, P.; Koker, S. D.; De_Geest, B. G.; Parak, W. J. *Nano Lett.* 2009, *9*, 4398-4402.

(14) Krzyzanek, V.; Sporenberg, N.; Keller, U.; Guddorf, J.; Reichelt, R.; Schoenhoff, M. *Soft Matter* 2011, *7*, 7034-7041.

(15) Yuan, W.; Lu, Z.; Li, C. M. *J. Mater. Chem.* 2011, *21*, 5148-5155.

(16) Kolbe, A.; del Mercato, L. L.; Abassi, A. Z.; Rivera_Gil, P.; Gorzini, S. J.; Huibers, W. H. C.; Poolman, B.; Parak, W. J.; Herrmann, A. *Macromol. Rapid Commun.* 2011, *32*, 186-190.

(17) Tong, W.; Zhu, Y.; Wang, Z.; Gao, C.; Möhwald, H. *Macromol. Rapid Commun* 2010, *31*, 1015-9.

(18) Ochs, M.; Carregal-Romero, S.; Rejman, J.; Braeckmans, K.; De Smedt, S. C.; Parak, W. J. *Angew. Chem., Int. Ed.* 2013, *52*, 695-699

(19) Alexander, C. M.; Maye, M. M.; Dabrowiak, J. C. *Chem. Commun.* 2011, *47*, 3418-3420.

(20) Wiederschain, G. Y. *The Molecular Probes handbook. A guide to fluorescent probes and labeling technologies*, 2011; Vol. 76.

(21) Bergstroem, F.; Mikhalyov, I.; Haeggloef, P.; Wortmann, R.; Ny, T.; Johansson, L. B. A. *J. Am. Chem. Soc.* 2002, *124*, 196-204.

(22) Ulrich, G.; Ziessel, R.; Harriman, A. *Angew. Chem., Int. Ed.* 2008, *47*, 1184-1201.

(23) Mikhalyov, I.; Gretskaya, N.; Bergstroem, F.; Johansson, L. B. A. *Phys. Chem. Chem. Phys.* 2002, *4*, 5663-5670.

(24) Kastl, L.; Sasse, D.; Wulf, V.; Hartmann, R.; Mircheski, J.; Ranke, C.; Carregal-Romero, S.; Martínez-López, J. A.; Fernández-Chacón, R.; Parak, W. J.; Elsaesser, H.-P.; Rivera_Gil, P. *ACS Nano* 2013, *7*, 6605-6618

(25) Merdan, T.; Kunath, K.; Fischer, D.; Kopecek, J.; Kissel, T. *Pharm. Res.* 2002, *19*, 140-146.

(26) Rejman, J.; Tavernier, G.; Bavarsad, N.; Demeester, J.; De Smedt, S. C. *J. Controlled Release* 2010, *147*, 385-91.

Nano Today (2013) 8, 480—493

Available online at www.sciencedirect.com

ScienceDirect

journal homepage: www.elsevier.com/locate/nanotoday

REVIEW

Distance control in-between plasmonic nanoparticles *via* biological and polymeric spacers

Xiang Yu[a,1], Dang Yuan Lei[b,1], Faheem Amin[a], Raimo Hartmann[a], Guillermo P. Acuna[c], Andrés Guerrero-Martínez[d], Stefan A. Maier[e], Philip Tinnefeld[c], Susana Carregal-Romero[a,f], Wolfgang J. Parak[a,g,*]

[a] *Fachbereich Physik, Philipps Universität Marburg, Marburg, Germany*
[b] *Department of Applied Physics, The Hong Kong Polytechnic University, Hong Kong, China*
[c] *NanoBioScience Group, Institute for Physical and Theoretical Chemistry, TU Braunschweig, Braunschweig, Germany*
[d] *Departamento de Química Física I, Facultad de Ciencias Químicas, Universidad Complutense, Madrid, Spain*
[e] *Department of Physics, Imperial College London, London, United Kingdom*
[f] *BIONAND, Andalucian Center for Nanomedicine & Biotechnology, Málaga, Spain*
[g] *CIC Biomagune, San Sebastian, Spain*

Received 4 May 2013 ; received in revised form 21 August 2013; accepted 2 September 2013
Available online 3 October 2013

KEYWORDS
Colloidal nanoparticles;
Plasmonics;
Biological linkers;
Polymeric linkers;
Size distribution

Summary For detailed experimental studies about the electromagnetic coupling between plasmonic nanoparticles, precisely-controlled nanoparticle groupings with adjustable inter-particle distance would be required. In the present review article, the possibilities of generating such groupings by using biological and polymeric spacers in between the nanoparticles are described. In particular, streptavidin—biotin and DNA are discussed as biological spacers, and layer-by-layer (LbL) assembled films as polymeric spacers. The concepts are visualized by experimental data, which also point out the pitfalls and current limits of such approaches. Calculation results reveal that while small variations in the diameter of plasmonic cores lead to small changes, small variations in the inter-particle distance due to soft linkers result in significant

* Corresponding author at: Fachbereich Physik, Philipps Universität Marburg, Marburg, Germany.
E-mail address: wolfgang.parak@physik.uni-marburg.de (W.J. Parak).
[1] Both authors contributed equally to this work.

1748-0132/$ — see front matter
http://dx.doi.org/10.1016/j.nantod.2013.09.001

changes in plasmonic coupling. In the case of protein-based spacers, nonspecific adsorption has to be considered as an obstacle for the formation of controlled groupings.

Introduction

Plasmonic nanoparticles (NPs) are a very exciting class of nanomaterials, in which the collective oscillation of conduction electrons on their resonant excitation by light (the so-called surface plasmon resonance, SPR) is exploited. Potential applications [1—3] comprise such diverse areas as sensing of (biological) molecules [4—6], for example by making use of localized enhancement of the electric field, photothermal heating [7—9], which makes use of localized production of heat caused by the conversion of surface plasmons to vibrations inside the ionic lattice during the plasmon decay, solar cells [10], optical filters [11], *etc*. Single metal NPs have a specific plasmon band depending on their material, size, shape, stabilizing agent but also on the roughness of their surface [12—15]. If brought to close distance, excited plasmons of adjacent NPs can couple, which can have significant impact on their optical properties. One prominent example is the change from red to blackish-blue color of suspensions of Au NPs upon (controlled) agglomeration, which is frequently exploited as read-out for sensing of analytes [4,16—18].

Coupling of plasmons is highly distance dependent and thus experimental procedures for NP assemblies with controlled spacing between the NPs are needed [19]. One approach in this direction is the generation of plasmonic structures on surfaces, in particular with lithography and related technologies [20—22], such as focused ion beam [23], or atomic force microscopy [24]. This approach offers amazing flexibility in the design of plasmonic patterns, but is often limited to creating very small defined distances of a few nanometers between the individual regions of the patterned plasmonic material. Note that lithography-free self-assembly methods, mainly based on the use of block copolymers as templates, has also emerged as a useful technique for creating plasmonic NP patterns over a large area [25,26]. For very small structures the assembly of colloidal plasmonic NPs offers an alternative approach [27]. Plasmonic NPs can easily be incorporated in macromolecular matrices, which can be, for example, formed by polymer assemblies [28—30] or other interconnected molecules such as cross-linked DNA [31]. Though the inter-NP distance in such assemblies is not controlled precisely, in the aforementioned examples coupling of plasmons between the adjacent NPs has remarkable effects, for example, on photothermal heating. However, in order to better study plasmonic coupling effects on a fundamental research level precisely defined inter-NP spacings would be desirable.

Self-assembled 2-dimensional NP lattices on a millimeter scale have been demonstrated [32—34]. Within these 2-dimensional lattices the NPs are virtually perfectly aligned and have a precisely defined inter-NP distance. However, these patterns have arguably limited flexibility in adjusting the spacing between adjacent NPs, and most importantly, they involve always a large number of NPs. Though these 2-dimensional NP lattices are perfectly suited for investigating collective plasmonic coupling, for a fundamental analysis small groupings of plasmonic NPs with defined geometry and controlled distance are of particular interest. Such controlled assemblies of colloidal plasmonic NPs can be made using biological or polymeric molecules as glue and spacers. The formation of such assemblies and in particular also the practical pitfalls and limitations of such approaches are the topic of this article. Besides a review about respective synthesis protocols, some experimental examples are given to demonstrate some of the principles. In contrast to previous reviews on the same topic [35], the embedded experimental section specifically points out the current experimental pitfalls and limitations. Thus we demonstrate for example that protein (streptavidin)-mediated coupling has low specificity and this unwanted interaction between the NPs is stronger than for example in the case of DNA-mediated coupling.

Requirements for NP assemblies concerning their usefulness in combination with theoretical predictions

Naturally, homogeneity of the experimental samples must be good enough that effects due to variations in the sample are smaller than the actual contribution of plasmonic coupling. Localized plasmons themselves depend on size, shape, and coating of the NPs, and plasmon coupling from the inter-NP distance. How narrow must the size distribution and the inter-NP distance distribution be that theoretically predicted effects of plasmonic coupling can be clearly observed? For reasons of simplicity we will focus on dimers of Au NPs, *e.g.* pairs of spherical Au NPs with an inorganic core diameter d_c and a distance D between the surfaces of the Au cores (*cf*. Fig. 1). It has to be noted that the surface of the Au cores is not the actual surface of the NPs, as in order to stabilize the NPs they need to be capped with typically an organic shell for providing steric or electrostatic repulsion

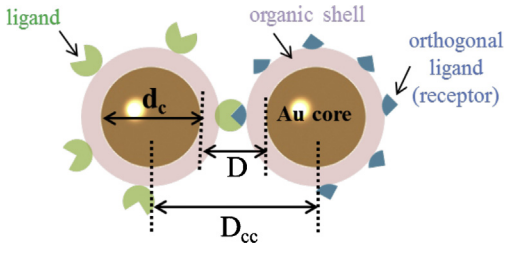

Figure 1 Dimer formation between two Au NPs in solution. Each Au NP is stabilized with an organic shell. The shell can optionally be functionalized with molecular ligands which promote NP binding *via* receptor—ligand specific interaction. As parameters the diameter of the inorganic (Au) part of the NPs (d_c), the distance between the Au surfaces of the adjacent NPs (D), and the distance between the centers of both NPs (D_{cc}) are indicated.

[30]. The Au NPs within one dimer are bound together by using functional groups present on the organic shell around the metallic Au core as molecular linkers/spacers. Such linkage can be provided by electrostatic attraction or more sophisticated *via* receptor—ligand interaction.

There are three main different approaches for forming dimers in solution. In the first approach, the whole surface of the Au NP has complementary ligands (*e.g.* one NP is modified with ligands specific for receptor molecules present on the other NP) or complementary charge, which promotes NP—NP binding. Such binding is a statistical process leading to a distribution of NP groupings with different amounts of NPs. Formation of dimers (or more precisely formation of smaller NP groupings) can be enriched by diluting the NP solution, minimizing the reaction time, in addition to fractionation after formation of the NP grouping. Though this method leads to an enriched proportion of NP dimers, there will be still also groupings of other stoichiometry present. In contrast, the second approach is based on the possibility of having only one functional group on the surface of each NP, which binds specifically to the other (complementary) functional group present on the surface of the other Au NP. Upon specific NP—NP binding, dimers are formed in this way. The task hereby lies in the monofunctionalization of the NPs [36]. Examples of both approaches will be demonstrated later. The third approach for forming NP dimers is based on trapping the NPs at the interface of a micro-emulsion using an amphiphilic block-copolymer, followed by the evaporation of the organic phase. Compared to the aforementioned two approaches, this method also enables the formation of NP clusters with controlled coordination number and high symmetry [37].

The changes of the plasmon resonance band upon the formation of dimers by bringing single NPs together can be simulated by the three-dimensional Finite-Difference Time-Domain (FDTD) method [38]. In Fig. 2A—D the extinction spectra of Au NP dimers with their characteristic plasmon peaks are shown in dependence of the Au core diameter d_c, and the distance D between the surfaces of Au cores. The data shows the dependence of red-shift in the plasmon peak due to plasmonic coupling as a function of D and d_c for a constant d_c and D, respectively. A summary of the dependencies shown in Fig. 2A—D is given in Fig. 2E—F.

It can be clearly seen from Fig. 2A and B that the localized plasmon resonance of NP dimers strongly red-shifts with decreasing the inter-NP distance. For example, the plasmon resonance wavelength red-shifts from ~530 nm to ~760 nm when reducing the inter-NP distance from 3 nm to 0.1 nm for a fixed NP diameter of 50 nm (see Fig. 2B). Moreover, by comparing the results in Fig. 2A and B, we find that for a fixed inter-NP distance, the dimer consisting of bigger NPs usually shows a larger red-shift than that consisting of smaller NPs. This difference can be understood by the fact that bigger NPs in a dimer often have a larger near-field interaction area with each other than the smaller ones, which results in stronger plasmonic coupling and a subsequent larger red-shift. Therefore, it is easier to observe plasmonic coupling effects in dimers consisting of larger NPs. At last, we notice that new resonances in the short-wavelength range emerge for dimers with extremely small inter-NP distances ($D \leq 0.2$ nm for $d_c = 5$ nm and $D \leq 1$ nm for $d_c = 50$ nm). For example, another two peaks appear in the short-wavelength range of the extinction spectrum for the dimer of $d_c = 50$ nm and $D = 0.1$ nm as shown in Fig. 2B. This observation is consistent with previous studies for nanowire dimers [39]. When the inter-NP distance approaches to zero, *i.e.* upon the formation of a singular touching point, the extinction spectrum of the dimer is expected to become continuous over a large spectral range due to the emergence of a large number of new resonances and their overlap with each other [40]. The dependence of the plasmon resonance wavelength on the inter-NP distance is summarized in Fig. 2E. The exponential behavior observed for both NP diameters comes from the fact that the evanescent electric field around each NP has an exponential decay with the distance, thus resulting in an exponential decay of the plasmonic coupling strength in the dimer.

Fig. 2C and D plots the extinction spectra for NP dimers of different diameters at a fixed inter-NP distance. We can see from Fig. 2C that increasing the NP diameter results in a slight red-shift for small NPs ($d_c = 3$—10 nm) with an inter-NP distance of 3 nm. Once the NP diameter increases and the inter-NP distance decreases (see Fig. 2D), the red-shift of the plasmon resonance becomes more significant because the plasmonic coupling effect is largely boosted up. These results are summarized in Fig. 2F. Different from the inter-NP distance dependence, the plasmon resonance wavelength shows a nearly linear dependence on the NP diameter at a fixed inter-NP distance for small NPs, and this linear relationship is even more obvious for large NPs (see the inset in Fig. 2F). Note that for NPs bigger than 10 nm the peak red-shift is a fully electrodynamic effect due to phase retardation, while for NPs smaller than 10 nm (*i.e.* in the quasi-static regime) the dependence of the permittivity of metals induced by quantum confinement has to be taken into account in order to have an accurate description of the plasmonic coupling effects [41], which is beyond the scope of this work.

Homogeneity of NP samples

Plasmonic NPs can be made from different materials, such as noble metals (Au, Ag, Pt), but also from metal alloys such as Al_xAg_{1-x} [42], CuTe [43], and $Cu_{2-x}Se$ [44]. In order to be colloidally stable the surface of the NPs needs to be coated, typically by organic molecules, which either provide steric or electrostatic repulsion [45,46]. Though different NP materials and different synthesis methods may lead to different surface chemistries, there are two approaches which work virtually for all plasmonic materials. First, as thiol groups stick to NPs of the above mentioned materials, the surface of the NPs can be modified using ligand exchange procedures involving thiol anchors [47]. Second, NPs can be wrapped in polymer shells either driven by electrostatic [48] or hydrophobic [49,50] forces, whereby the details of the original surface capping are in first order negligible. Thus, plasmonic NPs of nearly all materials can be coated or modified with the same (or at least highly similar) surface chemistry, which enables the approaches described in the following to be general and applicable for NPs made from all materials. For this reason and for the sake of simplicity we focus in the following on the example of Au NPs.

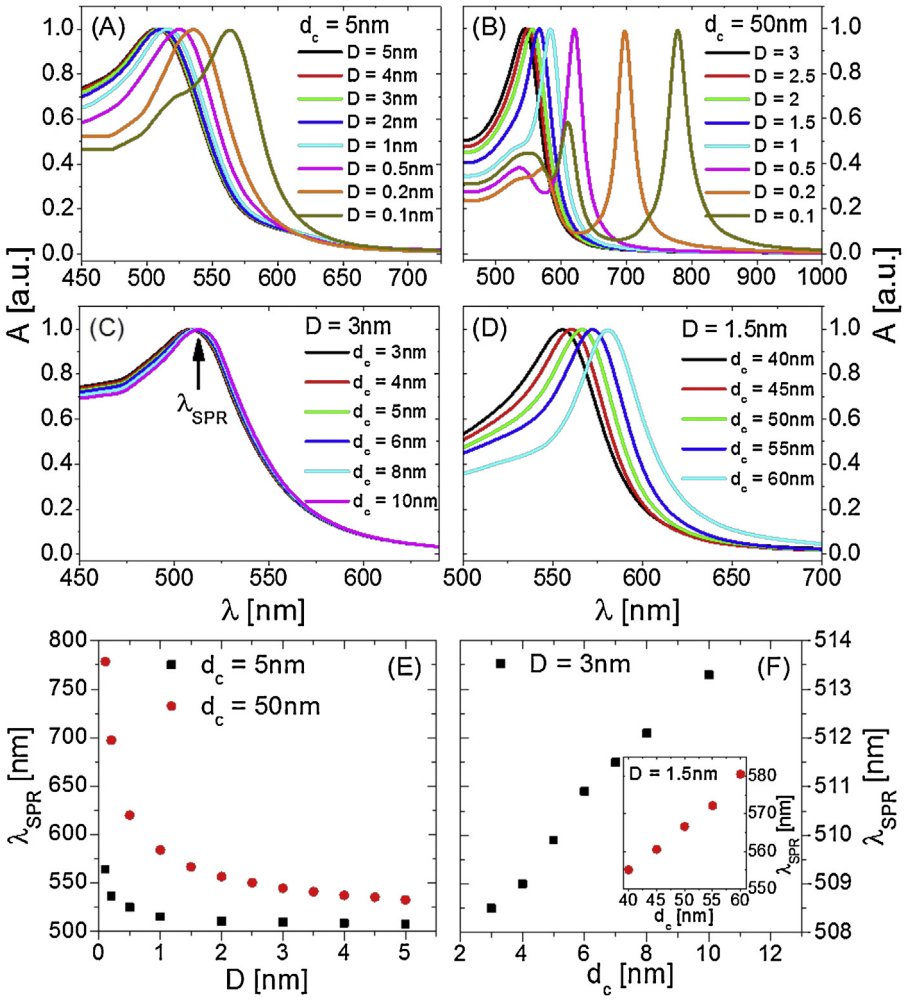

Figure 2 Plasmonic extinction response for NP dimers as a function of core diameter d_c and distance D between the surfaces of NP cores. Extinction spectra $A(\lambda)$ are shown for dimers of (A) $d_c = 5$ nm and (B) $d_c = 50$ nm (with variable D) and for dimers of (C) $D = 3$ nm and (D) $D = 1.5$ nm (with variable d_c). In the calculations a perfect spherical shape and a bare NP surface, *i.e.* Au cores without organic coating were assumed. The peaks in the extinction spectra, indicating the plasmon resonance wavelength λ_{SPR}, are plotted in (E) as a function of the distance D for dimers of $d_c = 5$ nm (black squares) and $d_c = 50$ nm (red circles), and in (F) for dimers of $D = 3$ nm (black squares) and $D = 1.5$ nm (inset, red circles).

Au NPs can be routinely synthesized with a variety of different protocols in different sizes and shapes (*e.g.* spherical, rod-shaped, star-shaped [51—55]) and they are also commercially available. Many strategies have been developed in order to tune the size of spherical Au NPs. The most commonly used synthesis is citrate-stabilized Au NPs as introduced by Turkevich et al. [56]. The synthesis is based on the reduction of Au^{3+} ions (in the form of $HAuCl_4$) by sodium citrate in boiling water. By varying the ratio of citrate/gold salt concentration, the solution pH, and the solvent, NPs of different sizes can be obtained. Nevertheless, NP quality in terms of shape, size, and size distribution as obtained with the original synthesis will be poor [57,58]. Seeded growth methods represent an advanced strategy to produce quasi-spherical Au NPs from 20 to 900 nm [59—62]. Though purification of the NP sample is often required, the quasi-spherical shape is better maintained in seeded growth methods than in the original one-step synthesis. Following the seeded growth strategy the presence of undesired Au NP shapes is as difficult to prevent as in the one-step synthesis, but the percentage of non-spherical NPs is at least reduced. Another aspect that has to be taken into account is the polyhedral morphology of large metal NPs as observed for gold or silver. Their surface cannot be considered smooth but faceted and rough [59]. NPs with similar size, composition, and shape can present slightly different plasmon bands due to the different surface roughness, leading to small differences in the plasmon coupling within dimers formed from similar metallic NPs [15].

Here we report on distributions in core diameter d_c and aspect ratio $s = d_{c,max}/d_{c,min}$ of nominally spherical commercial Au NPs. As the nominally spherical NPs in reality are rather asymmetric, we determined the minimum and maximum diameter $d_{c,min}$ and $d_{c,max}$, respectively, of each NP and calculated the aspect ratio s as information about the sphericity. In Fig. 3 the quasi-spherical shape of commercial citrate stabilized Au NPs [63] of different sizes has been analyzed with transmission electron microscopy

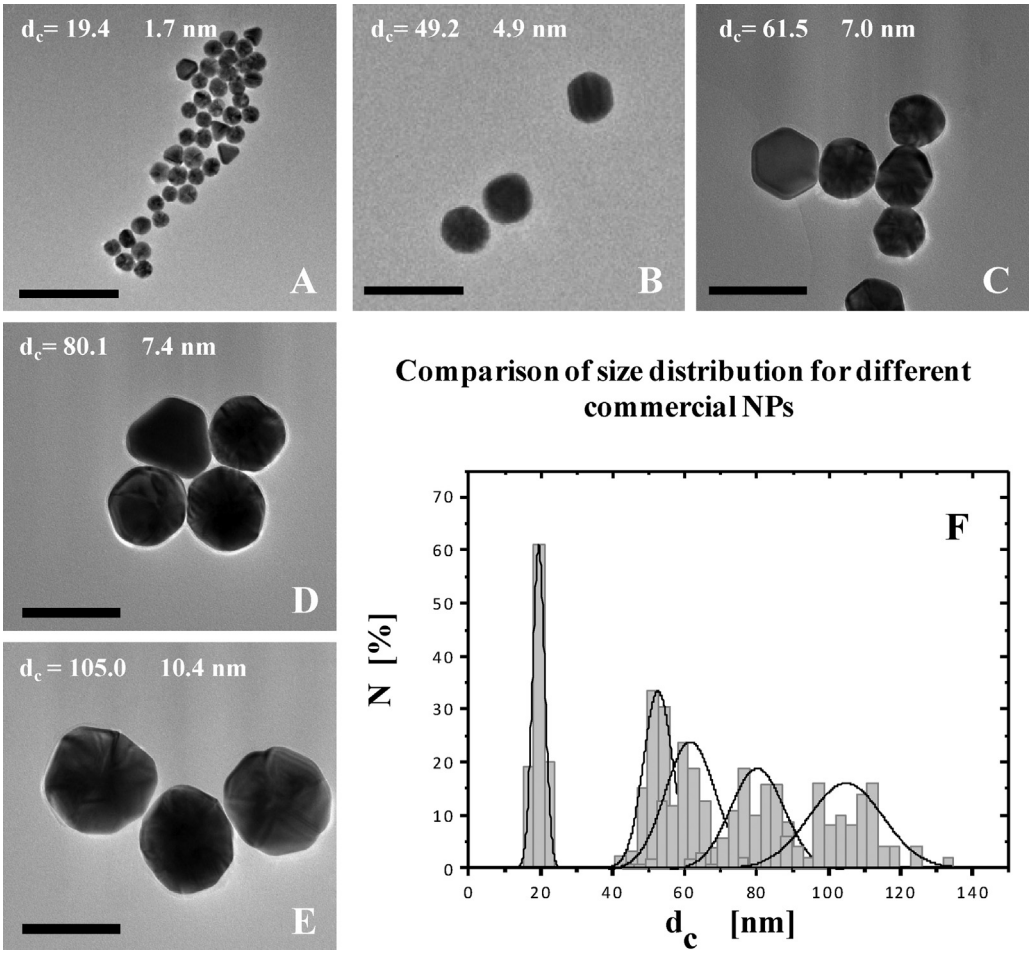

Figure 3 TEM images of commercial citric acid stabilized Au NPs of different core diameters (d_c): (A) 19.4 nm, (B) 49.2 nm, (C) 61.5 nm, (D) 80.1 nm and (E) 105.0 nm. The scale bars correspond to 100 nm. (F) In the histogram the size distribution $N(d_c)$ of the cores of the different sizes is shown and fitted with a Gaussian curve. From the fit the mean core diameters d_c and the standard deviation are derived. A similar statistics was previously published [65].

(TEM). Note that the contrast in TEM images originates from the Au cores, but not from the organic coating (in this case citric acid). The data indicate that the polydispersity of the NPs increases with the diameter of the NPs. The mean diameters and aspect ratios as obtained from the TEM data shown in Fig. 3 are summarized in Table 1. The aspect ratio of all the commercial NP samples was around $s = 1.1$, mainly caused by the presence of rod, triangular, or plate-like shape NPs as impurities. These impurities are produced during the synthesis of the quasi-spherical NPs as unwanted byproduct and are very difficult to remove from the solution because of their similar size. We further compared the commercial citric acid stabilized sample with custom synthesized Au NPs ($d_c \approx 50$ nm) which were also stabilized with citrate, *cf*. Table 1. We observed no significant differences in polydispersity ($d_c = 49.2 \pm 4.9$ nm for commercial Au NPs against $d_c = 49.3 \pm 6.7$ for custom synthesized Au NPs), aspect ratios ($s = 1.1$ in both cases), and the percentage of other residual NP shapes such as triangles, rods, or non geometrical forms, which has been determined to be less than 13% (*cf*. the Supporting Information). Therefore, studies about the formation of dimers were done with commercially available NPs with $d_c = 49.2 \pm 4.9$ nm. In addition, smaller NPs, as synthesized by the Brust method

Table 1 Core diameter (d_c) and aspect ratio (s) of citric acid stabilized commercial NPs of different sizes, of one batch polymer capped Au NPs[(1)], and of one batch of custom made citric acid stabilized NPs[(2)]. The hydrodynamic diameters d_c and the percentage of NPs with spherical shape Y and other residual shapes (*cf*. Supporting Information) were determined by analyzing TEM images with at least 250 NPs.

d_c [nm]	4.7[(1)] ± 0.8	19.4 ± 1.7	49.2 ± 4.9	49.3[(2)] ± 6.7	61.5 ± 7.0	80.1 ± 7.4	105.0 ± 10.4
s	1.08 ± 0.08	1.08 ± 0.06	1.11 ± 0.09	1.08 ± 0.06	1.10 ± 0.08	1.07 ± 0.05	1.13 ± 0.18
Y [%]	97.6 ± 0.8	84.1 ± 1.1	87.3 ± 0.9	86.2 ± 6.6	94.0 ± 0.9	85.8 ± 3.5	77.7 ± 4.2

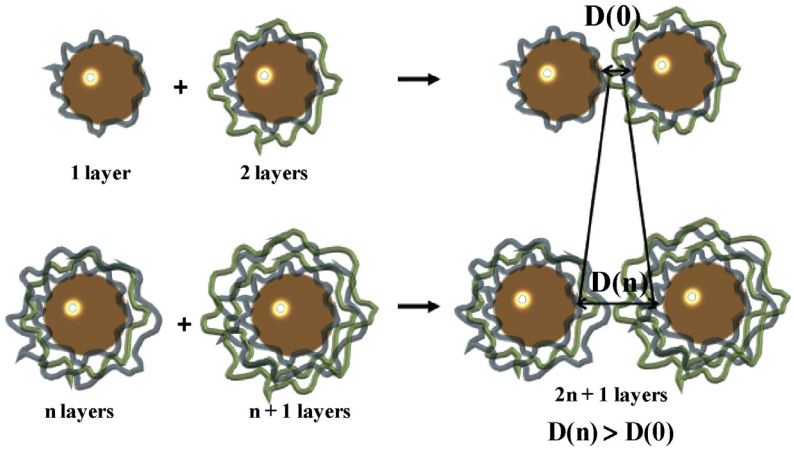

Figure 4 Schematic representation of the variation of inter-NP distance ($D(0)$, $D(1)$, ..., $D(n)$), defined as surface-to-surface distance, for dimers produced by electrostatic interactions between two NPs with an increasing number of charged polymer layers on the surface (where n is the number of PE layers).

[51] in organic solvent, followed by a phase transfer to aqueous solution by embedding them in a shell made out of an amphiphilic polymer [64] were also prepared. They were useful to analyze a second strategy for dimer formation. TEM studies determined a core diameter of $d_c = 4.7 \pm 0.8$ nm for these NPs (*cf*. Table 1). Thus TEM analysis provides an estimate about the polydispersity of the NP cores. For the bigger NPs the standard deviation of d_c corresponds to roughly 10% of the mean value; for the smaller NPs the standard deviation is bigger but the percentage of NPs with spherical shape is higher (*cf*. Supporting Information).

NP dimers generated by using polymer shells of controlled thickness as inter-NP spacer

Near-field interactions between plasmonic objects are distance dependent. This is not only true for plasmonic coupling of adjacent metal NPs, but also for enhancement/quenching effects of fluorophores close to plasmonic surfaces [66]. In order to investigate such properties the fluorophores can be linked to the NP surface at controlled distance. In this context, DNA [67] and polyethylenglycol (PEG) have been utilized as versatile molecular spacers [68,69]. More easily, the surface of plasmonic NPs can be covered with a thin insulating shell and the dye is then attached to the surface of the shell. This has been demonstrated for example with silica shells [70]. Alternatively, NPs can be coated also with multiple thin polyelectrolyte (PE) shells using the layer-by-layer self-assembly technique [48,71]. The technique is based on the electrostatically-driven alternated adsorption of cationic and anionic charged polymers in a layer-by-layer fashion, similar to the layer structure of an onion, *cf*. Fig. 4. Each layer contributes between 0.5 and 2 nm in thickness depending on the conditions during the self-assembly. In general, high ionic strengths favor the formation of thicker layers [72—74]. Though this technique has been applied to Au NPs as small as 7 nm [48,75], due to the required separation steps it is more suited for coating bigger NPs. By using different numbers of PE layers, shells with different thicknesses can be generated. Depending on the polarity the last polymer layer has, either positively or negatively charged NPs can be obtained. This gives the opportunity for an electrostatically-driven linkage. When negatively and positively charged NPs are mixed together under diluted concentrations, predominantly NP dimers will form besides some remaining NP monomers and some groupings which involve more than two NPs. Thus, the distance between the NP surfaces will be the sum of the thicknesses of the two PE shells around the NPs, *cf*. (Fig. 4).

Naturally the above described assembly will be statistical. When the reaction progresses in solution, bigger and bigger groupings of NPs will be formed. However, if the NPs are brought to a surface after appropriate reaction time, building-up of larger agglomerates can be avoided. In Fig. 5 such NP assemblies are shown. Around 30% of the NPs form dimers (*via* calculation of radial distribution functions, as will be described later), and the rest mainly remains as individual NPs, in addition to some bigger assemblies. Such moderate yield of dimers would exclude ensemble measurements (*e.g.* cuvette absorption spectroscopy) because the mixture of dimers with monomers usually results in a spectral broadening of the ensemble absorption peak compared to that of pure monomers, but the effect of plasmonic coupling may well be studied in a more quantitative way by monitoring the plasmon resonance shift through dark field analysis of individual dimers.

In our experiment, dimers have been formed from individual commercial citrate-stabilized Au NPs ($d_c = 49.2 \pm 4.9$ nm, $s = 1.1$) coated with (n) and ($n + 1$) layers of poly(styrene sulfonate) and poly(allylamine hydrochloride) both with around 15 kDa of molecular weight. The change of charge during the layer-by-layer coating process has been verified by zeta-potential measurements (*cf*. the Supporting Information). The mean thickness of each PE layer was $d_{PE} = 1.6$ nm as experimentally determined with dynamic light scattering (DLS) (*cf*. the Supporting Information). This value was considered as the maximum value of the thickness of each PE layer. In order to discriminate in the TEM images between dimers and free NPs or bigger groupings, we defined all pairs of NPs with a surface-to-surface distance below the thickness

Table 2 Surface-to-surface distance values D as obtained *via* TEM analysis for dimers ($d_c = 49.2 \pm 4.9$ nm, $s = 1.1$) made out of one NP with n and one NP with $n+1$ PE layers. The thickness of each PE layer d_{PE} was estimated as $d_{PE} = D/(2n+1)$.

n	1	2	3	4	5	6	7	8	9
D [nm]	0.64 ± 0.16	0.87 ± 0.2	1.01 ± 0.39	1.14 ± 0.16	1.06 ± 0.16	1.48 ± 0.85	1.42 ± 0.38	2.05 ± 0.55	2.53 ± 0.87
d_{PE} [nm]	0.21	0.17	0.14	0.12	0.10	0.11	0.09	0.12	0.13

of a theoretical $(2n+1)$ multilayer in which each layer is 1.6 nm thick, as dimers. Then, the inter-NP distance D was measured as the minimum surface-to-surface distance between NPs. Fig. 6 and Table 2 show the distance values D as measured for nine different dimers (with $n = 1-9$) with a growing number of PE layers on the Au NP surface.

The thickness of each PE layer $d_{PE}(n)$ for each dimer configuration n was calculated as $d_{PE} = D/(n+(n+1)) = D/(2n+1)$, as each dimer comprises one NP with n PE layers and another NP with $n+1$ PE layers. Results are summarized in Table 2. The average over all configurations leads to an average thickness per PE layer of $d_{PE} = 0.13 \pm 0.04$ nm. This value is quite below the value of $d_{PE} = 1.6$ nm as obtained by DLS. Discrepancies can be explained with differences in the detection methods. DLS, ellipsometry, atomic force microscopy (AFM), surface plasmon resonance (SPR) or quartz crystal microbalance (QCM) have been used to calculate the layer thickness of PSS and PAH coatings [76–78]. The obtained values were similar for all of them (around $d_{PE} = 1-2$ nm), even for different molecular weights of the PEs ranging from 15 to 76 kDa. TEM has also been applied to determine the thickness of every PE layer. Schneider et al. [72] determined through TEM image analysis the thickness of individual layers of PSS and PAH ($M_w \sim 15$ kDa) on Au NPs to be around $d_{PE} = 0.5$ nm, which is in the range of the layer thickness we have estimated by TEM, though slightly higher. TEM is in general not the best technique to estimate the thickness of shells of polymers, because they do not provide good contrast, and due to the vacuum conditions the PE shells shrink when they are dried on the TEM grid. DLS on the other hand determines hydrodynamic radii of NPs dissolved in aqueous solution, which involves swelling of the PE layers and also takes into account the adsorption of counter ions [79]. As pointed out above, the yield of dimers with the method described here is only 30% which excludes ensemble cuvette measurements of plasmonic coupling effects. In contrast, plasmonic coupling effects can be investigated more precisely at single NP level by using immobilized dimers or clusters. Such measurements are usually carried out either in air by using dark-field microscope [41] or in vacuum by using electron energy-loss spectroscopy (typically integrated in a TEM system) [80]. Thus TEM is to our opinion the most appropriate technique for determining D for the envisaged experimental conditions for investigating plasmonic coupling behavior within NP dimers which are immobilized on a substrate.

In Fig. 6, besides the specific D values for different configurations of dimers, the big standard deviation for every D obtained is noticeable. The deviations in these measurements are due to several factors (for a detailed analysis we refer to the Supporting Information). The first one is the polyhedral shape and the roughness of the NP surface. Moreover, the presence of a low percentage of plate-like, triangle or rod-shaped NPs also produces a deviation of the theoretical distance between two hard spheres with a specific shell thickness. Finally, dimers formed by non-specific agglomeration also need to be considered. To estimate the yield of NP dimers *via* non-specific agglomeration, we prepared a control sample in which the NPs were not coated with PE layers, and our TEM analysis reveals that the ratio of dimers through non-specific agglomeration to monomers is less than 5% (92.1% were monomers, 4.4% dimers and the rest other kinds of groupings).

In order to study the limits of producing dimers with tunable inter-NP distance D with PE coated Au NPs we increased the number of layers n up to 30 (*cf.* the Supporting Information). We found that D increased following approximately a linear trend and the determined layer thickness d_{PE} was consistently 0.13 ± 0.03 nm. However, for $n > 9$ the standard deviation of D increases dramatically, mainly due to the difficulty of producing PE coated Au NPs without non-specific agglomeration.

As mentioned above, inter-NP distances were derived from direct analysis of the TEM data. Due to the roughness of the NPs and their shape which is not perfectly spherical, estimations of NP distances based on determination of center-to-center distances D_{cc} between the NPs ($D = D_{cc} - d_c$) from the TEM images are less suitable, because they do not take into account these issues. This point is particularly important for large NPs with small inter-NP distances. Taking into account the polydispersity of NPs within the sample, such method could possibly lead to obtaining false values, such as negative values for D. Instead of direct determination of D_{cc} of individual dimers this value can also be calculated using the radial distribution/pair correlation function (RDF; for more details see the Supporting Information). RDF functions were calculated from different TEM images by using MATLAB (MathWorks) [79]. In case of two dimensions, the RDF is defined as $g(r) = N(r)/(2\pi \cdot r \cdot \rho \cdot dr)$, where $N(r)$ is the mean number of NPs which can be found in a ring of width dr at distance r from one NP, and ρ [m^{-2}] is the mean NP density. For each TEM image the NP positions were extracted and the RDF was generated with a binning distance dr of 1 pixel, equivalent to a spatial resolution of 0.5 nm. Artifacts due to image edges were reduced by dividing only through the fraction of the ring confined by the image dimensions instead of $2\pi r$. Finally, the distribution functions of all images were averaged. The percentage of dimers calculated through RDF analysis was around 30%. Assuming that two NPs touched each other, then there would be peak in the $g(r)$ distribution at $r = 2 \cdot (d_c/2) = d_c$. If there is a space between the NPs, the peak will be at higher r values.

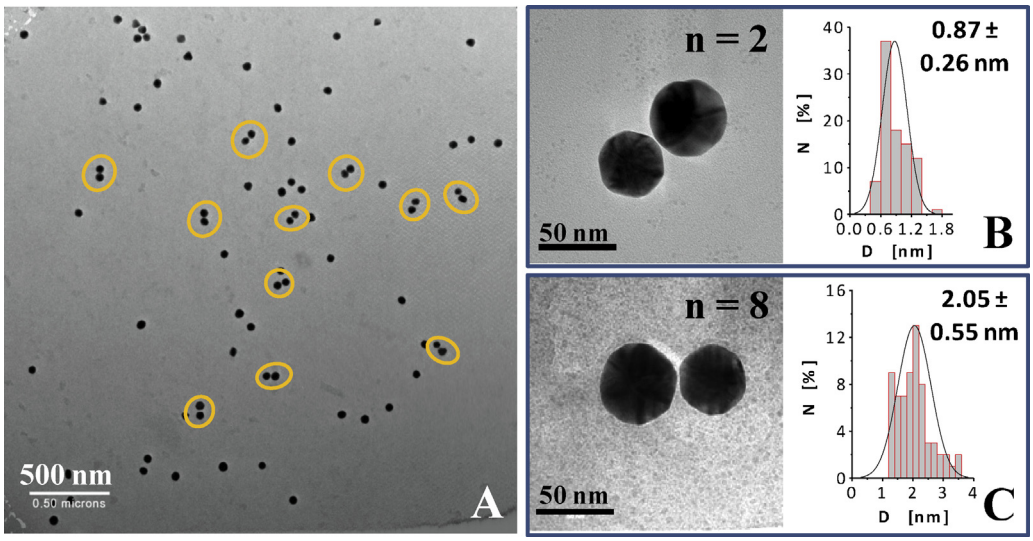

Figure 5 TEM images of dimers formed by electrostatic interactions between Au NPs ($d_c = 49.2 \pm 4.9$ nm, $s = 1.1$) coated with (n) and ($n+1$) number of PE layers. (A) 10 μm^2 area of a TEM grid which shows the abundance of dimers within the sample. (B) Dimers formed by mixing Au NPs coated with 2 and 3 PE layers and the distribution of the measured inter-NP distances. (C) Dimers formed by mixing Au NPs coated with 8 and 9 PE layers and the distribution $N(D)$ of the measured inter-NP distances.

Thus, the first peak in the $g(r)$ function refers to the center-to-center distance $r = D_{cc}$. The error ΔD_{cc} can be defined as the width at half-maximum of the peak $g(r = D_{cc})$. From the center-to-center distance D_{cc} the surface-to-surface distance D can be determined as $D = D_{cc} - d_c$. For the same data as shown in Figs. 5 and 6 we determined D_{cc} as a peak in the $g(r)$ distribution as $D_{cc} = 52 \pm 7$ nm ($n = 1$) and $D_{cc} = 54 \pm 13$ nm ($n = 9$), *cf.* the Supporting Information. Using the diameter of the NPs $d_c = 49.2 \pm 4.9$ nm yields to surface-to-surface distances $D = D_{cc} - d_c$ of $D = 2.8 \pm 0.5$ nm ($n = 1$) and $D = 4.8 \pm 1.3$ nm ($n = 9$). For the determination of the error we used $\Delta D/D = ((\Delta D_{cc}/D_{cc})^2 + (\Delta d_c/d_c)^2)^{1/2}$. In comparison to the direct determination of D from TEM images as shown in Fig. 6, the values for D here are much higher and have a larger error. This points out that for big NPs with

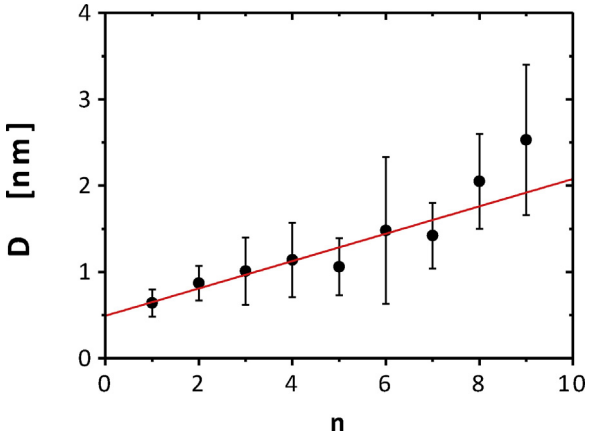

Figure 6 Inter-NP distance D of Au NPs dimers ($d_c = 49.2 \pm 4.9$ nm, $s = 1.1$) formed by electrostatic interactions between oppositely-charged NPs coated with (n) and ($n+1$) number of PE layers with $n = 1$–9. The red line is the linear regression that relates D and n.

$D_{cc} \approx d_c$ and thus $D \ll d_c$, direct determination of D from TEM images is the most reliable method. In the case of determination D as $D_{cc} - d_c$ the difference between two numbers of similar magnitude has to be calculated, which is quite prone to error. In particular, deviations due to surface roughness and non-spherical shape are the main reasons for bigger errors.

Our experimental values can now be compared to simulations. Experimentally we have one situation in which the Au NPs with $d_c = 49.2 \pm 4.9$ nm core diameter can be spaced with PE layers to a surface-to-surface distance of $D = 1.48 \pm 0.38$ nm ($n = 6$; *cf.* Table 2). What is the effect of the experimental uncertainties on plasmon coupling? On the one hand, Fig. 2F tells that for Au NPs with $d_c = 50 \pm 5$ nm (D fixed to 1.5 nm), the plasmon band lies in the interval $\lambda_{SPR} = 566 \pm 6$ nm. Thus, uncertainty in NP diameter plays a relatively weak role in the determination of the surface plasmon band. On the other hand, from Fig. 2E one can conclude that for Au NPs with $D = 1.5 \pm 0.7$ nm (d_c fixed to 50 nm), the position of the plasmon band is significantly affected: $\lambda_{SPR} = 566 \pm 12$ nm. Thus, fluctuations in the size distribution d_c play a minor role in comparison to variations in the surface-to-surface distance D as determined by the polymeric spacers. For practical purposes the size distribution of the present NPs is good enough, whereas distance control between the NPs should be improved.

NP dimers created by using biological linkers

Biological molecules can be used as molecular linkers for connecting NPs. For this purpose one NP needs to be modified with one molecule, and the other with a molecule which binds to the first one. Convenient linker systems which have been used in the past for this purpose are streptavidin (SA)—biotin (B), and complementary strands of DNA [81–85]. The trick of creating dimers starts with the modification

of NPs with the linkers. In case each NP has several linker molecules attached, it can eventually bind also to multiple NPs with the complementary linker, which would result in the formation of larger groupings [86]. Though the size of groupings can be reduced by appropriate reaction conditions (dilution, limited reaction time, mixing conditions), for an ultimate control of forming NP dimers in solution, NPs with exactly one linker per NP are required. Such control can be for example obtained by separation with gel electrophoresis [87–89] or by column chromatography [90,91]. In case NPs with a discrete number of linkers are fractionated by separation in size (such as in the case of gel electrophoresis or size-exclusion chromatography), the sample needs to be highly monodisperse and only small NPs can be used, as otherwise the increase in size upon binding of one single ligand does not create a sufficient change in size [89,92]. With the resulting NPs attached by a controlled number of linker molecules, defined structures such as dimers have been created [82,86]. One general problem associated with this approach is the size and flexibility of the linker molecules. As the SA-B system and complementary strands of DNA (for stable linkage typically at least 8 bases are required) have dimensions in the nm range, the smallest possible gap created by using such linkers will always be a few nm. Furthermore, biological linker molecules are flexible, with this intrinsic property being transferred to their attachment to the NP surface. Thus, in the case of NP dimers there will be a distribution of inter-NP distances, and hence the maximum distance is governed by the contour length of the linkers [86].

In our experiments, we illustrate the problem of biological linkers with the example of Au NPs linked together by the SA-B system. First, two types of Au NPs attached with exactly either one B molecule or one SA molecule per NP (Au-B or Au-B-SA) were prepared by fractionation with gel electrophoresis. They were mixed together and the resulting mixture was again fractionated with gel electrophoresis in order to separate the created NP dimers. Diluted solutions of dimers were then used for TEM image analysis. SA owns four identical binding pockets, each of which can accommodate one biotin (vitamin H) molecule [93]. The association between SA and B is among the strongest non-covalent bonds in nature. In addition to the creation of dimers, however, formation of trimers or bigger groupings is likely to happen simultaneously due to the non-specific adsorption process. Gel electrophoretic separation is thus a critical step in this strategy to form dimers. Fig. 7 shows TEM images of the nanoparticles at different steps in the formation of dimers *via* SA-B interaction. Fig. 7A renders the image of polymer-coated Au NPs ($d_c = 4.7 \pm 0.8$ nm in diameter) [94] (see the Supporting Information for more details), which were modified with exactly one biotin molecule per NP (Au-B NPs), or with exactly one SA molecule per NP (Au-B-SA NPs) [94,95] (see the Supporting Information for more details). The Au-B and Au-B-SA NPs were then mixed at a molar concentration ratio of 1:1, and the resulting Au-B-SA-B-Au dimers were fractionated *via* gel electrophoresis. Fig. 7B shows the corresponding TEM image, which demonstrates the successful formation of NP dimers. However, in the control sample of Au-B-SA NPs, some dimer-resembling NPs were also found. This result reveals the aforementioned general problem for NP assemblies linked *via* biological molecules: non-specific adsorption. If non-specific adsorption is not suppressed, bigger unwanted NP assemblies may be formed.

Traditional NP assemblies are based on linkage of Au NPs *via* complementary strands of DNA [81,96,97]. Although DNA also has some slight non-specific adsorption to NPs [89,98,99], the yield of intentionally formed dimers is relatively high, *i.e.* there are few remaining monomers and larger assemblies [86]. Proteins such as SA are known to tend to non-specifically adsorb to the surface of NPs, leading to the so-called protein corona [100,101]. Polymer-coated NPs with similar surface chemistry as the ones used in our present study can be covered with a monolayer of proteins [102], demonstrating the great extent of non-specific adsorption. Thus, in general, protein-coated NPs are ''sticky'' to other NPs, which may lead to unwanted NP agglomerates. The key issue in the formation of biomolecule-mediated NP assemblies is their quantitative analysis *versus* the background of non-specifically formed agglomerates. It is noteworthy that exactly the same technology can be employed for other NPs, such as fluorescent quantum dots of different colors (*cf.* the Supporting Information).

In order to analyze the amount of dimers formed by specific binding between Au-B and Au-B-SA NPs, and to quantify the surface-to-surface distance D, the RDF $g(r)$ was calculated as described above for each step of the dimer synthesis (see Fig. 7C). 20–40 different TEM-images (like the ones shown in Fig. 7), collected for Au NPs, Au-B NPs, Au-B-SA NPs, and Au-B-SA-B-Au dimers, were analyzed in detail. As in this case small Au NPs were used, the inter-NP distance was comparable to the NP diameter $D \approx d_c$ and direct surface-to-surface measurements turned out to be complicated. Therefore, RDFs were calculated in which the first maximum was assumed to be the center-to-center distance D_{cc} of two adjacent NPs and the surface-to-surface distance was derived as $D = D_{cc} - d_c$. In the case of Au NPs and Au-B NPs, $g(r)$ has almost no features and is more or less constant for all $r > D_{cc}$ (*cf.* Fig. 8C, $g(r)$ needs to be 0 for D_{cc}, as NPs cannot penetrate each other). This means that Au NPs as well as Au-B NPs are statistically distributed on TEM grids, without obvious interaction besides hard-core repulsion. In contrast, there is a sharp peak in the RDF for Au-B-SA-B-Au NP dimers at $r = D_{cc} = 7.0 \pm 3.0$ nm. This pronounced peak clearly indicates an attractive interaction between adjacent NPs, which are separated at an average center-to-center distance D_{cc}. However, there is also a peak in the RDF of Au-B-SA NPs at $r = D_{cc} = 7.5 \pm 2.7$ nm. This peak reveals the non-specific binding between Au NPs functionalized with SA that is mediated by the non-specific binding of proteins attached to every NP surface. The percentage of formed dimers was around 30% in both samples, Au-B-SA and Au-B-SA-B-Au. Due to the very similar center-to-center distances of non-specific Au-B-SA agglomerates and of specifically formed Au-B-SA-B-Au dimers ($D_{cc} = 7.5 \pm 2.7$ nm *versus* 7.0 ± 3.0 nm), it is impossible to distinguish between both cases from the TEM data. From this comparison, several conclusions can be drawn. First, for a quantitative understanding of NP groupings, simple visualization *via* TEM imaging is not sufficient and simple zooming of areas in which desired structures can be found are meaningless, as virtually anything can be found on the TEM grid if one searches long enough. Second, images over large areas, where many groupings are visible,

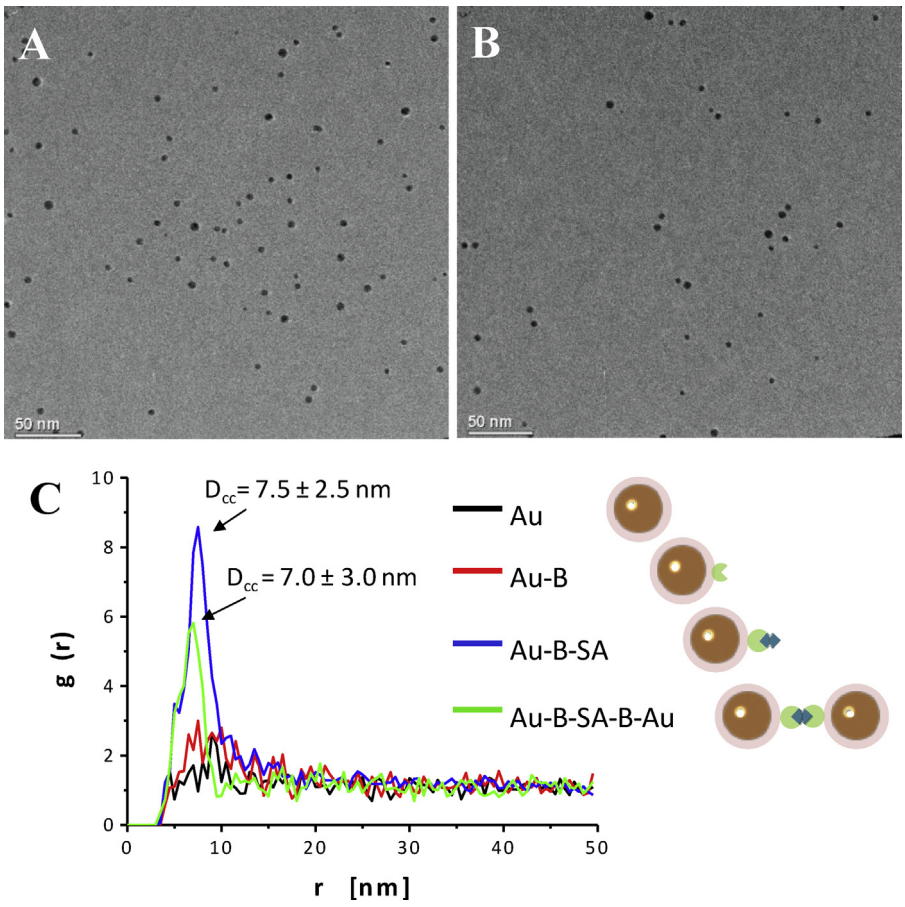

Figure 7 TEM images of (A) 4.7 ± 1.1 nm Au NPs, and (B) Au NP dimers formed by interaction within a 1:1 mix of Au-B and Au-B-SA NPs. Scale bars correspond to 50 nm. (C) Radial distribution functions (RDFs) of Au NPs, Au-B NPs, Au-B-SA NPs, and Au-SA-B-SA-Au dimers.

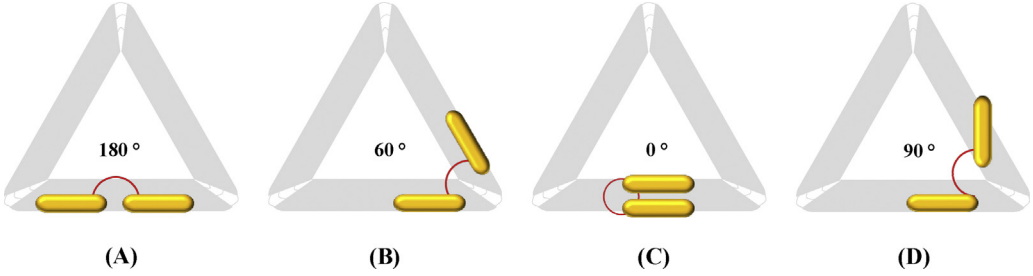

Figure 8 (A)—(D) Schematic representation of dimers constructed on triangular origami DNA where the angles between Au nanorods are 180, 60, 0 and 90°, respectively.

need to be shown in order to make a reliable conclusion about the dimer yield. Third, a quantitative analysis such as RDF calculations is required [86]. Specific formation of desired NP groupings needs to be compared with non-specifically formed small agglomerates. This effect cannot be neglected, as in the scenario (SA is more ''sticky'' than DNA) demonstrated experimentally in this study.

From the RDF the surface-to-surface distance D between the Au NPs in the case of SA-B mediated linkage can be calculated: $D = D_{cc} - d_c = 2.3 \pm 1.1$ nm with $d_c = 4.7 \pm 0.8$ nm. How do these distributions in D and d_c affect plasmon coupling? From Fig. 2F we can conclude that a finite size distribution of core diameter virtually has no effect on plasmon coupling: $d_c = 5 \pm 1$ nm ($D = 3$ nm fixed) $\Rightarrow \lambda_{SPR} = 510 \pm 1$ nm. Moreover, the relatively high fluctuation in surface-to-surface distance due to biological linkage has only a moderate effect, as the data from Fig. 2E shows: $D = 2.5 \pm 1.0$ nm ($d_c = 5$ nm fixed) $\Rightarrow \lambda_{SPR} = 515 \pm 5$ nm. Thus, for small NPs with diameters (here around 5 nm) comparable to the inter-NP distance D values, the effect of fluctuations ΔD has much less effect compared to bigger NPs (here around 50 nm).

NP dimers using rigid templates?

NPs can be also assembled using rigid (biological) templates, which may potentially result in smaller fluctuations $\Delta D/D$

[35]. Very interesting initial templates in this direction are 2-dimensional lattices of DNA, as introduced by Nadrian Seeman and coworkers [103,104]. Moreover, recent efforts have led to the design of nanoplasmonic materials with controlled 3-dimensional structures and morphologies using chiral rigid templates [105—107]. These geometries are better suited for the fabrication of periodic NP assemblies than for the creation of individual dimer structures. Because the templates have large dimensions and are usually fixed to a surface, mono-functionality of the NPs is required and inter-NP crosslinking is unlikely to happen. The introduction of DNA origami brought new flexibilities [108] for assembling nanostructures. In DNA origami structures, a long scaffold strand is hybridized with ~200 short, so-called staple strands to form predefined two- or three-dimensional objects. With scaffold strands of roughly 8000 bases, typical dimensions of DNA origami structures are 70 nm × 100 nm for a rectangular arrangement. DNA origami thus represents a molecular pegboard-like platform to which NPs can be attached with high accuracy using hybridization to single strands protruding from the DNA origami. In principle, DNA origami can provide subnanometer accuracy in placing objects [109]. In addition, more flexibility can be induced by the linkers between the DNA origami and NPs, which are commonly connected *via* several DNA strands. A recent estimate yielded a ~4 nm standard deviation as the upper limit of the distance distribution between a 10 nm (Au) NP and a fluorescent dye [110], where the NP had been connected to the DNA origami template by three DNA strands of 17 bases. A large fraction of this heterogeneity is static, and the position is comparably stiff for a single NP-dye pair, but varies for different pairs. The hybridization between strands can be performed in solution or by following surface immobilization of the DNA origami structure. The latter strategy has the advantages that less amount of sample is required and agglomeration is prevented.

Among others, the group of Hao Yan has been particularly active in this field developing DNA origami structures with spherical Au and Ag NPs of sizes up to 20 nm, forming monomers, dimers [111] and even self-similar nanoparticle chain structures [112]. Additionally, the same group was able to bind Au nanorods [113] at particular positions within a triangular DNA origami structure to form dimers at different angles, see Fig. 8.

The main drawback of employing DNA origami structures as a pegboard is that the lower limit for the distance D is constrained by the length of the linkers (capturing strands). In contrast, using surface immobilization NP dimers as big as 100 nm or structures of higher complexity are easily realized with high yields [65]. Since DNA origami structures are more rigid than, for example, double stranded DNA [114] and more complex 3-dimensional structures can be designed, in principle, it is possible to achieve any arbitrary arrangement of NPs of different materials and sizes. Furthermore, not only NPs can be arranged with respect to each other, but also molecules such as fluorescent dyes can be positioned within the DNA origami and with respect to the nanoparticles. This ability would become important for analytic assays in which changes of the plasmonic coupling or fluorescence enhancement are used to detect binding of an analyte [65,115]. The error $\triangle D$ arises mainly from the different numbers of capturing strands on the DNA origami employed to incorporate the NPs, typically three for spherical NPs and more for less symmetric structures such as nanorods, and also from the length of the strands which are generally not shorter than 15 bases. Based on the TEM images and on fluorescence quenching experiments, $\triangle D$ was estimated to be around ~4 nm [110,113] to first order, independent of the NP size. In single-molecule measurements where some of the authors also tried to control the orientation of NP dimers with respect to the excitation polarization, an additional source of inhomogeneous broadening is the distribution of orientations of the dimer axis [65,116]. Despite some efforts to align the DNA-NP-dye arrangement on the surface by selective B-SA chemistry, a significant orientational spread remained stemming already from the relative DNA-surface orientation [65].

Current limitations and future perspectives

Au NP dimers with perfectly tunable inter-NP distances are still difficult to be produced in large scale and high accuracy, particularly at small inter-NP distances. Nanolithography and related techniques are limited in creating very small and well-defined inter-NP distances of few nanometers. Alternatively, polymers and biomolecules can be used as spacers to tune the inter-NP distances of colloidal NPs. In principle, using colloidal approaches to achieve inter-NP distances below 1 nm is possible, which is required for the detection of quantum plasmonic effects such as charge transfer plasmons [117—119]. However, agglomeration due to non-specific attractive interaction between the NPs can be easily confused with the formation of dimers. In particular, protein-modified NPs are prone to this source of error. In other words, biological linkers are sticky. This unwanted effect can be reduced by using NPs with passivated surfaces (for example, PEGylation has been demonstrated to help in this direction). Thus, in order to show specific linkage statistics and assembly of NPs without linkers are required. Just some examples of TEM images of nicely formed dimers are not sufficient experimental proof. Most surprisingly, the size distribution ($\triangle d_c/d_c$) of presently available NPs typically is good enough for allowing studies of plasmon coupling. Fluctuations in surface-to-surface distance ($\triangle D/D$) effect plasmon coupling to a much higher degree. This effect is particularly pronounced for big NPs due to the fact that biological linkers are soft and flexible. In conclusion, we suggest that the major technical problems in investigating plasmonic coupling of adjacent NPs are neither fluctuations in surface-to-surface distances, nor in particular broad size distributions of the NP cores, but rather in the non-specific formation of small NP agglomerates due to non-specific adsorption effects, which severely limits the yield of specific dimers.

Acknowledgements

Part of this work was supported by the European Commission (project Namdiatream to WJP). DYL acknowledges the grants 1-ZVAL and 1-ZVAW administrated by The Hong Kong Polytechnic University. PT was supported by ERC StG SiMBA (ERC-2010-StG-20091118). AG-M acknowledges receipt of a Ramón y Cajal Fellowship from the Ministerio de Economía y Competitividad. XY acknowledges support by the Chinese (CSC, Nr. 2010691036) government and FA acknowledges support by DAAD/HEC.

Appendix A. Supplementary data

Supplementary data associated with this article can be found, in the online version, at http://dx.doi.org/10.1016/j.nantod.2013.09.001.

References

[1] A. Guerrero-Martinez, M. Grzelczak, L.M. Liz-Marzan, ACS Nano 6 (2012) 3655—3662.
[2] E.C. Dreaden, A.M. Alkilany, X. Huang, C.J. Murphy, M.A. El-Sayed, Chem. Soc. Rev. 41 (2012) 2740—2779.
[3] C.J. Murphy, A.M. Gole, J.W. Stone, P.N. Sisco, A.M. Alkilany, E.C. Goldsmith, S.C. Baxter, Acc. Chem. Res. 41 (2008) 1721—1730.
[4] J.J. Storhoff, R. Elghanian, R.C. Mucic, C.A. Mirkin, R.L. Letsinger, J. Am. Chem. Soc. 120 (1998) 1959—1964.
[5] R.A. Reynolds, C.A. Mirkin, R.L. Letsinger, JACS 122 (2000) 3795—3796.
[6] C. Sönnichsen, A.P. Alivisatos, Nanoletters 5 (2005) 304—310.
[7] D.P. O'Neal, L.R. Hirsch, N.J. Halas, J.D. Payne, J.L. West, Cancer Lett. 209 (2004) 171—176.
[8] X.H. Huang, P.K. Jain, I.H. El-Sayed, M.A. El-Sayed, Photochem. Photobiol. 82 (2006) 412—417.
[9] W.T. Lu, A.K. Singh, S.A. Khan, D. Senapati, H.T. Yu, P.C. Ray, J. Am. Chem. Soc. 132 (2010) 18103—18114.
[10] H.B. Yildiz, R. Tel-Vered, I. Willner, Adv. Funct. Mater. 18 (2008) 3497—3505.
[11] K. Wang, E. Schonbrun, P. Steinvurzel, B. Crozier Kenneth, Nat. Commun. 2 (2011) 469.
[12] I. Romero, F.J. Garcia de Abajo, Opt. Exp. 17 (2009) 22012—22022.
[13] C.M. Cobley, S.E. Skrabalak, D.J. Campbell, Y.A. Xia, Plasmonics 4 (2009) 171—179.
[14] R.A. Alvarez-Puebla, R. Contreras-Caceres, I. Pastoriza-Santos, J. Perez-Juste, L.M. Liz-Marzan, Angew. Chem. Int. Ed. 48 (2009) 138—143.
[15] J. Rodriguez-Fernandez, A.M. Funston, J. Perez-Juste, R.A. Alvarez-Puebla, L.M. Liz-Marzan, P. Mulvaney, PCCP 11 (2009) 5909—5914.
[16] J.H.W. Leuvering, P. Thal, M. Vanderwaart, A. Schuurs, J. Immunol. Methods 45 (1981) 183—194.
[17] S.G. Cull-Candy, I. Parker, Nature 295 (1982) 410—412.
[18] J. Stehr, C. Hrelescu, R.A. Sperling, G. Raschke, M. Wunderlich, A. Nichtl, D. Heindl, K. Kürzinger, W.J. Parak, T.A. Klar, J. Feldmann, Nano Lett. 8 (2008) 619—623.
[19] J. Gong, G. Li, Z. Tang, Nano Today 7 (2012) 564—585.
[20] J. Zhao, B. Frank, S. Burger, H. Giessen, ACS Nano 5 (2011) 9009—9016.
[21] S.R. Beyer, S. Ullrich, S. Kudera, A.T. Gardiner, R.J. Cogdell, J. Koehler, Nano Lett. 11 (2011) 4897—4901.
[22] Y. Zhang, F. Wen, Y.-R. Zhen, P. Nordlander, N.J. Halas, Proc. Natl. Acad. Sci. U.S.A. 1—5 (2013) 5.
[23] A. Kinkhabwala, Z. Yu, S. Fan, Y. Avlasevich, K. Muellen, W.E. Moerner, Nat. Photon. 3 (2009) 654—657.
[24] A. Bek, R. Jansen, M. Ringler, S. Mayilo, T.A. Klar, J. Feldmann, Nano Lett. 8 (2008) 485—490.
[25] M.R. Jones, K.D. Osberg, R.J. MacFarlane, M.R. Langille, C.A. Mirkin, Chem. Rev. 111 (2011) 3736—3827.
[26] K.D. Osberg, M. Rycenga, N. Harris, A.L. Schmucker, M.R. Langille, G.C. Schatz, C.A. Mirkin, Nano Lett. 12 (2012) 3828—3832.
[27] M. Grzelczak, J. Vermant, E.M. Furst, L.M. Liz-Marzan, Acs Nano 4 (2010) 3591—3605.
[28] A.S. Angelatos, B. Radt, F. Caruso, J. Phys. Chem. B 109 (2005) 3071—3076.
[29] D.V. Volodkin, N. Madaboosi, J. Blacklock, A.G. Skirtach, H. Mohwald, Langmuir 25 (2009) 14037—14043.
[30] S. Carregal-Romero, M. Ochs, P. Rivera_Gil, C. Gana, A.M. Pavlov, G.B. Sukhorukov, W.J. Parak, J. Control. Release 159 (2012) 120—127.
[31] C. Hrelescu, J. Stehr, M. Ringler, R.A. Sperling, W.J. Parak, T.A. Klar, J. Feldmann, J. Phys. Chem. C 114 (2010) 7401—7411.
[32] B. Nikoobakht, Z.L. Wang, M.A. El-Sayed, J. Phys. Chem. B 104 (2000) 8635—8640.
[33] A. Dong, J. Chen, S.J. Oh, W.-k. Koh, F. Xiu, X. Ye, D.-K. Ko, K.L. Wang, C.R. Kagan, C.B. Murray, Nano Lett. 11 (2011) 841—846.
[34] A. Guerrero-Martinez, J. Perez-Juste, E. Carbo-Argibay, G. Tardajos, L.M. Liz-Marzan, Angew. Chem. Int. Ed. 48 (2009) 9484—9488, S9484/9481—S9484/9484.
[35] S.J. Barrow, A.M. Funston, X. Wei, P. Mulvaney, Nano Today 8 (2013) 138—167.
[36] J.-M. Montenegro, V. Grazu, A. Sukhanova, S. Agarwal, J.M.d.l. Fuente, I. Nabiev, A. Greiner, W.J. Parak, Adv. Drug Deliv. Rev. 65 (2013) 677—688.
[37] N. Pazos-Perez, C.S. Wagner, J.M. Romo-Herrera, L.M. Liz-Marzan, F.J. Garcia de Abajo, A. Wittemann, A. Fery, R.A. Alvarez-Puebla, Angew. Chem. Int. Ed. 51 (2012) 12688—12693.
[38] D.M. Sullivan, Electromagnetic Simulation Using the FDTD Method, IEEE, New York, 2000.
[39] A. Aubry, D.Y. Lei, S.A. Maier, J.B. Pendry, Phys. Rev. Lett. 105 (2010) 233901.
[40] A. Aubry, D.Y. Lei, S.A. Maier, J.B. Pendry, ACS Nano 5 (2011) 3293—3308.
[41] K.H. Su, Q.H. Wei, X. Zhang, J.J. Mock, D.R. Smith, S. Schultz, Nano Lett. 3 (2003) 1087—1090.
[42] D.Y. Lei, J. Li, H.C. Ong, Appl. Phys. Lett. 91 (2007), 021112/021111—021112/021113.
[43] W.H. Li, R. Zamani, P.R. Gil, B. Pelaz, M. Ibanez, D. Cadavid, A. Shavel, R.A. Alvarez-Puebla, W.J. Parak, J. Arbiol, A. Cabot, J. Am. Chem. Soc. 135 (2013) 7098—7101.
[44] F. Scotognella, G. Della Valle, A.R.S. Kandada, D. Dorfs, M. Zavelani-Rossi, M. Conforti, K. Miszta, A. Comin, K. Korobcheyskaya, G. Lanzani, L. Manna, F. Tassone, Nano Lett. 11 (2011) 4711—4717.
[45] A. Roucoux, J. Schulz, H. Patin, Chem. Rev. (Washington, DC, U.S.) 102 (2002) 3757—3778.
[46] T. Pellegrino, S. Kudera, T. Liedl, A.M. Javier, L. Manna, W.J. Parak, Small 1 (2005) 48—63.
[47] A.C. Templeton, W.P. Wuelfing, R.W. Murray, Acc. Chem. Res. 33 (2000) 27—36.
[48] D.I. Gittins, F. Caruso, J. Phys. Chem. B 105 (2001) 6846—6852.
[49] T. Pellegrino, L. Manna, S. Kudera, T. Liedl, D. Koktysh, A.L. Rogach, S. Keller, J. Rädler, G. Natile, W.J. Parak, Nano Lett. 4 (2004) 703—707.
[50] F. Zhang, E. Lees, F. Amin, P. Rivera_Gil, F. Yang, P. Mulvaney, W.J. Parak, Small 7 (2011) 3113—3127.
[51] M. Brust, M. Walker, D. Bethell, D.J. Schiffrin, R. Whyman, J. Chem. Soc. Chem. Commun. (1994) 801—802.
[52] C.J. Murphy, N.R. Jana, Adv. Mater. 14 (2002) 80—82.
[53] J. Perez-Juste, L.M. Liz-Marzan, S. Carnie, D.Y.C. Chan, P. Mulvaney, Adv. Funct. Mater. 14 (2004) 571—579.
[54] P. Senthil Kumar, I. Pastoriza-Santos, B. Rodriguez-Gonzalez, F. Javier Garcia de Abajo, L.M. Liz-Marzan, Nanotechnology 19 (2008) 015606.
[55] J. Watt, S. Cheong, R.D. Tilley, Nano Today 8 (2013) 198—215.
[56] J. Turkevich, P.C. Stevenson, J. Hillier, Discuss. Faraday Soc. 11 (1951) 55—75.
[57] G. Frens, Nat. Phys. Sci. 241 (1973) 20—22.

[58] I. Ojea-Jimenez, F.M. Romero, N.G. Bastus, V. Puntes, J. Phys. Chem. C 114 (2010) 1800—1804.
[59] J. Rodriguez-Fernandez, J. Perez-Juste, F.J.G. de Abajo, L.M. Liz-Marzan, Langmuir 22 (2006) 7007—7010.
[60] N.G. Bastus, J. Comenge, V. Puntes, Langmuir 27 (2011) 11098—11105.
[61] S.D. Perrault, W.C.W. Chan, J. Am. Chem. Soc. 131 (2009) 17042—17043.
[62] N. Pazos-Perez, F.J. Garcia de Abajo, A. Fery, R.A. Alvarez-Puebla, Langmuir 28 (2012) 8909—8914.
[63] Commercial gold nanoparticles were delivered by British Biocell International (BBI) (http://www.buybbi.com/Products_GoldColloid_1.aspx).
[64] F. Amin, D.A. Yushchenko, J.M. Montenegro, W.J. Parak, ChemPhysChem 13 (2012) 1030—1035.
[65] G.P. Acuna, F.M. Moeller, P. Holzmeister, S. Beater, B. Lalkens, P. Tinnefeld, Science 338 (2012) 506—510.
[66] E.A. Coronado, E.R. Encina, F.D. Stefani, Nanoscale 3 (2011) 4042—4059.
[67] E. Dulkeith, M. Ringler, T.A. Klar, J. Feldmann, A.M. Javier, W.J. Parak, Nano Lett. 5 (2005) 585—589.
[68] M.T. Fernández-Argüelles, A. Yakovlev, R.A. Sperling, C. Luccardini, S. Gaillard, A.S. Medel, J.-M. Mallet, J.-C. Brochon, A. Feltz, M. Oheim, W.J. Parak, Nano Lett. 7 (2007) 2613—2617.
[69] F. Zhang, Z. Ali, F. Amin, A. Feltz, M. Oheim, W.J. Parak, ChemPhysChem 11 (2010) 730—735.
[70] X. Ma, K. Fletcher, T. Kipp, M.P. Grzelczak, Z. Wang, A. Guerrero-Martinez, I. Pastoriza-Santos, A. Kornowski, L.M. Liz-Marzan, A. Mews, J. Phys. Chem. Lett. 2 (2011) 2466—2471.
[71] E. Donath, G.B. Sukhorukov, F. Caruso, S.A. Davis, H. Möhwald, Angew. Chem. Int. Ed. 37 (1998) 2202—2205.
[72] G. Schneider, G. Decher, N. Nerambourg, R. Praho, M.H. Werts, M. Blanchard-Desce, Nano Lett. 6 (2006) 530—536.
[73] G. Schneider, G. Decher, Langmuir 24 (2008) 1778—1789.
[74] Z. Poon, J.B. Lee, S.W. Morton, P.T. Hammond, Nano Lett. 11 (2011) 2096—2103.
[75] K.S. Mayya, B. Schoeler, F. Caruso, Adv. Funct. Mater. 13 (2003) 183—188.
[76] J. Hierrezuelo, I. Szilagyi, A. Vaccaro, M. Borkovec, Macromolecules 43 (2010) 9108—9116.
[77] W.J. Tong, C.Y. Gao, H. Mohwald, Macromol. Rapid Commun. 27 (2006) 2078—2083.
[78] F. Caruso, K. Niikura, D.N. Furlong, Y. Okahata, Langmuir 13 (1997) 3422—3426.
[79] P. Rivera Gil, D. Jimenez de Aberasturi, V. Wulf, B. Pelaz, P. del Pino, Y. Zhao, J. de la Fuente, I. Ruiz de Larramendi, T. Rojo, X.-J. Liang, W.J. Parak, Acc. Chem. Res. 46 (2013) 743—749.
[80] A.L. Koh, K. Bao, I. Khan, W.E. Smith, G. Kothleitner, P. Nordlander, S.A. Maier, D.W. McComb, ACS Nano 3 (2009) 3015—3022.
[81] C.J. Loweth, W.B. Caldwell, X.G. Peng, A.P. Alivisatos, P.G. Schultz, Angew. Chem. Int. Ed. 38 (1999) 1808—1812.
[82] S.A. Claridge, S.L. Goh, J.M.J. Fréchet, S.C. Williams, C.M. Micheel, A.P. Alivisatos, Chem. Mater. 17 (2005) 1628—1635.
[83] A.J. Mastroianni, S.A. Claridge, A.P. Alivisatos, J. Am. Chem. Soc. 131 (2009) 8455—8459.
[84] F.A. Aldaye, H.F. Sleiman, J. Am. Chem. Soc. 129 (2007) 4130—4131.
[85] M.P. Busson, B. Rolly, B. Stout, N. Bonod, J. Wenger, S. Bidault, Angew. Chem. Int. 51 (2012) 11083—11087.
[86] D. Zanchet, C.M. Micheel, W.J. Parak, D. Gerion, S.C. Williams, A.P. Alivisatos, J. Phys. Chem. B 106 (2002) 11758—11763.
[87] D. Zanchet, C.M. Micheel, W.J. Parak, D. Gerion, A.P. Alivisatos, Nano Lett. 1 (2001) 32—35.
[88] R.A. Sperling, T. Pellegrino, J.K. Li, W.H. Chang, W.J. Parak, Adv. Funct. Mater. 16 (2006) 943—948.
[89] T. Pellegrino, R.A. Sperling, A.P. Alivisatos, W.J. Parak, J. Biomed. Biotechnol. (2007) 1—9, Article ID: 26796.
[90] R. Levy, Z.X. Wang, L. Duchesne, R.C. Doty, A.I. Cooper, M. Brust, D.G. Fernig, Chembiochem 7 (2006) 592—594.
[91] S.A. Claridge, H.W. Liang, S.R. Basu, J.M.J. Frechet, A.P. Alivisatos, Nano Lett. 8 (2008) 1202—1206.
[92] W.J. Parak, T. Pellegrino, C.M. Micheel, D. Gerion, S.C. Williams, A.P. Alivisatos, Nano Lett. 3 (2003) 33—36.
[93] M.D. Savage, G. Mattson, S. Desai, G.W. Nielander, S. Morgensen, E.J. Conklin, Avidin-Biotin Chemistry: A Handbook, Pierce, 1992 (downloaded from http://www.piercenet.com/files/Avidin-biotin-book2.zip).
[94] C.-A.J. Lin, R.A. Sperling, J.K. Li, T.-Y. Yang, P.-Y. Li, M. Zanella, W.H. Chang, W.J. Parak, Small 4 (2008) 334—341.
[95] M.S. Itano, A.K. Neumann, P. Liu, F. Zhang, E. Gratton, W.J. Parak, N.L. Thompson, K. Jacobson, Biophys. J. 100 (2011) 2662—2670.
[96] C.A. Mirkin, T.A. Taton, Nature 405 (2000) 626—627.
[97] A.P. Alivisatos, K.P. Johnsson, X. Peng, T.E. Wilson, C.J.M.P.B. Loweth Jr., P.G. Schultz, Nature 382 (1996) 609—611.
[98] P. Sandström, M. Boncheva, B. Åkerman, Langmuir 19 (2003) 7537—7543.
[99] P.A. Sandström, Björn, Langmuir 20 (2004) 4182—4186.
[100] T. Cedervall, I. Lynch, S. Lindman, T. Berggård, E. Thulin, H. Nilsson, K.A. Dawson, S. Linse, Proc. Natl. Acad. Sci. U.S.A. 104 (2007) 2050—2055.
[101] T. Cedervall, I. Lynch, M. Foy, T. Berggad, S. Donnelly, G. Cagney, S. Linse, K. Dawson, Angew. Chem. Int. Ed. 46 (2007) 5754—5756.
[102] X. Jiang, S. Weise, M. Hafner, C. Röcker, F. Zhang, W.J. Parak, G.U. Nienhaus, J. R. Soc. Interface 7 (2010) S5—S13.
[103] Y.Y. Pinto, J.D. Le, N.C. Seeman, K. Musier-Forsyth, T.A. Taton, R.A. Kiehl, Nano Lett. 5 (2005) 2399—2402.
[104] J. Zheng, P.E. Constantinou, C. Micheel, A.P. Alivisatos, R.A. Kiehl, N.C. Seeman, Nano Lett. 6 (2006) 1502—1504.
[105] A. Guerrero-Martinez, J.L. Alonso-Gomez, B. Auguie, M.M. Cid, L.M. Liz-Marzan, Nano Today 6 (2011) 381—400.
[106] A. Kuzyk, R. Schreiber, Z.Y. Fan, G. Pardatscher, E.M. Roller, A. Hogele, F.C. Simmel, A.O. Govorov, T. Liedl, Nature 483 (2012) 311—314.
[107] X. Shen, C. Song, J. Wang, D. Shi, Z. Wang, N. Liu, B. Ding, J. Am. Chem. Soc. 134 (2012) 146—149.
[108] P.W.K. Rothemund, Nature 440 (2006) 297—302.
[109] I.H. Stein, V. Schueller, P. Boehm, P. Tinnefeld, T. Liedl, ChemPhysChem 12 (2011) 689—695.
[110] G.P. Acuna, M. Bucher, I.H. Stein, C. Steinhauer, A. Kuzyk, P. Holzmeister, R. Schreiber, A. Moroz, F.D. Stefani, T. Liedl, F.C. Simmel, P. Tinnefeld, ACS Nano 6 (2012) 3189—3195.
[111] S. Pal, Z. Deng, B. Ding, H. Yan, Y. Liu, Angew. Chem. Int. Ed. 49 (2010) 2700—2704, S2700/2701—S2700/2722.
[112] B. Ding, Z. Deng, H. Yan, S. Cabrini, R.N. Zuckermann, J. Bokor, J. Am. Chem. Soc. 132 (2010) 3248—3249.
[113] S. Pal, Z. Deng, H. Wang, S. Zou, Y. Liu, H. Yan, J. Am. Chem. Soc. 133 (2011) 17606—17609.
[114] I.H. Stein, V. Schuller, P. Bohm, P. Tinnefeld, T. Liedl, Chemphyschem 12 (2011) 689—695.
[115] L. Rodriguez-Lorenzo, R. de la Rica, R.A. Alvarez-Puebla, L.M. Liz-Marzan, M.M. Stevens, Nat. Mater. 11 (2012) 604—607.
[116] J.J. Schmied, C. Forthmann, E. Pibiri, B. Lalkens, P. Nickels, T. Liedl, P. Tinnefeld, Nano Lett. 13 (2013) 781—785.
[117] J. Zuloaga, E. Prodan, P. Nordlander, Nano Lett. 9 (2009) 887—891.
[118] J. Zuloaga, E. Prodan, P. Nordlander, ACS Nano 4 (2010) 5269—5276.
[119] R. Esteban, G. Borisov Andrei, P. Nordlander, J. Aizpurua, Nat. Commun. 3 (2012) 825.

Xiang Yu is a PhD student in Wolfgang J. Parak's group at the Philipps Universität Marburg (Germany). He got his master degree in Biochemistry at Sichuan Agriculture University in 2010 (China). Currently his research interests are focused on the synthesis, characterization and application of multifunctional nanoparticles and microcapsules.

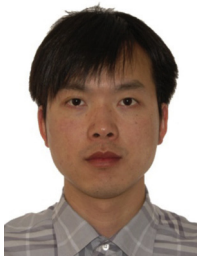

Dang Yuan Lei is an assistant professor in the Department of Applied Physics at the Hong Kong Polytechnic University. He received his BSc degree from Northwest University in China and an MPhil degree from the Chinese University of Hong Kong, respectively. He did his PhD studies and Postdoc research on nanoplasmonics and transformation optics under supervision of Prof Stefan Maier and in close collaboration with Prof Sir John Pendry at Imperial College London.

Faheem Amin is an Assitant Professor in the Center for Advanced Mathematics and Physics at the National University for Science and Technology, Islamabad, Pakistan. He received his M.Sc as well as his M.Phil degree from Quaid-e-Azam University Islamabad, Pakistan. He did his PhD from Philipps University Marburg, Germany on surface modification and functionalization of nanoparticles under supervision of Prof. Dr. Wolfgang J. Parak.

Raimo Hartmann graduated in Physics at the Philipps University of Marburg (Germany) in 2011 and is currently doing his PhD in the Biophysics Department at the same university under the supervision of Prof. Dr. Wolfgang J. Parak. His main focus of research is the field of Nanobiotechnolgy applied to life sciences.

Guillermo P. Acuna (Buenos Aires, Argentina, 1980) studied Physics at the Buenos Aires University. In 2010 he obtained his PhD at the Ludwig-Maximilans-Universität (Munich, Germany) under the supervision of Prof. Dr. Roland Kersting. Currently he is a Research Assistant at the NanoBioSciences group of Prof. Dr. Philip Tinnefeld at the TU Braunschweig (Braunschweig, Germany). His research interests include single molecule fluorescence, plasmonics and nanophotonics.

Andrés Guerrero-Martínez received his PhD degree in Chemistry under the supervision of Prof. G. Tardajos at the University Complutense in 2006, where he served as lecturer of Physical Chemistry between 2006 and 2007. He then joined the group of Prof. L. De Cola at the University of Münster as a ''Marie Curie'' postdoctoral fellow, from 2007 to 2009. Then, he held ''Juan de la Cierva'' and ''Parga Pondal'' Postdoctoral Fellowships in the group of Prof. L.M. Liz-Marzán at the Universidade de Vigo. Since 2012, he works as a ''Ramón y Cajal'' Postdoctoral Fellowship at the Universidad Complutense de Madrid, where he is investigating nanostructured materials with tailored optical properties based on molecular concepts.

Stefan Maier is Professor of Nanophotonics in the Physics Department of Imperial College London. He has published over 140 papers in the area of nanoplasmonics, is a fellow of OSA, and was awarded the Sackler Prize for the Physical Sciences (2010), the Paterson Medal of the Institute of Physics (2010), and a Wolfson Research Merit Award by the Royal Society (2011). His current research focuses on hybrid plasmonic-photonic systems for efficient energy collection, optoelectronics, and sensing.

Philip Tinnefeld studied chemistry in Münster, Montpellier, and Heidelberg. In 2002, he received his PhD at the University of Heidelberg in the group of Prof. J. Wolfrum. He carried out postdoctoral research with S. Weiss (UCLA), F.C. de Schryver (KU Leuven) and M. Sauer (Bielefeld) on the development of single-molecule fluorescence techniques. After three years as associate professor of biophysics at the Ludwig-Maximilians-Universität München he was appointed full professor of biophysical chemistry at Braunschweig University of Technology in 2010. His research interests include the development of microscopy techniques and applications of DNA nanotechnology to study problems at the interface of physics, chemistry and biology

Susana Carregal Romero received her PhD degree (2009) in Chemistry at University of Vigo (Spain) in the group of Prof. Pablo Hervés-Beloso and Prof. Luis M. Liz-Marzán. Then she obtained a postdoctoral fellowship from the Junta de Andalucía to join the group of W. J. Parak at the Philipps Universität Marburg (Germany) where she holds a postdoctoral position. Her current research involves synthesis and coating of nanoparticles, synthesis of capsules and applications of both in drug delivery and sensing.

Wolfgang J. Parak obtained his PhD at the LMU München, Germany (1999) in the group of Prof. Dr. Hermann Gaub. After a postdoctoral stay at the University of California, Berkeley, CA, USA in the group of Prof. Dr. Paul Alivisatos he returned 2002 to Munich as Assistant Professor. Since 2007 he is Full Professor at the Philipps Universität Marburg, Germany. He is also Associate Editor of ACS Nano.

Xiang Yu[1#], Dang Yuan Lei[2#], Faheem Amin[1], Raimo Hartmann[1], Guillermo P. Acuna[4], Andrés Guerrero-Martínez[5], Stefan A. Maier[3], Phillip Tinnefeld[4], Susana Carregal-Romero[1,6], Wolfgang J. Parak[1,7*]

[1] Fachbereich Physik, Philipps Universität Marburg, Marburg, Germany

[2] Department of Applied Physics, The Hong Kong Polytechnic University, Hong Kong, China

[3] Department of Physics, Imperial College London, London, United Kingdom

[4] NanoBioScience Group, Institute for Physical and Theoretical Chemistry, TU Braunschweig, Braunschweig, Germany

[5] Departamento de Química Física I, Facultad de Ciencias Químicas, Universidad Complutense, Madrid, Spain

[6] BIONAND, Andalucian Center for Nanomedicine & Biotechnology, Málaga, Spain

[7] CIC Biomagune, San Sebastian, Spain

[#] both authors contributed equally to this work

[*] corresponding author: wolfgang.parak@physik.uni-marburg.de

Distance control in-between plasmonic nanoparticles *via* biological and polymeric spacers

SUPPORTING INFORMATION

I) Synthesis of colloidal Au nanoparticles

II) Size distribution measurements of Au nanoparticles

III) Shape distribution measurements of Au nanoparticles

IV) LbL-coating of Au nanoparticles

V) Formation of Au nanoparticle dimers by electrostatic interactions

VI) Coating of Au nanoparticles with biotin and streptavidin

VII) Formation of Au nanoparticle dimers by biotin-streptavidin interaction

VIII) Coating of quantum dots with biotin and streptavidin

IX) Formation of quantum dot dimers by biotin-streptavidin interaction

X) References

I) Synthesis of colloidal Au nanoparticles

Hydrophilic citrate stabilized Au nanoparticles (NPs) were purchased from British Bio-cell International (BBI) [1] and stored at 4 °C: 20 nm (EM.GC20), 50 nm (EM.GC50), 60 nm (EM.G60), 80 nm (EM.GC80), and 100 nm (EM.GC100). Hydrophilic citrate stabilized Au nanoparticles (NPs) of 50 nm core diameter were synthesized using the seeded growth method developed by Bastus et al. [2].

Hydrophobic Au NPs were synthesized according to the recipe described in previous publications [3] based on the protocol by Brust et *al.* [4]. For the synthesis of Au NPs of 4-5 nm core diameter, hydrogen tetrachloroaurate (III) hydrate (AlfaAesar, #12325), sodium borohydride (Sigma, #45,288-2), and tetraoctylammonium bromide (Sigma, #294136) were used as chemicals. All chemicals were used without further purification. Ultrapure water with a resistance greater than 18.2 $M\Omega cm^{-1}$ was used for all experiments. All glassware was cleaned in aqua regia and rinsed with ultrapure water. The hydrophobic Au NPs were transferred into aqueous solution by coating them with an amphiphilic polymer made out of 1-dodecylamine (Sigma, #D222208) and poly(isobutylene-alt-maleic anhydride) PMA (Sigma, #531278, M_w = 6000 g mol^{-1}). For further details we refer to our previous publications [3, 5].

II) Size distribution measurements of Au nanoparticles

Transmission electron microscopy (TEM) images of the Au NPs were captured at different magnifications to study their size distribution. TEM imaging was performed with a JEOL Model JEM 3010 microscope operating at an acceleration voltage of 300 kV. Note that only the inorganic (Au) core is visible in TEM images, but not the organic surface coating [6]. The Image J (version 3.0) software was used to derive the core diameter (d_c) and the aspect ratio (s) from the Au NPs. The aspect ratio has taken into account the fact that the shape of the NPs is not perfectly spherical and was determined by measuring $d_{c,max}$ as the larger diameter and $d_{c,min}$ as the perpendicular diameter of $d_{c,max}$ for each Au NP, and then calculated as $s = d_{c,max}/d_{c,min}$, *cf.* Figure SI.II.1. Examples for size distributions are shown in Figures SI.II.2 and SI.II.3.

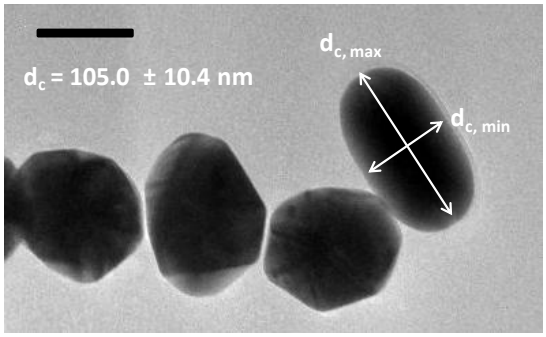

Figure SI.II.1. *TEM image of commercially available citrate-stabilized Au NPs with an average core diameter of d_c = 105 nm (nominally 100 nm). This example demonstrates how the aspect ratio is measured. The scale bar corresponds to 100 nm.*

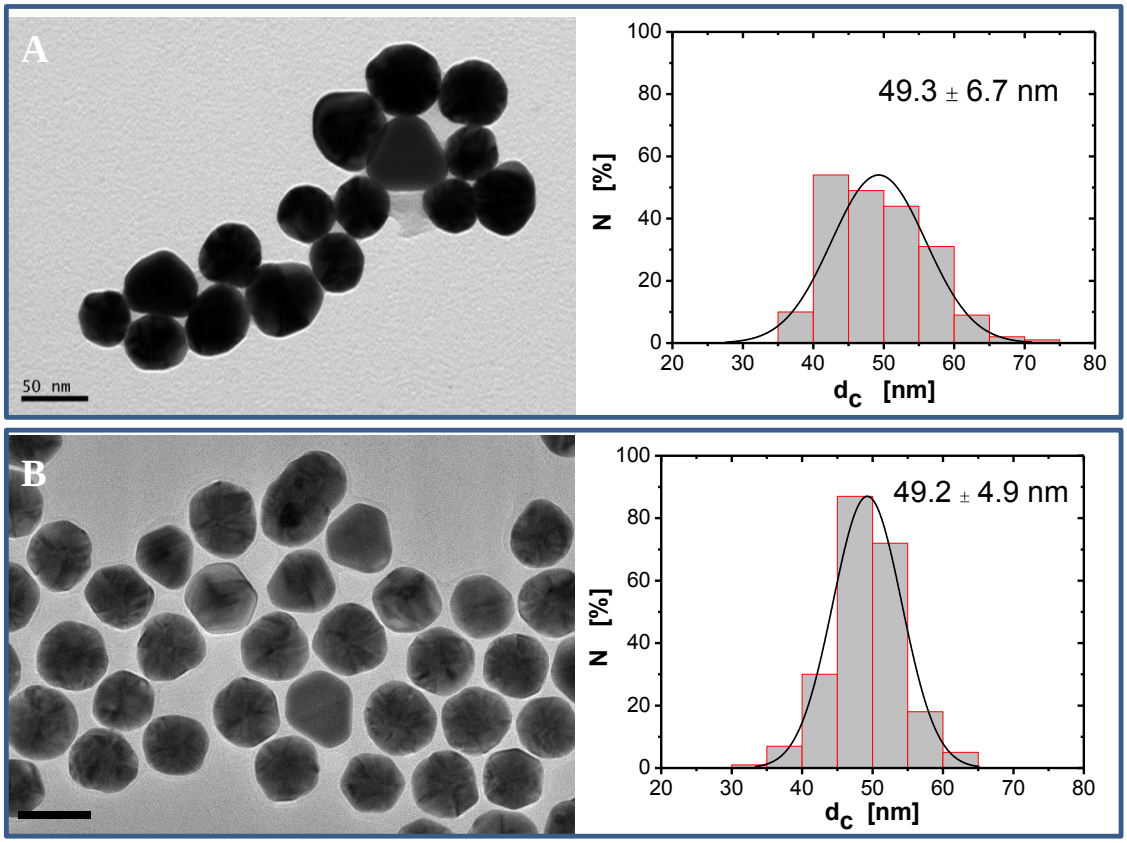

Figure SI.II.2. *TEM images of citrate-stabilized Au NPs and the corresponding size distribution $N(d_c)$ of their hard core diameter d_c: (A) NPs prepared using seeded growth method [2]. (B) Commercially available NPs, as purchased from BBI [1]. The scale bars correspond to 50 nm.*

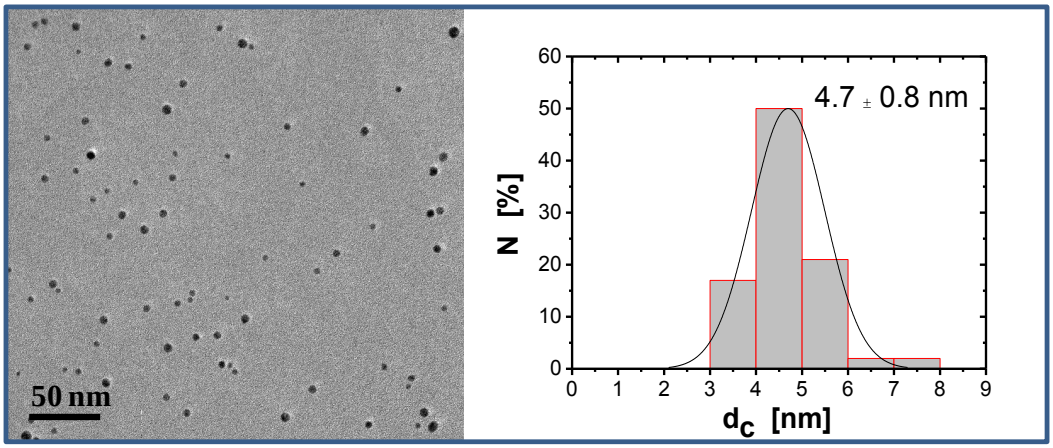

Figure SI.II.3. *TEM images of hydrophobic Au NPs as prepared according to a previously published report [3] and the corresponding size distribution $N(d_c)$ of their hard core diameter d_c: The scale bar corresponds to 50 nm.*

III) Shape distribution measurements of Au nanoparticles

Transmission electron microscopy images of the Au NPs were also used to estimate the percentage of NPs with spherical shape compared with other residual shapes such as rods or triangles. For all the analyzed samples the most common shapes besides the spherical were triangular, rod like shape, hexagonal and non-geometrical, as it is shown in Figure SI.III.1. Table SI.III.1 contains the distribution of different shapes of NPs for the samples with different size.

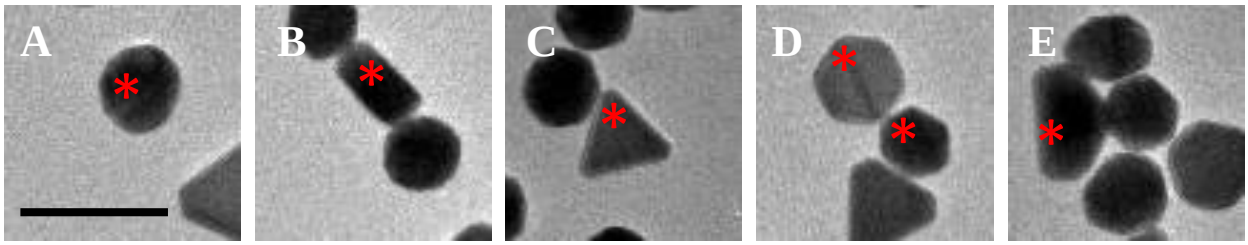

Figure SI.III.1. *TEM images of the different shapes of NPs. A) Spherical shape. B) Rod like shape. C) Triangular shape. D) Hexagonal shape. E) Non geometrical shape. (*) points out the NPs with the corresponding shape in the respective image. Between 250 and 600 NPs were analyzed for each NP sample with different size.*

d_c [nm]	% spheres	% rods	% triangles	% hexagons	% non geometrical shape
4.7	97.6 ± 0.8	0.4 ± 0.6	0	0.9 ± 0.01	1.0 ± 0.2
19.4	84.1 ± 1.1	4.6 ± 0.8	5.0 ± 0.8	0.9 ± 0.7	5.4 ± 2.2
49.2	87.3 ± 0.9	2.3 ± 0.6	1.3 ± 0.5	0.3 ± 0.4	8.8 ± 0.7
49.3[(1)]	86.2 ± 6.6	1.0 ± 1.6	0.9 ± 2.7	0	11.9 ± 5.9
61.5	94.0 ± 0.9	0.4 ± 1.1	1.2 ± 1.1	0.4 ± 0.8	3.9 ± 0.8
80.1	85.8 ± 3.5	1.8 ± 1.9	2.7 ± 1.4	3.6 ± 0.3	6.0 ± 2.2
105.0	77.7 ± 4.2	1.7 ± 2.0	4.8 ± 2.4	8.0 ± 2.7	7.8 ± 2.5

Table SI.III.1. *Distribution of NP populations with different shape in samples with different core diameter (d_c). The presence of residual shapes varied from 2.4 % for polymer capped Au NPs to 22.3 % for Au NPs with d_c = 105 nm d_c. Custom made citric acid stabilized NPs[(1)] showed similar shape distribution than commercial NPs.*

IV) LbL-coating of Au nanoparticles

Poly(styrene sulfonate) sodium salt (PSS, $M_w \approx 14.9$ kDa, #18061-2) was purchased from Polymer Standards Service. Poly(allylamine hydrochloride) (PAH, $M_w \approx 15$ kDa, #283215) and sodium chloride (NaCl, #S3014) were obtained from Sigma-Aldrich. Layer-by-layer (LbL) coating of citrate-stabilized Au NPs was carried out as follows: 2 mL commercial solution (from BBI, $5.16 \cdot 10^{-11}$ M assuming a molecular extinction coefficient of $2.2 \cdot 10^{10}$ $M^{-1}cm^{-1}$ at the surface plasmon peak [7]) of $d_c = 49.2 \pm 4.9$ nm (nominally $d_c = 50$ nm) citrate Au NPs was precipitated by centrifugation for 60 min at 620×g only in one time. The pellet was concentrated to finally obtain a solution of 500 µL of Au NPs (corresponding to an NP concentration of $2.1 \cdot 10^{-10}$ M, assuming a molecular extinction coefficient of $2.2 \cdot 10^{10}$ $M^{-1}cm^{-1}$ at the surface plasmon peak [7]). Under magnetic stirring the concentrated solution of Au NPs was added dropwise to a solution of 2.0 mg/mL (500 µL) of positively charged polyelectrolyte (PE: PAH; pH ~ 4.8). The mixture was kept under magnetic stirring in the dark for at least 1 hour. The Au NPs were then washed two times (2 centrifugation cycles at 930×g for 90 min each for precipitation, followed by redispersion in Milli-Q water) and finally redispersed in 500 µL of Milli-Q water. A second layer of negatively charged PE, PSS, was then added onto the positively charged Au NPs using the same procedure. Repetition of this LbL assembly with alternating positively and negatively charged PEs was continued up to 10 PE layers, *cf.* Figure SI.IV.1. The final LbL-coated Au NPs were stored at 4 ºC in solutions containing an excess of free PSS or PAH (depending on the PE which was used for the last assembled layer) in order to avoid aggregation. Before further experiments free PE had to be removed by centrifugation (discarding of the supernatant containing the free PE molecules and redissolution of the pellet containing the Au NPs).

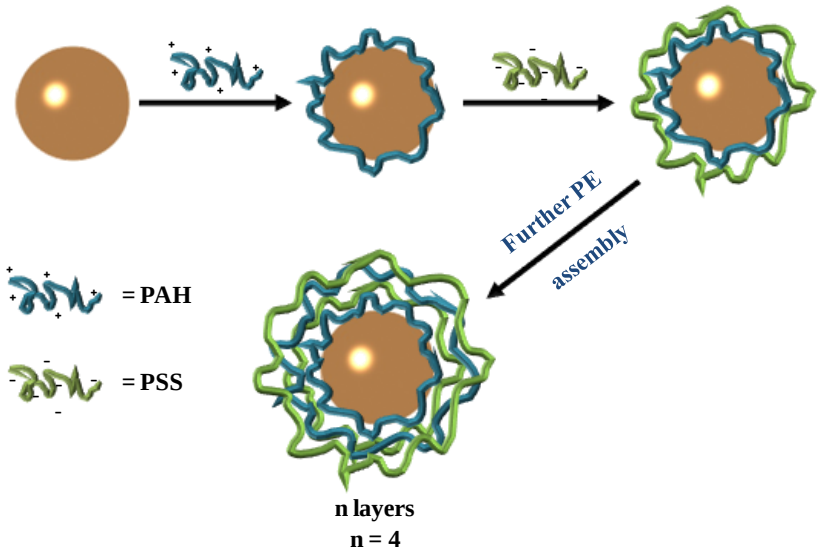

Figure SI.IV.1. *Schematic representation of an Au NP with n added PE layers by LbL deposition. In the present case n = 4 layers are shown.*

For spectroscopic characterization UV-Vis absorption spectra were recorded by using an Agilent Model 8453 UV-Vis spectrophotometer. Figure SI.IV.2 shows a slight change of the plasmon band during the LbL process, indicating that the addition of n layers of PEs on the Au NP surface produced a slight agglomeration of the sample.

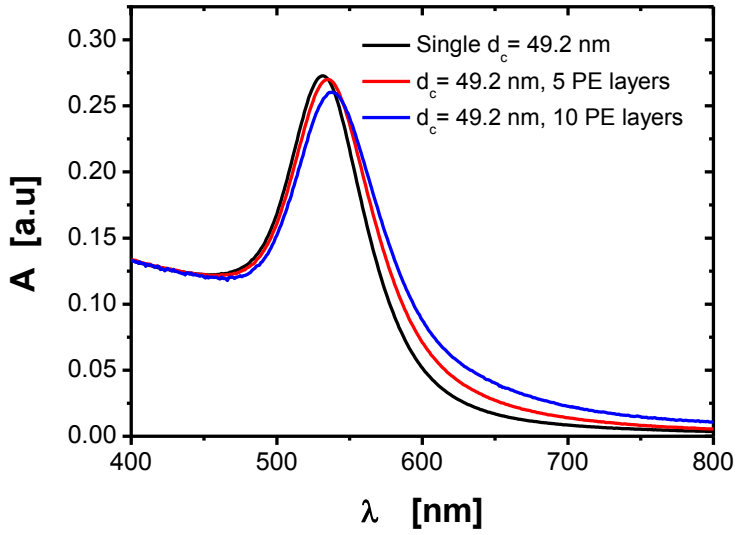

Figure SI.IV.2. *UV-Vis absorption spectra A(λ) of citrate stabilized Au NPs (d_c = 49.2 ± 4.9 nm, s = 1.1) before PE coating (black line), after (PAH, PSS)$_2$ PAH (n = 5; red line) and after (PAH, PSS)$_5$ (n = 10; blue line) coating.*

Zeta-potential measurements using dynamic light scattering (DLS) were performed on a Zetasizer Nano S system (Malvern Instruments, Malvern, U.K.) at detection angle of 173 degree with a 4 mW He-Ne laser operating at 633 nm wavelength. The zeta-potential following each PE adsorption step is plotted in Figure SI.IV.3. The intensity-averaged hydrodynamic NP diameter d_h and the polydispersity index (PDI) values were calculated from cumulant-type analysis. The rise of the hydrodynamic diameter d_h upon addition of PE layers is plotted in Figure SI.IV.4 and displayed in Table SI.IV.1. The thickness of the PE coating (n layers) was calculated as $½\cdot(d_h(n)-d_h(n=0))$. The average thickness of each single layer was calculated by assuming that PSS and PAH contribute equally in the increase of the shell thickness as $½\cdot(d_h(n)-d_h(n=0))/n$. The mean thickness of a single PE layer $d_{PE} = <½\cdot(d_h(n) - d_h(n=0))/n>$ was 1.6 ± 0.4 nm based on the values of Table SI.IV.1.

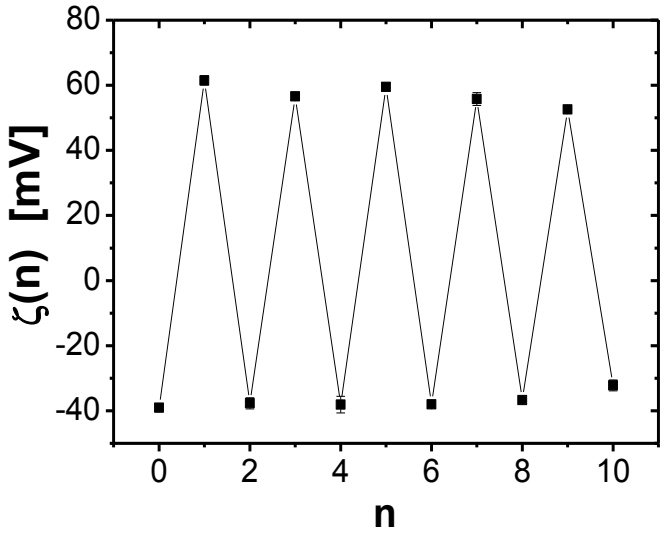

Figure SI.IV.3. *Zeta-potential ζ(n) of citrate-stabilized Au NPs (d_c = 49.2 ± 4.9 nm, s = 1.1) to which n PE layers were adsorbed, as recoded in water. The plain NPs (n = 0) are negatively charged due to their citric acid coating. Addition of the first PE layer (PAH, n = 1) changes the charge of the NPs to a positive sign. Measurements were carried out in water solutions.*

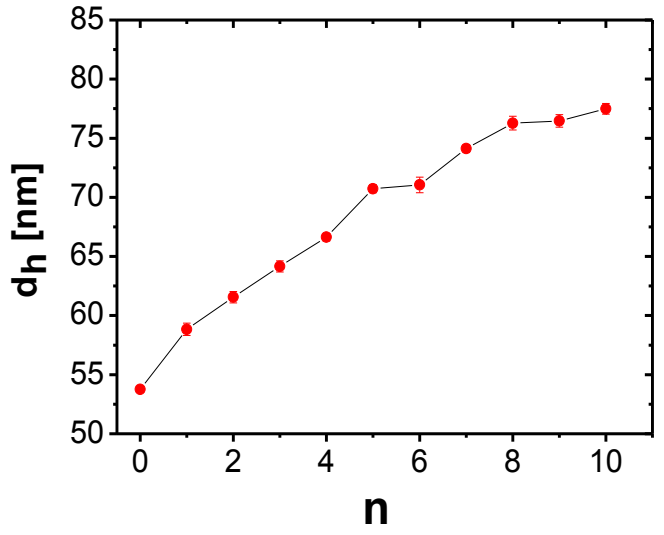

Figure SI.IV.4. *Hydrodynamic diameter d_h of citrate-stabilized Au NPs (d_c = 49.2 ± 4.9 nm, s = 1.1) upon layer-by-layer adsorption of n PEs layers. Data points correspond to mean values ± the standard deviation. Measurements were carried out in water solutions.*

n	0	1	2	3	4	5	6	7	8	9	10
d_h(n) [nm]	53.8 ±0.3	58.8 ±0.5	61.6 ±0.5	64.1 ±0.5	66.6 ±0.3	70.7 ±0.3	71.0 ±0.7	74.1 ±0.3	76.3 ±0.6	76.5 ±0.5	77.5 ±0.5
½·(d_h(n)-d_h(n=0)) [nm]	0	2.5	3.9	5.2	6.4	8.5	10.2	11.2	11.2	11.3	11.9
d_{PE} [nm]	0	2.5	1.9	1.7	1.6	1.7	1.4	1.4	1.4	1.3	1.2

Table SI.IV.1. *The hydrodynamic diameters d_h in dependence of the number n of the PE layers as displaced in Figure SI.IV.4. The increase of the shell thickness in Au NPs due to PE adsorption is given as ½·(d_h(n)-d_h(n=0), and the corresponding single layer thickness as* d_{PE} = ½·(d_h(n) - d_h(n=0))/n.

V) Formation of Au nanoparticle dimers by electrostatic interactions

Two solutions of Au NPs ($3\cdot10^{-13}$ M; d_c = 49.2 ± 4.9 nm, s = 1.1) with n and n+1 PE layers adsorbed (thus possessing charges of different signs) were first precipitated with centrifugation at 930×g for 90 min in order to remove free PE molecules which were present under storage conditions. The Au NPs were then redispersed in Milli-Q water and diluted 800 times respect to the initial concentration. Then, 100 µL of the two solutions of Au NPs coated with n and n+1 PE layers were mixed and after 10 min of gently shaking, a 10 µL drop of the mixture was deposited on a TEM grid, which was left to dry. TEM images were captured at different magnifications. We considered groupings of two Au NPs with an inter-NP distance less than (2n+1)·1.6 nm as dimers, whereby $\Delta d_{½}$ = 1.6 nm is the average thickness per PE layer as obtained by DLS, *cf.* Figure SI.V.1. Inter-NP distances D (surface-to-surface) were measured with the software Image-J (version 3.0) for at least 50 different dimers, *cf.* Figure SI.V.2 and Table SI.V.1. Non spherical NP shape complicated the analysis, *cf.* Figure SI.V.3.

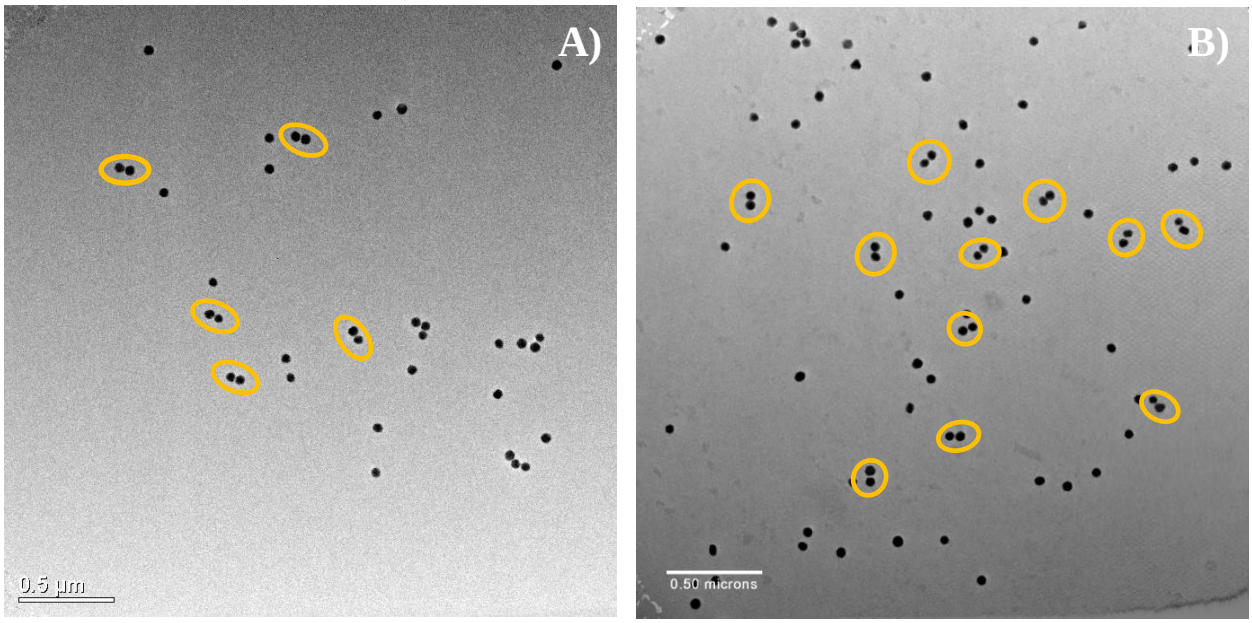

Figure SI.V.1. *TEM images showing an area of 10 µm^2 of a grid on which a mixture of Au NPs (d_c = 49.2 ± 4.9 nm) coated with n and n+1 PE layers had been deposited. A) Around 30% of dimers are found in a mixture of Au (PAH) and Au (PAH, PSS) NPs (n = 1). B) Around 30% of dimers are found in a mixture of Au (PAH, PSS)$_4$ PAH and Au (PAH, PSS)$_5$ (n = 9). The scale bars correspond to 500 nm.*

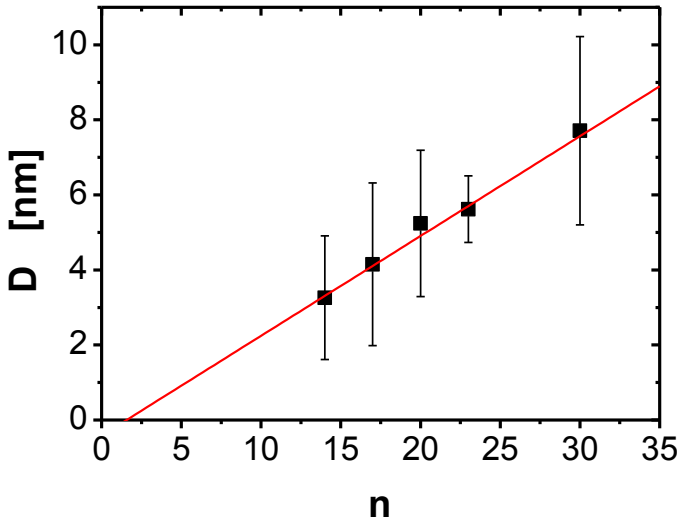

Figure SI.V.2. *Inter-NP distance D (surface-to-surface) of Au NP dimers formed by electrostatic interactions between oppositely charged NPs (d_c = 49.2 ± 4.9 nm) coated with n and n+1 PE layers (n = 14-30; data for smaller n are shown in the main manuscript). Data points correspond to mean values ± standard deviations. The red line is the linear regression that relates D and n.*

n	14	17	20	23	29
D [nm]	3.26 ±1.65	4.15 ±2.17	5.24 ±1.95	5.62 ±0.89	7.71 ±2.51
d_{PE} [nm]	0.11	0.12	0.13	0.12	0.13

Table SI.V.1. *Inter-NP distance D (surface-to-surface) of Au NPs dimers formed by electrostatic interactions between oppositely charged NPs (d_c = 49.2 ± 4.9 nm) coated with n and n+1 PE layers (n = 14-30; data for smaller n are shown in the main manuscript), corresponding to Figure SI.IV.2. The thickness of each PE layer is estimated as d_{PE} = D/(n+(n+1)) = D/(2n+1).*

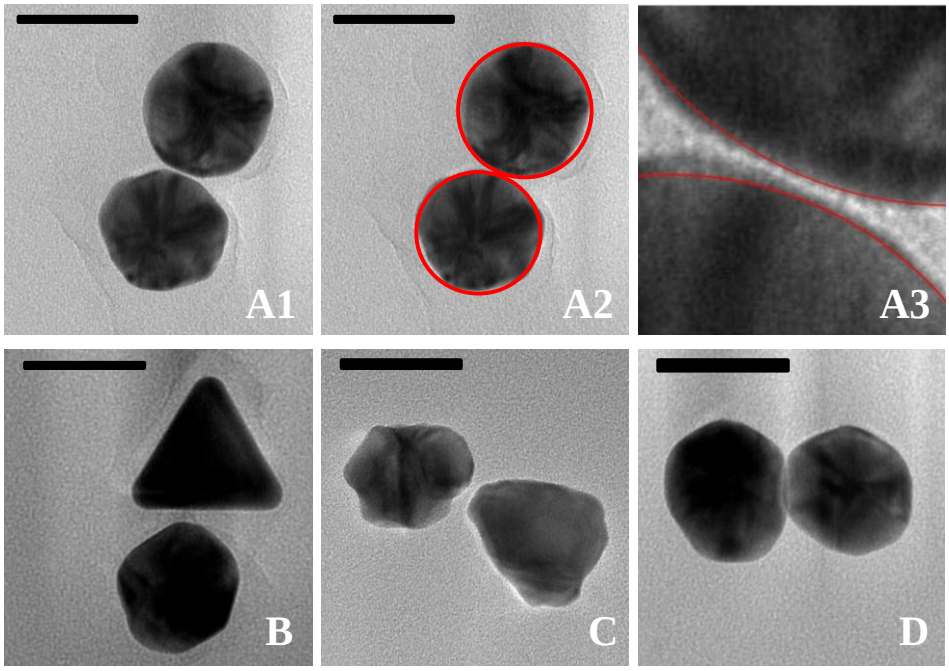

Figure SI.V.3. *TEM images of dimers formed by quasispherical Au NPs (d_c = 49.2 ± 4.9 nm) with polyhedral shape (A1-A3), triangular and polyhedral shapes (B), very rough surface (C) and overlap of the Au cores. Image A2 points out the difference between a perfectly spherical shape (red circle) and the polyhedral shape of most of the Au NPs. Image A3 shows a zoom of image A2, where the red lines correspond to the border of the Au cores fitted with a perfectly spherical shape. The scale bars correspond to 50 nm.*

Moreover, radial distribution function (RDF) analysis was performed for the TEM images. The raw images were inverted to assign high pixel values to features and low values to background pixels. Next, a real-space band-pass filter was applied to suppress pixel noise and long-range intensity variations allowing for the extraction of the relevant image information with the characteristic size of the NPs (*cf.* Figure SI.V.4.a). Finally the NPs were roughly identified by detecting all local intensity maxima. These positions were used as initial positions to calculate the exact coordinates by determining the center position of each centroid with sub-pixel accuracy.

Now for each NPs it's RDF $g(r) = N(r)/(2\pi \cdot r \cdot \rho \cdot dr)$ was calculated and RDFs of all NPs and all images were averaged. Each single RDF was calculated as follows: N(r) is the number of NPs which can be found in a ring of width dr at distance r from each NP, and ρ [m^{-2}] is the mean NP density of the image under consideration (Number of NPs divided by the area). The binning distance dr was set to 1 pixel, equivalent to a spatial resolution of 0.5 nm. The whole process is illustrated in Figure SI.V.4.b. As the area of the ring is increasing with increasing r, g(r) has to be normalized by the factor $2\pi \cdot r$. Artifacts due to image edges are avoided by dividing only through the fraction of the ring confined by the image dimensions.

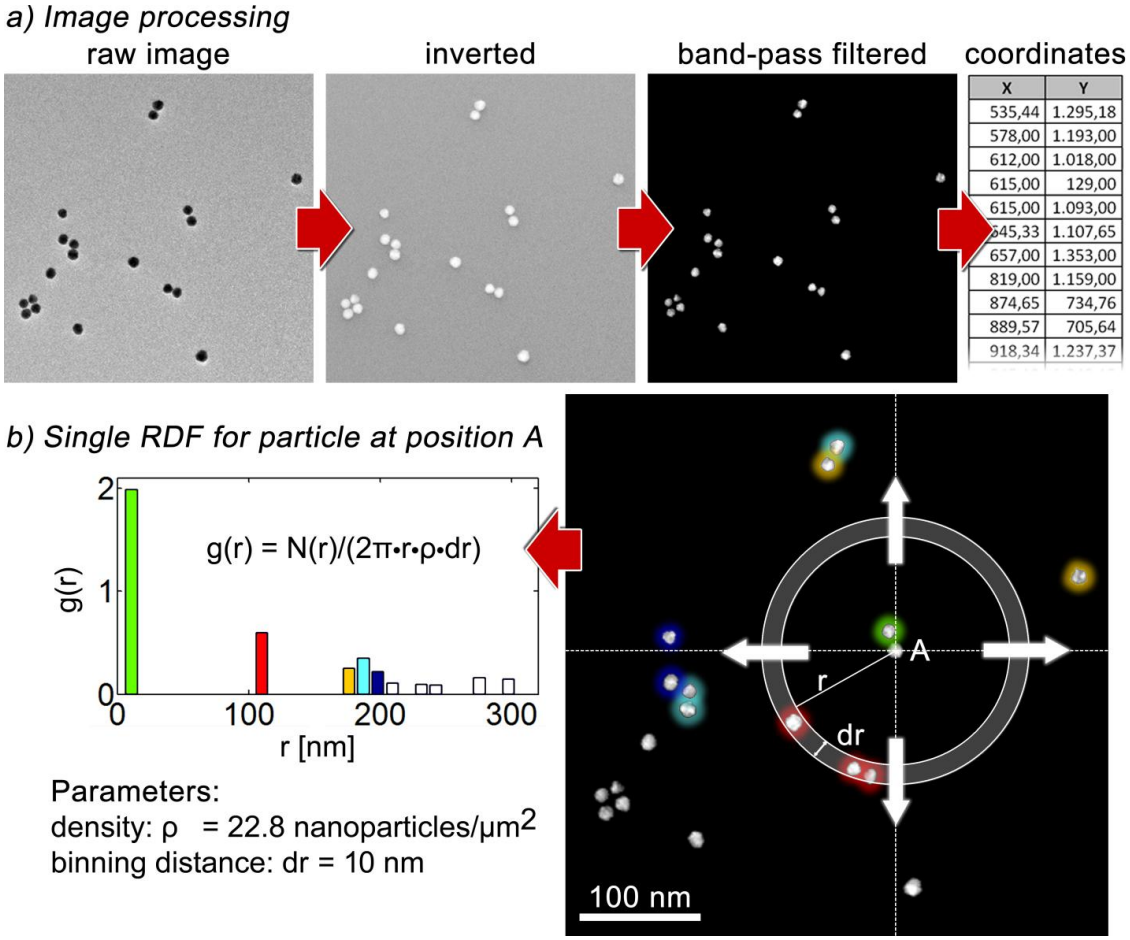

Figure SI.V.4. *Illustration, how the radial distribution function g(r) is obtained. Raw TEM-images are inverted and band-pass filtered to separate the NP features from the background. NP coordinates are obtained by calculating the center of mass of each feature (b). For the NP (d_c = 49.2 ± 4.9 nm) at position A the RDF is calculated exemplary with a binning distance of dr = 10 nm. In a shell of thickness dr and distance r from NP A the number of NPs N(r) is calculated and displayed in the corresponding bar-plot (b). Please note: The increased binning distance of 10 nm was only used in this figure to make it's content more comprehensible.*

Figure SI.V.5 shows RDFs g(r) for dimers made with n = 1 and n = 9. The position r of the peak in the RDFs corresponds to the mean center-to-center distance D_{cc} of the NPs in one dimer. The width of the peak g(r = D_{cc}) is defined as error $\Delta D_{cc.}$

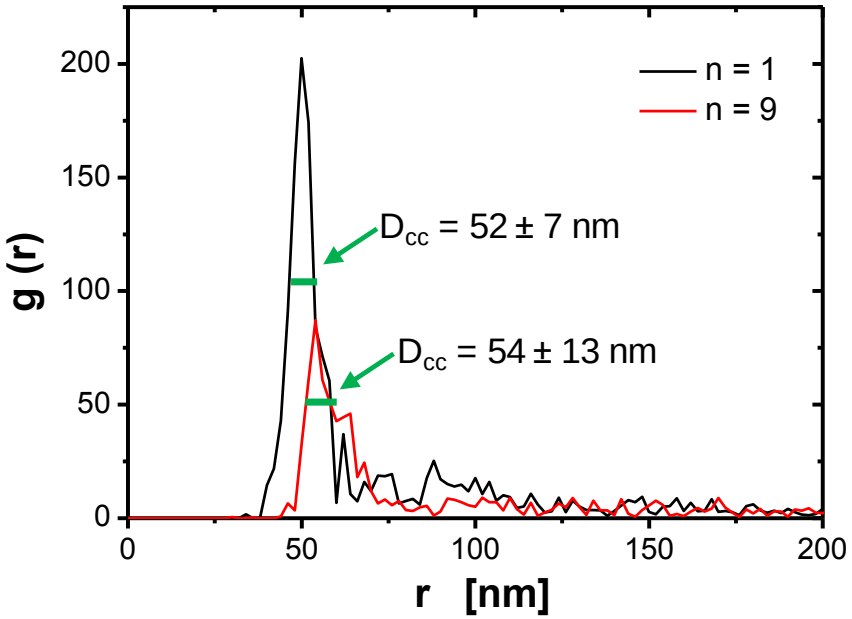

Figure SI.V.5. *Radial distribution functions g(r) of the samples n= 1 and n= 9 (d_c = 49.2 ± 4.9 nm). Data yield D_{cc} = 52 ± 7 nm (n = 1) and D_{cc} = 54 ± 13 nm (n = 9).*

The surface-to-surface analysis (*cf.* the main paper / Table SI.V.1) determined D = 0.6 and D = 2.5 nm for n = 1 and n = 9, respectively, which is a bit different to the obtained values as obtained with the RDF (*cf.* Figure SI.V.5) analysis, that correspond to distances of 2 and 4 nm for the same number of layers *(d_c = 49.2 ± 4.9 nm)* .

VI) Coating of Au nanoparticles with biotin and streptavidin

PMA-coated (and thus hydrophilic) Au NPs with core diameter of $d_c = 4.7 \pm 0.8$ nm were used as basis for further bioconjugation [3] and are termed here Au NPs, *cf.* Figure SI.VI.1.

These Au NPs were modified with biotin (B) and NPs with exactly one B per NP (termed here Au-B NPs, *cf.* Figure SI.VI.1) were fractionated. The biotinylated NPs were obtained by binding biotin-CONH-PEG-NH_2 (Rapp-Polymere, M_w = 5000 Dalton) *via* its NH_2-group with N-(3-Dimethylaminopropyl)-N'N'-ethylcarbodiimide hydrochloride (EDC; Sigma, #E7750) to a COOH-group on the PMA coating of the Au NPs [5]. The molar ratio of Au NPs / PEG / EDC was chosen as 1/500/700. The reaction was maintained at room temperature for 120 minutes. The conjugates were then run on an 2 % agarose gel (Ultrapure Agarose; Invitrogen, #15510-027) in tris borate-EDTA buffer (pH 8.4), *cf.* Figure SI.VI.2 [8]. Due to the PEG spacer the conjugates could be separated on the gel to Au NPs with no B (Au NPs) and Au NPs with exactly one B per NP (Au-B NPs) [5, 8], *cf.* Figure SI.VI.2. The bands containing Au NPs and Au-B NPs were cut from the gel and the NPs were extracted [5].

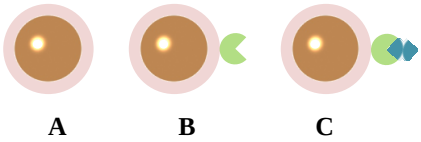

Figure SI.VI.1. *Schematic representation of bioconjugated PMA-coated Au NPs ($d_c = 4.7 \pm 0.8$ nm).The pink ring represents the organic shell of PMA. (A) Au NPs. (B) Au-B NPs. (C) Au-B-SA NPs.*

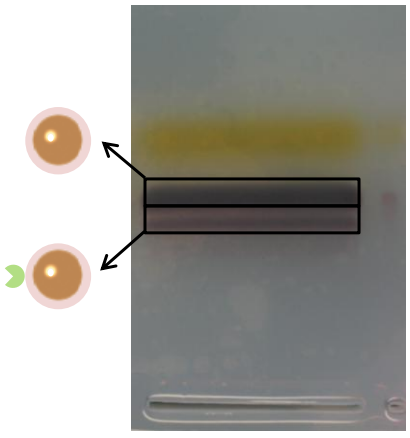

Figure SI.VI.2. *Electrophoretic separation of Au NPs having a discrete number of biotin molecules attached per NP. The two prominent bands correspond to Au NPs and Au-B NPs.*

Au NPs functionalized with one streptavidin (SA) molecule per NP were produced by binding SA on Au-B NPs, *cf.* Figure SI.VI.1. Au-B NPs and SA were mixed in phosphate buffered saline (PBS) at a ratio of Au-B NPs/SA of 1/8. The reaction was left overnight at 4 ºC without agitation to avoid any damage of the protein. The sample was then purified through size exclusion column chromatography (SEC). A S300 sephacryl gel matrix column and PBS were used as stationary and mobile phase, respectively [9]. Due to their bigger size the Au-B-SA NPs eluted first. The Au-B-SA NPs were then concentrated using 100 kDa centrifuge filters (Sartorius, # VS2042). For analysis purpose the three samples Au NPs, Au-B NPs, and Au-B-SA NPs were run simultaneously on one gel to confirm the conjugation of different molecules on their surface and to compare their corresponding mobilities, *cf.* Figure SI.VI.3.

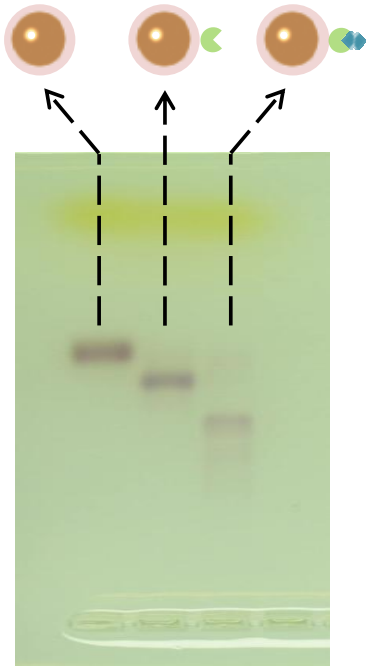

Figure SI.VI.3. *Electrophoretic separation of Au NPs, Au-B NPs, and Au-B-SA NPs. All NPs migrate from the loading wells at the bottom of the image towards the plus pole on the top of the image. The bigger the NPs are, the slower they migrate on the gel.*

VII) Formation of Au nanoparticle dimers by biotin-streptavidin interaction

In order to form Au NP dimers, Au-B and Au-B-SA NPs were mixed at different molar ratios in solution. Different reaction conditions may lead to the formation of various geometries. Such geometries could be monomers, dimers, trimers, tetramers, or bigger agglomerates, as formed by non-specific adhesion. In order to find the best condition favorable for the formation of Au-B-SA-B-Au dimers different conditions were analyzed with gel electrophoresis, *cf.* Figure SI.VII.1.

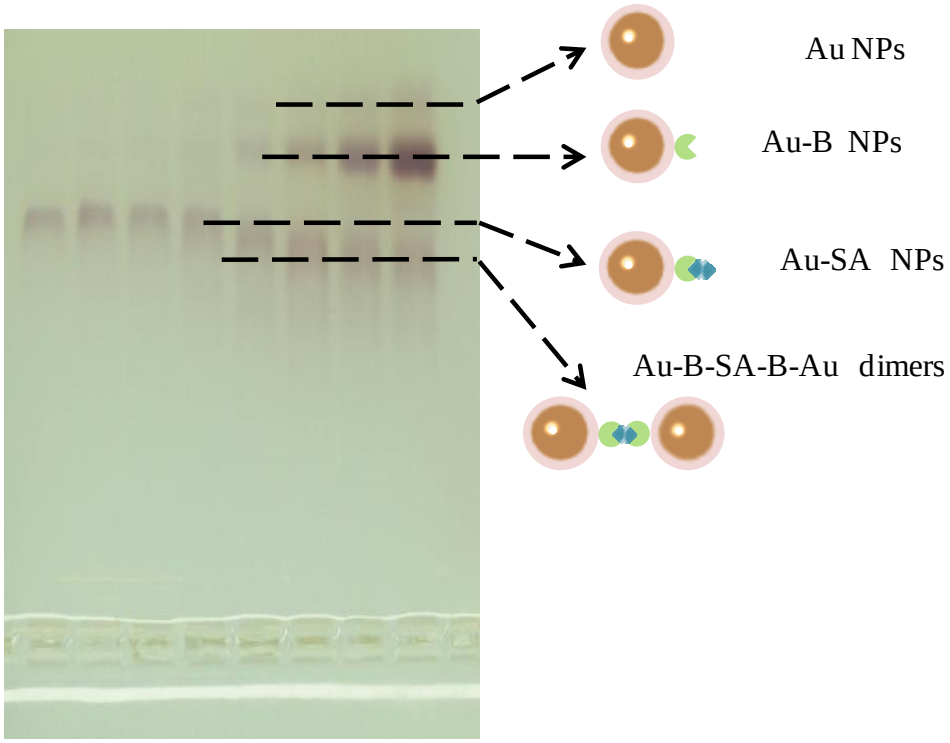

Figure SI.VII.1. *Au-B and Au-B-SA NPs were mixed at different ratios, and these mixtures were then run with gel electrophoresis. Hereby the concentration of Au-B NPs increased from left to right, and the concentration of Au-B-SA was kept constant. For low Au-B NP concentration the Au-B and Au-B-SA NPs run as separate bands, cf. the left side of the gel. Upon increasing the Au-B NP concentration the slower moving band gets more retarded. This can be ascribed to the fact that Au-B NPs bind to the Au-B-SA NPs, and the resulting Au-B-SA-B-Au dimers are more retarded than the Au-B-SA NPs, cf. the right side of the gel. The Au-B-SA-B-Au dimers were then extracted from the gel and analyzed with RDF, as is described in the main manuscript.*

VIII) Coating of quantum dots with biotin and streptavidin

Semiconductor NPs, so-called quantum dots (QDs), which are intrinsically fluorescent, were used alternatively to Au NPs in order to demonstrate the universality of our recipe reported here. Two types of QDs based on CdSe/ZnS core/shell NPs with different sizes and thus different fluorescent emission were used: green QDs (Abs: 513 nm, Em: 536 nm) and red QDs (Abs: 602 nm, Em: 620 nm) [10].

Commercial hydrophobic QDs (Evidot) were used. These QDs were transferred to water by overcoating with an amphiphilic polymer (PMA), similar to the procedure as described for the Au NPs [5, 11, 12].

Biotinylated QDs were obtained similar to the production of Au-B NPs, by binding biotin-CONH-PEG-NH_2 (Rapp-Polymere, M_w = 5000 Dalton) *via* its NH_2-group with EDC to a COOH-group on the PMA coating of the QDs [5]. Conjugates of QDs with exactly one or two B molecules per QD were obtained by fractionation using gel electrophoresis [8], *cf.* Figure SI.VIII.1.

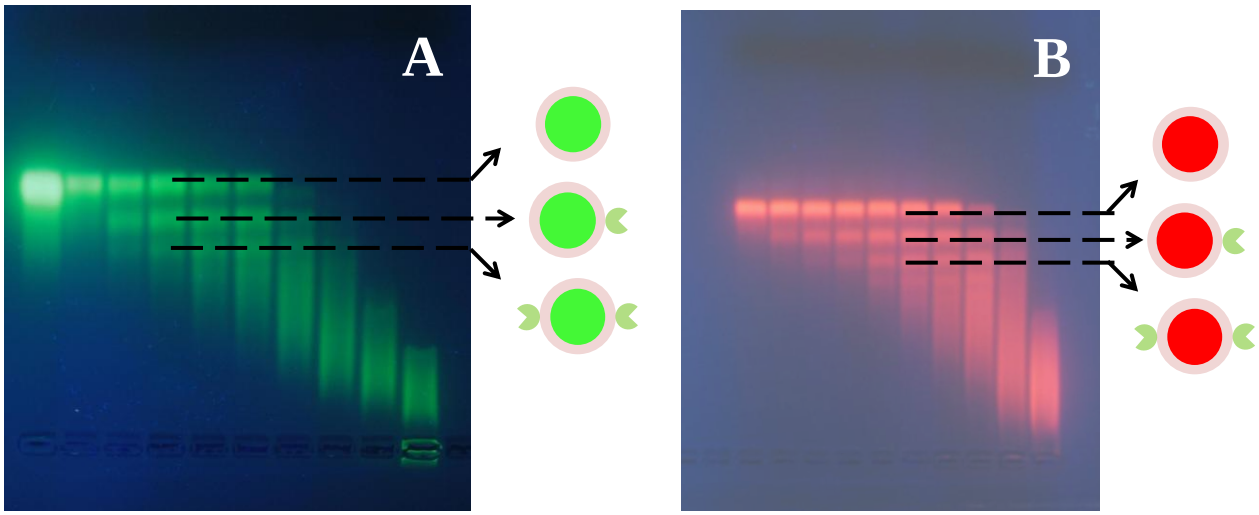

Figure SI.VIII.1. *PMA-coated QDs (A) green, B) red) were linked via EDC with biotin-CONH-PEG-NH_2. Different reaction mixtures in which the amount of added biotin-CONH-PEG-NH_2 per QD was varied were prepared. These mixtures were run on agarose gels, whereby the amount of added biotin-CONH-PEG-NH_2 per QD increases from left to right. Discrete bands can be observed on the gels, whereby the fastest, first band corresponds to QD without B, the 2nd band to QDs with exactly one B per QD, the 3rd band to QDs with exactly two Bs per QD, etc.*

SA-modified QDs were obtained similar to SA-modified Au NPs. QDs with one B per QD were mixed with SA in a ratio QD / SA of 1/8. SA-modified QDs were purified using SEC, *cf.* Figure SI.VIII.2.

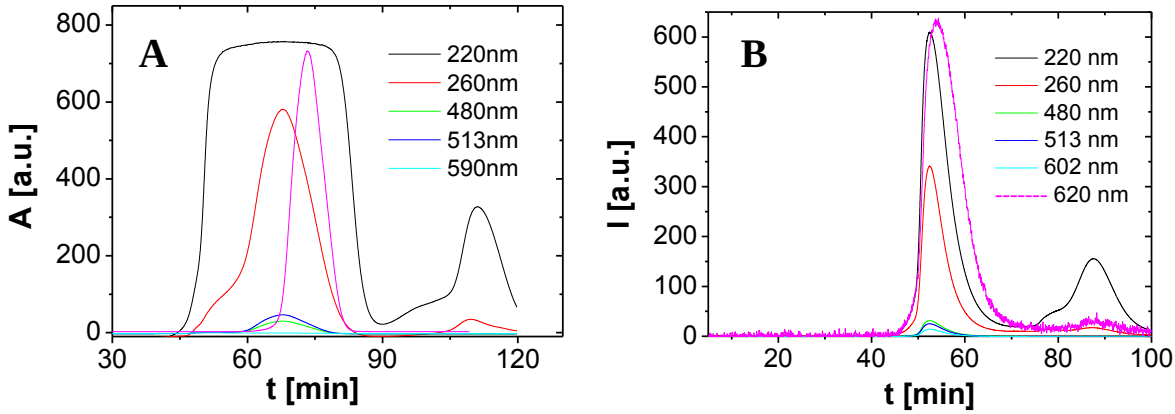

Figure SI.VIII.2. *Size exclusion chromatography (SEC) elution profiles of different samples. The absorption A(t) "DAD" (as recorded at different wavelengths λ of 220 nm, 260 nm, 480 nm, 513 nm, and 590 nm / 602 nm) and the fluorescence intensity I(t) "FLD" (as recoded at emission wavelength 620 nm, pink curve) are plotted versus the elution time t. A) Green QDs with one B molecule per QD were first purified with gel electrophoresis and then run on the SEC column in order to get an estimation of the retention time. B) Red QDs with one SA molecule per QD were purified with SEC in order to avoid the possible conformational change upon running gel electrophoresis. SEC turned out to be a more soft method of purification.*

Functionality of B-SA binding was probed by titration of fluorophore-modified SA with fluorophore-modified B. We used Atto520-labeled B and Atto590-labeled SA for this purpose. In this way the position of B and SA on the gels of electrophoresis experiments could be identified, *cf.* Figures SI.VIII.3 and SI.VIII.4.

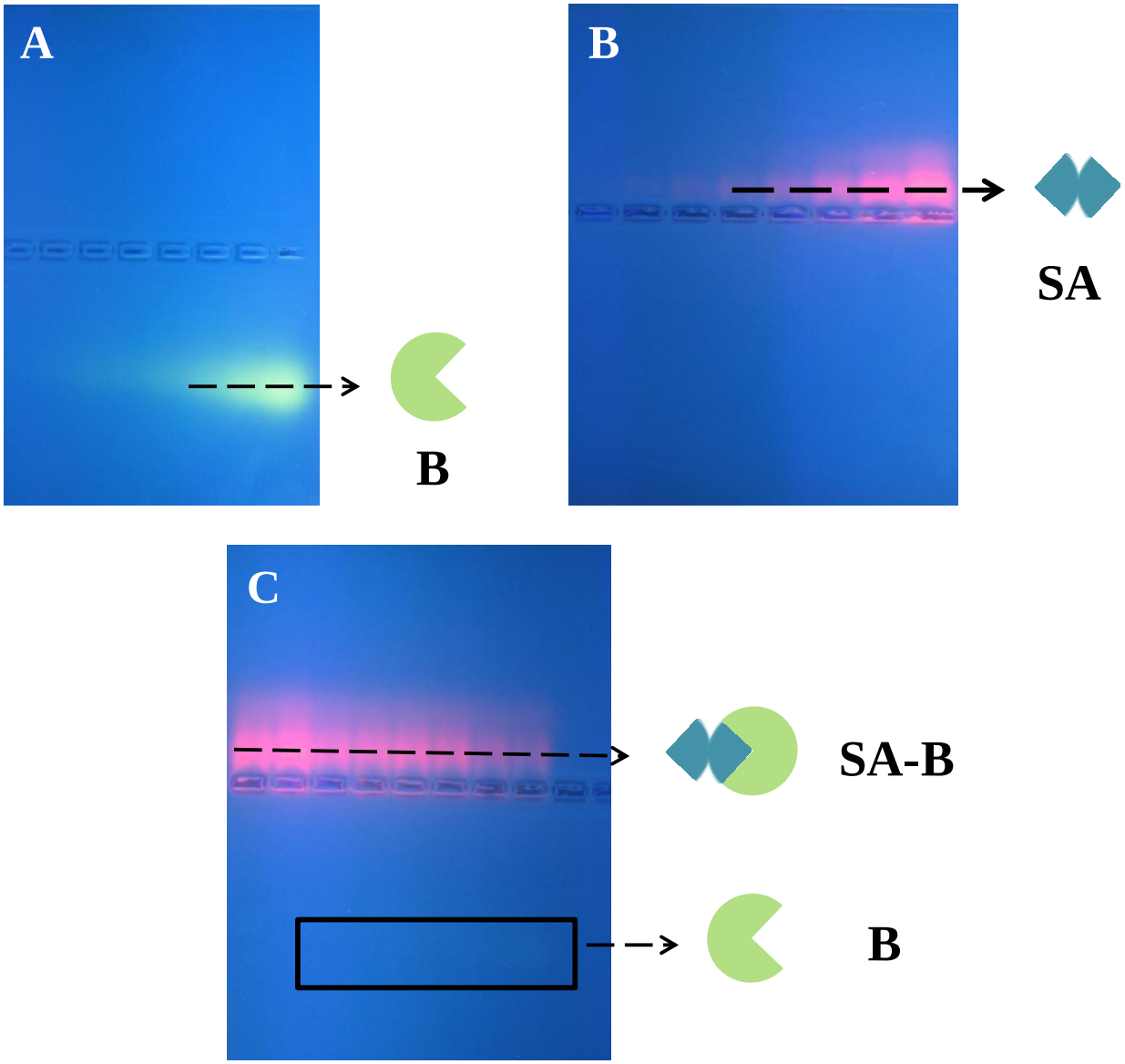

Figure SI.VIII.3. *Positions of Atto520-labeled B and Atto590-labeled SA on agarose gels after gel electrophoresis. The plus pole is on the top, the minus pole on the bottom, as for all gel images shown in this work. Before running electrophoresis, samples had been loaded in the wells which are visible in the middle of the gel. The gels were placed on an UV-illumination table and images were recorded with a digital camera. A) Increasing concentration of Atto520-labeled B from left to right in the range of 17 µM to 1 mM. The labeled B was found to run towards the negative pole. B) Increasing concentration of Atto590-labeled SA from left to right in the range of 18.5 µM to 1.12 mM. C) Mobility of mixtures of B and SA. The concentration of Atto520-labeled B was varied between 2.5 µM and 156 µM, whereas the concentration of Atto590-labeled SA was kept constant at 19.5 µM. The higher the B concentration, the lower the fluorescence in the SA containing band is.*

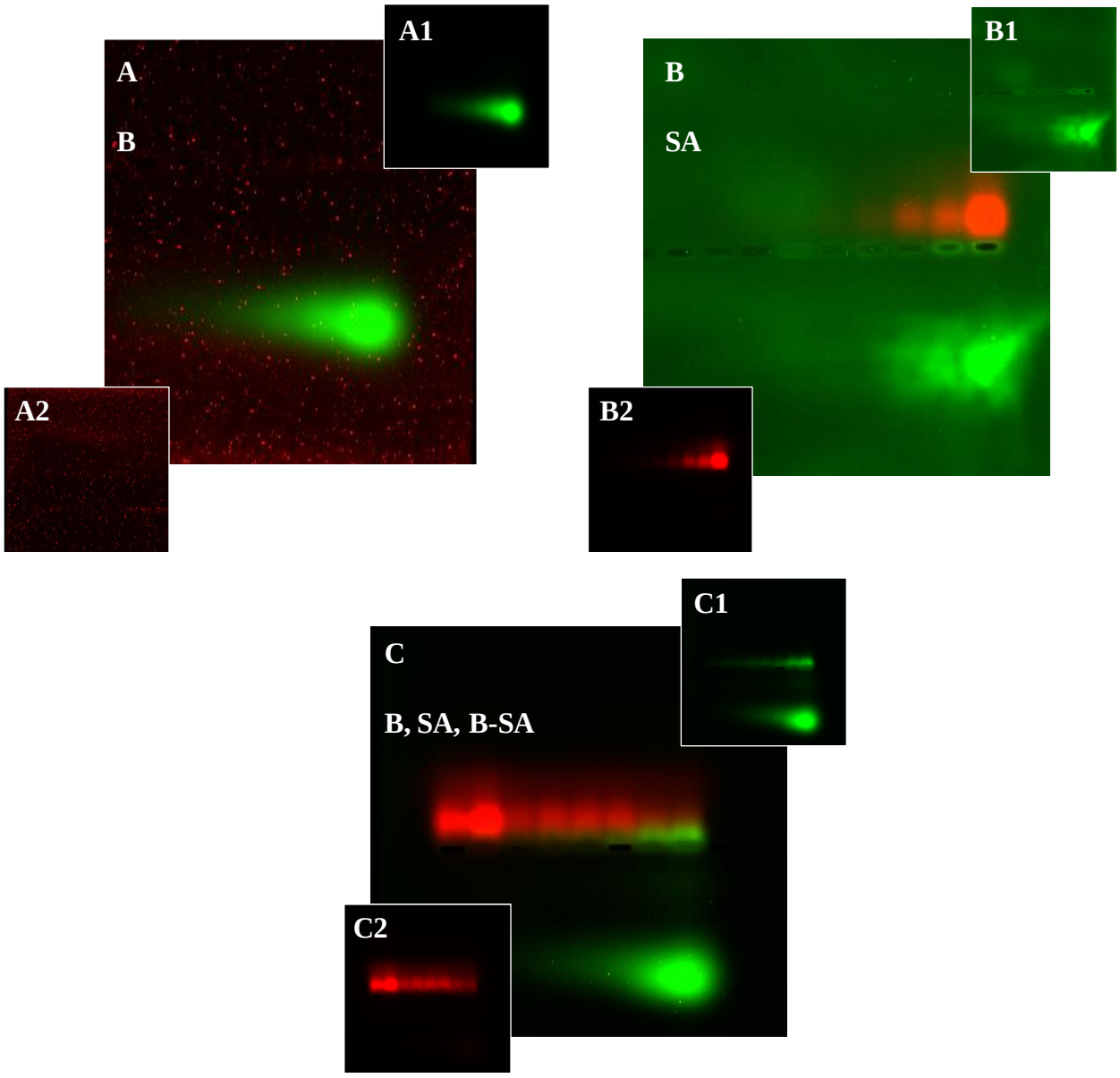

Figure SI.VIII.4. *Positions of Atto520-labeled B and Atto590-labeled SA on agarose gels after gel electrophoresis. The plus pole is on the top, the minus pole on the bottom, as for all gel images shown in this work. Before running electrophoresis, samples had been loaded in the wells which are visible in the middle of the gel. The gels were imaged with a gel scanner, in which excitation was performed at 488 nm and 532 nm for the green and red channel, respectively. In this way both fluorescence labels could be spectrally resolved. A) Atto520-labeled B has been used in order to observe the position of B on the gel. The concentration was raised from left to right. The insets A1) and A2) correspond to the two excitation wavelengths 488 nm and 532 nm used for the green and red channel, respectively. B) Atto590-labeled SA has been used in order to observe the position of SA on the gel. The concentration was raised from left to right. The insets B1) and B2) represent the green and red channel. The presence of green fluorescence in B1) is an artifact and does not originate from Atto590-labeled SA. C) Mobility of mixtures of B and SA.*

While the SA concentration was kept constant the B concentration was raised from left to right. In contrast to Figure SI.VII.3, which reports a similar experiment, due to the imaging with a gel scanner B and SA can be independently identified on the gel. The insets C1) and C2) represent the green and red channel. The presence of two different bands in the green channel confirms the binding of B to SA. The lower (green) band migrating towards the minus pole originates from free B. The upper (green) band which slightly migrates towards the plus pole originates from B bound to SA, and overlaps with the lower part of the (red) SA band. This demonstrates B-SA binding.

Functionality of the B and SA groups attached to the QDs were probed by titration with fluorophore-modified SA and B, respectively. We used Atto520-labeled B and Atto590-labeled SA for this purpose. In this way the position of B and SA on the gels of electrophoresis experiments could be identified, *cf.* Figures SI.VII.5 and SI.VII.6. The resulting bands were cut from the gel and analyzed with fluorescence spectroscopy, *cf.* Figure SI.VII.7.

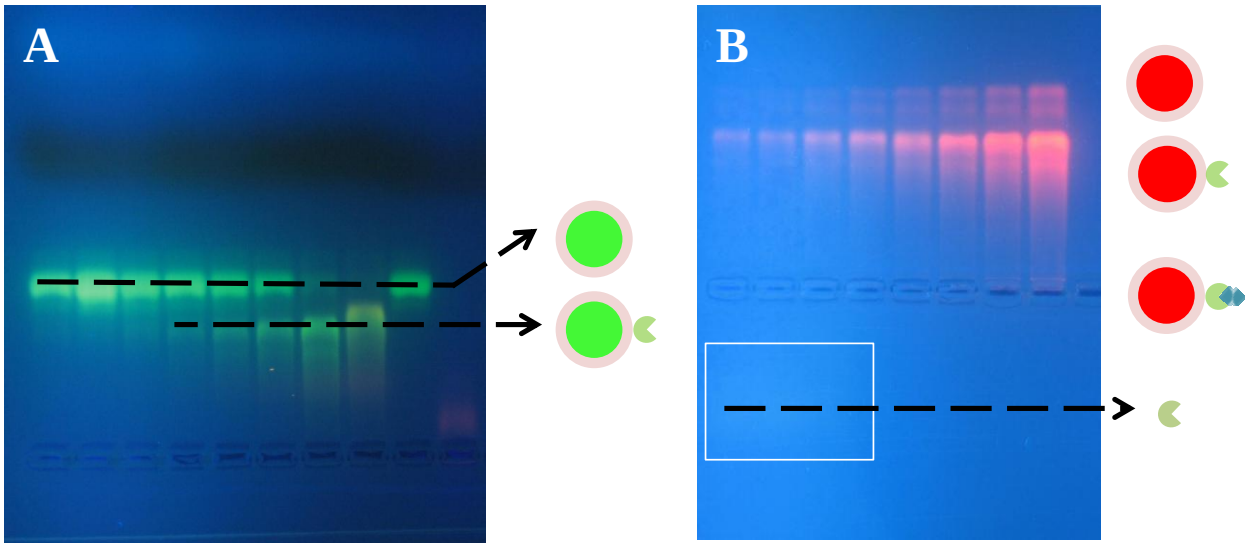

Figure SI.VIII.5. *A) Titration series of green fluorescent QDs with exactly one B bound per QD with (red) Atto590-labeled SA. The molar ratio SA / QD has been varied from 0.063 to 8. Thus, while the QD concentration was kept constant, the SA concentration was raised from left to right. The two lanes at the right correspond to green QDs with one B and free SA as controls. Upon presence of SA the formation of conjugates of QDs with B and SA begins, which can be seen by the retardation of the band in the gel. B) Titration series of SA conjugated red QDs with (green) Atto520-labeled B. The molar ratio B / QD has been varied from 0.063 and 8. Thus, while the QD concentration was kept constant, the B concentration was raised from left to right.*

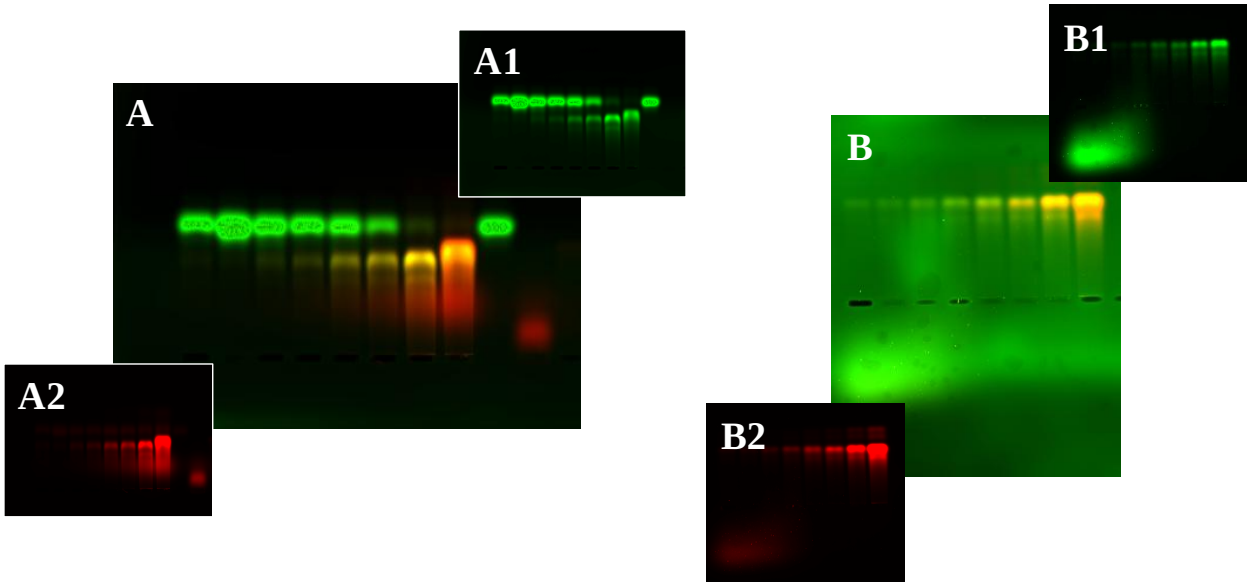

Figure SI.VIII.6. *A) Titration series of green fluorescent QDs with exactly one B bound per QD with (red) Atto590-labeled SA. While the QD concentration was kept constant, the SA concentration was raised from left to right. The two lanes at the right correspond to green QDs with one B and free SA as controls. The faster band in the green channel (A1) corresponds to biotinylated QDs, whereas the slower band corresponds to conjugates in which SA has bound to the biotinylated QDs. B) Titration series of SA conjugated red QDs with (green) Atto520-labeled B. While the QD concentration was kept constant, the B concentration was raised from left to right. For imaging the green and the red excitation channels at 488 nm and 532 nm were used, respectively. The image has been recorded from the same gel as the one shown in Figure SI.VII.5. In the insets 1) and 2) represent the green and red channels, respectively.*

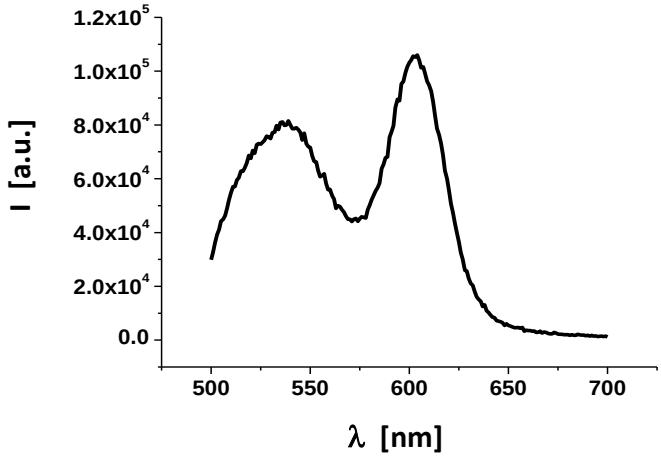

Figure SI.VIII.7. *Emission spectrum I(λ) of conjugates made by Atto520-labeled B bound to red fluorescence QDs with one SA per QD, which had been cut from the gels.*

IX) Formation of quantum dot dimers by biotin-streptavidin interaction

Dimers of QDs were attempted by mixing QDs with exactly one B per QD and QDs with exactly one SA per QD. In Figure SI.IX.1 homodimers, and in Figures SI.IX.2 and SI.IX.3 heterodimers are shown. In Figure SI.IX.4 the fluorescence spectrum of extracted heterodimers is shown.

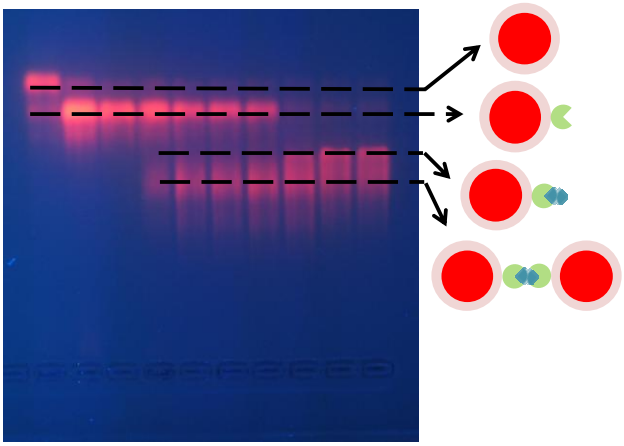

Figure SI.IX.1. *Image of a gel in which mixtures of red QDs with one B per QD and red QDs with one SA per QD have been run on an agarose gel.*

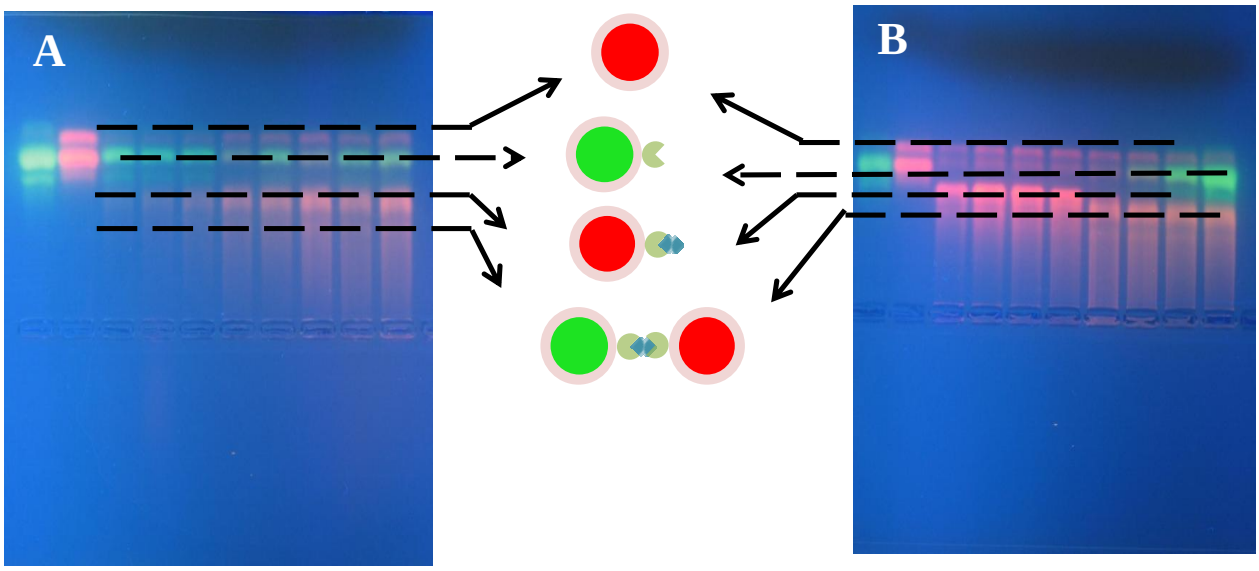

Figure SI.IX.2. *Image of gels in which green fluorescent QDs with one B per QD were mixed with red fluorescent QDs with one SA per QD and then run with gel electrophoresis. The two lanes on the left are controls. A) While the concentration of green B-modified QDs was kept constant the concentration of red SA-modified QDs is increased from left to right up to a ratio of red QD / green QD of 8 / 1. B) While the concentration of red SA-modified QDs was kept constant the concentration of green B-modified QDs is increased from left to right from a ratio of green QD / red QD of 0.063 / 1 until 8 / 1.*

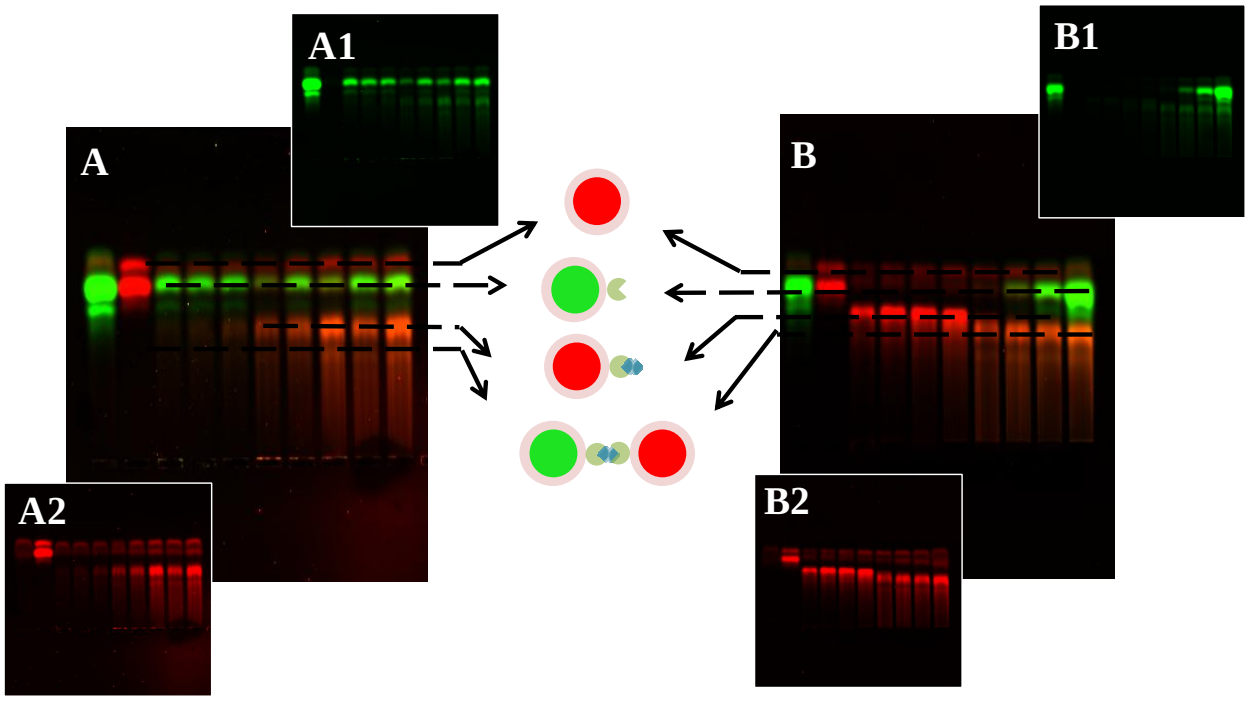

Figure SI.IX.3. *Images of the same gel as shown in Figure SI.VIII.2, however, recorded with a gel scanner with excitations at 488 nm and at 532 nm. Due to the imaging of the two types of QDs in two separated channels the formation of dimers (groupings) of the two QDs can be observed at the regions in which emission of both types of QDs colocalizes. In the insets 1) and 2) represent the green and red channels, respectively.*

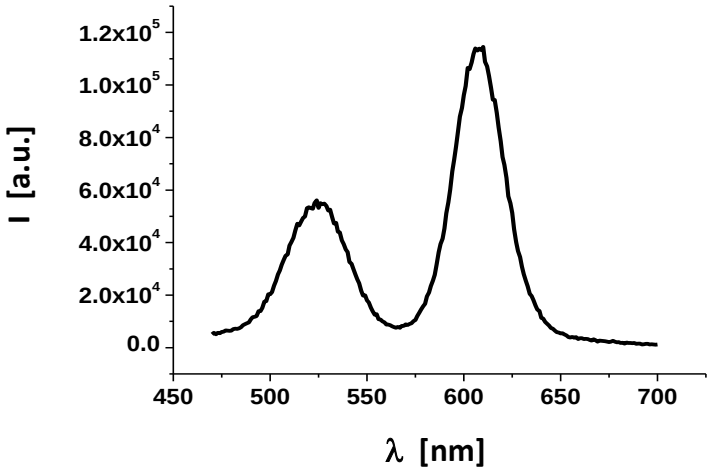

Figure SI.IX.4. Emission spectrum I(λ) of conjugates made by green QDs with one B per QD and red QDs with one SA bound per QD.

IX) References

[1] Commercial gold nanoparticles were delivered by British Bio-cell International (BBI).(http://www.buybbi.com/Products_GoldColloid_1.aspx).

[2] N.G. Bastus, J. Comenge, V. Puntes, Langmuir, 27 (2011) 11098-11105.

[3] F. Amin, D.A. Yushchenko, J.M. Montenegro, W.J. Parak, ChemPhysChem, 13 (2012) 1030-1035.

[4] M. Brust, M. Walker, D. Bethell, D.J. Schiffrin, R. Whyman, J. Chem. Soc., Chem. Commun., (1994) 801-802.

[5] C.-A.J. Lin, R.A. Sperling, J.K. Li, T.-Y. Yang, P.-Y. Li, M. Zanella, W.H. Chang, W.J. Parak, Small, 4 (2008) 334-341.

[6] P. Rivera Gil, D. Jimenez de Aberasturi, V. Wulf, B. Pelaz, P. del Pino, Y. Zhao, J. de la Fuente, I. Ruiz de Larramendi, T. Rojo, X.-J. Liang, W.J. Parak, Acc. Chem. Res., 46 (2013) 743-749.

[7] X.O. Liu, M. Atwater, J.H. Wang, Q. Huo, Colloids Surf., B, 58 (2007) 3-7.

[8] R.A. Sperling, T. Pellegrino, J.K. Li, W.H. Chang, W.J. Parak, Adv. Funct. Mater., 16 (2006) 943-948.

[9] R.A. Sperling, T. Liedl, S. Duhr, S. Kudera, M. Zanella, C.-A.J. Lin, W.H. Chang, D. Braun, W.J. Parak, J. Phys. Chem. C, 111 (2007) 11552 -11559.

[10] W.J. Parak, D. Gerion, T. Pellegrino, D. Zanchet, C. Micheel, S.C. Williams, R. Boudreau, M.A.L. Gros, C.A. Larabell, A.P. Alivisatos, Nanotechnology, 14 (2003) R15-R27.

[11] T. Pellegrino, L. Manna, S. Kudera, T. Liedl, D. Koktysh, A.L. Rogach, S. Keller, J. Rädler, G. Natile, W.J. Parak, Nano Lett., 4 (2004) 703-707.

[12] F. Zhang, E. Lees, F. Amin, P. Rivera_Gil, F. Yang, P. Mulvaney, W.J. Parak, SMALL, 7 (2011) 3113-3127.

Dear Author,

Here are the final proofs of your article. Please check the proofs carefully.

All communications with regard to the proof should be sent to bmcproductionteam2@spi-global.com.

Please note that at this stage you should only be checking for errors introduced during the production process. Please pay particular attention to the following when checking the proof:

- Author names. Check that each author name is spelled correctly, and that names appear in the correct order of first name followed by family name. This will ensure that the names will be indexed correctly (for example if the author's name is 'Jane Patel', she will be cited as 'Patel, J.').
- Affiliations. Check that all authors are cited with the correct affiliations, that the author who will receive correspondence has been identified with an asterisk (*), and that all equal contributors have been identified with a dagger sign (†).
- Ensure that the main text is complete.
- Check that figures, tables and their legends are included and in the correct order.
- Look to see that queries that were raised during copy-editing or typesetting have been resolved.
- Confirm that all web links are correct and working.
- Ensure that special characters and equations are displaying correctly.
- Check that additional or supplementary files can be opened and are correct.

Changes in scientific content cannot be made at this stage unless the request has already been approved. This includes changes to title or authorship, new results, or corrected values.

How to return your corrections

Returning your corrections via online submission:

- Please provide details of your corrections in the online correction form. Always indicate the line number to which the correction refers.

Returning your corrections via email:

- Annotate the proof PDF with your corrections.
- Send it as an email attachment to: bmcproductionteam2@spi-global.com.
- Remember to include the journal title, manuscript number, and your name when sending your response via email.

Note: in order to ensure timely publication, if we do not hear from you within 48 hours we may take the decision to sign-off the article on your behalf and proceed to publication.

After you have submitted your corrections, you will receive email notification from our production team that your article has been published in the final version. All changes at this stage are final. We will not be able to make any further changes after publication.

Kind regards,

BioMed Central Production Team 2

JOURNAL OF NANOBIOTECHNOLOGY

RESEARCH Open Access

Silicon particles as trojan horses for potential cancer therapy

Roberto Fenollosa[1], Eduardo Garcia-Rico[2], Susana Alvarez[3], Rosana Alvarez[3], Xiang Yu[4], Isabel Rodriguez[1], Susana Carregal-Romero[4], Carlos Villanueva[5], Manuel Garcia-Algar[6], Pilar Rivera-Gil[5], Angel R de Lera[3], Wolfgang J Parak[4*], Francisco Meseguer[1*] and Ramón A Alvarez-Puebla[6,7*]

Abstract

Background: Porous silicon particles (PSiPs) have been used extensively as drug delivery systems, loaded with chemical species for disease treatment. It is well known from silicon producers that silicon is characterized by a low reduction potential, which in the case of PSiPs promotes explosive oxidation reactions with energy yields exceeding that of trinitrotoluene (TNT). The functionalization of the silica layer with sugars prevents its solubilization, while further functionalization with an appropriate antibody enables increased bioaccumulation inside selected cells.

Results: We present here an immunotherapy approach for potential cancer treatment. Our platform comprises the use of engineered silicon particles conjugated with a selective antibody. The conceptual advantage of our system is that after reaction, the particles are degraded into soluble and excretable biocomponents.

Conclusions: In our study, we demonstrate in particular, specific targeting and destruction of cancer cells *in vitro*. The fact that the LD_{50} value of PSiPs-HER-2 for tumor cells was 15-fold lower than the LD_{50} value for control cells demonstrates very high *in vitro* specificity. This is the first important step on a long road towards the design and development of novel chemotherapeutic agents against cancer in general, and breast cancer in particular.

Background

Cancer is the second cause of death worldwide. In the case of breast cancer, epidemiological studies point to more than one million new cases diagnosed per year and an annual mortality rate close to 450,000 deaths. Particles have shown great potential [1] for drug delivery [2-4] and cancer treatment [5-8]. In most approaches, particles are directed to target cells by antibodies attached to their surfaces, which in the case of in vivo administration, supplements passive targeting through the EPR (enhanced permeability and retention) effect [9]. Some strategies involve heating particles with an external oscillating magnetic or electromagnetic field and causing apoptosis of the nearby cells through magnetothermia [10,11] or photothermia [6,12-15]. These materials suffer certain limitations, such as the large and expensive facilities (i.e. magnetic resonance imaging, MRI) necessary for magnetothermia, and the limited penetration depth of light in the body in the case of photothermia. Other approaches make use of antibody functionalized particles loaded with cancer drugs to deliver the drug to tumor cells [5,16-19]. Porous silicon particles (PSiPs) have been considered a very promising platform for cancer therapy because of their excellent biocompatibility [20] and biodegradability [5,21-23]. In all studies reported to date, PSiPs work either as a passive carrier of an anticancer cargo [5,16-19] or as an element activated by an appropriate trigger, namely light and acoustic waves for particle thermalization [14,24,25] or singlet oxygen generation in photodynamic therapies [8]. Here, we demonstrate that PSiPs themselves can be used as a drug for cancer treatment and how to modulate their activity by taking advantage of their surface functionalization and the enzymatic machinery of eukaryotic cells.

* Correspondence: wolfgang.parak@physik.uni-marburg.de; fmese@fis.upv.es; ramon.alvarez@urv.cat
[4]Fachbereich Physik, Philipps Universität Marburg, Marburg 35037, Germany
[1]Centro de Tecnologías Físicas, Unidad Asociada ICMM/CSIC-UPV, Universidad Politécnica de Valencia, Av. Los Naranjos s/n, Valencia, 46022 Spain and Instituto de Ciencia de Materiales de Madrid, CSIC, Madrid 28049, Spain
[6]Departamento de Química Física e Inorgánica, Universitat Rovira i Virgili and Centro de Tecnología Química de Catalunya, Carrer de Marcel·lí Domingo s/n, 43007 Tarragona, Spain
Full list of author information is available at the end of the article

Silicon is characterized by a reduction potential [26] of −1.697 eV to yield silicates or −0.91 eV to yield silica, which is ultimately dissolved as silicates in the presence of water. The low reduction potential makes the reactions violent and even explosive [27] in nanoscaled porous particles [28]. On the other hand, the high tendency of silicon to undergo oxidation is modulated by the spontaneous generation of a passivation layer of SiOx when exposed to open atmosphere. Notably, this passivation layer dissolves in water and particularly in slightly acidic media. The kinetics of the dissolution of this layer can be modulated by surface functionalization of the silica. Thus, by coating with a compact monolayer of an organic molecule, dissolution can be retarded or even prevented.

The processes for obtaining PSiPs have been well known for 20 years [29]. They are mainly based on wet chemistry methods, where the starting material, bulk silicon, is converted into porous silicon, by an electrochemical or stain-etching reaction, followed by a process such as ultrasonication, to break the porous layer into small particles [30,31]. Other, less studied methods, use a bottom-up approach based on chemical vapor deposition techniques, where the starting material is a precursor gas, namely silane or di-silane, which can be decomposed at high temperatures [26]. Under controlled conditions of pressure, temperature and time, such gases nucleate and nanometric porous silicon particles can be obtained [32]. This is a complex process, and the involved mechanisms are still under study (see Methods) [33,34]. In some manner PSiPs can be regarded as a macromolecule resulting from the polymerization of disilane with a dramatic capability of oxidation.

Herein we demonstrate that silicon particles coated with a native silica layer can be engineered with the bioorganic appropriate ligands to target and accumulate into tumour cells. Once inside the cell, the particles are driven to the lysosome were the enzymatic machinery of the cell metabolize the ligands. Then, the exposition of the soluble silica coating to the aqueous lysosomal solution degrades this layer allowing water to react violently with the silicon. As result the target cells dye while the particles are degraded into soluble and excretable biocomponents.

Results and discussion

Our process to obtain the particles used in this work stem from these methods [35]. The nanostructured particles were highly spherical with a diameter between 1.5 and 2 μm, with an intrinsic photoluminescence in between red and near infrared (Figure 1A and B) [36]. As prepared, and after extracting the materials from the reactor, exposure to atmospheric oxygen generated a thin layer of silicon oxide (Figure 2C and D). This coating acted as a protective shell and generated an easily functionalizable surface to couple an organic layer would protect the silica from dissolution in physiological media. The enzymatic machinery present in the cell can easily degrade this protective organic shell, which would consequently trigger oxidation reactions of the particles after their internalization by cells. To prove this concept, we used a glucopyranoside derivative that can be easily metabolized by the lysosomal enzyme α-*D-glucoside* glucohydrolase. The lysosome has been shown to be a target organelle for most nano- and microparticles [37,38] and thus it can be predicted that after internalization by cells, the particles would be exposed to α-*D-glucoside* glucohydrolase.

The sugar and the particle cannot be directly linked without previous modifications. Thus, PSiPs were capped with aminopropylsilane (APS) [39], while the glucopyranoside selected was 2-acetamido-2-deoxy-β-D-glucopyranosyloxyacetic acid (Figure 2, see Methods and SI for details). The benzotriazol-1-yloxytris(dimethylamino)phosphonium hexafluorophosphate/anhydrous 1-hydroxybenzotriazole (BOP/HOBt) coupling method was chosen to generate a peptide bond between the amine-functionalized particle surface and the carboxylic acid group attached to the carbohydrate. Notably, within this configuration, hybrid particles will resist oxidation in physiological media but should be degraded unselectively within any cell, following endocytosis and subsequent localization within the lysosome. Therefore, for anticancer therapy, a selective antibody that targets the surface receptor of the desired cell is necessary.

Consequently, the third step in the preparation of our immunotherapeutic material involved the coupling of a directing vector. HER-2-positive breast cancer is characterized by the amplification of this gene and high expression and activity of its protein [40]. In fact, there is a strong association between HER-2 (ErbB2) tyrosine kinase expression and the aggressiveness and prognosis of the disease. Fortunately, HER-2 amplification confers a selective target for specific treatment and several drugs targeting his receptor are actually used for breast cancer treatment in medical practice, including small molecule tyrosine kinase inhibitors (TKIs) such as gefitinib, erlotinib or lapatinib or monoclonal antibodies such as trastuzumab, pertuzumab or cetuximab [41]. HER-2 is also a standard receptor for specific targeting [42]. For our materials, rather than using standard carbodiimide chemistry, the HER-2 antibody was linked to the particles by taking advantage of its affinity for the sugar. Thus, one of the four glycosylation immunogenic regions was spontaneously coupled to the sugars present on the particle surface, allowing the other three to interact with the cell membrane receptors [43].

First, to test the interaction of our particles with the cells, the PSiP-HER-2 were internalized by the HER-2 positive cell line, SK-BR-3. The particles could be visualized, surrounded by the cell membrane (Figure 3A). Some

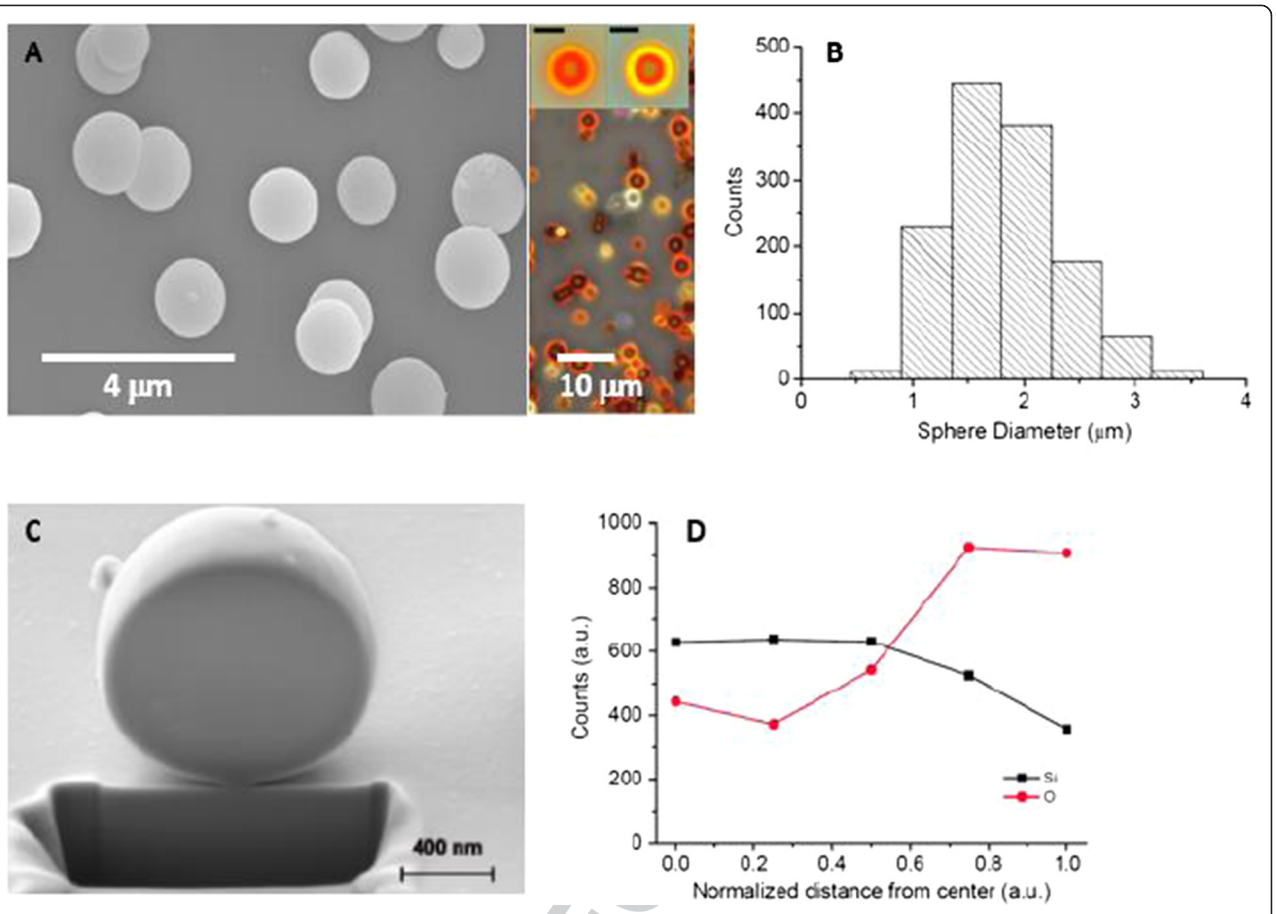

Figure 1 Silicon particle characterization. (A) SEM and optical microscopy images of the porous silicon particles as prepared and **(B)** their size distribution. All scale bars in the insets correspond to 2 µm. **(C)** SEM image of a porous silicon colloid carved using the focused ion beam (FIB) technique. **(D)** EDX analysis of materials inside a silicon colloid as a function of the distance from the sphere center, normalized to the sphere radius (d = distance from the sphere center/sphere radius). The graph shows the counts for the Si and O peaks of the EDX spectra at five different points of analysis. The points were selected along a line travelling from the nucleus (d = 0) to the sphere surface (d = 1).

particles remained in the extracellular space, while other particles were seen attached to the cell membrane. Despite their micro-size and the degree of agglomeration, the particles could be internalized by SK-BR-3 cells without affecting their viability at an early stage. This is in agreement with other work [37] showing that particles at the micro-scale can be safely incorporated by eukaryotic cells.

Next, we tested the efficiency of the PSiPs functionalized with antibodies against HER-2 receptors (PSiPs-HER-2) for their potential to selectively kill only cells overexpressing HER-2. To this end, we used two different cell lines, one overexpressing the HER-2 receptor (SK-BR-3) and one with its normal expression level (MDA-MB-435) [44]. The cells were seeded in 96-well plates and incubated with different quantities of PSiPs-HER-2 for 48 h, before a resazurin-based viability assay was performed. Resazurin is a nonfluorescent molecule that is reduced by metabolic active cells to the fluorescent resorufin. Thus, the number of viable cells can be determined by measuring resorufin fluorescence. Notably, when SK-BR-3 cells (cells overexpressing the HER-2 receptors) were treated with PSiPs-HER-2, their viability was clearly compromised (Figure 4, black points). On the other hand SK-BR-3 cells treated with PSiPs (Figure 4, blue points) or MDA-MB-435 cells treated with PSiPs or PSiPs-HER-2 (Figure 4, red and green points, respectively) showed a more delayed toxicological response. The LD_{50} (lethal dose killing 50% of the cell population) values are presented in Table 1. Only around 250 µg/mL PSiPs-HER-2 were needed to kill 50% of the SK-BR-3 cells, whereas much higher quantities of the same particles were required under the same conditions to kill the same proportion of MDA-MB-435 cells. On the other hand, PSiPs without attached HER-2 antibodies showed a much lower toxicological response, as their LD_{50} values were very high for both cell types.

These results confirm the efficacy of PSiPs-HER-2 to recognize the HER-2 receptors present on the surface of SK-BR-3 cells to a higher extent than that on MDA-MB-

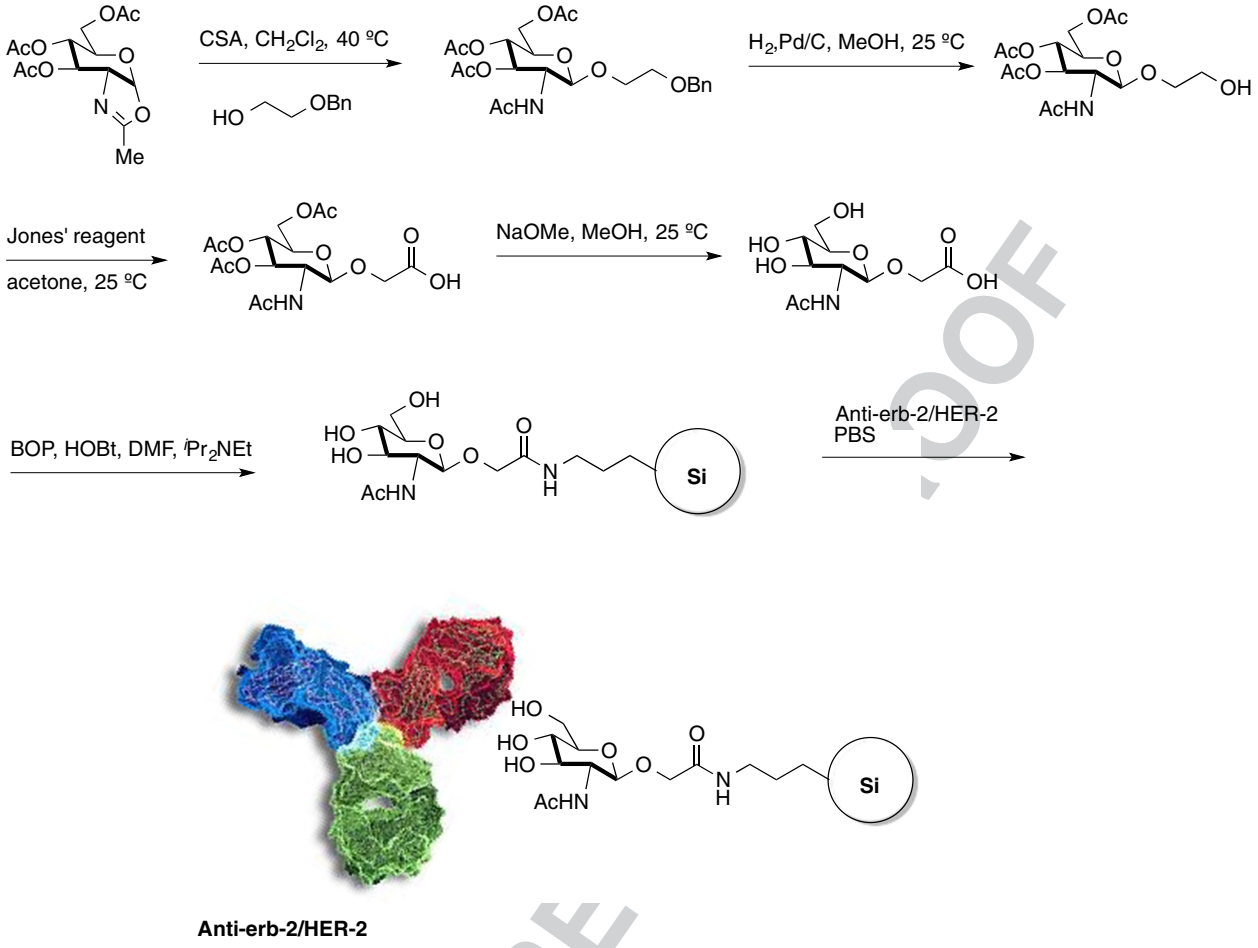

Figure 2 Synthesis and derivatization of the glucopyranose derivative, and the antibody coupling to the particles.

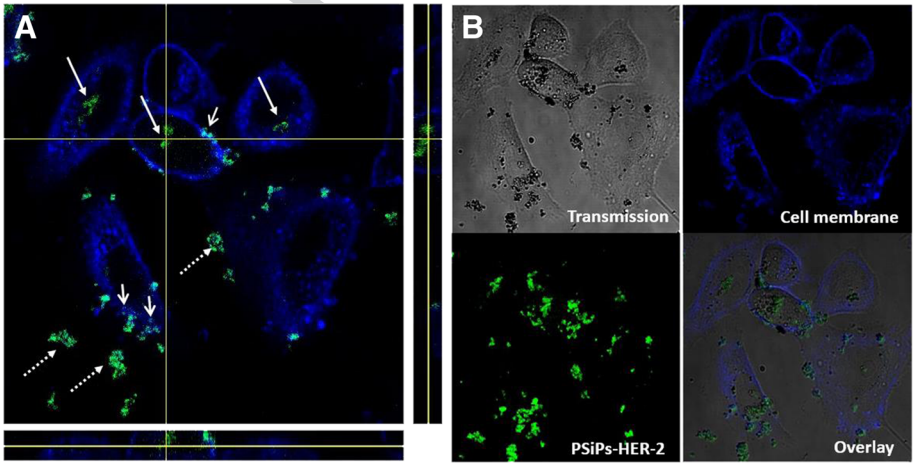

Figure 3 Particle localization into SK-BR-3 cell lines. SK-BR-3 (cell membrane labeled in blue) treated with PSiP-HER-2 particles (presented in green) for 24 h, showing the particles inside (arrow) and, outside (dashed arrow) the cells and at the cell membrane (opened arrow). **(A)** Orthogonal view in the 3 planes (X/Y, X/Z and Y/Z) of the particles pointed at the intersection of the X and Y axeis. As seen from all planes, the particles are surrounded by the cell membrane. **(B)** Images of the cells in the transmission and fluorescence channel of the cell membrane are shown. The PSiP-HER-2 were not labeled because these particles exhibit intrinsic photoluminescence.

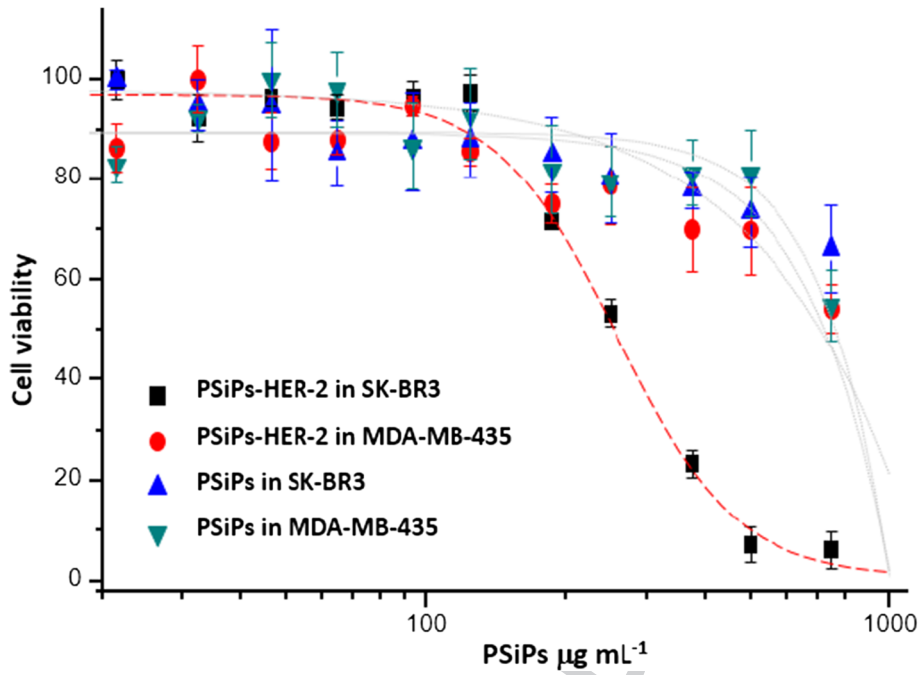

Figure 4 Cell viability. Relative cell viability after incubation of SK-BR-3 and MDA-MB-435 cells with PSiPs and PSiPs-HER-2 for 48 h.

435 cells and to effectively promote their local accumulation. The degree of targeting was more than sufficient to accelerate the death of the targeted cancer cells.

Conclusions

In summary, we present here an immunotherapy approach for potential cancer treatment. Our platform comprises the use of engineered silicon particles conjugated with a selective antibody. The conceptual advantage of our system is that after reaction, the particles are degraded into soluble and excretable biocomponents. In our study, we demonstrate in particular, specific targeting and destruction of cancer cells *in vitro*. The fact that the LD_{50} value of PSiPs-HER-2 for tumor cells was 15-fold lower than the LD_{50} value for control cells demonstrates very high *in vitro* specificity. This is the first important step on a long road towards the design and development of novel chemotherapeutic agents against cancer in general, and breast cancer in particular.

Table 1 Calculated LD50 obtained from the dose–response curves shown in Figure 4

Cell line	Type of NP	LD_{50} (µg/mL)	LD_{50} SD
SK-BR-3	PSiPs-HER-2	249	10
MDA-MB-435	PSiPs-HER-2	3776	180
SK-BR-3	PSiPs	5603	360
MDA-MB-435	PSiPs	2672	214

Methods

Synthesis of porous silicon microspheres

Our method for producing porous silicon microspheres is based on the decomposition of disilane gas (Si_2H_6) by chemical vapor deposition (CVD). This is similar to the synthesis of silicon colloids [45], where the gas is introduced in a reactor whose walls are heated at high temperatures for a certain time, usually higher than 400°C. During this procedure, Si_nH_m clusters grow in the gas phase [46] and these become highly spherical, micrometer-sized particles, through surface tension forces. At the same time, the process of hydrogen desorption from the clusters progressively reduces the hydrogen content until they become hydrogenated amorphous silicon (a:Si-H) colloids. To obtain porous silicon microspheres, the heating process is stopped at an early stage, before the formation of amorphous silicon colloids is complete. In this way, porous particles with an undetermined composition of silicon and hydrogen atoms are obtained.

Porous silicon particles for this work were synthesized using a di-silane decomposition temperature of 400°C. The absolute gas pressure in the reactor was about 0.25 atm at room temperature and we used decomposition times from 1 to 2 minutes, measured from the stage where the gas reaches the target temperature.

Silicon and oxygen content of porous silicon colloids were analyzed by electron dispersive X-ray (EDX) measurements. For this purpose, colloids were carved using a focus ion beam (FIB) technique (FEI Helios NanoLab

Omniprobe). Figure 1C shows a scanning electron microscope (SEM) image of a carved colloid, 1.2 μm in diameter. The carved surface appears to be flat because the ion gun of the FIB removes material and deposits it at the same time on the surface of the particle, thus hiding porous structures. Nevertheless, because the EDX interaction volume penetrates the region where pores are less modified by the FIB carving action, one can extract useful information about the cavity structure. Figure 1D shows the EDX analysis corresponding to silicon and oxygen in different regions of the particle, from the cavity center to the cavity surface. This shows two key results: a) the oxygen content appears to be completely within the cavity and b) the oxygen (silicon) concentration increases (decreases) from the center to the surface. This result supports the hypothesis that porous silicon colloids possess a gradient, or onion-like, porous structure, as images taken by optical microscopy suggest. In addition, it indicates that porosity is higher at the surface of the colloid than within it.

Synthesis of the 2-acetamido-2-deoxy-β-d-glucopyranosyloxyacetic acid

Solvents were dried according to published methods and distilled before use. All other reagents were commercial compounds of the highest purity available. Unless otherwise indicated, all reactions involving air- and moisture-sensitive materials were carried out under an argon atmosphere, while those not involving aqueous reagents were carried out in oven-dried glassware. Analytical thin layer chromatography (TLC) was performed on aluminum plates with Merck Kieselgel 60 F254 and visualized by UV irradiation (254 nm) or by staining with an ethanolic solution of phosphomolybdic acid. Flash column chromatography was carried out using Merck Kieselgel 60 (230–400 mesh) under pressure. ^{1}H NMR spectra were recorded in $CDCl_3$ and D_2O, at ambient temperature on an AMX-400 spectrometer at 400 MHz, with residual protic solvent as the internal reference [$CDCl_3$, $\delta_H = 7.26$ ppm]; chemical shifts (δ) are given in parts per million, and coupling constants (*J*) are given in Hertz. The proton spectra are reported as follows: δ (multiplicity, coupling constant *J*, number of protons, assignment).

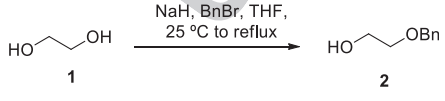

2-(Benzyloxy)ethanol 2. To a mixture of NaH (3.4 g, 0.085 mol, 60% w/w in mineral oil) in tetrahydrofuran (THF, 150 mL), ethylene glycol 1 (25.1 mL, 0.45 mol) was added and the mixture was stirred for 1 h at 25°C. Then, benzyl bromide (8.9 g, 0.075 mol) was added and the reaction was refluxed for 12 h. After cooling the mixture (0°C), a saturated aqueous solution of NH_4Cl was added, the solvent was evaporated and the mixture was extracted with EtOAc (3×). The combined organic layers were washed with a saturated aqueous solution of NH_4Cl and brine, and dried (Na_2SO_4). The solvent was evaporated to afford 11.22 g (98% yield) of a colorless oil identified as 2-(benzyloxy)ethanol 2. The spectroscopic data were identical to those described in the literature [47]. ^{1}H-NMR (400 MHz, $CDCl_3$): δ 7.40-7.30 (m, 5H), 4.58 (s, 2H), 3.78 (t, $J = 5.0$ Hz, 2H), 3.61 (t, $J = 4.9$ Hz, 2H), 2.06 (br, 1H, OH) ppm.

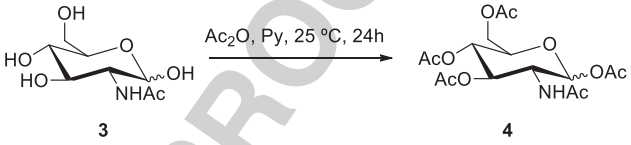

1,3,4,6-tetra-*O*-acetyl-α/β-*N*-acetylglucosamine 4. *N*-acetyl-D-glucosamine 3 (5 g, 22.6 mmol) was dissolved in pyridine (36 mL) and acetic anhydride (25 mL) was added dropwise at 0°C. The reaction mixture was stirred at 25°C for 24 h, then diluted with CH_2Cl_2 and washed consecutively with cold water, a saturated aqueous solution of $NaHCO_3$, and a 10% aqueous solution of $CuSO_4$. The organic layer was dried (Na_2SO_4) and the solvent was evaporated to obtain 6.60 g (75%) of a white solid identified as 1,3,4,6-tetra-*O*-acetyl-α/β-*N*-acetylglucosamine 4. The spectroscopic data were identical to those described in the literature [48]. ^{1}H-NMR (400 MHz, $CDCl_3$): δ 6.17 (d, $J = 3.6$ Hz, 1H), 5.64 (d, $J = 9.3$ Hz, 1H), 5.30-5.20 (m, 2H), 4.49 (ddd, $J = 10.6$, 8.9, 3.6 Hz, 1H), 4.25 (dd, $J = 12.5$, 4.1 Hz, 1H), 4.07 (dd, $J = 12.5$, 2.4 Hz, 1H), 4.00 (ddd, $J = 9.6$, 4.0, 2.3 Hz, 1H), 2.20 (s, 3H), 2.09 (s, 3H), 2.06 (s, 3H), 2.05 (s, 3H), 1.94 (s, 3H) ppm.

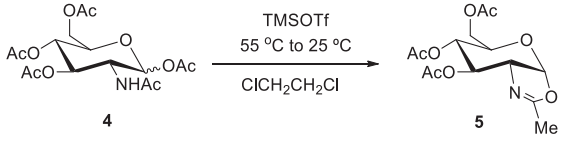

4′,5′-Dihydro-2′-methyloxazolo [5′,4′:1,2]-3,4,6-tri-*O*-acetyl-1,2-dideoxy-α-D-glucopyranoside 5. To a solution of 1,3,4,6-tetra-*O*-acetyl-α/β-*N*-acetylglucosamine 4 (2.49 g, 6.4 mmol) in dichloroethane (25 mL) TMSOTf (1.8 mL, 9.6 mmol) was added and the reaction was stirred for 2 h at 55°C and for 12 h at 25°C. A saturated aqueous solution of $NaHCO_3$ was added and the mixture was extracted with CH_2Cl_2 (3×). The combined organic layers were washed with a saturated aqueous solution of $NaHCO_3$ and dried (Na_2SO_4) and the solvent was evaporated. The resulting residue was purified by column chromatography (silicagel,

97:3 CH_2Cl_2/MeOH) to afford 1.86 g (78%) of 4′,5′-dihydro-2′-methyloxazolo [5′,4′:1,2]-3,4,6-tri-*O*-acetyl-1,2-dideoxy-α-D-glucopyranoside 5. The spectroscopic data were identical to those described in the literature [49]. ^{1}H-NMR (400 MHz, $CDCl_3$): δ 5.98 (d, *J* = 7.4 Hz, 1H), 5.27 (t, *J* = 2.4 Hz, 1H), 4.94 (ddd, J = 9.2, 2.0, 1.2 Hz, 1H), 4.19-4.14 (m, 3H), 3.62 (dt, *J* = 8.8, 4.3 Hz, 1H), 2.12 Hz (s, 3H), 2.11 (s, 3H), 2.10 (s, 3H), 2.09 (s, 3H) ppm.

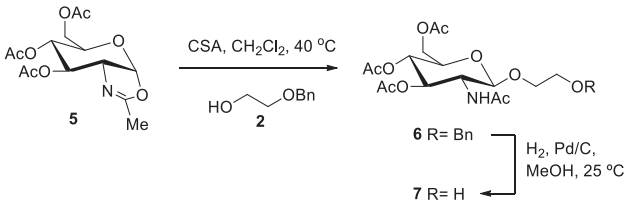

2-Hydroxyethyl-2-acetamido-3,4,6-tri-O-acetyl-2-deoxy-β-D-glucopyranoside 7. 10-(*R*)-camphorsulfonic acid (1.40 g, 5.02 mmol) and 2-(benzyloxy)ethanol 2 (7.63 g, 50.2 mmol) were added to a stirred solution of 4′, 5′-dihydro-2′-methyloxazolo [5′,4′:1,2]-3,4,6-tri-*O*-acetyl-1,2-dideoxy-α-D-glucopyranoside 5 (1.86 g, 5.02 mmol) and powdered 4 Å molecular sieves (ca. 8 g) in CH_2Cl_2 (30 mL) and the reaction was stirred at 40°C for 14 h. The mixture was cooled to 0°C and a saturated aqueous solution of $NaHCO_3$ (60 mL) and CH_2Cl_2 (30 mL) was added. The layers were separated and the organic layer was washed with a saturated aqueous solution of $NaHCO_3$, brine and dried (Na_2SO_4), and the solvent then evaporated. The residue was purified by column chromatography (hexane/EtOAc 50:50 to CH_2Cl_2/MeOH 95:5) providing 2-*O*-benzyloxyethyl-2-acetamido-3,4,6-tri-O-acetyl-2-deoxy-β-D-glucopyranoside 6 as a colorless solid. The spectroscopic data of the product were identical to those described in the literature [50]. ^{1}H-NMR (400 MHz, $CDCl_3$): δ 7.4-7.3 (m, 5H), 5.50 (d, *J* = 8.8 Hz, 1H), 5.25 (dd, *J* = 10.4, 9.4 Hz, 1H), 5.09 (t, *J* = 9.6 Hz, 1H), 4.76 (d, *J* = 8.4 Hz, 1H), 4.56 (app s, 2H), 4.27 (dd, *J* = 12.3, 4.7 Hz, 1H), 4.20-4.15 (m, 2H), 3.99 (dt, *J* = 11.5, 3.9 Hz, 1H), 3.80 (ddd, *J* = 18.2, 14.7, 11.2 Hz, 1H), 3.70-3.65 (m, 3H), 2.09 (s, 3H), 2.06 (s, 3H), 2.03 (s, 3H), 1.87 (s, 3H) ppm.

A mixture of 2-*O*-benzyloxyethyl-2-acetamido-3,4,6-tri-*O*-acetyl-2-deoxy-β-D-glucopyranoside 6 (0.19 g, 0.36 mmol) and Pd/C (10%, 0.02 g) in MeOH (3 mL) was stirred under an H_2 atmosphere for 7 h at 25°C. The reaction was filtered through Celite and the solvent was evaporated to afford 0.15 g (96%) of a solid identified as 2-hydroxyethyl-2-acetamido-3,4,6-tri-*O*-acetyl-2-deoxy-β-D-glucopyranoside 7. The spectroscopic data of the product were identical to those described in the literature [50]. ^{1}H-NMR (400 MHz, $CDCl_3$): δ 5.58 (d, *J* = 9.0 Hz, 1H), 5.25 (dd, *J* = 10.6, 9.4 Hz, 1H), 5.07 (t, *J* = 9.6 Hz, 1H), 4.71 (d, *J* = 8.3 Hz, 1H), 4.2-4.10 (m, 2H), 3.9-3.8 (m, 2H), 3.7-3.6 (m, 2H), 2.58 (br, 1H, OH), 2.11 (s, 3H), 2.06 (s, 3H), 2.05 (s, 3H), 1.98 (s, 3H) ppm.

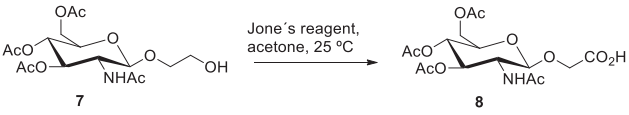

2-Acetamido-3,4,6-tri-*O*-acetyl-2-deoxy-β-D-glucopyranosyloxyacetic acid 8. Jones reagent (3.5 M, 0.2 mL, 0.69 mmol) was added to a stirred solution of 2-hydroxyethyl-2-acetamido-3,4,6-tri-*O*-acetyl-2-deoxy-β-D-glucopyranoside 7 (0.15 g, 0.35 mmol) in acetone (2 mL) at 0°C and the reaction was stirred for 13 h at 25°C. Isopropanol was added and the solvent was evaporated. After the addition of CH_2Cl_2 (10 mL) and brine (10 mL), the layers were separated, the organic layer was washed with brine and dried (Na_2SO_4), and the solvent was evaporated to afford 0.11 g (73%) of a white solid that was identified as 2-acetamido-3,4,6-tri-*O*-acetyl-2-deoxy-β-D-glucopyranosyloxyacetic acid 8 The spectroscopic data of the product were identical to those described in the literature [50]. ^{1}H-NMR (400 MHz, $CDCl_3$): δ 6.57 (br s, 1H), 5.22 (t, *J* = 9.6 Hz, 1H), 5.11 (t, *J* = 9.6 Hz, 1H), 4.75 (d, *J* = 8.1 Hz, 1H), 4.35 (app s, 2H), 4.28 (dd, *J* = 12.1, 4.9 Hz, 1H), 4.15 (dd, *J* = 10.7, 2.1 Hz, 1H), 4.1-4.0 (m, 1H), 3.7-3.6 (m, 1H), 2.11 (s, 3H), 2.06 (s, 3H), 2.03 (s, 3H), 1.97 (s, 3H) ppm.

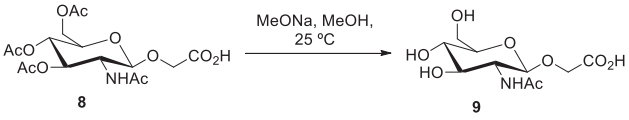

2-Acetamido-2-deoxy-β-D-glucopyranosyloxyacetic Acid 9. Sodium methoxide (0.02 g, 0.332 mmol) was added to a stirred solution of 2-acetamido-3,4,6-tri-*O*-acetyl-2-deoxy-β-D-glucopyranosyloxyacetic acid 8 (0.114 g, 0.255 mmol) in MeOH (6 mL) and the reaction mixture was stirred at 25°C for 24 h. After the addition of Dowex-200 the mixture was filtered and the solvent was evaporated. The residue was dissolved in H_2O and dried under vacuum to afford 0.071 g (99%) of a solid identified as 2-acetamido-2-deoxy-β -D-glucopyranosyloxyacetic acid 9. The spectroscopic data of the product were identical to those described in the literature [50]. ^{1}H-NMR (400 MHz, D_2O): δ 4.49 (d, *J* = 8.4 Hz, 1H), 4.18 (s, 2H), 3.83 (d, *J* = 12.2 Hz, 1H), 3.70-3.60 (m, 2H), 3.50-3.40 (m, 1H), 3.40-3.30 (m, 2H), 1.97 (s, 3H) ppm.

Particle functionalization

A suspension of aminopropylsilane (APS)-coated silicon particles was produced by treatment of 0.1 g silica particles with APS (20 μL) in 2-propanol (5 mL) at 80°C for

2 h. The particles were centrifuged at 3800 rpm for 30 min to remove the excess APS, followed by replacement of the supernatant solution by isopropanol. The particles were re-dispersed by shaking (ultrasound) for 10 min. This protocol was repeated two more times [51].

The particles were centrifuged at 3800 rpm for 30 min and the supernatant was replaced by dimethylformamine (DMF). Then, a solution of 2-acetamido-2-deoxy-β-D-glucopyranosyloxyacetic acid 9 (14 mg), benzotriazol-1-yloxy) tris(dimethylamino)phosphonium hexafluorophosphate (BOP, 29 mg), hydroxybenzotriazole (HOBt, 7 mg) in DMF (3 mL) and diisopropylethylamine (30 μL) were added and the suspension was stirred for 12 h at 25°C. The particles were centrifuged at 3800 rpm for 30 min, washed with DMF and the supernatant then replaced by H_2O. The particles were re-dispersed by shaking (ultrasound) for 10 min. The supernatant was replaced by phosphate buffered saline (PBS, 1×).

To a suspension of the particles in PBS (2 mL) 250 μL of a solution of anti-erbB-2/HER-2 (1 μL/L in PBS) was added and the mixture was shaken at 0°C for 12 h. The particles were centrifuged at 3800 rpm for 10 min, and the supernatant was replaced with PBS. The particles were re-dispersed by shaking (ultrasound) for 3 min at 0°C.

Cell culture and viability assay

Materials: Dulbecco's modified eagle's medium (DMEM, #30-2002) and McCoy's 5a medium (#30-2007) were purchased from ATCC. Fetal bovine serum (FBS, #S0615) was obtained from Biochrom AG and penicillin/streptomycin (#15140-122) from Gibco (#15140-122). L-glutamine (#25030-024) was purchased from Life Technologies. The viability assay based on Resazurin (#TOX8) and the 96-well plates (#CLS3603) in which the viability assay was carried out were obtained from Sigma-Aldrich (St Louis, MO, USA).

MDA-MB-435 human epithelial cells (ATCC #HTB-129) were seeded and grown in growth medium (DMEM with 4.5 g/L glucose supplemented with 10% FBS, 1% L-glutamine (200 mM) and 1% penicillin/streptomycin. SK-BR-3 human breast adenocarcinoma cells (ATCC #HTB-30) were seeded and grown in another growth medium (McCoy's medium supplemented with 10% FBS, 1% L-glutamine (200 mM) and 1% penicillin/streptomycin.

Imaging of the particle internalization: SK-BR-3 cells were seeded on an Ibidi 8-well plate (2E4 cells/well) and left to adhere and grow for 4 days. Subsequently, the cells were incubated with 30 μg/mL PSiP-HER-2 particles for 24 h. The cells were then washed intensively and the cell membrane stained with 20 μg/mL cell mask deep red for 10 min at 37°C before imaging. Images of living cells using transmitted and reflected light were taken with a confocal laser scanning microscope (NIKON TE2000-E). A 650 LP filter was used to collect the fluorescence signal of the cell membrane after excitation at 633 nm, whereas a 515/30 BP filter was used to collect the light reflected by the PSiP-HER-2 after irradiation with a 488 nm laser line. As previously reported, the particles exhibit intrinsic photoluminescence because of the presence of the microcavities [35,36].

Viability assay: 20,000 cells (MDA-MB-435 or SK-BR-3) were seeded per well in a 96-well plate and incubated in 100 μL of the corresponding cell medium for 48 h at 37°C and 5% CO_2. After this time, different concentrations of particles (PSiNPs or PSiNPs-HER-2) were added and cells were incubated for another 48 h. The viability assay was repeated three times at each concentration. Control viability assays were performed using cells without particles and particles without cells. After incubation, cellular viability was probed. Cells were washed with PBS and a solution of 10% of resazurin in growth medium was added to each well. Cells were placed in the incubator for 3 h (37°C and 5% CO_2). Resazurin is a nonfluorescent molecule that is reduced from the oxidized to the reduced form, resofurin, by metabolically active cells. Resofurin is fluorescent, has a maximum emission wavelength at 585 nm (red emission), and can be excited from 530 to 560 nm. The fluorescent emission intensity originating from resofurin is proportional to the number of metabolically active (=living) cells. Fluorescence emission was measured with a Fluorolog-3 spectrofluorometer equipped with a microwell plate reader (MicroMax 384) from Horiba JOBIN YVON. The samples were excited at 560 nm and the emission spectra were collected from 572 to 650 nm. Background was subtracted from the spectra. As the position of the maximum emission, wavelength can be slightly shifted, so the peak emission was averaged from 584 to 586 nm. The emission peak intensity values were normalized, considering a cell viability of 100% for the control experiments, in which no particles had been added to the cells. The normalized fluorescence emission peak intensities were plotted against the logarithm of the particle concentration, *cf.* Figure 4. Dose–response curves were obtained for SK-BR-3 and MDA-MB-435 exposed to different concentrations of Si-NPs and SiNPs-HER2, *cf.* Figure 4. The results were fitted to sigmoidal curves and the inflexion point was calculated. The inflexion point represents the LD_{50} value, which in this case is the concentration of particles at which cell viability is reduced to 50%, i.e. 50% of the cells are no longer metabolically active. The calculated LD_{50} values are shown in Table 1.

Competing interests
The authors declare that they have no competing interests.

Authors' contributions
RAA-P, FM, CV, EG-R conceived the idea. RF, IR and FM synthetized the silicon particles; SA, RA, ARdL synthetized the sugar and coupled the antibody to the particles; SC-R, XY, MG-A, PRG and WJP carried out the viability assays. All the authors participated in scientific discussions and wrote the paper. All authors read and approved the final manuscript.

Acknowledgements
The authors acknowledge financial support from the following projects FIS2009-07812, MAT2012-35040, PROMETEO/2010/043, CTQ2011-23167, CrossSERS, FP7 MC-IEF 329131, and HSFP (project RGP0052/2012) and Medcom Tech SA. Xiang Yu acknowledges support by the Chinese government (CSC, Nr. 2010691036).

Author details
[1]Centro de Tecnologías Físicas, Unidad Asociada ICMM/CSIC-UPV, Universidad Politécnica de Valencia, Av. Los Naranjos s/n, Valencia, 46022 Spain and Instituto de Ciencia de Materiales de Madrid, CSIC, Madrid 28049, Spain. [2]Servicio de Oncología, Hospital Universitario Madrid-Torrelodones, Madrid 28250, Spain. [3]Departamento de Química Orgánica, Universidade de Vigo, Vigo 36310, Spain. [4]Fachbereich Physik, Philipps Universität Marburg, Marburg 35037, Germany. [5]Medcomtech SA, C/ Catalunya, 83-85 Viladecans, Barcelona 08840, Spain. [6]Departamento de Química Física e Inorgánica, Universitat Rovira i Virgili and Centro de Tecnología Química de Catalunya, Carrer de Marcel•lí Domingo s/n, 43007 Tarragona, Spain. [7]ICREA, Passeig Lluís Companys 23, 08010 Barcelona, Spain.

Received: 24 July 2014 Accepted: 3 September 2014

References

1. Prasad PN: *Introduction to Nanomedicine and Nanobioengineering.* New York: Wiley; 2012.
2. Randall CL, Leong TG, Bassik N, Gracias DH: **3D lithographically fabricated nanoliter containers for drug delivery.** *Adv Drug Del Rev* 2007, **59:**1547–1561.
3. Reibetanz U, Chen MHA, Mutukumaraswamy S, Liaw ZY, Oh BHL, Venkatraman S, Donath E, Neu BR: **Colloidal DNA carriers for direct localization in cell compartments by pH sensoring.** *Biogeosciences* 2010, **11:**1779–1784.
4. Tasciotti E, Liu X, Bhavane R, Plant K, Leonard AD, Price BK, Cheng MM-C, Decuzzi P, Tour JM, Robertson F, Ferrari M: **Mesoporous silicon particles as a multistage delivery system for imaging and therapeutic applications.** *Nat Nano* 2008, **3:**151–157.
5. Park J-H, Gu L, von Maltzahn G, Ruoslahti E, Bhatia SN, Sailor MJ: **Biodegradable luminescent porous silicon nanoparticles for in vivo applications.** *Nat Mater* 2009, **8:**331–336.
6. Hong C, Lee J, Son M, Hong SS, Lee C: **In-vivo cancer cell destruction using porous silicon nanoparticles.** *Anti-Cancer Drugs* 2011, **22:**971–977. 910.1097/CAD.1090b1013e32834b32859c.
7. Canham LT: **Device Comprising Resorbable Silicon for Boron Capture Neutron Therapy. UK Patent Nr. 0302283.7.** In *Book Device Comprising Resorbable Silicon for Boron Capture Neutron Therapy. UK Patent Nr. 0302283.7 (Editor ed.^eds.).* Edited by City: UK Patent Nr. 0302283.7; 2003.
8. Xiao L, Gu L, Howell SB, Sailor MJ: **Porous silicon nanoparticle photosensitizers for singlet oxygen and their phototoxicity against cancer cells.** *ACS Nano* 2011, **5:**3651–3659.
9. Gil PR, Parak WJ: **Composite nanoparticles take Aim at cancer.** *ACS Nano* 2008, **2:**2200–2205.
10. Gomella LG: **Is interstitial hyperthermia a safe and efficacious adjunct to radiotherapy for localized prostate cancer?** *Nat Clin Pract Urol* 2004, **1:**72–73.
11. Maier-Hauff K, Ulrich F, Nestler D, Niehoff H, Wust P, Thiesen B, Orawa H, Budach V, Jordan A: **Efficacy and safety of intratumoral thermotherapy using magnetic iron-oxide nanoparticles combined with external beam radiotherapy on patients with recurrent glioblastoma multiforme.** *J Neuro-Oncol* 2011, **103:**317–324.
12. Lal S, Clare SE, Halas NJ: **Nanoshell-enabled photothermal cancer therapy: Impending clinical impact.** *Acc Chem Res* 2008, **41:**1842–1851.
13. Lee C, Kim H, Hong C, Kim M, Hong SS, Lee DH, Lee WI: **Porous silicon as an agent for cancer thermotherapy based on near-infrared light irradiation.** *J Mater Chem* 2008, **18:**4790–4795.
14. Osminkina LA, Gongalsky MB, Motuzuk AV, Timoshenko VY, Kudryavtsev AA: **Silicon nanocrystals as photo- and sono-sensitizers for biomedical applications.** *Appl Phys B* 2011, **105:**665–668.
15. Jain PK, Huang X, El-Sayed IH, El-Sayed MA: **Noble metals on the nanoscale: optical and photothermal properties and some applications in imaging, sensing, biology, and medicine.** *Acc Chem Res* 2008, **41:**1578–1586.
16. Serda RE, Godin B, Blanco E, Chiappini C, Ferrari M: **Multi-stage delivery nano-particle systems for therapeutic applications.** *Biochim Biophys Acta* 1810, **2011:**317–329.
17. Xu R, Huang Y, Mai J, Zhang G, Guo X, Xia X, Koay EJ, Qin G, Erm DR, Li Q, Liu X, Ferrari M, Shen H: **Multistage vectored siRNA targeting ataxia-telangiectasia mutated for breast cancer therapy.** *Small* 2013, **9:**1799–1808.
18. Park JS, Kinsella JM, Jandial DD, Howell SB, Sailor MJ: **Cisplatin-loaded porous Si microparticles capped by electroless deposition of platinum.** *Small* 2011, **7:**2061–2069.
19. Xue M, Zhong X, Shaposhnik Z, Qu Y, Tamanoi F, Duan X, Zink JI: **pH-operated mechanized porous silicon nanoparticles.** *J Am Chem Soc* 2011, **133:**8798–8801.
20. Canham LT: **Bioactive silicon structure fabrication through nanoetching techniques.** *Adv Mater* 1995, **7:**1033–1037.
21. Popplewell JF, King SJ, Day JP, Ackrill P, Fifield LK, Cresswell RG, Di Tada ML, Liu K: **Kinetics of uptake and elimination of silicic acid by a human subject: a novel application of 32Si and accelerator mass spectrometry.** *J Inorganic Biochem* 1998, **69:**177–180.
22. Shabir Q, Pokale A, Loni A, Johnson DR, Canham LT, Fenollosa R, Tymczenko M, Rodríguez I, Meseguer F, Cros A, Cantarero A: **Medically biodegradable hydrogenated amorphous silicon microspheres.** *Silicon* 2011, **3:**173–176.
23. Chen Y, Wan Y, Wang Y, Zhang H, Jiao Z: **Anticancer efficacy enhancement and attenuation of side effects of doxorubicin with titanium dioxide nanoparticles.** *Int J Nanomed* 2011, **6:**2321–2326.
24. Mackowiak SA, Schmidt A, Weiss V, Argyo C, von Schirnding C, Bein T, Bräuchle C: **Targeted drug delivery in cancer cells with Red-light photoactivated mesoporous silica nanoparticles.** *Nano Lett* 2013, **13:**2576–2583.
25. Li Z, Barnes JC, Bosoy A, Stoddart JF, Zink JI: **Mesoporous silica nanoparticles in biomedical applications.** *Chem Soc Rev* 2012, **41:**2590–2605.
26. O'Mara WC, Herring B, Hunt P: *Handbook of Semiconductor Silicon Technology.* New Jersey: Noyes Publication; 1990.
27. Mikulec FV, Kirtland JD, Sailor MJ: **Explosive nanocrystalline porous silicon and its Use in atomic emission spectroscopy.** *Adv Mater* 2002, **14:**38–41.
28. Clement D, Diener J, Gross E, Kunzner N, Timoshenko VY, Kovalev D: **Highly explosive nanosilicon-based composite materials.** *Phys Stat Sol A* 2005, **202:**1357–1359.
29. Canham LT: **Silicon quantum wire array fabrication by electrochemical and chemical dissolution of wafers.** *Appl Phys Lett* 1990, **57:**1046–1049.
30. Canham LT: *Properties of Porous Silicon.* United Kindom: INSPEC; 1997.
31. Heinrich JL, Curtis CL, Credo GM, Sailor MJ, Kavanagh KL: **Luminescent colloidal silicon suspensions from porous silicon.** *Science* 1992, **255:**66–68.
32. Littau KA, Szajowski PJ, Muller AJ, Kortan AR, Brus LE: **A luminescent silicon nanocrystal colloid via a high-temperature aerosol reaction.** *J Phys Chem* 1993, **97:**1224–1230.
33. Menz WJ, Shekar S, Brownbridge GPE, Mosbach S, Körmer R, Peukert W, Kraft M: **Synthesis of silicon nanoparticles with a narrow size distribution: a theoretical study.** *J Aerosol Sci* 2012, **44:**46–61.
34. Swihart MT, Girshick SL: **Thermochemistry and kinetics of silicon hydride cluster formation during thermal decomposition of silane.** *J Phys Chem B* 1998, **103:**64–76.
35. Fenollosa R, Ramiro-Manzano F, Tymczenko M, Meseguer F: **Porous silicon microspheres: synthesis, characterization and application to photonic microcavities.** *J Mater Chem* 2010, **20:**5210–5214.
36. Ramiro-Manzano F, Fenollosa R, Xifré-Pérez E, Garín M, Meseguer F: **Porous silicon microcavities based photonic barcodes.** *Adv Mater* 2011, **23:**3022–3025.
37. Kastl L, Sasse D, Wulf V, Hartmann R, Mircheski J, Ranke C, Carregal-Romero S, Martínez-López JA, Fernández-Chacón R, Parak WJ, Elsasser HP, Rivera-Gil P: **Multiple internalization pathways of polyelectrolyte multilayer capsules into mammalian cells.** *ACS Nano* 2013, **7:**6605–6618.
38. Schweiger C, Hartmann R, Zhang F, Parak W, Kissel T, Rivera_Gil P: **Quantification of the internalization patterns of superparamagnetic iron oxide nanoparticles with opposite charge.** *J Nanobiotech* 2012, **10:**28.
39. Sanles-Sobrido M, Exner W, Rodríguez-Lorenzo L, Rodríguez-González B, Correa-Duarte MA, Álvarez-Puebla RA, Liz-Marzán LM: **Design of SERS-encoded, submicron, hollow particles through confined growth of encapsulated metal nanoparticles.** *J Am Chem Soc* 2009, **131:**2699–2705.
40. Slamon D, Eiermann W, Robert N, Pienkowski T, Martin M, Press M, Mackey J, Glaspy J, Chan A, Pawlicki M, Pinter T, Valero V, Liu MC, Sauter G, von Minckwitz G, Visco F, Bee V, Buyse M, Bendahmane B, Tabah-Fisch I, Lindsay MA, Riva A,

Crown J: **Adjuvant trastuzumab in HER2-positive breast cancer.** *N Engl J Med* 2011, **365:**1273–1283.
41. Agus DB, Gordon MS, Taylor C, Natale RB, Karlan B, Mendelson DS, Press MF, Allison DE, Sliwkowski MX, Lieberman G, Kelsey SM, Fyfe G: **Phase I clinical study of pertuzumab, a novel HER dimerization inhibitor, in patients with advanced cancer.** *J Clin Oncol* 2005, **23:**2534–2543.
42. Colombo M, Mazzucchelli S, Montenegro JM, Galbiati E, Corsi F, Parak WJ, Prosperi D: **Protein oriented ligation on nanoparticles exploiting O6-alkylguanine-DNA transferase (SNAP) genetically encoded fusion.** *Small* 2012, **8:**1492–1497.
43. Franklin MC, Carey KD, Vajdos FF, Leahy DJ, de Vos AM, Sliwkowski MX: **Insights into ErbB signaling from the structure of the ErbB2-pertuzumab complex.** *Cancer Cell* 2004, **5:**317–328.
44. Paris L, Cecchetti S, Spadaro F, Abalsamo L, Lugini L, Pisanu ME, Lorio E, Natali PG, Ramoni C, Podo F: **Inhibition of phosphatidylcholine-specific phospholipase C downregulates HER2 overexpression on plasma membrane of breast cancer cells.** *Breast Cancer Res* 2010, **12:**R27.
45. Fenollosa R, Meseguer F, Tymczenko M: **Silicon colloids: from microcavities to photonic sponges.** *Adv Mater* 2008, **20:**95–98.
46. Jasinski JM, Gates SM: **Silicon chemical vapor deposition one step at a time: fundamental studies of silicon hydride chemistry.** *Acc Chem Res* 1991, **24:**9–15.
47. Xiao Q, Liu Y, Qiu Y, Zhou G, Mao C, Li Z, Yao Z-J, Jiang S: **Potent antitumor mimetics of annonaceous acetogenins embedded with an aromatic moiety in the left hydrocarbon chain part.** *J Med Chem* 2010, **54:**525–533.
48. Allman SA, Jensen HH, Vijayakrishnan B, Garnett JA, Leon E, Liu Y, Anthony DC, Sibson NR, Feizi T, Matthews S, Davis BG: **Potent fluoro-oligosaccharide probes of adhesion in toxoplasmosis.** *ChemBioChem* 2009, **10:**2522–2529.
49. Chambers DJ, Evans GR, Fairbanks AJ: **Elimination reactions of glycosyl selenoxides.** *Tetrahedron* 2004, **60:**8411–8419.
50. Tomabechi Y, Suzuki R, Haneda K, Inazu T: **Chemo-enzymatic synthesis of glycosylated insulin using a GlcNAc tag.** *Bioorg Med Chem* 2010, **18:**1259–1264.
51. Pastoriza-Santos I, Gomez D, Perez-Juste J, Liz-Marzan LM, Mulvaney P: **Optical properties of metal nanoparticle coated silica spheres: a simple effective medium approach.** *Phys Chem Chem Phys* 2004, **6:**5056–5060.

doi:10.1186/s12951-014-0035-7
Cite this article as: Fenollosa *et al.*: Silicon particles as trojan horses for potential cancer therapy. *Journal of Nanobiotechnology* 2014 **12**:35.

Supplementary information:

Silicon nanoparticles as Trojan horses for cancer immunotherapy

Roberto Fenollosa,[1] Eduardo Garcia-Rico,[2] Susana Alvarez,[3] Rosana Alvarez,[3]Xiang Yu,[4] Susana Carregal-Romero,[4] Carlos Villanueva,[5] Pilar Rivera_Gil,[5] Angel R. de Lera,[3] Wolfgang J. Parak,[4] Francisco J. Meseguer,[1,*] Ramón A. Alvarez-Puebla,[6,7,*]

[1]Centro de Tecnologías Físicas, Unidad Asociada ICMM/CSIC-UPV, Universidad Politécnica de Valencia, Av. Los Naranjos s/n, Valencia, 46022 Spain and Instituto de Ciencia de Materiales de Madrid, CSIC, Madrid, 28049 Spain

[2]Servicio de Oncologia, Hospital Universitario de Torrelodones, Hospital de Madrid, Madrid, Spain

[3]Departamento de Quimica Organica, Universidade de Vigo, Vigo, 36310 Spain

[4]Fachbereich Physik, Philipps Universität Marburg, Marburg, 35037 Germany

[5]Medcomtech SA. C/ Catalunya, 83-85 Viladecans, Barcelona, 08840 Spain

[6]Departamento de Quimica Fisica e Inorganica, Universitat Rovira i Virgili and Centro de Tecnología Química de Catalunya, Carrer de Marcel•lí Domingo s/n, 43007 Tarragona, Spain

[7]ICREA, Passeig Lluís Companys 23, 08010 Barcelona, Spain

METHODS

Synthesis of porous silicon microspheres

The method for obtaining porous silicon microspheres is based on the decomposition of disilane gas (Si_2H_6) by means of chemical vapour deposition (CVD). It is similar to the synthesis procedure of silicon colloids,[1] where the gas is introduced in a reactor whose walls are heated at high temperatures for a certain time, usually higher than 400 ºC. During this procedure, Si_nH_m clusters grow in the gas phase[2]and they become highly spherical micrometer size particles thanks to surface tension forces. At the same time, there is a hydrogen desorption process from the clusters that makes the hydrogen content decrease progressively until they become hydrogenated amorphous silicon (a:Si-H) colloids. In order to obtain porous silicon microspheres, the heating process is stopped at an early stage, before the formation of amorphous silicon colloids has finished. In this way, porous particles with an undetermined composition of silicon and hydrogen atoms are obtained.

Porous silicon microspheres were synthesized by using a low temperature for decomposing disilane, namely 400ºC, rather than higher temperatures because this allowed us an optimal control of the process timing. The absolute gas pressure in the reactor was about 130 kPa at room temperature, and we utilized decomposition times (DT from now on) from 1 to 2 minutes. Because it takes several minutes for the gas to reach the desired temperature and start decomposing, we monitored the path of a He-Ne laser through the reactor. This allowed us controlling when particle formation starts. The laser path can actually be seen inside the reactor when floating particles exist in the gas even although such particles are much smaller than the wavelength of the laser, i.e. 613 nm, by virtue of Rayleigh scattering. This time is taken as the reference starting point to measure DT.

Synthesis of the 2-acetamido-2-deoxy-β-d-glucopyranosyloxyacetic acid

Solvents were dried according to published methods and distilled before use.All other reagents were commercial compounds of the highest purity available. Unless otherwise indicated all reactions involving air- and moisture-sensitive materials were carried out under argon atmosphere, and those not involving aqueous reagents were carried out in oven-dried glassware. Analytical thin layer chromatography (TLC) was performed on aluminium plates with Merck Kieselgel 60F254 and visualised by UV irradiation (254 nm) or by staining with an ethanolic solution of phosphomolibdic acid. Flash column chromatography was carried out using Merck Kieselgel 60 (230-400 mesh) under pressure. ^{1}H NMR spectra were recorded in $CDCl_3$ and D_2O, at ambient temperature on AMX-400 spectrometer at 400 MHz, with residual protic solvent as the internal reference [$CDCl_3$, δ_H = 7.26 ppm]; chemical shifts (δ) are given in parts per million (ppm), and coupling constants (*J*) are given in Hertz (Hz). The proton spectra are reported as follows: δ (multiplicity, coupling constant *J*, number of protons, assignment).

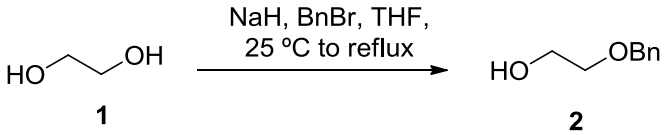

1 **2**

2-(Benzyloxy)ethanol 2. To a mixture of NaH (3.4 g, 0.085 mol, 60% w/w in mineral oil) in THF (150 mL), ethylene glycol **1** (25.1 mL, 0.45 mol) was addedand the mixture was stirred for 1 h at 25 ºC. Then, benzyl bromide (8.9 g, 0.075 mol) was added and the reaction was refluxed for 12 h. After cooling down the mixture (0 ºC), a saturated aqueous solution of NH_4Cl was added, the solvent was evaporated, and the mixture was extracted with EtOAc (3x). The combined organic layers were washed with a saturated aqueous solution of NH_4Cl and brine, and dried (Na_2SO_4).

The solvent was evaporated to afford 11.22 g (98% yield) of a colorless oil identified as 2-(benzyloxy)ethanol **2.** The spectroscopic data were identical to those described in the literature.[31] **H-NMR** (400 MHz, $CDCl_3$): δ 7.40-7.30 (m, 5H), 4.58 (s, 2H), 3.78 (t, *J*= 5.0 Hz, 2H), 3.61 (t, *J*= 4.9 Hz, 2H), 2.06 (br, 1H, OH) ppm.

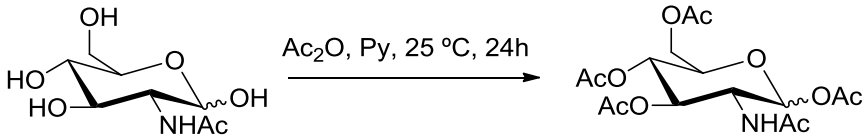

3 **4**

1,3,4,6-tetra-*O*-acetyl-α/β-*N*-acetylglucosamine 4.*N*-acetyl-D-glucosamine **3** (5 g, 22.6 mmol) was dissolved in pyridine (36 mL) and acetic anhydride (25 mL) was added dropwise at 0 ^{o}C. The reaction mixture was stirred at 25 ºC for 24 h, then diluted wth CH_2Cl_2 and washed consecutively with cold water, a saturated aqueous solution of $NaHCO_3$, and a 10% aqueous solution of $CuSO_4$. The organic layer was dried (Na_2SO_4) and the solvent was evapotared to obtain 6.60 g (75%) of a white solid identified as 1,3,4,6-tetra-*O*-acetyl-α/β-*N*-acetylglucosamine **4**. Thespectroscopic data were identical to those described in the literature.[41] **H-NMR** (400 MHz, $CDCl_3$): δ 6.17 (d, *J*= 3.6 Hz, 1H), 5.64 (d, *J*= 9.3 Hz, 1H), 5.30-5.20 (m, 2H), 4.49 (ddd, *J*= 10.6, 8.9, 3.6 Hz, 1H), 4.25 (dd, *J*= 12.5, 4.1 Hz, 1H), 4.07 (dd, *J*= 12.5, 2.4 Hz, 1H), 4.00 (ddd, *J*= 9.6, 4.0, 2.3 Hz, 1H), 2.20 (s, 3H), 2.09 (s, 3H), 2.06 (s, 3H), 2.05 (s, 3H), 1.94 (s, 3H) ppm.

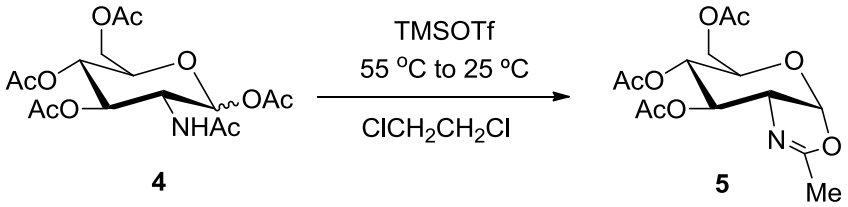

4 **5**

4',5'-Dihydro-2'-methyloxazolo[5',4':1,2]-3,4,6-tri-*O*-acetyl-1,2-dideoxy-α-D-glucopyranoside5.To a solution of 1,3,4,6-tetra-*O*-acetyl-α/β-*N*-acetylglucosamine

4 (2.49 g, 6.4 mmol) in dichloroethane (25 mL) TMSOTf (1.8 mL, 9.6 mmol) was added and the reaction was stirred for 2 h at 55 ^{o}C and for 12 h at 25 ºC. A saturated aqueous solution of $NaHCO_3$ was added and the mixture was extracted with CH_2Cl_2 (3x). The combined organic layers were washed with a saturated aqueous solution of $NaHCO_3$ and dried (Na_2SO_4) and the solvent was evaporated. The resulting residue was purified by column chromathography (silicagel, 97:3 CH_2Cl_2/MeOH) to afford 1.86 g (78%) of 4',5'-dihydro-2'-methyloxazolo[5',4':1,2]-3,4,6-tri-*O*-acetyl-1,2-dideoxy-α-D-glucopyranoside **5.** Thespectroscopic data were identical to those described in the literature.[51] **H-NMR** (400 MHz, $CDCl_3$): δ 5.98 (d, *J*= 7.4 Hz, 1H), 5.27 (t, *J*= 2.4 Hz, 1H), 4.94 (ddd, J= 9.2, 2.0, 1.2 Hz, 1H), 4.19-4.14 (m, 3H), 3.62 (dt, *J*= 8.8, 4.3 Hz, 1H), 2.12 Hz (s, 3H), 2.11 (s, 3H), 2.10 (s, 3H), 2.09 (s, 3H) ppm.

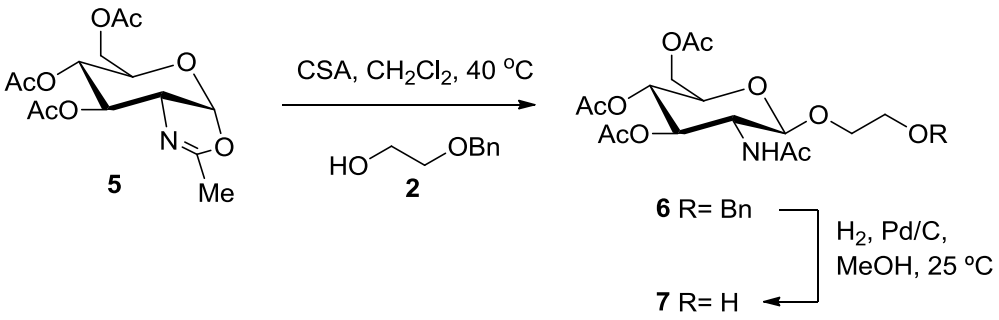

2-Hydroxyethyl-2-acetamido-3,4,6-tri-O-acetyl-2-deoxy-β-D-glucopyranoside

7. 10-(*R*)-Camphorsulfonic acid (1.40 g, 5.02 mmol) and 2-(benzyloxy)ethanol **2** (7.63 g, 50.2 mmol) were added to a stirred solution of 4', 5'-dihydro-2'-methyloxazolo[5',4':1,2]-3,4,6-tri-*O*-acetyl-1,2-dideoxy-α-D-glucopyranoside **5** (1.86 g, 5.02 mmol) and powdered 4 Å molecular sieves (ca. 8 g) in CH_2Cl_2 (30 mL) and the reaction was stirred at 40 ^{o}C for 14 h. The mixture was cooled down to 0 ºC, and a saturated aqueous solution of $NaHCO_3$ (60 mL) and CH_2Cl_2 (30 mL) were added. The layers were separated and the organic layer was washed with a saturated aqueous solution of $NaHCO_3$, brine and dried (Na_2SO_4), and the solvent was

evaporated. The residue was purified by column chromatography (hexane/EtOAc 50:50 to CH_2Cl_2/MeOH 95:5) providing 2-*O*-benzyloxyethyl-2-acetamido-3,4,6-tri-O-acetyl-2-deoxy-β-D-glucopyranoside **6** as a colorless solid. Thespectroscopic data of the product were identical to those described in the literature.[61] **^{1}H-NMR** (400 MHz, $CDCl_3$): δ 7.4-7.3 (m, 5H), 5.50 (d, *J*= 8.8 Hz, 1H), 5.25 (dd, *J*= 10.4, 9.4 Hz, 1H), 5.09 (t, *J*= 9.6 Hz, 1H), 4.76 (d, *J*= 8.4 Hz, 1H), 4.56 (app s, 2H), 4.27 (dd, *J*= 12.3, 4.7 Hz, 1H), 4.20-4.15 (m, 2H), 3.99 (dt, *J*= 11.5, 3.9 Hz, 1H), 3.80 (ddd, *J*= 18.2, 14.7, 11.2 Hz, 1H), 3.70-3.65 (m, 3H), 2.09 (s, 3H), 2.06 (s, 3H), 2.03 (s, 3H), 1.87 (s, 3H) ppm.

A mixture of 2-*O*-benzyloxyethyl-2-acetamido-3,4,6-tri-*O*-acetyl-2-deoxy-β-D-glucopyranoside **6** (0.19 g, 0.36 mmol) and Pd/C (10%, 0.02 g) in MeOH (3 mL) was stirred under H_2 atmosphere for 7h at 25 ºC. The reaction was filtered through Celite and the solvent was evaporated to afford 0.15 g (96%) of a solid identified as 2-hydroxyethyl-2-acetamido-3,4,6-tri-*O*-acetyl-2-deoxy-β-D-glucopyranoside **7.** Thespectroscopic data of the product were identical to those described in the literature.[61] **^{1}H-NMR** (400 MHz, $CDCl_3$): δ 5.58 (d, *J*= 9.0 Hz, 1H), 5.25 (dd, *J*= 10.6, 9.4 Hz, 1H), 5.07 (t, *J*= 9.6 Hz, 1H), 4.71 (d, *J*= 8.3 Hz, 1H), 4.2-4.10 (m, 2H), 3.9-3.8 (m, 2H), 3.7-3.6 (m, 2H), 2.58 (br, 1H, OH), 2.11 (s, 3H), 2.06 (s, 3H), 2.05 (s, 3H), 1.98 (s, 3H) ppm.

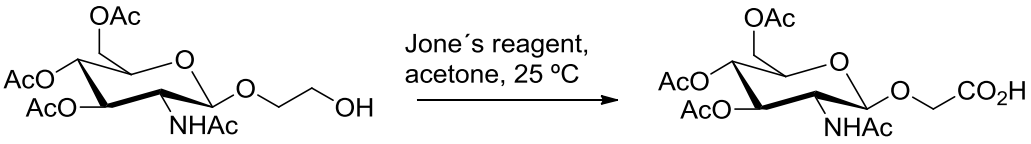

7 **8**

2-Acetamido-3,4,6-tri-*O*-acetyl-2-deoxy-β-D-glucopyranosyloxyacetic acid 8. Jones reagent (3.5 M, 0.2 mL, 0.69 mmol) was added to a stirred solution of 2-

hydroxyethyl-2-acetamido-3,4,6-tri-*O*-acetyl-2-deoxy-β-D-glucopyranoside **7** (0.15 g, 0.35 mmol) in acetone (2 mL) at 0 ^{o}C and the reaction was stirred for 13 h at 25 ºC. Isopropanol was added and the solvent was evaporated. After the addition of CH_2Cl_2 (10 mL) and brine (10 mL), the layers were separated, the organic layer was washed with brine and dried (Na_2SO_4), and the solvent was evaporated to afford 0.11 g (73%) of a white solid that was identify as 2-acetamido-3,4,6-tri-*O*-acetyl-2-deoxy-β-D-glucopyranosyloxyaceticacid **8**The spectroscopic data of the product were identical to those described in the literature[6]. **^{1}H-NMR** (400 MHz, $CDCl_3$): δ 6.57 (br s, 1H), 5.22 (t, *J*= 9.6 Hz, 1H), 5.11 (t, *J*= 9.6 Hz, 1H), 4.75 (d, *J*= 8.1 Hz, 1H), 4.35 (app s, 2H), 4.28 (dd, *J*= 12.1, 4.9 Hz, 1H), 4.15 (dd, *J*= 10.7, 2.1 Hz, 1H), 4.1-4.0 (m, 1H), 3.7-3.6 (m, 1H), 2.11 (s, 3H), 2.06 (s, 3H), 2.03 (s, 3H), 1.97 (s, 3H) ppm.

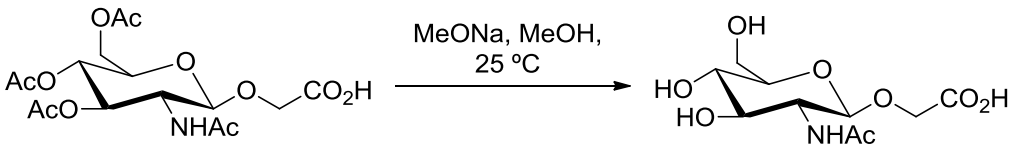

8 **9**

2-Acetamido-2-deoxy-β-D-glucopyranosyloxyacetic Acid 9. Sodium methoxide (0.02 g, 0.332 mmol) was added to a stirred solution of 2-acetamido-3,4,6-tri-*O*-acetyl-2-deoxy-β-D-glucopyranosyloxyaceticacid **8** (0.114 g, 0.255 mmol) in MeOH (6 mL) and the reaction mixture was stirred at 25 ºC for 24 h. After the addition of Dowex-200 the mixture was filtered and the solvent was evaporated. The residue was dissolved in H_2O and dried under vacuum to afford 0.071 g (99%) of a solid identified as 2-acetamido-2-deoxy-β-D-glucopyranosyloxyacetic acid **9**. THespectroscopic data of the product were identical to those described in the literature[6]. **^{1}H-NMR** (400 MHz, D_2O): δ 4.49 (d, *J*= 8.4 Hz, 1H), 4.18 (s, 2H), 3.83 (d,

J= 12.2 Hz, 1H), 3.70-3.60 (m, 2H), 3.50-3.40 (m, 1H), 3.40-3.30 (m, 2H), 1.97 (s, 3H) ppm.

Nanoparticle Functionalization

A suspension of APS-coated silica particles was produced by treatment of 0.1 g silica particles with aminopropylsilane (APS, 20 μL) in 2-propanol (5 mL) at 80 ^{o}C for 2h. The beads were centrifuged at 3800 rpm for 30 min to remove the excess APS, followed by replacement of the supernatant solution by isopropanol. The particles were re-dispersed by shaking (ultrasound) for 10 min. This protocol was repeated two more times.[7]

The beads were centrifuged at 3800 rpm for 30 min and the supernatant was replaced by DMF. Then, a solution of 2-acetamido-2-deoxy-β-D-glucopyranosyloxyacetic acid **9** (14 mg), BOP [benzotriazol-1-yloxy)tris(dimethylamino)phosphonium hexafluorophosphate, 29 mg], HOBt (7 mg) in dimethylformamine (DMF, 3mL) and diisopropylethylamine (30 μL) were added and the suspension was stirred for 12 h at 25 ºC. The beads were centrifuged at 3800 rpm for 30 min and washed with DMF and the supernatant was replaced by H_2O. The particles were re-dispersed by shaking (ultrasound) for 10 min. The supernatant was replaced by phoshate buffered saline (PBS, 1x).

To a suspension of the particles in PBS (2 mL) 250 μL of a solution of Anti-erbB-2/HER-2 (1 μL/L in PBS) was added and the mixture was shaken at 0 ^{o}C for 12 h. The beads were centrifuged at 3800 rpm for 10 min, and the supernatant was

replaced by PBS. The particles were re-dispersed by shaking (ultrasound) for 3 min at 0 ^{o}C.

Cell culture and viability assay

Materials: Dulbecco's modified eagle's medium (DMEM, #30-2002) and McCoy´s 5a medium (#30-2007) were purchased from ATCC. Fetal bovine serum (FBS, #S0615) was obtained from Biochrom AG and penicillin/streptomycin (#15140-122) from Gibco (#15140-122). L-glutamine (#25030-024) was purchased from Life Technologies. The viabilityassaybased on Resazurin (#TOX8) and the 96 well plates (#CLS3603) in whichthe viabilityassay was carried out were obtained from Sigma-Aldrich.

MDA-MB-435 human epithelial cells (ATCC #HTB-129) were seeded and grown in growth medium (DMEM with 4.5 g/L glucose supplemented with 10% FBS, 1% L-glutamine (200 mM) and 1% penicillin/streptomycin. SK-BR-3 human breast adenocarcinoma cells (ATCC #HTB-30) were seeded and grown in another growth medium (McCoy´s medium supplemented with 10% FBS, 1% L-glutamine (200 mM) and 1% penicillin/streptomycin.

Viabilityassay:

20,000 cells (MDA-MB-435 orSK-BR-3) were seeded per well in a 96 well plate and incubated in 100 µL of the corresponding cell medium for 48 h at 37 °C and 5% of CO_2. After this time, different concentrations of particles (SiNPs or SiNPs-HER-2) were added and cells were incubated for another 48 h. For each concentration the viability assaywas repeated three times. Control viability assayswere performedwith cells withoutparticles, and with particles without cells. After incubationcellular viability

was probed. Cells were washed with PBS and a solution of 10% of Resazurin in growth medium was added to each well. Cells were placed in the incubator for 3 h (37 °C and 5% CO_2). Resazurin is a nonfluorescent molecule which is reduced from the oxidized to the reduced form called resofurin by metabolically active cells. Resofurin is fluorescent, has a maximum emission wavelength at 585 nm (red emission), and can be excited from 530 to 560 nm. The fluorescent emission intensity originating from resofurin is proportional to the number of metabolically active (= living) cells. Fluorescence emission was measured with aFluorolog-3 spectrofluorometer equipped with a microwell plate reader (MicroMax 384) from Horiba JOBIN YVON. The samples were excited at 560 nm and the emission spectra were collected from572 nm to650 nm. Background was subtracted from the spectra. As the position of the maximum emission wavelength can be slightly shifted the peak emission was averaged from 584 nm - 586 nm.Theemission peakintensity values were normalized, considering a cell viability of 100 % for the control experiments in which no particles has been added to the cells. The normalized fluorescence emission peak intensities were plotted against the logarithm of the particle concentration, *cf*. Figure 3. Dose-response curves were obtained for SK-BR-3 and MDA-MB-435 exposed to different concentrations of Si-NPs and SiNPs-HER2, *cf*. Figure 3. The results were fitted to sigmoidal curves and the inflexion point was calculated. The inflexion point represents the LD_{50}valuw, which in this case is the concentration of particles at which cell viability is reduced to 50%, i.e. 50% of the cells are no longer metabolically active.The calculated LD_{50}valuesshown in Table 1.

REFERENCES:

1. Fenollosa, R., Meseguer, F. & Tymczenko, M. Silicon colloids: From microcavities to photonic sponges. *Advanced Materials***20**, 95-98 (2008).

2. Jasinski, J.M. & Gates, S.M. Silicon chemical vapor deposition one step at a time: fundamental studies of silicon hydride chemistry. *Accounts of Chemical Research***24**, 9-15 (1991).
3. Xiao, Q. et al. Potent Antitumor Mimetics of Annonaceous Acetogenins Embedded with an Aromatic Moiety in the Left Hydrocarbon Chain Part. *Journal of Medicinal Chemistry***54**, 525-533 (2010).
4. Allman, S.A. et al. Potent Fluoro-oligosaccharide Probes of Adhesion in Toxoplasmosis. *ChemBioChem***10**, 2522-2529 (2009).
5. Chambers, D.J., Evans, G.R. & Fairbanks, A.J. Elimination reactions of glycosyl selenoxides. *Tetrahedron***60**, 8411-8419 (2004).
6. Tomabechi, Y., Suzuki, R., Haneda, K. & Inazu, T. Chemo-enzymatic synthesis of glycosylated insulin using a GlcNAc tag. *Bioorganic & Medicinal Chemistry***18**, 1259-1264 (2010).
7. Pastoriza-Santos, I., Gomez, D., Perez-Juste, J., Liz-Marzan, L.M. & Mulvaney, P. Optical properties of metal nanoparticle coated silica spheres: a simple effective medium approach. *Physical Chemistry Chemical Physics***6**, 5056-5060 (2004).